

Digital Elevation Models and Delineation of Antarctic Glaciers Using Stereo Capabilities of ASTER Satellite Images

Steps on the way for a glacier monitoring on the Antarctic Peninsula

Doctoral Thesis
at the
Fakultät für Forst – und Umweltwissenschaften
Albert-Ludwigs-Universität
Freiburg i. Brsg.

submitted by
Ricardo Jaña Obregón
from Maipú

Freiburg im Breisgau
2006

Dekan: Prof. Dr. H. Rennenberg

Referent: Prof. Dr. H. Goßmann

Korreferent: Prof. Dr. B. Koch

Tag der mündlichen Prüfung: 18. Dezember 2006

*Dedicated to Ingrid,
to my parents
and
to Felipe, Renate, Gabriel and Pablo*

“... Difficulties are just things to overcome, after all.”

Sir Ernest Shackleton, 11 December 1908

Diary entry of the NIMROD Expedition

Acknowledgements

This work it would not have been possible without the aid and the friendship of many people that I have had the gift to find and of whom sincerely I am indebted.

First of all, my special thanks go to my “Doktor Vater”, Prof. Hermann Goßmann, for his wise advice, huge patience and enormous faith that permitted me to find the light at the other side of the tunnel. He has been not only the advisor that provided me guiding and stimulating discussions, but also, he provided me crucial support along all my work allowing me to reach this stage. Thanks again, because you forced me to endure and produce when you gave me all that encouragement to finish. Furthermore, I would like to thank the Prof. Barbara Koch who kindly agreed to act as a second reviewer of this work.

I am very grateful of persons that encouraged me to endeavor this adventure. Dr. Steffen Vogt opened me the door to come to Freiburg after we met in Antarctica several times for cooperative fieldwork. But, as Chilean governmental employee that I am, it was Dn. Oscar Pinochet de la Barra, the former Director of the Chilean Antarctic Institute (INACH), who authorized me to do a Ph.D. supporting my application to the 'Presidente de la República Scholarship'. Later, Dr. José Retamales, who superseded to Dn. Oscar as Director of INACH, confirmed to me the INACH's support. He also pushed me to a greater involvement with INACH's international activities during my stay in Germany. Thanks to you all three.

I would like to thank all my colleagues from the Department of Physical Geography of Freiburg University, for all the friendship and the help that you provided me during my stay in Freiburg. Especially I would like to thank to Dr. Helmut Saurer for your critic advice that always moved me ahead; to Dr. Klaus Braun for the computer assistance; Dr. Christoph Schneider and Dr. Matthias Braun for the advice and cooperative plans for the future; Dr. Frank Rau for the time dedicated to teach me in remote sensing techniques in my two firsts years in Freiburg; Dr. Steffen Vogt for the permanent help in many details of my work; and last but not least Jorge Arigony my office mate, for his constructive discussions and cooperative work.

I am also grateful of all my colleagues from INACH in Chile who not only cheer up me continuously but also did their job to make things easy to me when I was abroad. Especially I must recognize the consideration received from my colleagues from the Scientific Department, who as scientists, understood my interests and approved my requirements.

I would like to also give special thanks to all our friends in Freiburg that helped me and my family while we were far from our homeland. They took care of us and contributed to our comfort. Thanks Celia and Peter Höft, Elsbeth Schiller, Steffen Vogt and Susana Ginés, Jorge Arigony and Milene Stangler, and Enrique Muñoz, without your help things would have been not so nice.

My friends from the distant Chile also were crucial for the success of this work. Thanks Patricia Vicuña, Gonzalo Benavides, Laura Encina and Arturo Cares, your words contributed significantly to continue ahead.

I also wish to express my sincere gratitude to my parents for whom I could not fail and to whom this work is dedicated. Their good example made me prepared to complete this expedition.

Finally “thank you” seems to be inadequate to show how very much supportive my wife, Ingrid, has been during these years while indeed she was also doing her own Ph.D. and we both needed to take care of our children together.

This work has been possible thanks to the “Beca Presidente de la República” scholarship assigned to me by the Chilean Ministry of Planning (MIDEPLAN) and thanks to the support of the Chilean Antarctic Institute (INACH), that commissioned me to course this grade.

Summary

Ongoing climate warming on the AP indicates that changes in the glacial system are occurring as a sensible reaction to the climatic variations. Considering the warming trend not only are expected changes in the ice shelves, which seems to have a more fast reaction to external disturbances, but also in the other components that react with lower response times. Moreover, in despite that ice masses changes are connected with climate variations, it has been stressed that it is not clear the relation between changes on glacier geometry and climate variations. Thus, the interaction is more complex than is usually assumed.

To study how develops this phenomena the Antarctic Peninsula represents a source for cases study. The Peninsula stretch out roughly 1,500 km along a south to north axe from the 75°S to the 60°S, presenting an almost completely covered by ice and snow (98%) mountainous territory. Thus, the area comprises a complex glaciation with several merging ice caps, ice shelves, extensive mountainous terrain, outlet glaciers, and ice covered offshore islands. Surface rises up from the coast level to over 2,000 m a.s.l. at the central plateau, facing westward and eastward along the Peninsula, two different climatic regimens: the maritime polar at the Bellingshausen Sea sector on the western side, and the polar continental at the Weddell Sea sector on the eastern side of the Peninsula.

To monitor changes in the variety of elements that compound the glacial system of the Antarctic Peninsula, a systematic analysis of an adequate inventory of glaciological features present in the region is required. The establishment of such an inventory is currently being coordinated and performed by the Department of Physical Geography of Freiburg University (IPG Freiburg). IPG Freiburg hosts the GLIMS Regional Center for the Antarctic Peninsula. Because of the vastness of the region and the logistic difficulties associated to the demanding sampling of field based glaciology activities, working approaches consisting in the extraction of glaciological parameters based on the use of remote sensing data are being used.

However, a glacier inventory relies strongly on the geometry and geo-location of its features. The measuring of morphometric glacier parameters such as length, width, area, glacier front position, basin boundaries, and others morphometric measures where 3D coordinates are needed, requires a consistent spatial frame of reference.

Only in this case will be possible to compare variations in time in order to detect changes. An additional aspect to consider is the reliability of the delineation of boundaries made manually by operators. Subjectivity of this approach by different levels of skills should be avoided if automatic procedures perform the task.

Consequently, one of the big concern is the lack of geodetic and topographic data sets in the Antarctic Peninsula. Large scale topographic information also is sparse. Furthermore, both horizontal and vertical resolution of existent digital elevation models (DEMs) that cover the Antarctic Peninsula (RAMP DEM) limit detailed terrain modelling at larger scales. Consequently, for glacier mapping at catchment scale there is a need to produce cartography and terrain elevation models that provide sufficient spatial resolution. This necessity is also required for geo-coding and geometrical correction of satellite data being used for the extraction of other glaciological parameters.

Considering all this requirements and pursuing the idea that the use of satellite stereo imagery methods for topographic data generation along the Antarctic Peninsula offers interesting possibilities, we focused our research around this topic.

Consequently, we investigated into the use of near infra-red stereo pairs acquired by the *Advanced Spaceborne Thermal Emission and Reflection Radiometer* (ASTER) instrument, to derive digital elevation models on the snow and ice covered terrain that is found in the Antarctic Peninsula.

Based on a software tool that uses image matching method to derive the stereo parallaxes and corresponding terrain altitudes we were able to produce 24 different DEMs using several combinations of processing parameters (i.e. 15 m grid size, several search window sizes, yes or no extended correlation and yes or no water detection). These DEMs were post-processed by median filter in a double sequence to minimize the high frequency noise and artefacts on individual DEMs; and later, on a median stack for the set of 24 DEMs, resulting in our MED-MED model. A second approach consisted in the generation of a multi-temporal DEM considering several ASTER stereo pairs from different dates. In the multi-temporal approach it was used only one combination of processing parameters (3DEM_ model) evaluated as the most cost-effective solution. In order to exclude extreme artefacts it was also applied a median filtering resulting in a improved MT-MED model.

Models were evaluated against the reference TUD model in the Marguerite Bay test site evidencing a better agreement than it is shown by the standard RAMP model. Accuracy assessments of the models by profile line comparisons and by visual comparisons against real terrestrial pictures gave stimulating results that later were confirmed numerically. Inside the test site 622,345 altitude values representing cells of 30x30 were compared against the reference altitude. The results for RAMP, MED-MED and MT-MED models were: [RMS: 181.1; 79.6; 47.5], [Mean: -25.4; -32.1; -8.5] and [St.Dev.: 179.3; 72.8; 46.8]. Additionally can be stated that the MT-MED model has 83.9% of its values under 50 m, 48.1% lower than 20 m and 26% inferior to 10 m. Consequently, it is demonstrated a better quality compared with that of RAMP. On the other hand some artefacts were detected in the TUD reference model reason why the comparison can be more favourable for the MT-MED model.

Finally, MT-MED model was used to derive ice drainage catchments in the area of Marguerite Bay test site using a GIS-based automatic hydrological extraction. Method worked accordingly and post-processing allowed to remove spurious min-basins formed in the glacier cross-section used in the coastal ice cliff front. The location of ice divides was also easily analyzed with the additional support of three-

dimensional representation of the terrain draped with the orthorectified ASTER scene, contour lines from the DEM and basins polygons. All this approach proved to be suitable to support the task of gathering of geometric parameters of glaciological features.

Zusammenfassung

Die anhaltende Klimaerwärmung im Bereich der Antarktischen Halbinsel weist darauf hin, dass Veränderungen in den glazialen Systemen als sensible Reaktion auf die Klimaänderungen auftreten. Berücksichtigt man den Trend der Erwärmung, so sind nicht nur weitere Veränderungen in den Eisschelfen zu erwarten, sondern auch in den anderen Komponenten der glazialen Systeme, die langsamere Reaktionszeiten aufweisen.

Wie sich diese Phänomene in der Antarktischen Halbinsel entwickeln bietet Material für zahlreiche Fallstudien. Die Halbinsel erstreckt sich als fast vollständig eis- und schneebedecktes Gebirge entlang einer etwa 1500 km langen Achse von Süd nach Nord von 75°S bis 60°S Breite. Das Gebiet besteht aus einer komplexen Vergletscherung mit mehreren verbundenen Eiskappen, Eisschelfen, ausgedehnten gebirgigen Gebieten, Auslassgletschern, und der Küste vorgelagerten, eisbedeckten Inseln. Das Gelände steigt von der Küste bis auf 2000 m über dem Meer im Zentralplateau an. Entlang der Halbinsel können zwei Klimaregime auf der Ost- und der Westseite unterschieden werden: ein maritim-polares Klima im Sektor der Bellingshausen-See auf der Westseite, und ein kontinental-polares Klima im Sektor der Weddell-See auf der Ostseite.

Für ein Monitoring der Veränderungen in den einzelnen Komponenten der glazialen Systeme der Antarktischen Halbinsel ist eine systematische Analyse eines geeigneten Inventars glaziologischer Objekte notwendig. Der Aufbau eines solchen Inventars wird zur Zeit vom Institut für Physische Geographie der Universität Freiburg (IPG Freiburg) koordiniert und durchgeführt. Am IPG Freiburg ist das GLIMS Regional Center für die Antarktische Halbinsel beheimatet. Aufgrund des ausgedehnten Gebietes und der logistischen Schwierigkeiten bei der Durchführung von glaziologischen Feldarbeiten im Bereich der Halbinsel werden fernerkundungsbasierte Methoden zur Ableitung glaziologischer Parameter benutzt.

Die Grundvoraussetzung für ein sinnvoll nutzbares Gletscherinventar stellt jedoch die Verfügbarkeit der exakten Geometrie und Georeferenz ihrer Objekte dar. Das Erfassen morphometrischer Gletscherparameter für die 3d-Koordinaten benötigt werden, wie z.B. Länge, Breite, Fläche, Position der Gletscherfront oder Einzugsgebietsgrenzen, erfordert ein konsistenten räumlichen Bezugsrahmen als

Referenz. Nur damit ist es möglich, zeitliche Veränderungen zu erkennen. Ein weiterer Aspekt der beachtet werden muss, ist die Konsistenz und Vergleichbarkeit bei manuell durch Bearbeiter abgeleiteten Grenzen. Die Subjektivität solcher Verfahren kann vermieden werden, wenn automatisierte Prozessierungsschritte implementiert werden.

Folglich ist das Fehlen geodätischer und topographischer Daten für das Gebiet der Antarktischen Halbinsel eine der größten Schwierigkeiten sowohl beim Aufbau eines Gletscherinventars als auch bei einschlägigen Studien, die auf diesem Inventar basieren. Großmaßstäbige topographische Daten sind kaum verfügbar. Dazu ist sowohl die horizontale und vertikale Auflösung der vorhandenen, die gesamte Halbinsel abdeckenden, digitalen Geländemodelle ungenügend. Für Gletscherkartierungen im Maßstab von Einzugsgebieten besteht also Bedarf an Kartographie und Geländemodellen mit entsprechend ausreichender räumlicher Auflösung. Dieser Bedarf besteht auch für das Georeferenzieren und die geometrische Korrektur von Satellitendaten, die für die Ableitung weiterer glaziologischer Parameter benutzt werden.

Unter Berücksichtigung dieser Bedürfnisse und der Idee folgend, dass die Nutzung stereoskopischer Satellitenbilder zur Erzeugung topographischer Daten für die Antarktische Halbinsel interessante Möglichkeiten eröffnet, konzentrieren wir unsere Arbeiten im folgenden auf diese Thematik.

Wir untersuchen die Anwendung von Stereo-Bildpaaren aufgenommen mit dem *Advanced Spaceborne Thermal Emission and Reflection Radiometer* (ASTER) Sensor zur Ableitung digitaler Geländemodelle im schnee- und eisbedeckten Terrain der Antarktsichen Halbinsel.

Mit Hilfe einer Software, die Image-Matching-Methoden verwendet um Parallaxen und entsprechende Geländehöhen zu berechnen, konnten wir unter Benutzung verschiedener Kombinationen von Prozessierungsparametern aus einem Ausgangsdatensatz 24 unterschiedliche Geländemodelle ableiten. Diese Geländemodelle wurden einem Post-Processing mit einem doppelten Median-Filter unterworfen. Zunächst wurde das hochfrequente Rauschen und Artefakte in den einzelnen Geländemodellen unterdrückt. Danach wurde der gesamte Stapel der 24 Geländemodelle mit einem Median-Filter gefiltert. Diese doppelte Filterung hatte das MED-MED-Modell zum Ergebnis. Ein zweiter Ansatz bestand im Erzeugen eines multitemporalen Geländemodells, das mehrere ASTER Stereopaare von unterschiedlichen Aufnahmezeitpunkten als Ausgangsdatensätze mit einbezog. Bei diesem multitemporalen Ansatz wurde nur eine Kombination von Prozessierungsparametern berücksichtigt. Dies hatte sich als effektivstes Prozessierungsverfahren herausgestellt. Um noch verbliebene extreme Artefakte zu eliminieren wurde ein Median-Filter angewandt. Das Ergebnis ist das nochmals verbesserte MT-MED Modell.

Die Modelle wurden mit dem TUD-Referenz-Modell im Marguerite Bay Testgebiet verglichen. Diese Vergleiche lieferten weit bessere Ergebnisse als für das weit verbreitete RAMP-Geländemodell. Beurteilungen der Genauigkeit der Modelle basierend auf Analysen von Profilen entlang von Schnitten und durch visuelle Vergleiche mit Photographien des Geländes ergaben vielversprechende Resultate. Diese konnten dann mit numerischen Verfahren bestätigt werden. Im Testgebiet wurden 622 345 Höhenwerte, die sich jeweils auf Zellen von 30mx30m beziehen, mit Referenzhöhen verglichen. Die Ergebnisse für RAMP, MED-MED und MT-MED Modelle sind: [RMS: 181.1;79,6;47.5], [Mittelwert: -25.4; -32.1; -8.5] und

[Standardabweichung: 179.3; 72.8; 46.8]. Das MT-MED Modell liefert 83.9% Werte mit Höhendifferenzen weniger als 50 m, 48.1% weniger als 20 m und 26% weniger als 10 m. Das zeigt die verbesserte Qualität des aus ASTER-Daten abgeleiteten MT-MED Geländemodells verglichen mit dem RAMP-Modell. Zusätzlich konnten noch Artefakte im TUD-Referenzmodell nachgewiesen werden. Dies weist darauf hin, dass ein Vergleich mit diesem Referenzmodell die Qualität des MT-MED eher noch unterschätzt.

Abschließend wurde das MT-MED Modell im Gebiet der Marguerite Bay erfolgreich als Eingangsdatensatz zur Ableitung von Gletschereinzugsgebietsgrenzen mit einem aus der Hydrologie kommenden automatisierten GIS-Verfahren verwendet. Durch anschließendes Post-processing konnten die Mini-Einzugsgebiete eliminiert werden, die sich fälschlich an den Querschnitten entlang den Eiskliffs an der Küste gebildet hatten. Die Lage der Eisscheiden konnte mit Hilfe von dreidimensionalen Darstellungen des Geländes aus Geländemodell und darübergerlegtem Orthobild der ASTER-Szene, von Höhenlinien abgeleitet aus dem Geländemodell und von Polygonen der Einzugsgebietsgrenzen einfach bestimmt werden. Es zeigte sich, dass dieser integrierte Ansatz geeignet ist, geometrische Parameter für glaziologische Objekte abzuleiten.

Contents

Acknowledgements	I-1
Summary / Zusammenfassung.....	II-1
Contents	III-1
Index of Tables	IV-1
Index of Figures	V-1
Abbreviations.....	VI-1

1	Introduction	1-1
1.1	Motivation	1-1
1.2	Thesis	1-3
1.3	Aims.....	1-4
2	Terrain Modelling of the Glacial Systems on the Antarctic Peninsula	2-1
2.1	Antarctic Peninsula Geographical Setting.....	2-1
2.2	Antarctic Ice Drainage Basins.....	2-6
2.3	Digital Elevation Models For The Antarctic Peninsula	2-12
3	Aster DEM Generation	3-1
3.1	ASTER Satellite Data	3-1
3.1.1	Terra satellite, sensor description and ASTER stereo capability	3-1
3.1.2	ASTER Data Products	3-6
3.1.3	ASTER Data Catalogues	3-8

3.2	Available ASTER DEMs and their Problems.....	3-11
3.3	Generation of Digital Elevation Models using ASTER Imagery.....	3-14
3.3.1	Selected ASTER Data.....	3-14
3.3.2	ASTER-DEM Processing	3-18
3.3.2.1	Image matching as crucial point.....	3-18
3.3.2.2	Processing chain.....	3-24
3.3.3	ASTER-DEMs First Examples – Encouragement and Questions	3-26
4	ASTER Derived DEMs and Reality	4-1
4.1	Marguerite Bay Test Site and its Reference Terrain Model	4-1
4.1.1	Test site area description	4-1
4.1.2	Area occupation and scientific activities.....	4-3
4.1.3	Technical University of Darmstadt Digital Terrain Model (TUD DTM) and Base General San Martín Photo Map (TUD Karte) datasets.....	4-6
4.1.4	Post-Processing of the TUD DTM.....	4-8
4.2	Post-Processing of ASTER DEMs	4-11
4.3	Visual Comparison of Derived ASTER DEMs, TUD-DTM and Reality.....	4-14
4.3.1	Real and virtual landscapes	4-14
4.3.2	Profile comparison	4-16
4.4	Multi-temporal Approach.....	4-20
4.4.1	Method.....	4-20
4.4.2	Profiles comparison.....	4-27
4.5	Statistical Comparison of ASTER Derived DEMs, RAMP and the TUD Reference Model.....	4-32
5	Drainage Basins Delineation.....	5-1
5.1	From DEM to Catchment Extraction	5-1
5.2	Algorithm and Workflow	5-2
5.3	Results of Derivation of Ice Catchments on Marguerite Bay Test Site.	5-5
6	Results And Outlook.....	6-1
6.1	Review of Results	6-1
6.1.1	Data needs.....	6-1
6.1.2	New data source	6-2
6.1.3	ASTER DEM generation	6-2

6.1.4	ASTER derived DEMs and Reality.....	6-3
6.1.5	Drainage Basin Delineation.....	6-5
6.2	Outlook	6-6
6.2.1	Use of DEMs and corresponding orthorectified images	6-6
6.2.2	Enhancement of GLIMS database over the Antarctic Peninsula	6-6
6.2.3	Glacier basin delineations	6-6
7	References.....	7-1
8	Annex 1: CD-ROM	
8.1	Virtual Flight	
8.2	High resolution Figures	
8.3	PDF file Thesis	

Index of Tables

Table 2.1a:	Continental ice drainage delineations in Antarctica.	2-7
Table 2.1b:	Regional and large scale ice drainage delineations in the Antarctic Peninsula.	2-10
Table 2.2:	Digital elevation models (DEMs) covering the Antarctic Peninsula.	2-13
Table 3.1:	General specifications of the Terra spacecraft	3-2
Table 3.2:	Spectral range and spatial resolution of the fourteen ASTER bands.....	3-3
Table 3.3:	ASTER standard data products.....	3-6
Table 3.4:	Standard ASTER Level 4 Digital Elevation Model products (AST14DEM) already produced for the Antarctic Peninsula region.	3-12
Table 3.5:	List of the selected ASTER Level-1A scenes (L1A) for DEM generation in the Antarctic Peninsula region.	3-16
Table 3.6:	Names for the 24 digital elevation models generated using the AsterDTM v2.24 software selecting different combinations of processing parameters ‘water detection’, ‘extended correlation’ and ‘correlation matrix size’.	3-23
Table 4.1:	Parameters of Technical University Darmstadt Digital Terrain Model (TUD-DTM) data set.....	4-6
Table 4.2:	Statistical comparison of original and reprojected TUD model (TUD-DTM).....	4-10

Table 4.3:	L1A scenes used for the derivation of the Multi-temporal Median DEM (MT-MED model) on the Marguerite Bay Test Site.....	4-26
Table 4.4:	Basic statistics of MT-MED model and its derived RMS grid.....	4-26
Table 4.5:	Basic statistics parameters of altitude deviations between different elevation models (TUD – RAMP, TUD - MED-MED and TUD - MT-MED)	4-36
Table 4.6:	Distribution of altitude deviations between different elevation models (TUD – RAMP, TUD - MED-MED and TUD - MT-MED): Absolute and relative frequencies in classes used in Figure 4.20. .	4-37
Table 4.7:	Distribution of altitude deviations between three different elevation models (TUD – RAMP, TUD - MED-MED and TUD - MT-MED): Median (P50), Quartiles (P25, P50, P75) and selected Deciles (P10, P40, P60, P90).....	4-38

Index of Figures

Figure 2.1:	Major features and small scale topography of Antarctic Peninsula derived from Antarctic Digital Database (ADD) and RADARSAT Antarctic Mapping Mission Project (RAMP) Digital Elevation Model (DEM), two standard geo-datasets.	2-2
Figure 2.2:	Ice cap, glaciers and small ice-shelf of James Ross Island; in the background Prince Gustav Channel and Louis Philippe and Laclavère Plateaus, northern Antarctic Peninsula.	2-4
Figure 2.3:	Ice field and deep cut glacier valleys at Cape Northrop. Rock outcrops located at photography's lower right hand, prolongs up to Hodges Point; in the foreground ice grounding zone of Larsen Ice Shelf.	2-5
Figure 2.4:	Steps in delineation of ice divides in Antarctica at continental scale by different authors.	2-8
Figure 2.5:	The two most recent maps of catchment basin boundaries and ice flow of Antarctica at continental scale.	2-9
Figure 2.6:	Relief and ice divides of James Ross Island after Rabassa et al. (1983).	2-10
Figure 2.7:	Delineation of glacial drainage systems on Davis and Danco Coast by Williams et al. (1989).	2-10
Figure 2.8:	Three delineations for ice catchments of King George Island Ice Cap; based on visual interpretation and manual delineation of SPOT different methods over topographic maps, digital elevation models and SPOT satellite mosaics.	2-11
Figure 2.9:	One of the most recent ice drainage basin delineation in the Antarctic Peninsula region.	2-12

Figure 2.10:	Antarctic Peninsula topography based on the RADARSAT Antarctic Mapping Project Digital Elevation Model (RAMP DEM), (Liu et al., 2001) and the Antarctic Digital Database (ADD Consortium, 2004) coast line datasets.	2-15
Figure 2.11:	Shaded relief sections of RAMP DEM v2; a remarkable level of detail is appreciated in these three examples from the Antarctic Peninsula.	2-16
Figure 2.12:	Digital elevation model of the surroundings of the Base General San Martin (IfPK TUD, 1999).	2-18
Figure 3.1:	Terra spacecraft and payload.	3-2
Figure 3.2:	ASTER Visible and Near Infrared (VNIR) subsystem telescopes design.	3-4
Figure 3.3:	Imaging geometry and data acquisition timing for ASTER along-track stereo.	3-5
Figure 3.4:	Coverage of ASTER scenes Level 1A over Antarctic Peninsula region and surrounding Seas acquired between 17.11.2000 and 30.09.2005.	3-10
Figure 3.5:	Coverage of ASTER Level 1A diurnal scenes over land ice in the Antarctic Peninsula region acquired between 17.11.2000 and 30.09.2005.	3-10
Figure 3.6:	Location of the 16 standard AST14DEM-relative digital elevation model products for the Antarctic Peninsula already available for distribution in the EOS Data Gateway (EDG) website.	3-11
Figure 3.7:	Examples of AST14DEM standard products, showing problems (holes without data) caused by low image matching correlation over flat snow surfaces.	3-13
Figure 3.8:	Location of ASTER Level 1A scenes selected for DEM generation in the Antarctic peninsula region.	3-15
Figure 3.9:	Principle of ASTER stereo capability with its nadir and backward viewing pushbroom scanners.	3-19
Figure 3.10 a:	Error for elevation and across-track components of parallax geometry within the Nadir channel and the Backward channel of ASTER scene.	3-19
Figure 3.10 b:	Along-track components of parallax geometry between the Nadir channel beam and Backward channel beam for any point within the ASTER scene.	3-20
Figure 3.11:	Band 3N (left) and 3B (right) of ASTER scene SC:AST_L1A.003:2030971130, Sept. 19, 2005, 13:33:26, Fallières Coast, Marguerite Bay area.	3-21

Figure 3.12:	Area-based matching between Nadir and Backward images of an ASTER scene.	3-22
Figure 3.13:	Cross-Correlation Coefficients between pixel values of templates and the matching window during the shift of the template along the quasi-epipolar line.	3-23
Figure 3.14:	Flow diagram for DEM generation using AsterDTM v2.24 software. Chain of different processes starting with an ASTER Level 1A stereo pair [bands 3N and 3B] to produce a digital elevation model (DEM), corresponding correlation matrix and orthorectified image.	3-25
Figure 3.15:	ASTER digital elevation model of James Ross Island, with different related data sets and aspects.	3-28
Figure 3.16:	ASTER digital elevation model of the northern part of Detroit Plateau, Trinity Peninsula, with different related data sets and aspects.	3-29
Figure 3.17:	ASTER digital elevation model of Fallières Coast, Marguerite Bay area with different related data sets and aspects.	3-30
Figure 4.1:	Image map of Fallieres Coast, Marguerite Bay. Main geographical features and historical and recent research bases.	4-2
Figure 4.2:	Panoramic photos taken during the United States Antarctic Service Expedition (USASE), East Base party, showing the weather station installed on the plateau (ca. 1800 m) and surrounding landscape during summer 1940-41.	4-4
Figure 4.3:	IPG's field camp and corner reflector settled on the McClary Glacier during the 1994 ground truth campaign within DYPAG project activities.	4-5
Figure 4.4:	Base General San Martin aerial photo map prepared within the DYPAG project. Original scale 1:50.000, reduced by factor 4.	4-7
Figure 4.5:	Map of Debenham Islands and front of McClary and Northeast glaciers based on raster representation of TUD-DTM, according to the original 30 m grid cell size and Lambert Conformal Conic projection.	4-8
Figure 4.6:	Three dimensional representation of the Technical University of Darmstadt digital terrain model (TUD-DTM) generated by photogrammetric techniques draped out with its corresponding hill shaded image.	4-8
Figure 4.7:	Flow diagram used to process the TUD-DTM raw data and to prepare it for registration and comparison with ASTER and RAMP DEMs.	4-9

Figure 4.8:	Profile section crossing glaciers and ridges along test site on Marguerite Bay region, which will be used for comparison of the effect of median filtering with different kernels in Figure 4.9.	4-12
Figure 4.9:	Profile AA' over a 15 m spatial resolution model (ASTER DEM3, see Table 3.6) after application of median filter of different kernel sizes.	4-12
Figure 4.10:	MED-MED model overlayed by the orthorectified ASTER scene, (SC:AST_L1A.003:2030971130, Sept. 19, 2005, 13:33:26) of Marguerite Bay test site.	4-13
Figure 4.11:	Photos of DYPAG field campaigns and an overflight and corresponding ASTER virtual landscape.	4-15
Figure 4.12:	Location of vertical profiles in the test site area.	4-17
Figure 4.13:	Comparison of hypsometric profiles taken from RAMP (magenta), TUD (blue) and the ASTER derived MED-MED (green) models.	4-19
Figure 4.14 a:	Accuracy evaluation of 24 ASTER derived elevation models for Marguerite Bay test site by analysis of altitude scatterograms.	4-22
Figure 4.14 b:	Accuracy evaluation of 24 ASTER derived elevation models for Marguerite Bay test site by analysis of altitude scatterograms.	4-23
Figure 4.15:	Demonstration of differences and impact of artefacts between two ASTER derived DEMs using images of shaded relief (hill shading).	4-24
Figure 4.16:	Flow diagram for the multi-temporal ASTER scenes processing approach	4-25
Figure 4.17:	Comparison of the Multi-temporal Median model (MT-MED) against other hypsometric profiles. Curves are taken from the ASTER derived MED-MED model (green), TUD-DTM (blue) and the ASTER derived MT-MED model (red).	4-27
Figure 4.18a:	Ice divide of McClary Glacier (see Profile DD').	4-28
Figure 4.18b:	Cross sections NW-SE over three glaciers (Todd Glacier, McClary Glacier and Northeast Glacier; section of Profile AA')	4-29
Figure 4.18c:	Down-slope profile of the Northeast Glacier (section of Profile BB').	4-29

Figure 4.18d:	Moraine ramp between head of Northeast Glacier and Plateau of the Antarctic Peninsula (the so-called Sodabread Slope; section of Profile BB'; see figure 4.12).	4-30
Figure 4.19a:	Problems detected in the different models: Weak co-registration between the TUD model and both MED-MED and MT-MED ASTER derived models.	4-30
Figure 4.19b:	Problems detected in the different models: Impact of artefacts within the available number of ASTER scenes.	4-31
Figure 4.19c:	Problems detected in the different models: Uncertainties in the TUD reference model due to artefacts (holes and some noise).	4-31
Figure 4.20	Altitude deviations between TUD reference model vs. ASTER derived models and RAMP DEM.	4-33
Figure 4.21	Frequency curves of altitude deviations between different elevation models	4-36
Figure 5.1:	Flow diagram for the ArcGIS based method to derive glacier basins from large scale ASTER DEMs.	5-4
Figure 5.2:	Raw results from the ArcGIS based catchment extraction method applied to MT-MED DEM.	5-6
Figure 5.3:	Example of derived boundaries: Overlay of automatically extracted basin boundary of McClary and Northeast glaciers in the area of Butson Ridge over the aerial photo map of the Technical University of Darmstadt.....	5-7
Figure 5.4:	Northeast Glacier catchment area resulting from manual post-processing of the automatically derived raw basin data.	5-9
Figure 5.5:	Different views on Northeast and McClary glaciers. Flow arrows. The 3D-views produced on the basis of an orthorectified ASTER "L1B" mosaic	5-10

List of Abbreviations

AAD	Australian Antarctic Division
AOS	ASTER Operation Segment
AP	Antarctic Peninsula
ASCII	American Standard Code for Information Interchange
ASTER	Advanced Spaceborne Thermal Emission and Reflection Radiometer
ATBD	Algorithm Theoretical Basis Documents
AWI	Alfred Wegener Institute
BPRC	Byrd Polar Research Center
BKG	Bundesamt für Kartographie und Geodäsie
CCD	Charged Coupled Detector
CERES	Clouds and the Earth's Radiant Energy System
CGA	Composite Gazetteer of Antarctica
CSMS	Communication and System Management Segment
DAAC	Distributed Active Archive Center
DEM	Digital Elevation Model
DGS	Data Gateway System
DTM	Digital Terrain Model
DYPAG	Dynamic Processes of the Antarctic Geosystems
ECS	EOSDIS Core System
EDC-DAAC	EROS Data Center of the DAAC
EDG	Earth Observing System Data Gateway
ELA	Equilibrium Line Altitude

EOS	Earth Observing System
EOSDIS	Earth Observing System Data and Information System
EROS	Earth Resources Observation and Science
ERSDAC	Earth Remote Sensing Data Analysis Center
ESA	European Space Agency
GARS	German-Chilean Antarctic Receiving Station
GCPs	Ground Control Points
GDS	Ground Data System
GIS	Geographical Information System
GLIMS	Global Land Ice Measurement from Space
HDF	Hierarchical Data Format
HRV	High Resolution Visible
IfAG	Instituts für Angewandte Geodäsie
IFOV	Instantaneous Field of View
IPG	Department of Physical Geography of Freiburg University
JERS	Japanese Earth Resources Satellite
JPL	Jet Propulsion Laboratory
JRI	James Ross Island
L1A	Level-1A ASTER product
L1B	Level-1B ASTER product
LP DAAC	Land Processes Distributed Active Archive Center
METI	Japan Ministry of Economy, Trade and Industry
MISR	Multi-angle Imaging Spectro-Radiometer
MODIS	Moderate-resolution Imaging Spectroradiometer
MOPITT	Measurement of Pollution in the Troposphere
NASA	National Aeronautics and Space Administration
OSU91A	Ohio State University Geoid 91A
RAMP	RADARSAT Antarctic Mapping Mission Project
SCAR	Scientific Committee on Antarctic Research
SDPS	Science Data Processing Segment
SDTS	US Spatial Data Transfer Standard
SPOT	Système Pour l'Observation de la Terre
SWIR	Shortwave Infrared
TIR	Thermal Infrared
URL	Unique Resource Locator
USASE	United States Antarctic Service Expedition

USGS	U.S. Geological Survey
VNIR	Visible and Near Infrared
WAIS	West Antarctica Ice Sheet
WGS84	World Geodetic System 1984
XS	Multi-spectral

1 Introduction

1.1 Motivation

The Antarctic Peninsula is one of the areas where a persistent increase of the mean air temperature has been reported in the last decades (VAUGHAN ET AL., 2001; HANSEN ET AL., 1999; KING & HARANGOZO, 1998; KING, 1994). This warming suggests that changes in the glacial system occur as a sensible reaction to the climatic variations. Coincidentally, ice-shelf disintegration events of pronounced magnitudes have been registered repeatedly for the northern part of the Peninsula (SKVARCA & DE ANGELIS, 2003; SCAMBOS ET AL., 2003). This phenomenon is affecting not only ice shelves but also other components of the glacial system that react to external disturbances with slower response times. The changes in glacier geometries such as thinning or thickening of ice volumes, advances or retreats of frontal positions, and shrinking or expansion of ice area coverage, are related to climate changes.

To monitor these changes in the variety of elements that compound the glacial system of the Antarctic Peninsula, a systematic analysis of an adequate inventory of glaciological features present in the region is required. The establishment of such an inventory is currently being coordinated and performed by the Department of Physical Geography of Freiburg University (IPG Freiburg). IPG Freiburg hosts the GLIMS Regional Center for the Antarctic Peninsula. This regional center is part of the international project Global Land Ice Measurement from Space (GLIMS). GLIMS aims at establishing a global inventory of glaciers based on remotely sensed data. The inventory until now has not been completed yet. Methodologies for different types of analysis of the respective data still are being investigated.

The region of the Antarctic Peninsula is vast, stretching southward from 60°S for more than 1,500 km up to 75°S. It is widely glaciated, forming a continuum of ice and snow only interrupted by rock outcrops which complicate the delineation of glaciological features.

Traditionally, the remoteness and harsh environmental conditions that occur in this region have prevented the access to most parts of the region. This has resulted in a lack of geodetic information collected by field parties. For instance an adequate Ground Control Point (GCP) database is not available. Large scale topographic information also is sparse. Furthermore, both horizontal and vertical resolution of

existent digital elevation models (DEMs) that cover the Antarctic Peninsula (USGS, 1996; BAMBER & BINDSCHADLER, 1997; LIU ET AL., 2001) limit detailed terrain modeling at larger scales. Consequently, for glacier mapping at catchment scale there is a need to produce cartography and terrain elevation models that provide sufficient spatial resolution.

Information about relevant glaciological parameters can be extracted from the currently available multi-sensor and multi-temporal satellite data. Some methods that use space borne optical sensor data to retrieve such parameters have been tested mainly for alpine and temperate glacier regions (PAUL, 2001; PAUL ET AL., 2002). Nevertheless, in the Antarctic Peninsula some factors related to the specific characteristics of this maritime polar environment (e.g. cloudiness, high reflection of snow covered surfaces, morphology of the terrain, etc.) render the application of these digital image processing methods difficult. Consequently, investigation, testing and adaptation of these traditional algorithms for application on the Antarctic Peninsula is required.

A glacier inventory relies strongly on the geometry and geo-location of its features. The measuring of morphometric glacier parameters such as length, width, area, glacier front position, basin boundaries, and others where 3D coordinates are needed, requires a consistent spatial frame of reference. Only in this case will be possible to compare variations in time in order to detect changes.

Considering this the use of satellite stereo imagery methods for topographic data generation along the Antarctic Peninsula offers interesting possibilities for research. With this focus we will investigate into the use of near infra-red stereo pairs acquired by the *Advanced Spaceborne Thermal Emission and Reflection Radiometer* (ASTER) instrument. The ASTER visible/near infra-red bands sub-system offers 15 m of spatial resolution. The geometry of the acquisition has a base-to-height ratio of 0.6, considered acceptable for DEM generation (ABRAMS ET AL., 2002). In many regions of the Earth it has been demonstrated that the ASTER stereo system allows the generation of DEMs with an acceptable accuracy (KÄÄB, 2002; TOUTIN & CHENG, 2002; HIRANO ET AL., 2003; FUJISADA ET AL., 2005; KÄÄB, 2005). ASTER satellite data has been envisaged as a source to support GLIMS activities (RAUP ET AL., 2000).

The along-track stereo has advantages compared with across-track systems, because the radiometric variations between images taken on subsequent satellite revolutions usually heavily affect the resulting DEM. For this, using ASTER stereo pairs is a better choice compared to across-track data with similar spatial resolution because of the simultaneous along-track acquisition during a single pass (TOUTIN & CHENG, 2003). For glaciology applications this is the preferable option (KÄÄB, 2005).

A successful generation of digital elevation models data sets for specific sectors of the Antarctic Peninsula region will contribute to fill the current gaps of topographic data. Based on these DEMs it also should be possible to perform geometric corrections of satellite data and to establish automatic derivation of ice drainage catchments.

Some complementary Antarctic datasets, such as digital cartography and glacier attributes data are also available. Digital cartography from the Antarctic Digital Database v4.1 (ADD; ADD CONSORTIUM, 2004) and names for geographic features from the SCAR Composite Gazetteer of Antarctica (CGA) assist in generating a well documented description of geographical elements under study. These products provide a well established reference to document glaciological features.

However, the delineation of glacier limits and ice drainage catchments boundaries is not easy in a landscape covered mostly by ice and by snow. The central plateau of the Antarctic Peninsula, with an altitude of ca. 2000 m a.s.l., stretches in a north to south orientation, defining the main relief feature that controls the distinctive mountainous character of its topography. Steep slopes fall to the eastern and western sides. The relief spreads out interrupting the coverage of ice and snow only by the occurrence of rock cliffs, nunataks and rock outcrops. In some places, exposed rocks and the sea at the coastline give some contrast but in others even the limits against the sea are difficult to identify due to the presence of sea-ice.

Finally, because the Antarctic Peninsula is a vast region automatic or/and semi-automatic processing is desirable in order to facilitate an efficient analysis. Results of the processing procedures should be reproducible and must enable the estimation of errors due to inaccuracies of the various input data sets and that must be available before operational analysis starts.

Based on these constraints and opportunities, it is suggested to follow a line of investigation to explore the implementation of reliable methodologies that contribute to solve the tasks of GLIMS Regional Center for the Antarctic Peninsula.

1.2 Thesis

We suggest that based on the stereo along-track data of *Terra's* ASTER instrument, for the Antarctic Peninsula terrain it is possible to generate reasonably accurate digital elevation models (DEMs) of improved spatial resolution compared to existing models.

These enhanced ASTER derived digital elevation models with 30 m spatial resolution will fill the current gaps of large scale terrain information, providing the source topographic data to delineate ice drainage catchment boundaries with the required accuracy. Furthermore, the monitoring of dynamic glacier parameters by remote sensing techniques would be improved by the use of geometrically corrected imagery based on these DEMs.

Manual delineation of ice catchments in the Antarctic Peninsula is a time consuming method and products may have discussible reliability. The results depend strongly on the geo-coding of the data and on the skill of the operators. Consequently, to extract ice drainage basins and catchments areas, the use of an automatic GIS-based approach build on these DEMs should provide reproducible raw data sets. Subsequently, the raw ice basins can be analyzed and integrated following a standard procedure that minimizes the subjective interpretations of boundaries of glaciological features.

Also, a positive impact can be expected from the minimization of spatial distortions due to the orthorectification based on the ASTER derived DEMs. The geo-location of extracted ice drainage limits will be more reliable in this mountainous region after geometrically correcting the satellite imagery.

Consequently, ASTER derived DEMs will contribute substantially to the establishment of a spatial database needed to create reproducible products that facilitate the automatic delineation and detection of glacier limits.

1.3 Aims

The general intention of this work is to contribute to the tasks that the Department of Physical Geography of Freiburg University pursues as Regional Center for the Antarctic Peninsula inside of the wider international project Global Land Ice Measurement from Space (GLIMS).

The main efforts will be related to the evaluation of methods based on the use of ASTER stereo imagery to extract topographic information and to derive complementary data sets. Major parts of the work will be dedicated to the evaluation of the accuracy of the resulting DEMs.

The expected result of the work is an integrated method that permits the compilation of large scale DEMs in any place of the Antarctic Peninsula from suitable ASTER L1A imagery data. These DEMs, because of their enhanced spatial resolution and accuracy, then will facilitate the automatic delineation of ice drainage basins and catchments of the Antarctic Peninsula region.

The generation of this methodological approach and the provision of DEMs and derived products will contribute to the Antarctic Peninsula Glacier Inventory, already initiated in accordance with the GLIMS specifications. Thus the measuring of geometric and dynamic parameters (width, length, area, velocities, etc.) can be associated to defined ice drainage catchments using GIS based tools.

2 Terrain Modelling of the Glacial Systems on the Antarctic Peninsula

If we wish to provide a methodology for boundary delineation of the glacial systems' components in the region of Antarctic Peninsula (AP), we first need to collect the basic knowledge about the main physical characteristics of its natural environment. With this regard a suitable description of its surface topography is a fundamental piece of information. For that reason, before describing our own work, we synthesize existing material to answer the following key questions:

- What is the physiography of the Antarctic Peninsula?
- Which are the components of the Antarctic Peninsula glacial systems? What characteristics do they have?
- Which criteria can be considered to delineate the components?
- What has been done up to now in the field of terrain modelling and catchment delineation within this area?
- What kind of Antarctic Peninsula terrain information exists? Which are the characteristics of this information?

In this chapter we provide this background information by the sections 2.1 – AP Geographical Setting, 2.2 – Ice drainage basins, and 2.3 - Available Digital Elevation Models for the AP.

2.1 Antarctic Peninsula Geographical Setting

The Antarctic Peninsula (Figure 2.1), is one of the constituent parts of the West Antarctica Ice Sheet region (WAIS). Usually it is defined as the area located between 62° and 75° latitude South and 55° and 85° longitude West, including the South Shetland Islands and the islands in the north western Weddell Sea (INGÓLFSSON ET AL., 2003; WEIDICK & MORRIS, 1998). It consists of a narrow less than 250 km wide landmass, which stretches from the Antarctic continent almost 1250 km to the north.

From a geological and geo-tectonical point of view it is quite similar to the cordillera of the Andes in southernmost South America, separated only by the Drake Passage (DOMACK ET AL., 2003). Before the final break of Gondwana, the southern Andean arc complex and the pre-Jurassic basement rocks were most likely contiguous with the linear feature of the Antarctic Peninsula. The AP basement rocks are referred to as the Trinity Peninsula Group which consist of intermediate grade metamorphic rocks formed in an accretionary prism (BARKER ET AL., 1991).

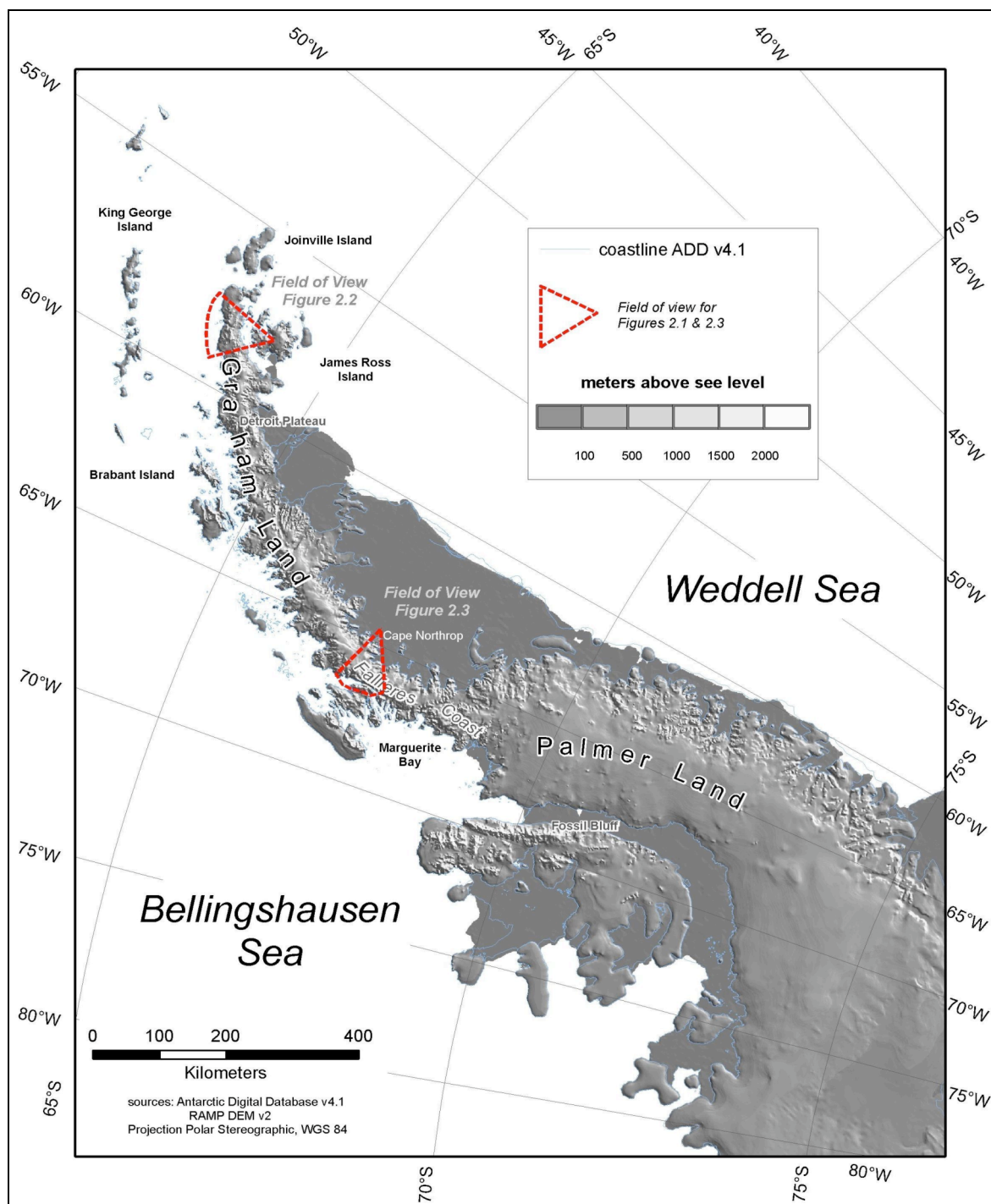


Figure 2.1: Major features and small scale topography of Antarctic Peninsula derived from Antarctic Digital Database (ADD) and RADARSAT Antarctic Mapping Mission Project (RAMP) Digital Elevation Model (DEM), two standard geo-datasets.

Data sources: ADD v4.1 (ADD CONSORTIUM, 2004) and RAMP-DEM v2 (LIU ET AL., 2001)

A variety of sedimentary and igneous rocks has been identified in specimens collected from nunataks, including a marine sandstone dated as Cretaceous on paleontologic evidence. The disturbed attitude of the beds in the outcrops and lithologic associations indicate that the nunataks and associated ranges were developed in a marine mobile belt, subjected to volcanic and orogenic activity, and are part of a folded mountain chain forming a continuation of the folded ranges in the northern part of the region (LAUDON ET AL., 1964).

Climatologically the Antarctic Peninsula can be divided into two climatic zones: polar maritime on the western side and polar continental east of the Peninsula. The northern and central parts of the Antarctic Peninsula are under the influence of strong westerly winds while, in the southernmost parts of the region, coastal easterlies prevail. Thus, mountains of the Peninsula provide an effective barrier to the low-level northwesterly flow (KING ET AL., 2003). As consequence we find along the west coast a frequent change of air masses, while the east coast is dominated by an influence of Weddell Sea cold polar air.

This results in considerable differences in temperatures and precipitation between west and east. The annual mean temperature at the Weddell Sea coast is about 7 or 8K lower than on the other side (-3° against -11° at 65° , -7° against -15° at 70° , REYNOLDS (1981)). Compared with other regions of Antarctica the Antarctic Peninsula receives very high precipitation rates. TURNER ET AL. (1995), reported that most of the precipitation on the west coast came from synoptic scale weather systems moving across Bellingshausen Sea. Here precipitation may exceed 1,000 to 1,500 mm water equivalent yr^{-1} , while east of the topographic divide on the AP precipitation is in the range of 100 to 200 mm water equivalent yr^{-1} (INGÓLFSON ET AL., 2003). Most winter precipitation falls as snow but, during summer, snow and rain occur with approximately equal frequencies. A large variation in local accumulation due to the mountainous orography of the Antarctic Peninsula has been reported (KING ET AL., 2003).

These differences in both precipitation and temperatures are reflected in the position of the equilibrium line altitude (ELA): because of heavier precipitation on the western side of the AP the ELA often is located at less than 100 m a.s.l., while due to a combination of low temperatures and low precipitation it can locally lie above 400 m a.s.l. on the Weddell Sea side (Ingólfson et al., 2003).

A relatively high plateau, about 2.000 m a.s.l., with peaks rising to over 2.500 m a.s.l. is forming the central spine of the Antarctic Peninsula, providing a source of ice for valley and outlet glaciers. Spreading to the west and east sides, ridges with spectacular mountains tower above an icing landscape of steep valley walls flanked by tidewater glaciers that calve into an iceberg-studded system of deep fjords (HANSOM & GORDON, 1998). To the east attached to the inland ice system, vast ice shelves float and calve into the Weddell Sea. These recently have shown dramatic changes (SKVARCA & DE ANGELIS, 2003; SCAMBOS ET AL., 2003). In some cases, mostly in the north the glaciers end on land but generally the ELA is below sea level in this region (WEIDICK & MORRIS, 1998). This results in the wide glaciated characteristic of the region.

Thus, the area comprises a complex glaciation with several merging ice caps, ice shelves, extensive mountainous terrain, outlet glaciers, and ice covered offshore islands. According to the Antarctic Digital Database v4.1 (ADD CONSORTIUM, 2004), its area -including the South Shetland Islands archipelago and surrounding island but excluding the ice shelves- totalizes to approximately 375.340 km^2 , from which rocks

outcrops cover approximately 7.102 km², i.e. about 1.9% of the Antarctic Peninsula territory.

On the eastern side the asymmetry of the Antarctic Peninsula in all physiographic and climatic parameters is manifest in the extended Larsen ice-shelf. The ice-shelf calves into the Weddell Sea, which is nearly permanently covered by compact sea-ice. In contrast, the western coast with its tidewater glaciers calving into open fjords is covered with compact coastal sea-ice in the Bellingshausen Sea only during winter.

Two aerial photographs taken in March (end of summer) shown in Figures 2.2 and 2.3, may help to illustrate the physiographic setting of common elements that are found on the Antarctic Peninsula.



Figure 2.2: Ice cap, glaciers and small ice-shelf of James Ross Island; in the background Prince Gustav Channel and Louis Philippe and Laclavère Plateaus, northern Antarctic Peninsula. View from southeast; field of view marked in Figure 2.1.

Source: Aerial picture from NASA AirSAR mission, March 16, 2004

NASA Photo: ED04-0056-137, photo by James Ross.

The first photo, taken looking to the northwest over James Ross Island (JRI) at about 64° southern latitude (Figure 2.2), shows the insular and coastal environment typical of the northern area. A relatively open sea is observed in the Prince Gustav Channel between the Antarctic Peninsula and JRI. In the lower half of the photo we can examine how an ice-shed is feed by ice coming from small coalescing glacier basins. Then, at the grounding line, the ice is forming a small ice-shelf that calves into the Weddell Sea (lower left corner). Tidewater glaciers ending at Prince Gustav Channel have a characteristic ice front of ca. 30 m altitude. Several sectors with terrain free of ice and snow are also visible.



Figure 2.3: Ice field and deep cut glacier valleys at Cape Northrop. Rock outcrops located at photography's lower right hand, prolongs up to Hodges Point; in the foreground ice grounding zone of Larsen Ice Shelf. View from the East, field of view marked in Figure 2.1.

Source: Aerial picture from NASA's AirSAR mission, March 13, 2004
 NASA Photo: ED04-0056-114; photo by James Ross.

The second photo, taken looking to the east over Cape Northrop at about 67° south latitude in the western margin of the Larsen C Ice Shelf (Figure 2.3), shows a close up of the central plateau, one of the main features of the Antarctic Peninsula. Exposed rocks on nunataks, ridges and steep rock-wall flanks are the only places where terrain is not covered by ice and snow. Well developed cirques exhibit very impressive rock cliffs topped with a thick layer of ice on the plateau. Outlet glaciers collect ice through avalanches coming from the plateau. Cones of accumulation are also visible at the foot of rock cliffs. The ice grounding line is visible marking the point where ice starts floating as part of the Larsen C Ice Shelf.

In general in the Antarctic Peninsula the continuity of the ice coverage is only disrupted by sporadic rock outcrops. This hampers the use of traditional approaches to delineate glacier boundaries. Nevertheless, the huge territorial extension requires the use of remote sensing data to cost-effectively derive such limits.

However, even the manual delineation of ice limits based in the skill of an operator requires a basic ontological schema that provides the rules to identify the encompassing elements of the glacier systems belonging to the Antarctic Peninsula.

In the next section we will first elaborate on the definition of catchment delineation and then review existing works on catchment delineations in Antarctica and specifically on the Antarctic Peninsula.

2.2 Antarctic ice drainage basins

We agree with WEIDICK & MORRIS (1998), when they write ...“further work is needed to establish mass-balance curves for the region, but the primary need is mapping on a sufficiently detailed scale to resolve the form of local glaciers and enable more precise estimates of their area to be made”. For other authors such as BAMBER & GOMEZ-DANS (2005) or WUNDERLE & SCHMIDT (1997) glacier mapping is also a basic requirement to support further glaciological studies.

The starting point for a systematic mapping of glaciers of the Antarctic Peninsula is to have a clear definition of the elements that encompass its glacial systems. The delineation of these elements can then be performed at an adequate scale according to the topographic base information and according to the required level of detail for the different glaciological applications.

But which operational definitions for the glaciological elements can we use on the Antarctic Peninsula?

During the preliminary stages of mapping the topography and/or geomorphology is the most significant criterion employed in differentiating land systems. Land systems are divided in smaller components called units and elements. Using a general classification of the land systems concept it is possible to characterize an area having common terrain attributes which are different to those of adjacent areas (EVANS, 2003). The logical, rational delineation of spaces on the globe depends on the criteria to be used, but geographic research offers few established, widely accepted rules about what these criteria should be or how they might be employed (CUTTER ET AL., 2002). However, a formal specification of the ontology of a domain of reality is a prerequisite for effective representations to support scientific computing.

The work of MARK & SMITH (2004) suggests to use the US Spatial Data Transfer Standard (SDTS), a US Federal Information Processing Standard (USGS, 1994) that provides a list of 199 ‘entity types’ – the SDTS term for kinds of geospatial things that exist in the real world. In order to be represented in an SDTS-compliant database, any landform (or other geographic feature) must be assigned to one of these 199 entity types. A group of these entity types seem to fall under the category of ‘landform’ that we need to use for delineation of our glaciological elements, i.e.: *basin, catchment, cirque, cliff, gap, moraine, mount, mount range, peak, plateau, ridge, ridge line, and valley*. The entity of higher hierarchy correspond to *catchment*, that is defined in hydrological terms as “a natural drainage area that may coincide with a river basin ...”.

Other hydrologic definitions of a catchment are: “the total area of land drained by a river and its tributaries” (CLARK, 1992) or as “the area that lies upstream of a point” (JONES, 2002). These must be adapted for glaciers instead of rivers extending the “point” to include a “cross section” for each glacier identity. That can be a section of coastline or a profile between exposed landmarks. However, it must be noted that depending on the scale considered ice flow does not necessarily converge into one outlet glacier because large-scale units can be aggregated.

In accordance with HARDY ET AL. (2000) we have to define “*an ice drainage basin as an independent geographical unit that is bounded by ice divides*”. This again is important in Chapter 5, when we have to combine basins extracted by our model to catchment areas.

A literature survey on examples describing delineation of drainage basins in Antarctica reveals that scientists (Tables 2.1a and 2.1b), mostly start with the ice divides and draw their lines down to the coastal ice cliffs using recognizable streamlines. In the following short overview about these findings we separate by geographical scale between ice divide maps for the great ice sheets of East- and West-Antarctica (continental scale), listed in Table 2.1a; and ice catchment delineations in some smaller areas of the Antarctic Peninsula, (regional and local scale), listed in Table 2.1b.

Table 2.1a : *Continental ice drainage delineations in Antarctica. Different demarcations based in the use of marine charts, topographic maps, aerial photography, satellite data, computational processing manual delineation were achieved. Variations between results are explained by the use of different base data, topographic scale and on non neglected operator processing errors.*

Author	Area	Method used	Remarks
GIOVINETTO (1964)	Continental scale.	Delineation by hand, normal to contour lines over topographic map	Contour interval 200 m. Antarctic Peninsula without delineations.
GIOVINETTO & BENTLEY (1985)	Continental scale.	Delineation by hand over 100 m contour interval enhanced Antarctica topographic map (Drewry, 1983)	Contour interval 500 m. A central ice-divide is delineated along the Antarctic Peninsula.
VAUGHAN ET AL. (1999)	Continental scale.	Automatic computation of slope magnitude and slope aspect.	Basin polygons represented. Antarctic Peninsula north of latitude 70° S without delineations.
LIU (1999)	Continental scale.	Automatic GIS approach to obtain basins.	Ice flow and ice divides delineated.
LANG (2004)	Continental scale.	Automatic computation of basins.	Basin polygons based on previous report (Vaughan, 1999). Antarctic Peninsula without delineations..
RIGNOT & THOMAS (2002)	Continental scale.	Derived from map of ice-sheet balance velocities	Antarctic Peninsula without delineations.

Table 2.1a summarizes ice drainage delineations performed in Antarctica at continental scale. Important stages in the development of continental scale catchment delineations correspond to the names GIOVINETTO (1964), GIOVINETTO & BENTLEY (1985), VAUGHAN ET AL. (1999), LIU (1999), LANG (2002) and RIGNOT & THOMAS (2002).

Comparing the different maps in Figures 2.4 and 2.5, we see the great progress since the last decade of the past century, when Radar interferometry and Radar altimetry data became available for altitude measurements and the more and more powerful GIS-technology offered new processing capabilities for catchment delineation.

All these works do not satisfy the requirements of drainage basin description at regional scale as it is needed for the Peninsula's glacial system. The main reason are the constraints on the application of radar altimetry in the mountainous region of the Antarctic Peninsula because of the altimeter footprint size and the difficulty to integrate data over homogeneous areas. ESA's Cryosat mission featured a novel

interferometric radar altimeter with smaller footprints. For the first time this type of radar altimeter potentially might have been capable of mapping with more detail at least parts of the topography of the Antarctic Peninsula region. Unfortunately the mission failed during launch in 2005.

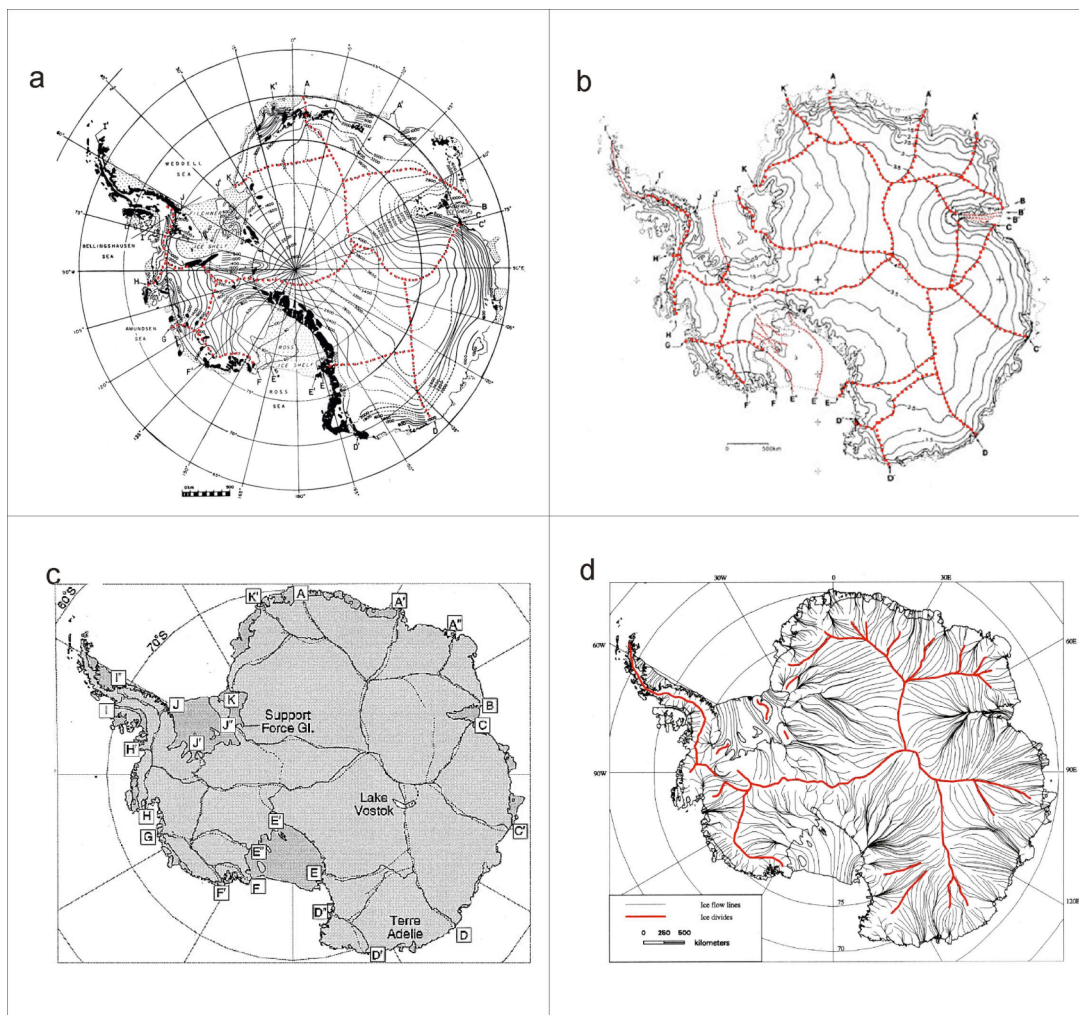


Figure 2.4: Steps in delineation of ice divides in Antarctica at continental scale by different authors. Advances in source data and methods have increased the knowledge on continental scale glacier basins.

a: Map of ice surface topography and ice divides in Antarctica from GIOVINETTO (1964); contour intervals are 200 m, ice divides marked in red. Ice divide lines were drawn by hand inland, normal to contour lines, from the coast until ridges were met; from there, drawing was continued along the inferred crest of the ridges. Ten drainage systems were delineated for the continent. The complex topography of the Antarctic Peninsula prevented from tracing its ice divides.

b: Modified from GIOVINETTO AND BENTLEY (1985), an updated Antarctica's ice surface and drainage systems delineation maps; ice divides marked in red color determine 26 distinct physiographical basins. Contour interval is 500 m. Nevertheless ice divides were traced by hand over the 100 m contour interval of DREWRY'S (1983) topographic compilation.

c: VAUGHAN ET AL. (1999), determine the drainage pattern using an automatic approach to compute slope magnitudes and slope aspect (10 km grid size); based on a digital elevation model (DEM) derived from ERS-1 satellite altimetry (BAMBER, 1994) and additional elevation data. Dotted lines indicate those drawn by GIOVINETTO AND BENTLEY (1985). Solid lines indicate the drainage basins derived by VAUGHAN ET AL. (1999).

d: LIU (1999), as a validation of the topological consistency of the RAMP DEM, derived the ice drainage pattern and ice flow lines using an automatic GIS approach. The author reports that ice divides and ice flow lines compared favourably with the ice drainage map in DREWRY (1983).

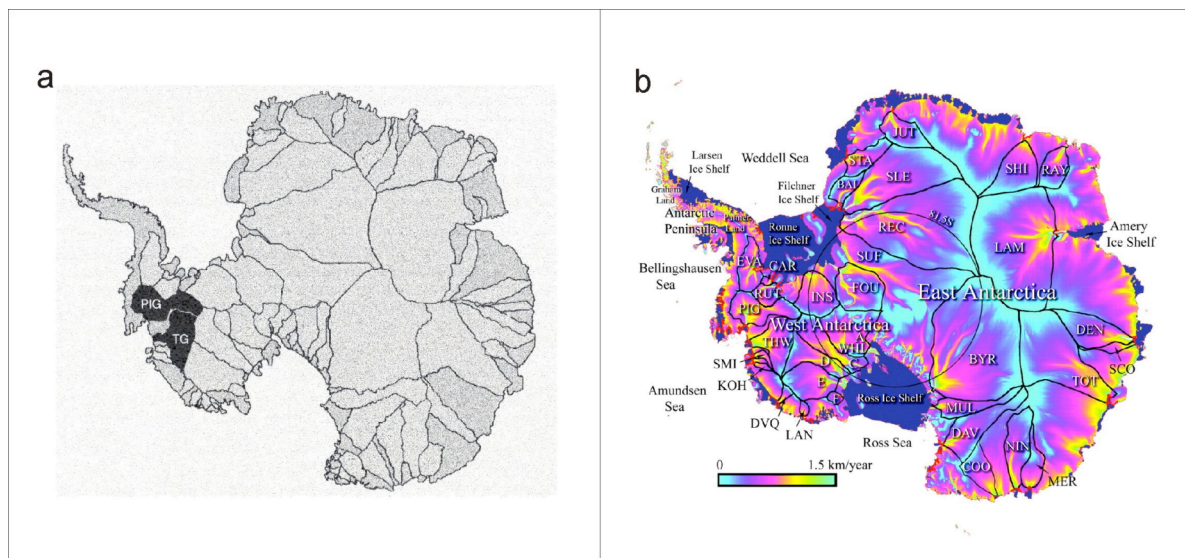


Figure 2.5: The two most recent maps of catchment basin boundaries and ice flow of Antarctica at continental scale. No limits are depicted for Antarctic Peninsula in both examples.

a: LANG (2002), uses a delineation of the ice drainage basins (VAUGHAN, 1999), to depict Pine Island and Thwaites Glaciers basins. VAUGHAN (1999) determined 70 major Antarctic ice catchments based on the use of a DEM and their correspondent balance flux as the mass of ice that must be drained to maintain the present basin state.

b: RIGNOT & THOMAS (2002). It shows 33 major basins of Antarctica derived from ice-sheet balance velocities by BAMBER ET AL. (2000) and Radar interferometry.

Colors: Flow velocities

Black: Ice divides

Dark blue : Ice shelves

A similar review considering the Antarctic Peninsula region gave the results summarized in Table 2.1b and presented in figures 2.6, 2.7, 2.8 and 2.9.

Nearly all studies are dedicated to islands. In all cases the basin delineation is done by hand using maps and optical remote sensing data, i.e. aerial photography, Landsat or SPOT imagery. The results can be used as independent datasets for comparison with the results of our technology in future work. Interesting is to note the different results obtained by BRAUN ET AL. (2001) and BREMER ET AL. (2004), using the same data and methodology. This shows the subjectivity of manual interpretation by operators.

Table 2.1b: Regional and large scale ice drainage delineations in the Antarctic Peninsula. Different demarcations were achieved based in the use of charts, topographic maps, aerial photography, satellite data, computational processing and manual delineation. Variations between results are explained by the use of different base data, topographic scale and on the subjectivity of operator-based manual processing.

Author	Area	Method used	Remarks
RABASSA ET AL. (1983)	James Ross Island	Manual delineation based on visual interpretation of topographic maps, aerial photography and Landsat imagery.	Delineations are part of a glacier inventory of James Ross Island. Map has no geodetic reference.
WILLIAMS ET AL. (1989)	Davis and Danco Coast	Manual delineation over US charts.	Map has no geodetic reference.
SIMÕES ET AL. (1999)	King George Island	Manual delineation over SPOT near infra-red mosaic and topographic map.	Delineation of 70 basins on King George Island.
BRAUN ET AL. (2001)	King George Island	Manual delineation using contour lines from DEM and SPOT image mosaic.	DEM of 100 m grid cell size used in addition to SPOT image mosaic
BREMER ET AL. (2004)	King George Island	Manual delineation using contour lines from DEM (Braun et al., 2001) and SPOT satellite image.	Same data as Braun et al. (2001) with slightly different results.
AHLERT ET AL. (2005)	Brabant Island	Manual delineation using Landsat images and 250 m contour lines interval digital cartography (ADD).	Criteria for glacier classification defined.

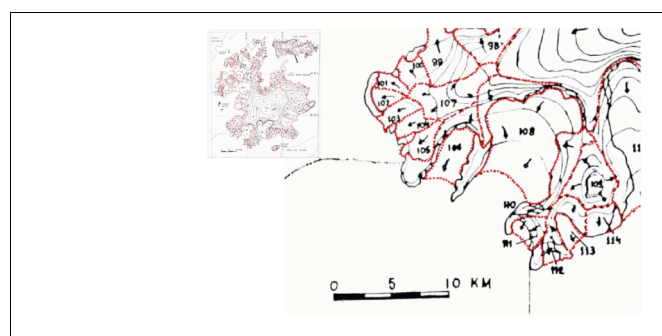
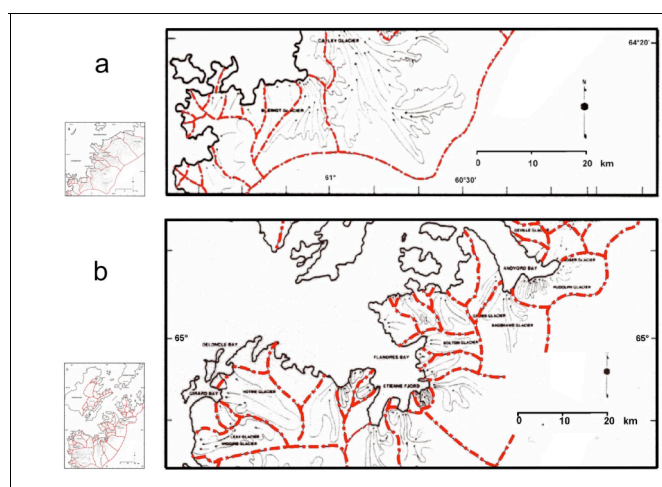


Figure 2.6: Relief and ice divides of James Ross Island after RABASSA ET AL. (1983). Contours lines taken from Argentine and British medium scale maps. Catchment boundaries derived by integration of visual interpretation of aerial photography and Landsat imagery (NASA ERTS E-2740-11461 and 11461, bands 4 and 7, 31 January 1977) with field knowledge and topographic information.



a: Davies Coast and northern Danco Coast, western Antarctic Peninsula. Flow lines are indicated by arrows and drainage divides by red dashed lines. The Cayley Glacier is the largest system comprising some 820 square kilometers (WILLIAMS ET AL., 1989).

b: Danco Coast and eastern Anvers Island, western Antarctic Peninsula. Flow lines are indicated by arrows and drainage divides by red dashed lines. These systems drain the northern end of the Bruce Plateau, have steep longitudinal gradients and are smaller than those located over Davies Coast.

Figure 2.7: Delineation of glacial drainage systems on Davis and Danco Coast by WILLIAMS ET AL. (1989). Catchment boundaries were drawn on U.S. Mapping Agency coastal charts using Landsat images taken over a number of years for visual interpretation.

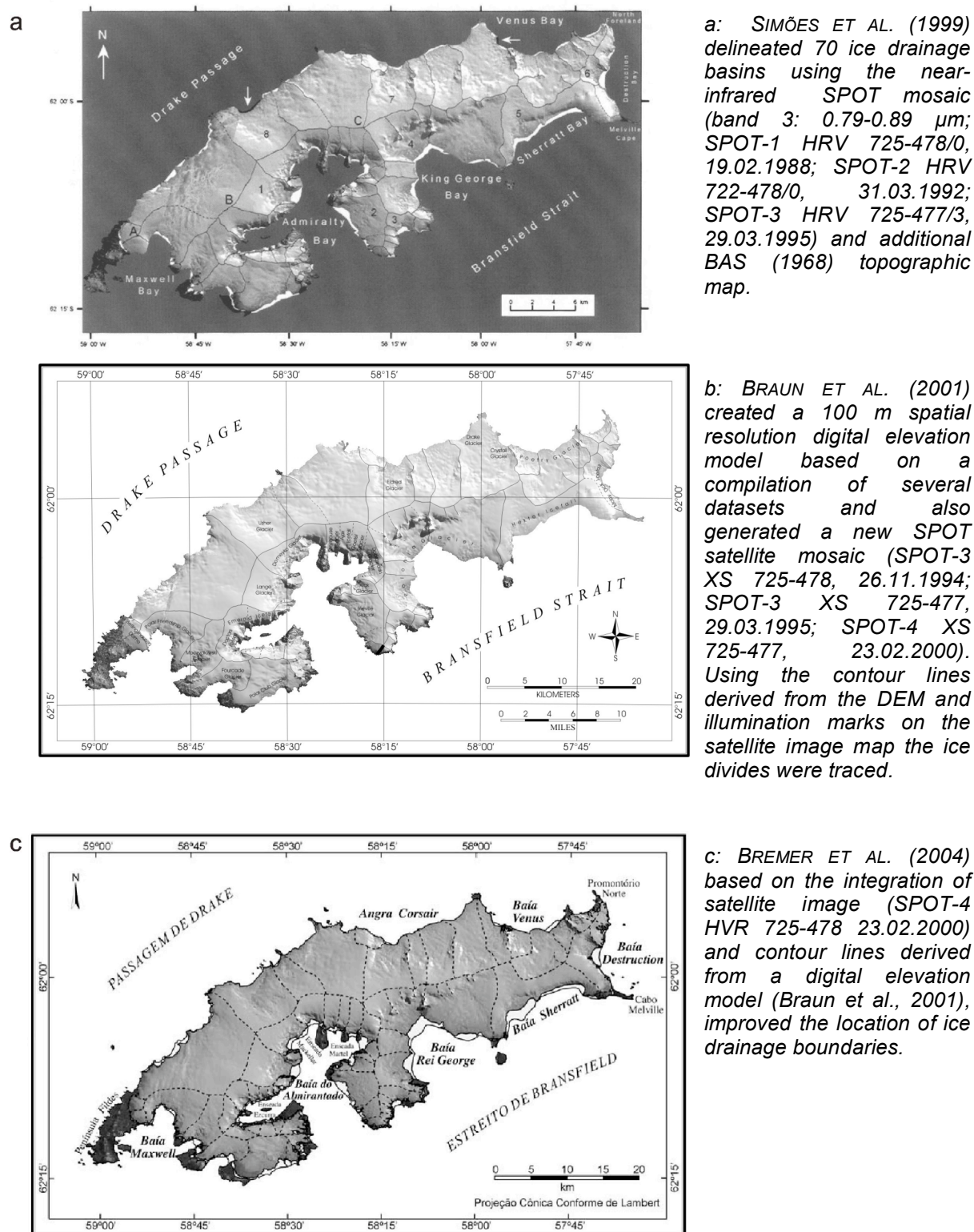


Figure 2.8: Three delineations for ice catchments of King George Island Ice Cap; based on visual interpretation and manual delineation of SPOT different methods over topographic maps, digital elevation models and SPOT satellite mosaics. Results are similar, but might differ considerably at drainage basin scale.

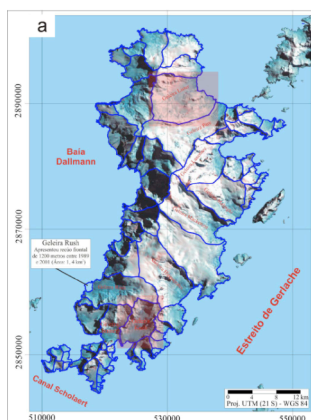


Figure 2.9: One of the most recent ice drainage basin delineation in the Antarctic Peninsula region.

Ice drainage basin delineation in Brabant Island by AHLERT ET AL. (2005). Visual interpretation of Landsat images (Landsat 4 TM 219/105, 26 November 1989; LANDSAT 7 218/105 21 February 2001) and analysis of texture and pattern characteristics, were integrated with the digital cartography (ADD, contour interval 250 m) to delineate ice divides by hand.

2.3 Digital Elevation Models for the Antarctic Peninsula

To use an automatic or semi-automatic approach to delineate basins and catchments it is required to use topographic data in the form of a digital elevation model (DEM). Such data sets can be created from elevation information extracted from conventional sources (e.g. maps), produced from aerial photographs or derived from satellite stereoscopic data. But before start creating our own DEMs we needed to know which DEMs exist for our area of interest for two reasons:

- on the one hand existing models can contribute as basic datasets for basin generation, or
- on the other hand some of these models may be used as independent data sets for comparison allowing evaluation of our own products.

DEMs covering the entire area of the Antarctic Peninsula that potentially can be used for one of the previous two purposes are listed in Table 2.2.

DEMs in Table 2.2 are compiled from medium to small scale cartographic sources or from Radar altimetry data. We have to note the absence of DEMs based on optical satellite data. Traditional methods of derivation produces results in weak accuracy on surfaces of ice and snow because of over-saturation and missing texture.

Additionally the sparse coverage of polar areas due to the orbit parameters, the polar night and the high cloud coverage affect the use of space borne optical data for these areas. DEM-production based on microwave remote sensing is very promising. However, due to the footprints of the up to now used GEOSAT and ERS1/2, Radar Altimetry systems cannot achieve a sufficient spatial resolution and altitude accuracy over areas with the relief properties of the Antarctic Peninsula.

Table 2.2 : Digital elevation models (DEMs) covering the Antarctic Peninsula.

Dataset	Author	Spatial resolution	Remarks
SEASAT and GEOSAT Altimetry Data for the Antarctic and Greenland Ice Sheets (IAS-1)	ZWALLY & BRENNER (1998)	Grid 10 km for GEOSAT data and 20 km for SEASAT data	Radar altimetry data. SEASAT data collected for a continuous 90 days in 1978, up to 72 degrees South GEOSAT data collected between April 1985 and September 1986. surface topography of the ice sheets relative to the OSU91A geoid
GEOSAT Radar Altimetry Atlas of the Antarctic North of 72.1 Degrees South	HERZFELD & MATASSA (1999)	Grid 3 km	Radar altimetry data. Spatial interpolation by kriging technique. 28 atlas pages are available in both UTM and latitude/longitude coordinates.
Antarctic 5-km Digital Elevation Model from ERS-1 Altimetry	BAMBER & BINDSCHADLER (1997)	Grid 5 km	Radar altimetry data. Orthometric heights to to 81.5 degrees south latitude referenced to the OSU91A geoid
GTOPO30	USGS (1996)	horizontal grid spacing is 30-arc seconds	Antarctica region based on ADD data. Horizontal coordinate system is decimal degrees of latitude and longitude referenced to WGS84. The vertical units represent elevation in meters above mean sea level.
GLOBE	GLOBE TASK TEAM ET AL., (1999)	1 km (30" arc)	horizontal coordinate system is seconds of latitude and longitude referenced to World Geodetic System 84 (WGS84). The vertical units represent elevation in meters above Mean Sea Level
DTIM2	IHDE ET AL., (2002)	latitude gridspace of 0.05 and longitude grid space of 0.2	ERS-1/2 Radar altimetry data.
Radarsat Antarctic Mapping Project Digital Elevation Model Version 2	LIU ET AL., (2001)	200m, 400m, 1km	Radar altimetry data and compilation of other sources. Geolocation accuracies Horizontal: $\pm 100\text{m}$ over rugged mountainous areas, $\pm 15\text{ m}$ steeply sloped coastal regions, $\pm 1\text{m}$ on ice shelves, $\pm 7.5\text{m}$ gently sloping interior ice sheet and ± 17.5 on ice sheet perimeter Vertical:

Given the spatial resolution of the DEMs listed in Table 2.2 the Radarsat Antarctic Mapping Project Digital Elevation Model (RAMP-DEM) is the only one that is of potential use in our study. It is the only one that can represent glacial catchments in the Antarctic Peninsula region, however at a limited level of detail.

The RAMP-DEM was generated at the Byrd Polar Research Center (BPRC) as an independent dataset to support the data handling of the Radarsat Antarctic Mapping Project (LIU ET AL., 2001). The it was developed for the orthorectification of Radarsat Antarctic SAR imagery, enabling to produce a seamless mosaic of the imagery (see <http://www-bprc.mps.ohio-state.edu/rsl/radarsat/Images/>, visited June 2006).

The DEM incorporates topographic data from satellite radar altimetry, airborne radar surveys, most of the vector data from the Antarctic Digital Database (ADD v.2), and large-scale topographic maps from the U.S. Geological Survey (USGS) and the Australian Antarctic Division (AAD). Data were collected between the 1940s and present, with the majority collected during the 1980s and 1990s. Although the RAMP DEM was created to aid in processing RAMP radar data, it does not utilize any RAMP radar data.

The 1 km, 400 m, and 200 m DEM data are provided in ARC/INFO and binary grid formats, and the 1 km and 400 m DEMs are also available in ASCII format. Data access is unrestricted, but users should register to receive e-mail notification of product updates and changes in processing (<http://nsidc.org/data/nsidc-0082.html>, visited March 2006). Elevations for points in this data set are measured in meters [m] above both the WGS84 ellipsoid and the OSU91A geoid.

The real horizontal resolution of the DEM varies from place to place according to the density and scale of the original source data. The developers of the data set estimate that the horizontal resolution of the DEM is about 200 m in the Transantarctic Mountains and Antarctic Peninsula, and about 400 m in the sloped coastal regions. For ice shelves and the inland ice sheet covered by satellite radar altimeter data, the horizontal resolution is about 5 km, but where the airborne radar sounding data were used, the horizontal resolution is about 1 km. For the plateau inside 81.5 degrees south latitude, horizontal resolution is estimated at about 10 km.

The accuracy of geolocation (i.e., the accuracy of the position of a given feature on the DEM) is governed by the accuracy of the topographic source data, and is generally better than the horizontal resolution of the DEM.

The vertical accuracy of the RAMP-DEM is ± 100 m over rugged mountainous areas, ± 15 m for steeply sloped coastal regions, ± 1 m on the ice shelves, ± 7.5 m for the gently sloping interior ice sheet, and ± 17.5 m for the relatively rough and steeply sloped portions of the ice sheet perimeter. For latitudes south of 81.5 degrees south, within the interior East Antarctic ice sheet and away from the mountain ranges, vertical accuracy is estimated to be ± 50 m (LIU ET AL., 1999).

Therefore the RAMP-DEM is at the moment one the standard relief representations of Antarctica. Version 2 improves upon the original version by incorporating new topographic data, error corrections, extended coverage. Better data selection and better surface constraints has been achieved by using updated coastlines and grounding lines derived from the SAR mosaic coastline for the entire continent.

As we can see in figures 2.10 and 2.11a-c, in spite of its continental approach, the RAMP-DEM presents a new depth of regional information. Nevertheless we will see in the ongoing sections of our work the limitations of this model for regional applications. It will be very informative to compare this database with ASTER derived

DEMs and in a regional test site with a stereo-model derived from airborne data. The terrain sections given in figure 2.11a-c can be found again in the corresponding Figures 3.7, as well as in Figures 3.15, 3.16 and 3.17.

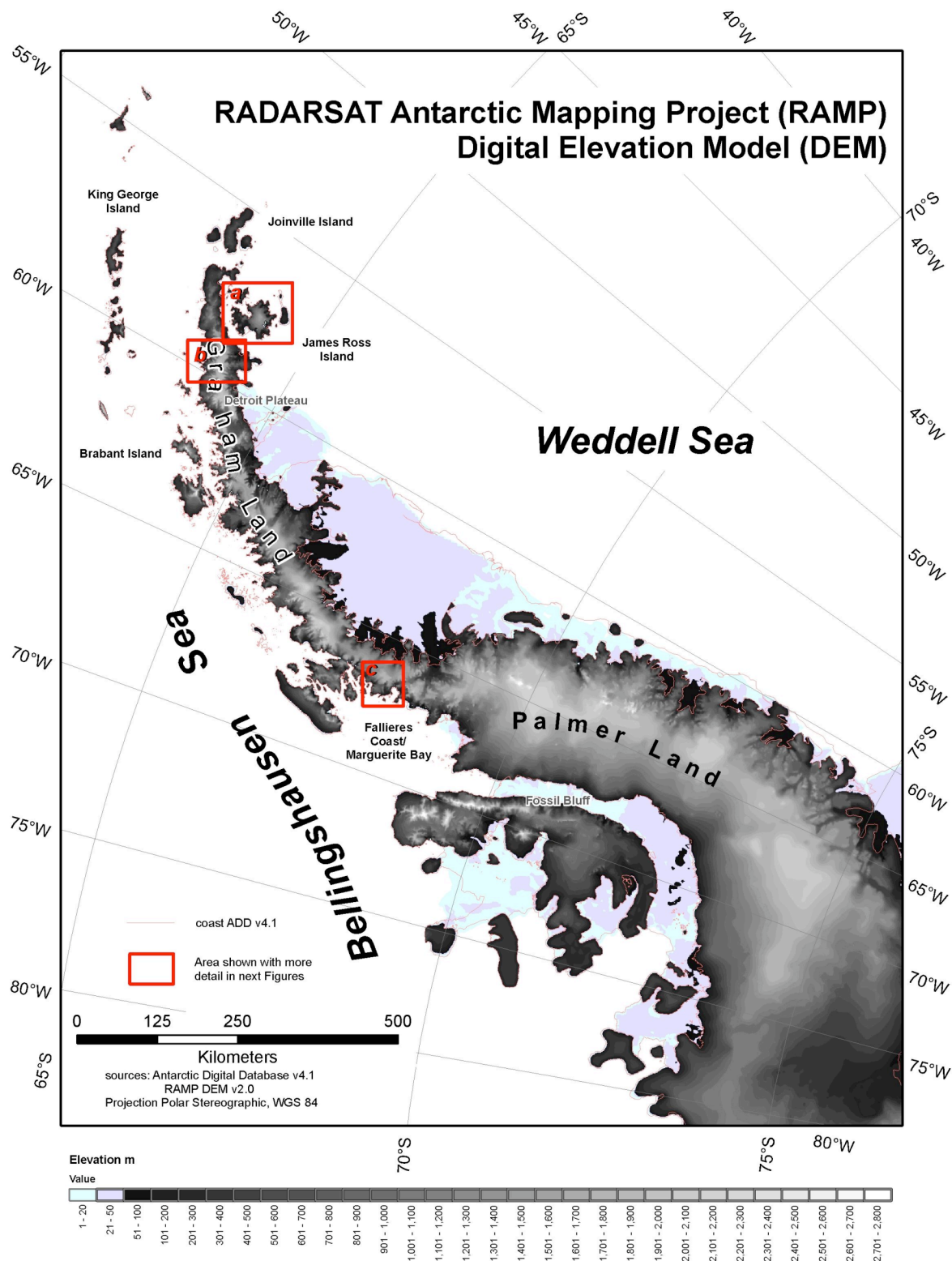
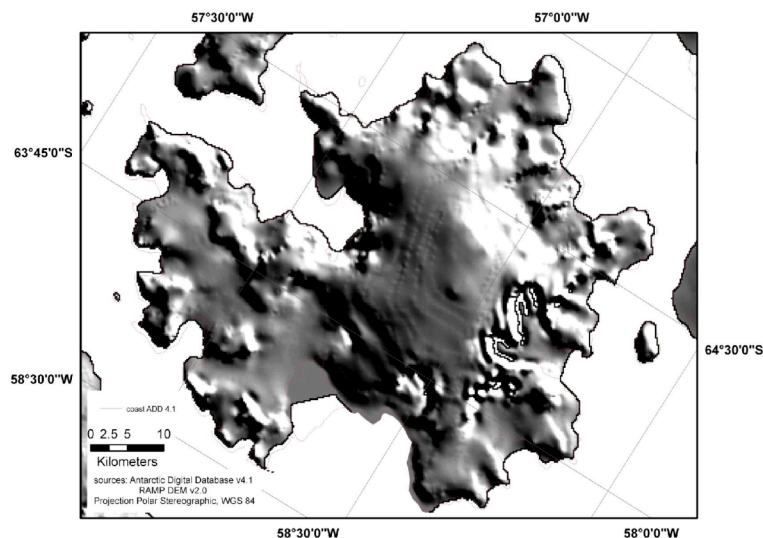


Figure 2.10: Antarctic Peninsula topography based on the RADARSAT Antarctic Mapping Project Digital Elevation Model (RAMP DEM), (LIU ET AL., 2001) and the Antarctic Digital Database (ADD CONSORTIUM, 2004) coast line datasets.

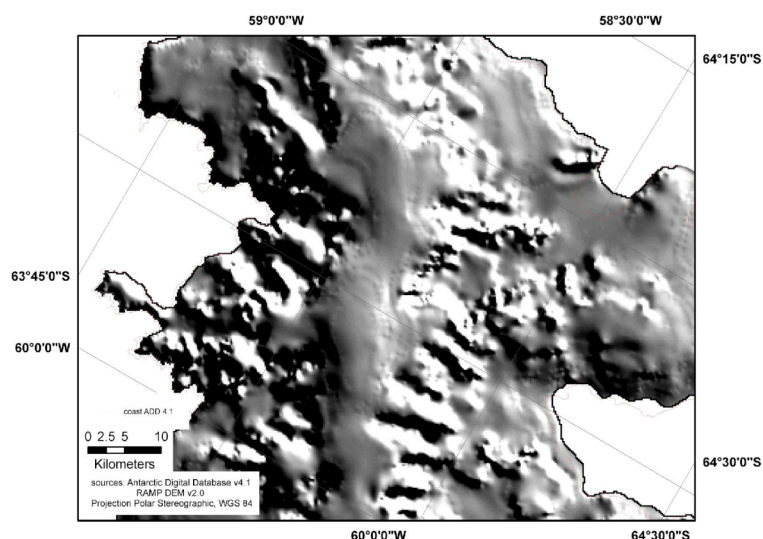
a: James Ross Island shaded relief based on the RAMP DEM; solar elevation 30°, azimuth 50°, scale 1:500,000. Some artefacts are detectable on central ice cap slopes.

Source: RAMP DEM v2 (LIU ET AL., 2001); ADD v4.1 (ADD CONSORTIUM, 2004).



b: Shaded relief of the northern Detroit Plateau, based on the RAMP DEM; solar elevation 30°, azimuth 50°, scale 1:500,000. Some artefacts are detectable in the upper boundaries of the plateau and where steep surface changes occur.

Source: RAMP DEM v2 (LIU ET AL., 2001); ADD v4.1 (ADD CONSORTIUM, 2004).



c: Shaded relief of central Fallières Coast sector, based on the RAMP DEM; solar elevation 30°, azimuth 50°, scale 1:500,000. Artefacts are detectable across Northeast Glacier. The ridge between McClary and Todd Glaciers is not represented.

Source: RAMP DEM v2 (LIU ET AL., 2001); ADD v4.1 (ADD CONSORTIUM, 2004).

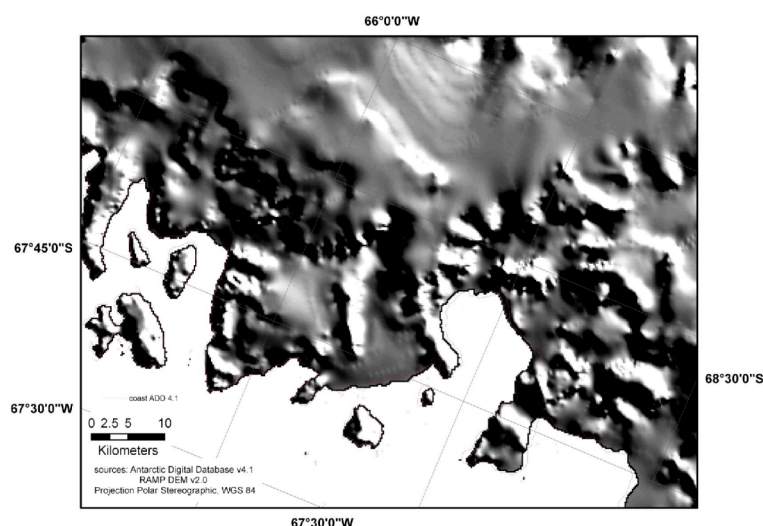


Figure 2.11: Shaded relief sections of RAMP DEM v2; a remarkable level of detail is appreciated in these three examples from the Antarctic Peninsula. Artefacts noticeable in some parts are the result of interpolation processing in a rugged topography.

The area represented in figure 2.11c correspond with our main test site used in later Chapters 4 and 5.

As we have seen there is no DEM available covering the entire Peninsula with sufficient level of detail for our purpose. However, for the purpose of evaluating our ASTER DEMs an elevation model covering only a small test site would be sufficient. Two DEMs of this kind have been accessible. One of the available large scale DEMs with a spatial resolution sufficient for this study is covering Fossil Bluff area. This DEM was rejected because the topography was considered not representative for this study.

The other accessible and suitable DEM is the Technical University of Darmstadt Digital Terrain Model (TUD-DTM or TUD model) of Base General San Martin region, Marguerite Bay. The TUD model provides a representation of the terrain that allows the use of scales up to 1:25.000. This spatial resolution is comparable to the resolution of the DEMs that we will produce later.

The TUD model was generated by researchers from the Technical University of Darmstadt under the frame of the German Federal Minister for Education, Science, Research and Technology project "Dynamic Processes of the Antarctic Geosystems" (DYPAG, Project 03PL016A, Wrobel et al., 2000).

The Argentine General San Martin station is located at 68°07 S and 67°06 W, on Barry Island, Debenham Islands, Marguerite Bay, adjacent to the central part of Fallières Coast, on West Antarctic Peninsula. Aerial photographs acquired by BKG (former IfAG) and AWI in 1989 were used as the source information.

New stereophotogrammetric techniques have been applied to produce a high resolution topographic data set. Two very different digital photogrammetric procedures that were adjusted to the specific requirements of the Antarctic were employed: FACETS STEREO VISION and the software PHODIS of Carl Zeiss company. WROBEL ET AL. (2000) describe the procedure and the results of evaluations obtained in the test site. The TUD model is distributed in two ASCII files corresponding to a regular grid with 30 m spatial resolution. The full coverage of the TUD model is represented in its original projection in Figure 2.12.

Additionally, using the DEM and the original photographs the Technical University of Darmstadt and the BKG (former IfAG) at Frankfurt produced an orthorectified image and edited it together with contour lines and topographical information as digital Aerial Photo Map Base General San Martin (TUD Karte) and published it in printed form at scale 50 000 (see Figure 4.4).

Since this material will play a key role for the evaluation of our techniques in ASTER DEM generation, it is presented in more detail together with test site properties in section 4.1.

In the next chapter we will describe a procedure to create comparable models with similar resolution from readily available space borne data. If the procedure proves to be successful and robust it would allow to fill the lack of terrain information for most parts of the Antarctic Peninsula.

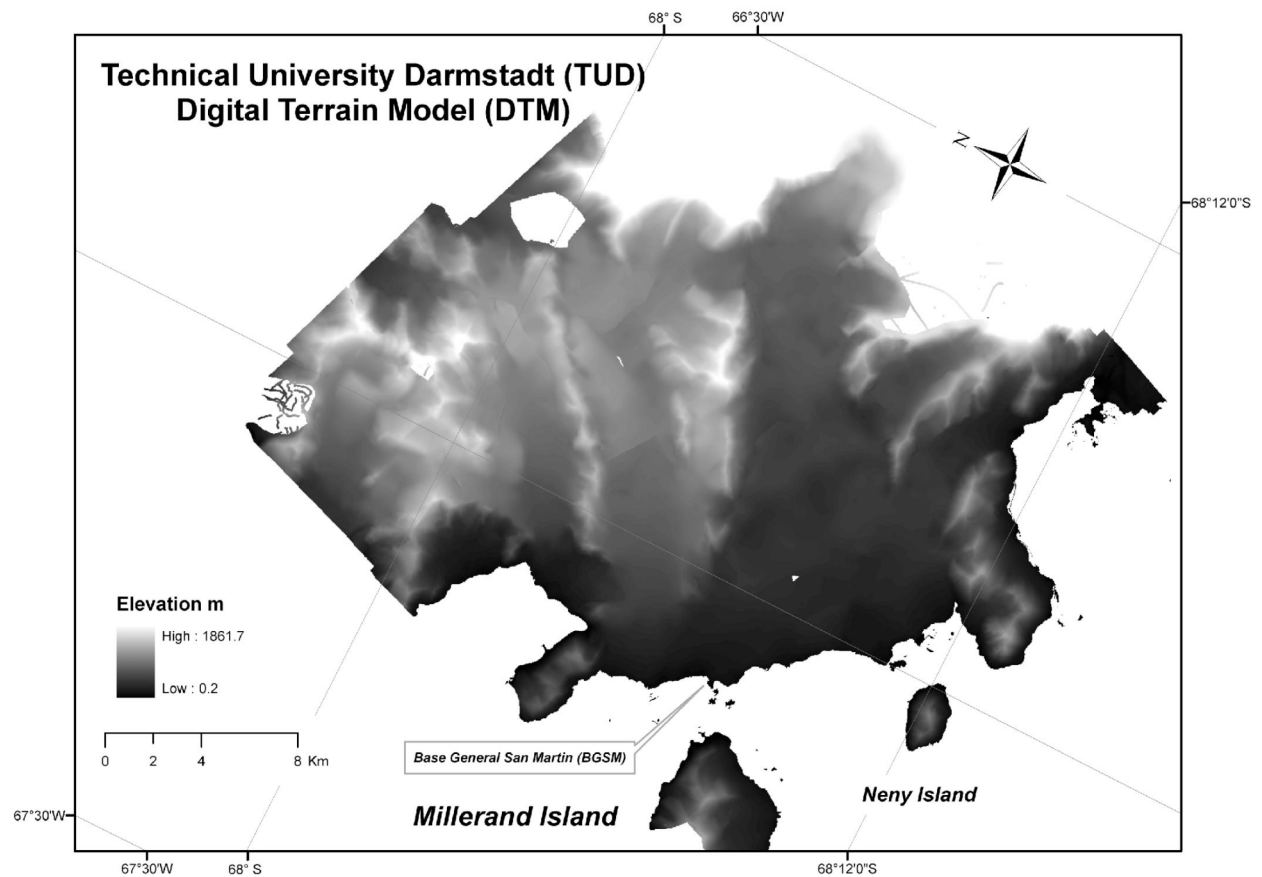


Figure 2.12: Digital elevation model of the surroundings of the Base General San Martín (IfPK TUD, 1999). Generated under a semi-automatic processing from aerial photo coverage (BKG 1988-89 campaign), has 30 m grid cell size and the following accuracies:

- ±3-10 m: mountain ranges, rock areas, snow-free zones;
- ±10-20 m: crevasses, ice faults, structured, snow covered terrain;
- ±50 m or more: monotonous snow-covered areas without structures.

Lambert Conformal Conic (WGS 72) cartographic projection.

3 ASTER DEM generation

As we argued in Chapter 1 progress in the production of digital elevation models (DEMs) to map the ice masses of Antarctica can be expected from the new generation of Earth observing satellites and their sensor systems. One of these newer systems is the Advanced Spaceborne Thermal Emission and Reflection Radiometer (ASTER) instrument flying on the TERRA satellite. Theoretically, its along-track stereoscopic capability and its spatial resolution offer promising conditions to derive DEMs in the Antarctic Peninsula. However, DEM production from ASTER data in this area is hindered by the frequent presence of clouds and by the lack of contrast on snow covered terrain under specific conditions of illumination.

In this chapter we will explore the characteristics of the ASTER satellite data and evaluate its availability over the Antarctic Peninsula. In the following we will investigate into a reliable and robust method to extract topography from its stereo channels. Finally we will establish a processing chain that allows us to generate a series of high resolution ASTER derived DEMs for the Antarctic Peninsula.

3.1 ASTER satellite data

3.1.1 Terra satellite, sensor description and ASTER stereo capability

The United States National Aeronautics and Space Administration (NASA) has declared: “*Terra* is the flagship of the Earth Observing System (EOS), a series of spacecraft that represents the next landmark step in the NASA’s role to observe Earth from the unique vantage point of space. Focused on key measurements identified by a consensus of U.S. and international scientists, Terra enables new research into the ways Earth’s land, oceans, air, ice and life function as a total environmental system”.

Terra is a multi-national, multi-disciplinary mission involving U.S. agencies in partnerships with the aerospace agencies of Canada and Japan. Managed by [NASA’s Goddard Space Flight Center](#), the mission also receives key contributions

from the [Jet Propulsion Laboratory](http://terra.nasa.gov/) and [Langley Research Center](http://terra.nasa.gov/) (<http://terra.nasa.gov/>, visited 5.2.2006).

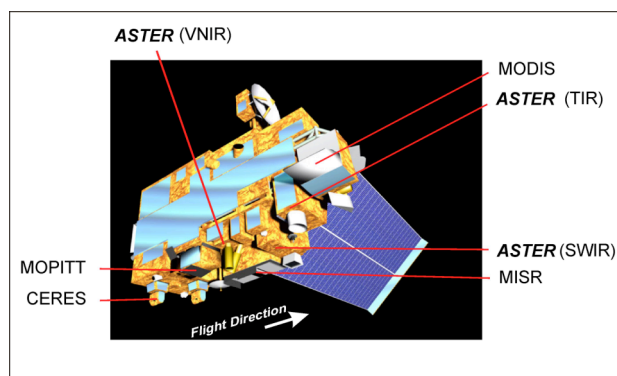
Terra was launched into sun-synchronous Earth orbit on December 18, 1999, and started sending data back to the Earth in February 2000, (<http://asterweb.jpl.nasa.gov/eos.asp>, visited 05.02.2006).

Table 3.1: General specifications of the Terra spacecraft.

Source: Adapted from Jet Propulsion Laboratory (JPL) web contents (<http://asterweb.jpl.nasa.gov/eos.asp>, visited 31 January 2006).

Launch date:	18 December 1999
Orbit:	700 – 737 km altitude (705 km on the equator), sun-synchronous, so that at any given latitude it crosses directly overhead at the same time each day.
Orbit inclination:	98.3 degrees from the Equator
Orbit period:	98.88 minutes
Equator crossing:	10.30 a.m. (north to south)
Ground track repeat cycle:	16 days, i.e. every 16 days (or 233 orbits) the pattern of orbits repeats itself
Instruments:	ASTER: Advanced Spaceborne Thermal Emission and Reflection Radiometer CERES: Clouds and the Earth's Radiant Energy System MISR: Multi-angle Imaging Spectro-Radiometer MODIS: Moderate-resolution Imaging Spectroradiometer MOPITT: Measurement of Pollution in the Troposphere

The most relevant parameters and characteristics of Terra configuration are summarised in Table 3.1. Terra carries five scientific instruments: CERES - Clouds and the Earth's Radiant Energy System; MISR - Multi-angle Imaging Spectro-Radiometer; MODIS - Moderate-resolution Imaging Spectroradiometer; MOPITT - Measurement of Pollution in the Troposphere; and **ASTER** - Advanced Spaceborne Thermal Emission and Reflection Radiometer. The last one is “our instrument” on which we focus on because ASTER data form the basis of the research presented here. The location of the instruments on the satellite payload is represented in Figure 3.1.



Source: Image adapted from ABRAMS, M. (2005).

Figure 3.1: Terra spacecraft and payload. The Terra satellite (formerly EOS AM-1) provides measurements that significantly contribute to the understanding of the Earth system. It carries five instruments with the mission to obtain information about: the physical and radiative properties of clouds; air-land and air-sea exchanges of energy, carbon and water; and measurement of trace gases; needed to understand global climate change. The ASTER VNIR sensor also provides along-track stereo capability allowing the generation of digital elevation models with high spatial resolution.

The ASTER instrument was built in Japan for the Ministry of Economy, Trade and Industry (METI). A joint U.S./Japan Science Team is responsible for instrument design, calibration, and data validation. Unlike the other instruments aboard Terra, ASTER does not collect data continuously; rather, it collects an average of 8 minutes of data per 98-minute orbit. It consists of three separate subsystems: The Visible and Near Infrared (VNIR), the Shortwave Infrared (SWIR), and the Thermal Infrared (TIR). Each subsystem operates in a different spectral region, has its own telescope(s), and they were all built by a different Japanese company. All three ASTER telescopes (VNIR, SWIR, and TIR) are pointable in across-track direction (ABRAMS ET AL., 2002).

ASTER is the only high spatial resolution instrument on the Terra platform. ASTER's ability to serve as a 'zoom' lens for the other Terra instruments is particularly important for change detection, calibration/validation and land surface studies. ASTER obtains high-resolution images (15 to 90 square meters per pixel) of the Earth in 14 different bands of wavelengths of the electromagnetic spectrum, ranging from visible to thermal infrared light. Table 3.2 shows the main characteristics of the three subsystems: VNIR with three visible and near-infrared channels between 0.52 and 0.86 μm , with 15-m resolution; SWIR with six shortwave infrared channels between 1.6 and 2.43 μm , with 30-m resolution; and TIR with five TIR channels between 8.25 and 11.65 μm , with 90-m resolution. The instrument acquires data over a 60- km swath whose center is pointable cross-track $\pm 8.55^\circ$ in the SWIR and TIR, with the VNIR pointable out to $\pm 24^\circ$. ASTER's pointing capabilities are such that any point on the globe is accessible at least once every 16 days in all 14 bands and once every 5 days in the three VNIR channels (ABRAMS ET AL., 2002).

Table 3.2: Spectral range and spatial resolution of the fourteen ASTER bands. Band 3 has nadir (3N) and backward (3B) sights; all other bands have only nadir sight.

Source: ERSDAC (2005)

Subsystem	Band No.	Spectral Range (μm)	Spatial Resolution (m)
VNIR	1	0.52 – 0.60	15
	2	0.63 – 0.69	
	3N	0.78 – 0.86	
	3B	0.78 – 0.86	
SWIR	4	1.600 – 1.700	30
	5	2.145 – 2.185	
	6	2.185 – 2.225	
	7	2.235 – 2.285	
	8	2.295 – 2.365	
	9	2.360 – 2.430	
TIR	10	8.125 – 8.475	90
	11	8.475 – 8.825	
	12	8.925 – 9.275	
	13	10.25 – 10.95	
	14	10.95 – 11.65	

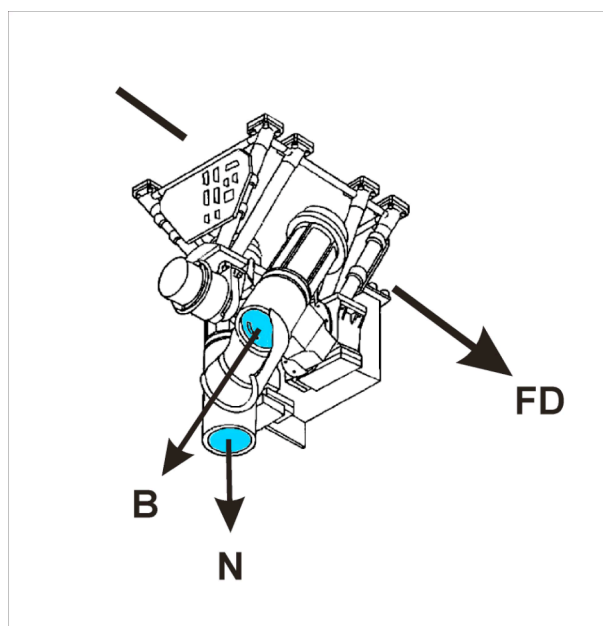


Figure 3.2: ASTER Visible and Near Infrared (VNIR) subsystem telescopes design.

FD: Flight direction

N: Nadir viewing telescope

B: Backward viewing telescope

Source: Adapted from FUJISADA ET AL. (2005)

The VNIR subsystem consists of two independent telescope assemblies to minimize image distortion in the backward and nadir viewing telescopes. Very important for our work is the existence of the additional backward pointing VNIR telescope shown in Figure 3.2, covering the wavelength range of Band 3. By combining data of these bands 3N (Nadir) and 3B (backward), stereo views can be created, with a Base-to-Height ratio of 0.6 (see Figure 3.3a-b).

Since the planning phase of the mission it was a main goal to use the high resolution of the VNIR bands of ASTER and its stereoscopic capability to produce images and detailed terrain height models. The idea was to assemble a global data set at resolutions of up to 15 meters per pixel in roughly 5 years and to be able to create a very detailed digital elevation map of our planet's surface.

The present work deals mainly with specific problems to match this goal on the Antarctic Peninsula. The terrain mostly covered by snow and ice and the lack of ground control data require the search of a suitable approach to overcome these problems.

Band 3N has a dimension of 4200 pixels along track by 4100 pixels across track, and band 3B has 5400 pixels along track by 5000 pixels across track (see Figure 3.11). The detectors for each of the bands consist of 5000 elements of silicon charge-coupled detectors (CCD's). Only 4100 of these detectors are used at any one time. A time lag occurs between the acquisition of the backward image and the nadir image as can be observed in Figure 3.3b. During this time Earth rotation displaces the image center. The VNIR subsystem automatically extracts the correct 4100 pixels based on orbit position information supplied by the EOS platform.

The backward looking telescope focal plane contains only a single detector array and uses an interference filter for wavelength discrimination. The focal plane of the nadir telescope contains 3 line arrays and uses a dichroic prism and interference filters for spectral separation allowing all three bands to view the same area simultaneously. For regions as the Antarctic Peninsula where the reflection is very high as a result of the high albedo of snow, a low gain setting may be used to prevent the sensor from overloading. The absolute radiometric accuracy is $\pm 4\%$ or better (ABRAMS ET AL., 2002).

The band-to-band registration accuracy in the subsystem is better than 0.1 pixels and that between subsystems is better than 0.2 pixels. This means that the geometric

database is determined accurately and the image matching method based on a cross-correlation function is effective in the operational usage (IWASAKI & FUJISADA, 2005).

The VNIR subsystem produces by far the highest data rate of the three ASTER imaging subsystems. With all four bands operating (3 nadir and 1 backward) the data rate including image data, supplemental information and subsystem engineering data is 62 Mbps (ABRAMS ET AL., 2002).

The imaging geometry of ASTER's along-track stereo capability is presented in Figures 3.3a and 3.3b. Important details of these figures are:

- the time span of 9 seconds needed to scan one of the 60 km long scenes
- the angle of 27 degree between nadir viewing and backward viewing scan sight resulting in a Base-to-Height ratio considered suitable to extract the elevation of the surface by satellite stereoscopy techniques
- the orbit altitude of 705 km above sea level with a time delay of 55 seconds between the nadir viewing and the backward viewing to scan the same line on the ground.

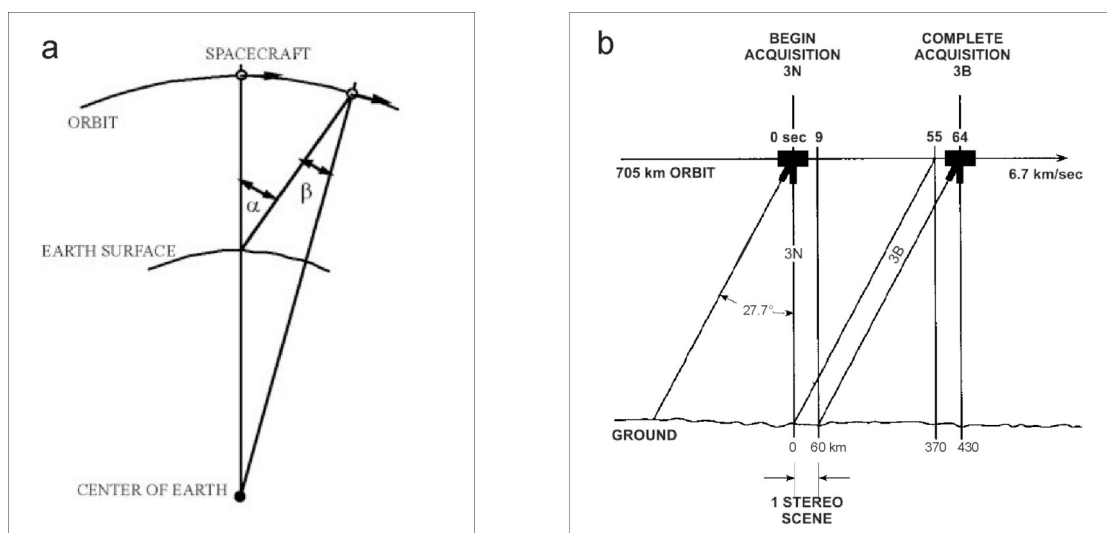


Figure 3.3: Imaging geometry and data acquisition timing for ASTER along-track stereo. Nadir and backward viewing sights of the ASTER sensor system.

- a) Base-to-Height ($B/H = \tan \alpha$) ratio is 0.6. [$\alpha = 30.96^\circ$, $\beta = 27.70^\circ$].
- b) VNIR telescopes require 9 seconds to acquire a 60 x 60 km scene; 64 seconds are required to acquire a stereo pair.

Sources: a) adapted from ERSDAC (2005), p.3;

b) adapted from WELSH ET AL. (1998).

There exists a vast amount of additional technical information on the Terra satellite and its ASTER sensor, but that is regarded out of scope for this investigation. These contents can be found in a large collection of documentation available in the two main web sites of the project: ASTER Science Team (<http://www.science.aster.ersdac.or.jp/en/index.html>, visited 05.02.2006), Japan; and ASTER Project (<http://asterweb.jpl.nasa.gov/>, visited 05.02.2006), USA.

3.1.2 ASTER Data Products

From the ASTER instrument a total of thirteen different ASTER standard data products are produced to satisfy the demand from diverse scientific disciplines. These products are listed in Table 3.3. They are derived from ASTER Level-0, L1A or L1B data according to a series of standard algorithms.

Two types of Level-1 data are produced: Level-1A (L1A) and Level-1B (L1B). They are stored in the HDF-EOS standard format together with its metadata for distribution. Details about the specific characteristics of the products, as well as about their processing are documented in the corresponding Algorithm Theoretical Basis Documents (ATBD) that can be found at NASA EOS (2006) website.

Table 3.3: ASTER standard data products. Products Level 1A, L1B and AST14DEM will play an important role for our work and will be referenced again in following sections.

Source: Jet Propulsion Laboratory (JPL), http://asterweb.jpl.nasa.gov/data_products.asp, (visited 31 Jan. 2006).

Level	Product	Description
1A	Radiance at sensor (L1A)	Image data plus radiometric and geometric coefficients. Data are separated by telescope
1B	Registered radiance at sensor (L1B)	1A data with radiometric and geometric coefficients applied
1AE	Radiance at sensor	Expedited L1AE data product created from ASTER Expedited Level-0. Image data plus radiometric and geometric coefficients. Data are separated by telescope
1BE	Registered radiance at sensor	Expedited L1BE data product created from ASTER Expedited Level-1AE. 1AE data with radiometric and geometric coefficients applied
2	AST06 Decorrelation stretch	Enhanced color composites for each telescope
2	AST04 Brightness temperature	Radiance at the sensor converted to temperature
2	AST09 Surface radiance-VNIR,SWIR	Radiance corrected for atmospheric effects
2	AST09T Surface radiance-TIR	Radiance corrected for atmospheric effects
2	AST07 Surface reflectance-VNIR,SWIR	Derived from surface radiance with topographic corrections
2	AST08 Surface kinetic temperature	Temperature-emissivity separation algorithm applied to atmospherically corrected surface radiance data.
2	AST05 Surface emissivity	Temperature-emissivity separation algorithm applied to atmospherically corrected surface radiance data.
2	AST13. Polar Surface and Cloud Classification	Classifies pixels of polar scenes into one of eight classes: water cloud, ice cloud, aerosol/dust, water, land, snow/ice, slush ice, and shadow.
4	AST14DEM - Digital elevation model	DEM produced by stereo correlation of nadir and aft Band 3 data - Absolute DEM Created using Ground Control Points - Relative DEM Created only from 3N and 3B data

For the purposes of this work three different standard data products are relevant:

- The Level 1A “Radiance at sensor”. All data collected by ASTER is processed to Level 1A data. This product contains depacketized, demultiplexed and realigned instrument image data with geometric correction coefficients and radiometric calibration coefficients appended but not applied. These coefficients include correcting for the SWIR parallax as well as inter- and intra-telescope registration. The spacecraft ancillary and instrument engineering data are also included. The radiometric calibration coefficients, consisting of offset and sensitivity information, are generated from a database for all detectors, and are updated periodically. The geometric correction is the coordinate transformation for band-to-band co-registration. We will use bands 3N and 3B.
- Level 1B “Registered radiance at sensor”. This data is the L1A data with the radiometric and geometric coefficients applied. The L1B data product is generated, by default, in UTM projection in swath orientation with a Cubic Convolution resampling at full instrument resolutions. This means that the raw digital counts of L1A data are converted to radiance values, and a transformation is applied to register the image to a coordinate system. The Level-1B data generation also includes registration of the SWIR and TIR data to the VNIR data. For SWIR in particular the parallax errors due to the spatial locations of all of its bands are corrected. Level 1B can be used for spectral analysis without any pre-processing. Only cloudless scenes are processed to Level 1B.

Not all of the scenes used in this study have already been processed to L1B by the ASTER system. Using a convenient procedure supported by “commercial of the shelf” software we were able to produce an equivalent product (“L1B”) for the VNIR bands from the available ASTER L1A scenes (see figure 3.14).

- Level 4 “Digital elevation model” (AST14DEM). These data are produced in the EDC-DAAC facility, i.e. the Earth Resources Observation and Science (EROS) Data Center of the Distributed Active Archive Center (EDC-DAAC) at the U.S. Geological Service (USGS). They are generated from bands 3N and 3B of ASTER L1A images. They cover ca. 60 km x 60 km with 30 m resolution and are projected to UTM. AST14DEMs can be generated either with or without ground control points (GCPs). An absolute DEM is created with GCPs that are supplied by the end-user who has requested the product. These DEMs “have an absolute horizontal and vertical accuracy of up to 7 meters with appropriate GCPs and up to 10 meters without GCPs” (ABRAMS ET AL., 2002). Alternatively, a relative DEM can also be generated without GCPs. ASTER DEMs are expected to meet map accuracy standards for scales from 1:50,000 to 1:250,000” (ABRAMS ET AL., 2002).

These three types of ASTER data should theoretically provide directly or indirectly a DEM of specific areas in our region of interest. Nevertheless, as is discussed in more detail in section 3.2, available AST14DEM standard products for our region of interest contain large and abundant holes of no-data (see Figures 3.7a-c). Furthermore, because this is a “On-Demand” product, only few are produced each

day, taking several months to complete a processing request for a specific stereo pair.

This situation is one of the motivations for this study. There is a demand for a functional, robust and valid schema to produce our own DEMs directly from the available ASTER L1A and L1B scenes. Thus, the next consideration is which of these two possible data levels L1A or L1B provides the best results for our purpose.

Two decisive facts have to be considered:

- the availability of L1A scenes is greater because not all ASTER L1A scenes are processed to L1B, and
- the resampling applied to L1B scenes during processing might affect the result of the image matching of its stereo bands, leaving them less suitable for DEM extraction.

Consequently, we based our approach in the use of ASTER L1A scenes.

The following section is directed towards the questions: For which areas on the Antarctic Peninsula exist L1A scenes? And how many of these are cloud-free?

3.1.3 ASTER Data Catalogues

The use of on-line data catalogues is necessary to investigate the availability of ASTER products covering land ice on the Antarctic Peninsula. The catalogues allow to analyze relevant parameters indicating quality of acquisition and to extract the metadata needed to order the data. The most important points of entry where ASTER metadata can be searched are:

- The **GLIMS ASTER image service**

Access point: <http://www.glims.org/MapsAndDocs/astermap.html>

The GLIMS ASTER image service is related to the Global Land Ice Measurement from Space (GLIMS) project. It can be found at the GLIMS project site. It contains a set of interactive maps to search availability of ASTER scenery in the Flagstaff ASTER image database. They use ArcIMS technology. Users of ESRI's ArcExplorer4.x (freeware) and ArcGIS software may access the service directly by adding an Internet Server to their application (Map Server (URL): <http://webgis.wr.usgs.gov> and Map Service: *Aster_glacier_footprints*).

A query for L1A and L1B data for the Antarctic Peninsula on August 2004 returned metadata inconsistencies (e.g. a search for scenes acquired at day time reported scenes acquired at night). The contents had been updated only very irregularly (last added record November 2002).

- The **Ground Data System (GDS) catalogue**

Access point: http://www.gds.aster.ersdac.or.jp/gds_www2002/index_e.html

GDS is located in Japan. It is ASTER's ground system which commands and controls the ASTER instruments. It also processes, analyzes, archives and distributes data transmitted from the ASTER instruments. ASTER GDS consists of three primary components: 1. AOS (ASTER Operation Segment) which

operates the ASTER instrument, 2. SDPS (Science Data Processing Segment) which processes, analyzes, archives, and distributes scientific data, and manages the user interface, and 3. CSMS (Communication and System Management Segment) which connects and controls the above operations.

Here it is possible to quickly find excellent quick looks; the metadata is up-to-date but not all keywords are reported.

- The **EOS Data Gateway (EDG)**

Access point: <http://edcimswww.cr.usgs.gov/pub/ims/welcome/>

The EDG is organized by the Earth-Sun System Division from the Land Processes Data and Services in partnership with the USGS, especially with the EROS data center. One node of the EDG is the Land Processes Distributed Active Archive Center (LP-DAAC). LP-DAAC is part of NASA's [EOS](#) Data and Information System ([EOSDIS](#)) initiative to process, archive, and distribute land-related data collected by EOS sensors. The role of LP-DAAC includes the higher-level processing and distribution of [ASTER](#) data, and the distribution of [MODIS](#) land products derived from data acquired by the Terra and Aqua satellites.

The LP-DAAC EDG site offers a complete interface for advanced searches, the metadata is complete and can readily be downloaded. However, the drawback of this catalogue interface is that it is slow and the size of the quick looks is rather small.

Using mainly the EDG catalogue we were able to collect all the associated metadata of ASTER L1A scenes acquired over the Antarctic Peninsula and surrounding Seas from November 2000 to September 2005. For the efficient use of this information a dedicated database had to be implemented. The database should allow to add new records according to the stage of acquisitions of raw scenes. To readily analyze its records it should facilitate efficient interactive geographical searches and the display of maps showing scene coverage.

To this end a GIS-based stand-alone ASTER L1A tool was implemented. The so-called “ArcMap ASTER L1A Catalogue” application was created using ArcMap software. The application allows to search the database conveniently and provides for display of the scene footprints. The database and the corresponding application files are provided as supporting data set in Annex 1.

Using this tool we filtered the database with all available ASTER-L1A scenes and found the number, location and quality of available ASTER L1A scenes over the land of the Antarctic Peninsula. Figures 3.4 and 3.5 show the answers for the basic first two of such queries.

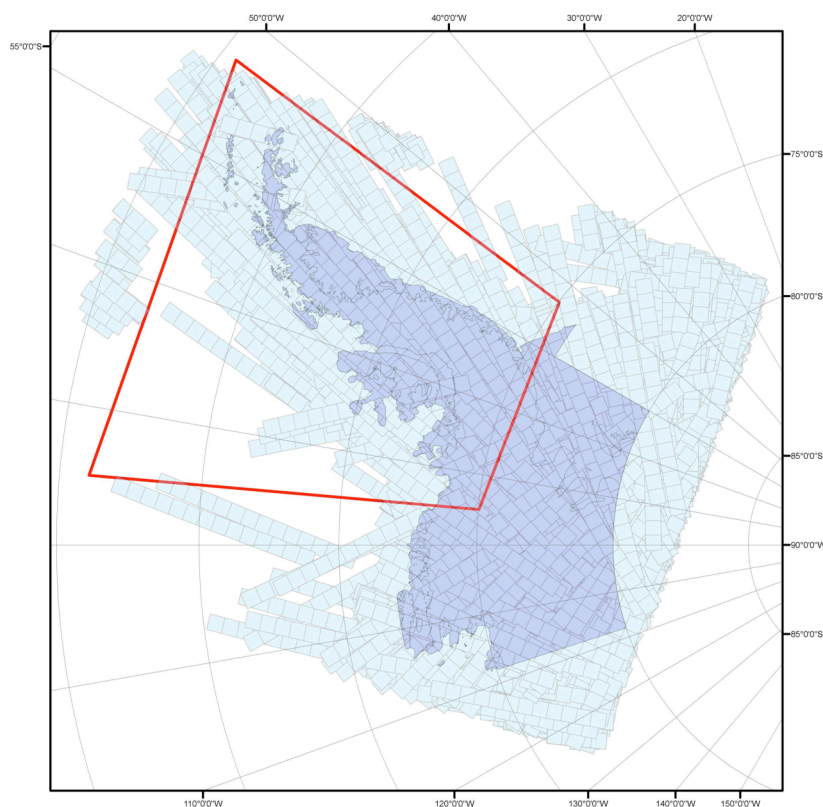


Figure 3.4: Coverage of ASTER scenes Level 1A over the Antarctic Peninsula region and surrounding Seas acquired between 17.11.2000 and 30.09.2005. Using our “ArcMap ASTER L1A Catalogue” and based on metadata available in the EOS Data Gateway (EDG) website, the four corner coordinates of 14.370 scenes were used to create polygons that correspond with the footprint of the scenes. 4.896 scenes fall inside of the red polygon. From these only 3.658 cover land ice masses of the Antarctic Peninsula.

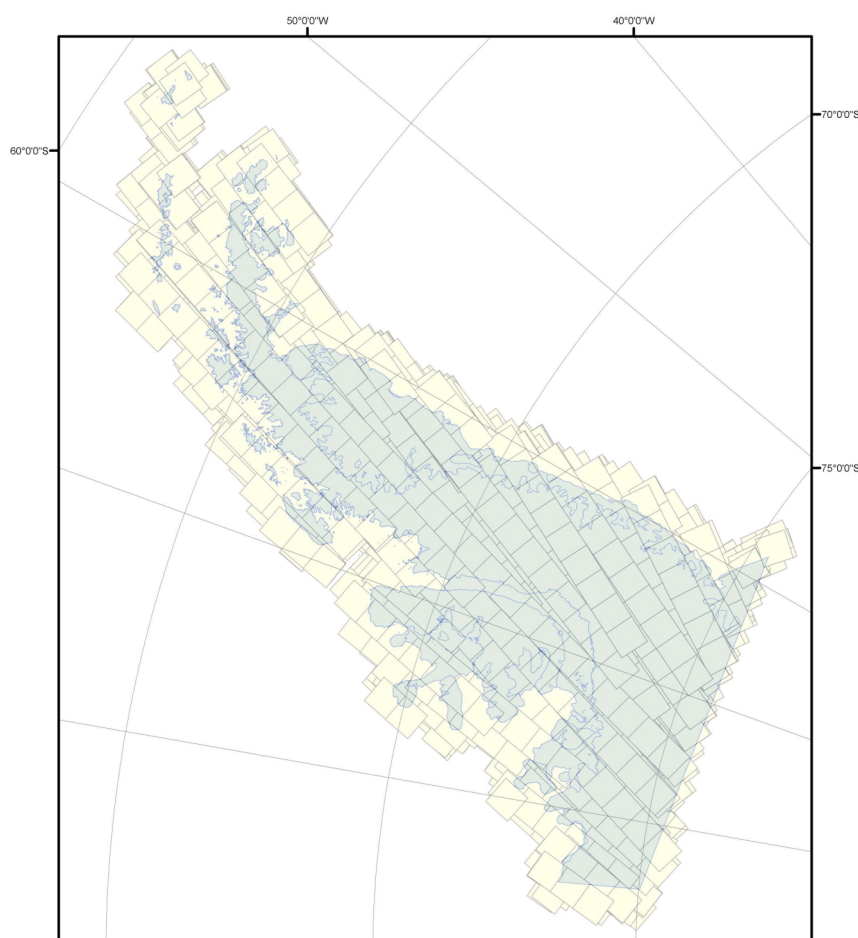


Figure 3.5: Coverage of ASTER Level 1A diurnal scenes over land ice in the Antarctic Peninsula region acquired between 17.11.2000 and 30.09.2005. A preliminary test showed that slightly dark images such as those acquired during the summer dawn on the Antarctic Peninsula do not give an acceptable result for the image matching process. Consequently, we needed to filter the ASTER L1A scenes database considering only scenes acquired during full daylight. The map shows the location of the 3.280 scenes acquired during full daylight between November 2000 and September 2005. By exclusion other 378 (~10%) scenes acquired during night time were discarded.

3.2 Available ASTER DEMs and their problems

Some of the problems related with the available standard AST14DEM product data set have already been outlined in Section 3.1.2. These problems are related with access to data and with the quality achieved by the already available DEMs that cover the Antarctic Peninsula region.

The AST14DEM is an On-Demand product and only 1 or 2 DEMs are created every day at the EDC-DAAC (ASTER web site; ABRAMS ET AL. 2002). Consequently a normal order requesting a DEM requires several months to be completed. Unfortunately this prevents from having access to a greater number of independent topographic data sets for this study.

Nevertheless, we were able to access and analyze each of the sixteen AST14DEM products already available for the Antarctic Peninsula region. The identification and basic parameters of acquisition for each of the data products are included in Table 3.4. Their corresponding geographic location is shown in Figure 3.6.

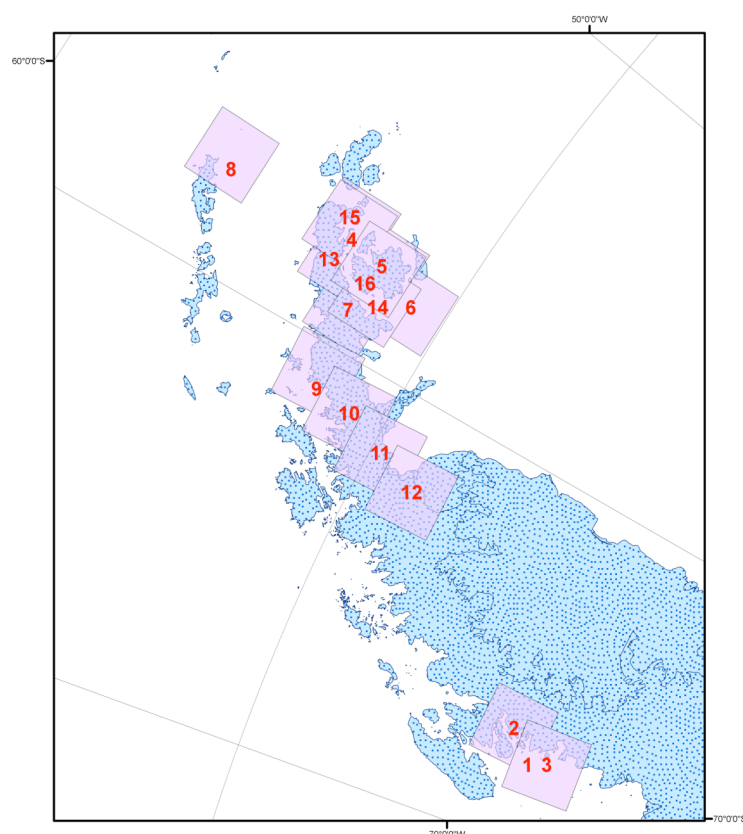


Figure 3.6: Location of the 16 standard AST14DEM-relative digital elevation model products for the Antarctic Peninsula already available for distribution in the EOS Data Gateway (EDG) website. Numbers inside of footprints correspond to those indicated in the column ID in Table 3.4.

These data sets are produced in the EROS Data Center of the Distributed Active Archive Center (EDC-DAAC), and are distributed by the Land Processes Distributed Active Archive Center (LP-DAAC), both facilities of the U.S. Geological Survey (USGS) Center for Earth Resources Observation and Science (EROS) <http://LPDAAC.usgs.gov>.

The analysis of this reduced number of automatically produced DEMs (compared to the total 3.280 diurnal-scenes available) showed that these DEMs are heavily contaminated by holes of no data. These holes occur mainly in places where the image matching algorithm is not able to obtain correlation values above the minimal threshold specified in the processing chain due to low image contrast. This situation can be observed in the examples depicted in the Figure 3.7a-c.

The standard processing chain at EDC-DAAC is based on the use of the PCI Orthoengine software. An independent evaluation has verified the inferior quality of AST14DEMs compared with those produced with other commercial packages

(WATANABE, 2005, slides 48-51). Even more, WATANABE concludes that in the standard processing chain the software platform should be replaced. The reason for the low performance of the PCI Orthoengine software is apparently related to deficiencies in the blunder detection algorithm within its module (KÄÄB, 2005).

Table 3.4: Standard ASTER Level 4 Digital Elevation Model products (**AST14DEM**) already produced for the Antarctic Peninsula region.

DEM ID 1 has been created from a version V002 of the ASTER L1A source product, all others were created from version V003 products. DEMs ID 1 and ID 3 correspond to the same scene acquired on 04 Jan 2001 at 13:40:52. DEMs with IDs 3, 7 and 16 (rows marked in bold), are shown in the following Figures 3.7a - 3.7c.

Source: Search performed on 3 Feb. 2006 at the EOS Data Gateway (EDG), <http://edcimswww.cr.usgs.gov/pub/imswelcome/>.

ID	GRANULE	LOCAL GRANULE ID	START DATE	CENTER POINT
1	SC:AST14DEM.002:2029948656	ASTER_DEM20011128141106.hdf	04 Jan 2001, 13:40:52	-68.19 Lat -67.49 Lon
2	SC:AST14DEM.003:2030008671	ASTER_DEM20030307225913.hdf	04 Jan 2001, 13:40:43	-67.7 Lat -66.87 Lon
3	SC:AST14DEM.003:2030008670	ASTER_DEM20031218114515.hdf	04 Jan 2001, 13:40:52	-68.19 Lat -67.49 Lon
4	SC:AST14DEM.003:2030008703	ASTER_DEM20041130094314.hdf	08 Jan 2001, 13:14:40	-63.61 Lat -57.22 Lon
5	SC:AST14DEM.003:2030008693	ASTER_DEM20011210080955.hdf	08 Jan 2001, 13:14:49	-64.11 Lat -57.68Lon
6	SC:AST14DEM.003:2030008721	NA	08 Jan 2001, 13:14:57	-64.61 Lat -58.17 Lon
7	SC:AST14DEM.003:2030057219	ASTER_DEM20011207141730.hdf	26 Sep 2001, 13:26:54	-64.05 Lat -59.03 Lon
8	SC:AST14DEM.003:2030094704	ASTER_DEM20020614105556.hdf	15 Nov 2001, 13:12:16	-62.12 Lat -57.36 Lon
9	SC:AST14DEM.003:2030094751	ASTER_DEM20030508131018.hdf	22 Nov 2001, 13:19:07	-64.12 Lat -60.75 Lon
10	SC:AST14DEM.003:2030094750	ASTER_DEM20030509112557.hdf	22 Nov 2001, 13:19:15	-64.62 Lat -61.24Lon
11	SC:AST14DEM.003:2030094741	ASTER_DEM20030509132003.hdf	22 Nov 2001, 13:19:24	-65.11 Lat -61.74 Lon
12	SC:AST14DEM.003:2030094748	ASTER_DEM20030512080209.hdf	22 Nov 2001, 13:19:33	-65.61 Lat -62.26 Lon
13	SC:AST14DEM.003:2030092089	ASTER_DEM20041129185034.hdf	18 Jan 2002, 13:10:59	-63.74 Lat -58.03 Lon
14	SC:AST14DEM.003:2030092086	ASTER_DEM20041130164951.hdf	18 Jan 2002, 13:11:08	-64.24 Lat -58.48 Lon
15	SC:AST14DEM.003:2030126401	NA	29 Dec 2002, 13:03:32	-63.6 Lat -57.3 Lon
16	SC:AST14DEM.003:2030126396	ASTER_DEM20041130133950.hdf	29 Dec 2002, 13:03:40	-64.1 Lat -57.77 Lon

The occurrence of large areas with lack of data inside of the AST14DEM products impact on our goal to find the ice divides in comparably flat surface areas on the Antarctic Peninsula. Figures 3.7a-c show the location of holes resulting from low correlation values determined by the EDC-DAAC processing.

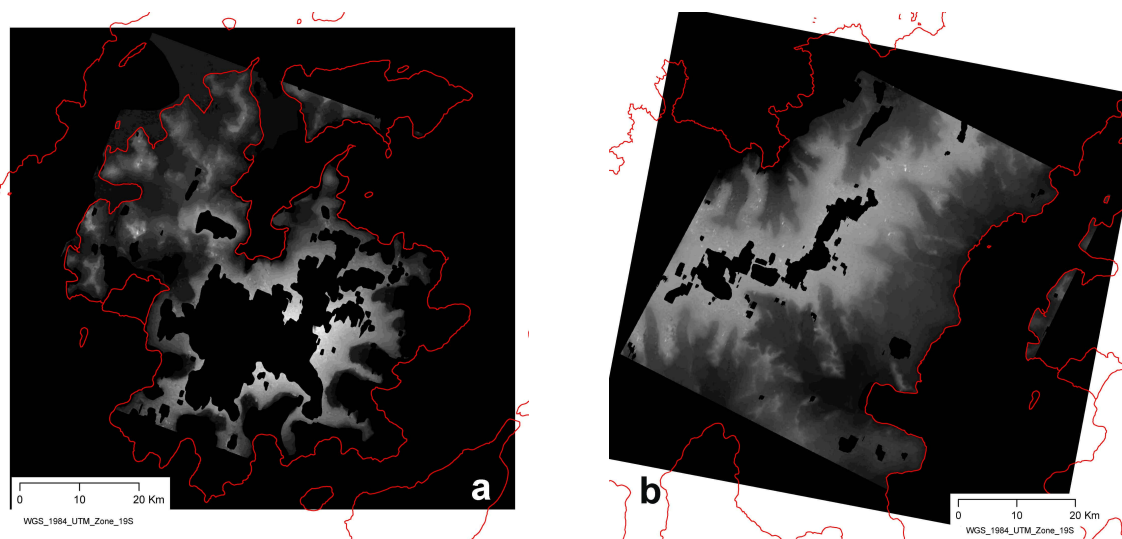


Figure 3.7: Examples of AST14DEM standard products featuring large holes without data. This is mainly caused by low image matching correlation over flat snow surfaces.

a: James Ross Island: holes without data distribute over the ice cap.

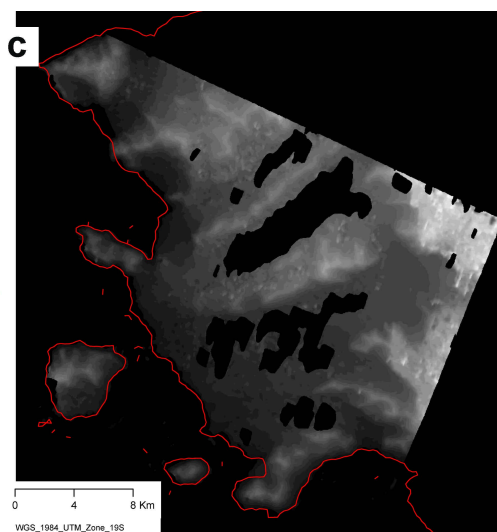
[Local Granule ID ASTER_DEM20041130133950, acquired on 29 Dec 2002 at 13:03:40]

b: Detroit Plateau: holes in the central part of plateau hiding the location of the ice divide.

[Local Granule ID ASTER_DEM20011207141730, acquired on 26 Sep. 2001 at 13:26:54]

c: Sub-scene from Northeast and McClary Glaciers, Marguerite Bay region: areas with lack of data on flat glacier surfaces.

[Local Granule ID ASTER_DEM20031218114515, acquired on 04 Jan 2001 at 13:40:52]



Red: coastline; black: data holes or open sea; bright grey: high altitudes; dark grey: low altitudes.

The size and the typical location of the void areas in sectors of our special interest prevent from using automatic routines to extract the catchment settings in this relief. The selected examples show the limited use of the AST14DEM products for the given application. For example it is not possible to answer the questions where the ice divides on the ice cap of James Ross Island (Figure 3.7a) are located. It is also not possible to derive the central ice divide of Detroit Plateau or the McClary ice divide on Marguerite Bay area.

These examples again show the relevance of finding alternative methodologies, which can provide better results than the standard AST14DEMs derived from the ASTER data.

This moves us forward to the next step to select ASTER L1A data to derived DEMs using a reliable methodology.

3.3 Generation of Digital Elevation Models using ASTER-Imagery

3.3.1 Selected ASTER Data

Before starting to generate DEMs based on ASTER L1A scenes, we had to identify suitable data covering parts of the Antarctic Peninsula. Consequently, we performed a search of relevant ASTER L1A metadata and built a database for efficient management and analysis of this metadata (see Section 3.1.3). Filtering of available scenes based on the metadata and the visual inspection of quicklooks lead to the identification of 84 scenes as the most suitable to derive DEMs. The spatial distribution of these scenes is shown in Figure 3.8 and the corresponding list is given in Table 3.5.

The selection of ASTER L1A scenes was produced by the following procedure:

Using the parameter “*Scene Cloud Coverage*” we made a filtering from the total 3.280 day-scenes covering glaciers on the Antarctic Peninsula acquired until the 30.09.2005. This allowed us to pre-selected 537 scenes reported as scenes with cloud coverage less than 5% (CCLE5 scenes; layer *L1A_fp_300905_ogAP_ccle5* in the ArcMap ASTER L1A Catalogue, see Annex 1).

All CCLE5 scenes then were visually inspected looking for the location and distribution of clouds using the on-line quicklook browsing interface from the GDS Catalogue. We verified that the estimation of the “*Scene Cloud Coverage*” parameter that appears in the metadata is not always correct. In many cases coverage of clouds is underestimated. Moreover, a second drawback was the fact that a large number of “good” scenes were located outside of our area of interest (e.g. over the ice shelf), further reducing the number of scenes from our pre-selection.

These two reasons moved us to change our approach to search suitable scenes. We chose 19 areas of interest based on the locations of the best pre-selected scenes. In the areas of these sites we did a more extensive pre-selection to include additional scenes. The extended filtering was based on the metadata parameters “*Upperleftquad-cloudcoverage*”, “*Upperrightquad-cloudcoverage*”, “*Lowerleftquad-cloudcoverage*” and “*Lowerrightquad-cloudcoverage*”. Based on the visual inspection of the quicklooks we identified an additional number of scenes which featured cloud-free quadrangles over sectors covering our areas of interest. This explains why in Table 3.5 some scenes are included despite of having a high value for “*Scene Cloud Coverage*”.

Finally we were able to select the 84 ASTER L1A scenes presented in Table 3.5 as the most suitable to produce DEMs from in the Antarctic Peninsula. The scenes are distributed over 19 sites of interest each site featuring a sufficient number of scenes for DEM production.

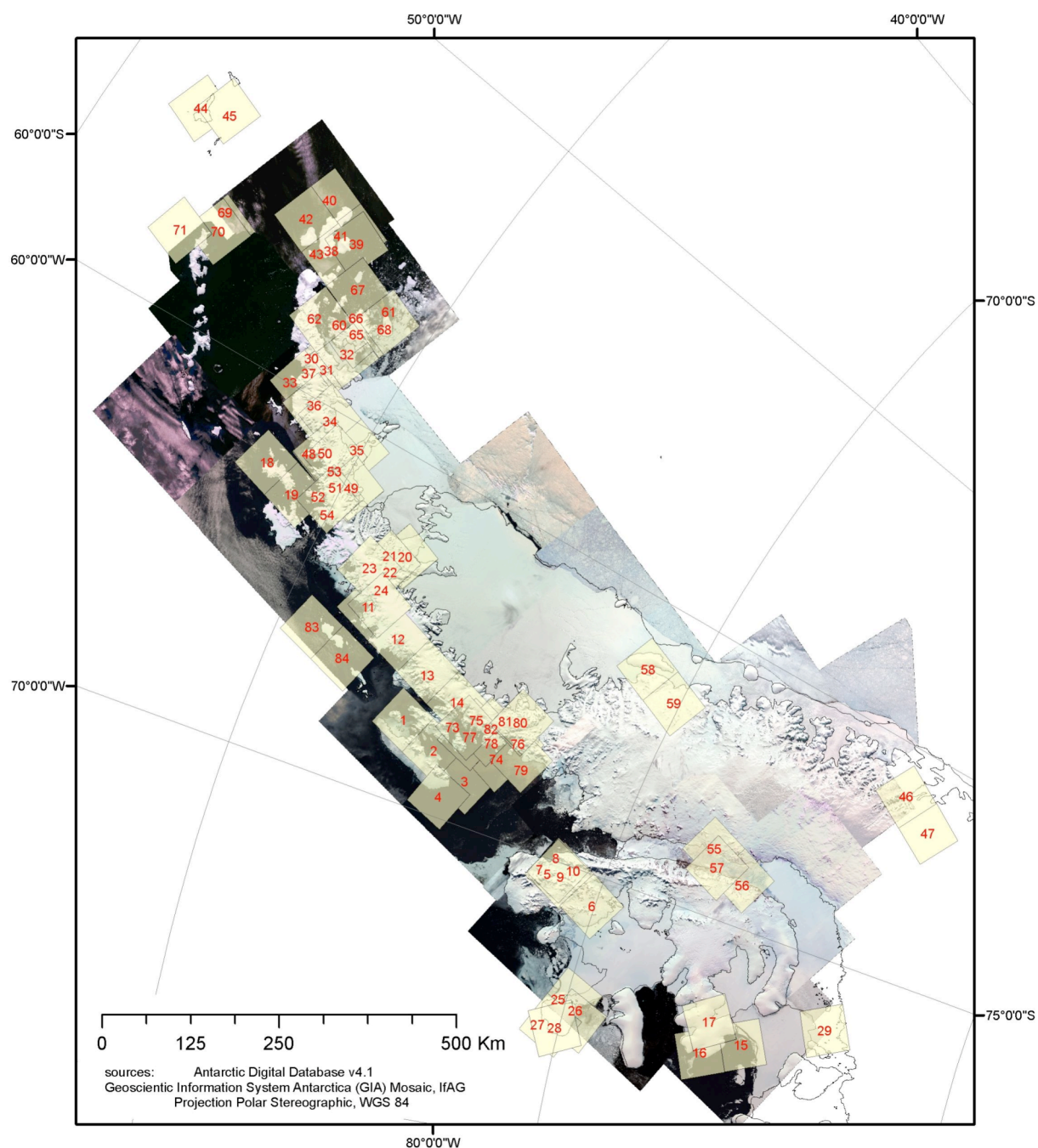


Figure 3.8: Location of ASTER Level 1A scenes suitable for DEM generation in the Antarctic Peninsula region.

Following a series of filtering and the inspection of quicklooks to identify the scenes with a low “scene cloud coverage” parameter, the 3.280 available day-scenes over land were reduced to 84 scenes at 19 different sites. These scenes are considered the most suitable as data sources for DEM generation.

Numbers in red correspond to those indicated under column NUM in Table 3.5.

Table 3.5: List of the selected ASTER Level-1A scenes for DEM generation in the Antarctic Peninsula region.

Area codes used in column "SITE" correspond to: ADI – Adelaide Island; AXI – Alexander Island; AVP – Avery Plateau; BEP – Beethoven Peninsula; BRI – Brabant Island; BRP - Bruce Plateau; CHI – Charcot Island; DEI – Deatley Island; DEP – Detroit Plateau; DJD - D'Urville, Joinville & Dundee Islands; ELI - Elephant Island; FMG – Fenton & Mosby Glaciers; FBP - Forbidden Plateau; FBF - Fossil Bluff; HAG – Hearst Island & Anthony Glacier; JRI – James Ross Island; KGI - King George Island; MGB – Marguerite Bay; REI - Renaud Island

NUM	SITE	CALENDAR DATE	TIME	SCENE CLOUD COVER AGE	GEOME TRIC DATAB ASE	RADIOMETRIC DATABASE	PGEV VERSION	SOLAR AZIMUTH	SOLAR ELEVATION	GRANULE ID
1	ADI	11 Jan 2004	13:41:20	0	2.00	2.16	04.00R10	53.7542	36.9455	SC:AST_L1A.003:2019764229
2		11 Jan 2004	13:41:29	0	2.00	2.16	04.00R10	54.2203	36.9478	SC:AST_L1A.003:2019764222
3		11 Jan 2004	13:41:38	0	2.00	2.16	04.00R10	54.4104	36.3644	SC:AST_L1A.003:2019764217
4		23 Oct 2004	13:51:48	5	3.00	2.18	05.00R00	42.9325	28.7286	SC:AST_L1A.003:2026309852
5	AXI	12 Mar 2002	13:30:11	1	2.00	2.06		53.1694	16.2725	SC:AST_L1A.003:2006269757
6		12 Mar 2002	13:30:19	25	2.00	2.06		53.6226	15.4497	SC:AST_L1A.003:2006269762
7		20 Aug 2003	13:40:22	0	2.00	2.13	04.00R09	44.4431	2.1399	SC:AST_L1A.003:2016528789
8		11 Jan 2004	13:42:05	0	2.00	2.16	04.00R10	55.4344	34.8338	SC:AST_L1A.003:2019764199
9		30 Dec 2004	13:28:05	0	3.00	2.19	05.00R01	58.6306	35.1833	SC:AST_L1A.003:2027186462
10		13 Jan 2005	13:40:24	5	3.00	2.19	05.00R01	55.9547	34.3286	SC:AST_L1A.003:2027470154
11	AVP	19 Sep 2005	13:32:51	1	3.00	2.21	06.10R01	41.8973	16.8712	SC:AST_L1A.003:2030971097
12		19 Sep 2005	13:33:00	0	3.00	2.21	06.10R01	42.3249	16.5880	SC:AST_L1A.003:2030971107
13		19 Sep 2005	13:33:09	0	3.00	2.21	06.10R01	42.7714	15.8717	SC:AST_L1A.003:2030971115
14		19 Sep 2005	13:33:17	5	3.00	2.21	06.10R01	43.0677	15.2886	SC:AST_L1A.003:2030971127
15	BEP	16 Dec 2003	05:00:29	0	2.00	2.15	04.00R10	178.6738	5.4401	SC:AST_L1A.003:2019423887
16		16 Dec 2003	05:00:37	0	2.00	2.15	04.00R10	179.1672	4.9609	SC:AST_L1A.003:2019423882
17		30 Dec 2004	05:23:08	22	3.00	2.19	05.00R01	174.0808	5.0715	SC:AST_L1A.003:2027185768
18	BRI	21 Dec 2004	13:32:23	0	3.00	2.19	05.00R01	50.9389	42.1080	SC:AST_L1A.003:2027139547
19		21 Dec 2004	13:32:32	0	3.00	2.19	05.00R01	50.9704	41.5259	SC:AST_L1A.003:2027139569
20	BRP	06 Jan 2001	13:27:50	13	2.00	2.04		53.0854	38.7124	SC:AST_L1A.003:2004085797
21		22 Nov 2001	13:19:42	5	2.00	2.05		48.6377	37.6041	SC:AST_L1A.003:2005067309
22		07 Nov 2002	13:28:43	26	2.00	2.09		44.4468	34.6570	SC:AST_L1A.003:2009058258
23		27 Jan 2004	13:40:36	8	2.00	2.16	04.00R10	50.9378	35.6365	SC:AST_L1A.003:2020246915
24	CHI	08 Jan 2005	13:20:56	34	3.00	2.19	05.00R01	56.7022	37.5682	SC:AST_L1A.003:2027367164
25		26 Jan 2002	14:02:14	0	2.00	2.06		54.6006	31.2049	SC:AST_L1A.003:2005906533
26		04 Jan 2003	14:06:51	37	2.00	2.11		53.5396	35.6703	SC:AST_L1A.003:2010457856
27		16 Jan 2004	14:00:42	2	2.00	2.16	04.00R11	55.9379	33.5308	SC:AST_L1A.003:2023506738
28	DEI	08 Jan 2005	05:17:37	0	3.00	2.19	05.00R01	178.0724	2.3356	SC:AST_L1A.003:2027367001
29		16 Dec 2003	05:00:11	0	2.00	2.15	04.00R10	177.2135	6.5473	SC:AST_L1A.003:2019423879
30		26 Sep 2001	13:26:54	6	2.00	2.05		38.6537	22.4274	SC:AST_L1A.003:2004337053
31		15 Nov 2001	13:12:52	44	2.00	2.05		46.3893	38.0705	SC:AST_L1A.003:2005556226
32	DEP	18 Jan 2002	13:11:08	0	2.00	2.06		54.3938	37.5878	SC:AST_L1A.003:2005839335
33		02 Oct 2003	13:20:44	13	2.00	2.14	04.00R10	41.0065	23.9155	SC:AST_L1A.003:2017716438
34		02 Oct 2003	13:20:52	0	2.00	2.14	04.00R10	41.1849	23.3397	SC:AST_L1A.003:2017716437
35		02 Oct 2003	13:21:01	0	2.00	2.14	04.00R10	41.5624	22.9304	SC:AST_L1A.003:2017716436
36	DJD	16 Feb 2004	13:15:34	49	2.00	2.16	04.00R11	52.4117	29.6489	SC:AST_L1A.003:2021136501
37		22 Oct 2004	13:07:40	46	3.00	2.18	05.00R00	45.3020	30.6841	SC:AST_L1A.003:2026307431
38		28 Sep 2001	13:14:18	33	2.00	2.05		38.7702	23.3594	SC:AST_L1A.003:2004349253

(Continuation Table 3.5)

NUM	SITE	CALENDAR DATE	TIME	SCENE CLOUD COVER AGE	GEOME TRIC DATAB ASE	RADIOMETRIC DATABASE	PGEV VERSION	SOLAR AZIMUTH	SOLAR ELEVATION	GRANULE ID
39		23 Jan 2003	12:57:17	1	2.00	2.11		55.4072	36.8888	SC:AST_L1A.003:2010935347
40		22 Feb 2003	13:09:09	4	2.00	2.12	04.00R09	48.0963	29.5549	SC:AST_L1A.003:2014333604
41	DJD	22 Feb 2003	13:09:18	5	2.00	2.12	04.00R09	48.3398	29.1087	SC:AST_L1A.003:2014333603
42		25 Feb 2004	13:08:52	23	2.00	2.16	04.00R11	48.5454	28.3599	SC:AST_L1A.003:2021396754
43		25 Feb 2004	13:09:01	0	2.00	2.16	04.00R11	48.8775	27.9669	SC:AST_L1A.003:2021396868
44	ELI	29 Oct 2003	13:01:36	2	2.00	2.14	04.00R10	44.1847	35.8411	SC:AST_L1A.003:2018317292
45		25 Feb 2004	13:08:26	1	2.00	2.16	04.00R11	48.1394	29.9033	SC:AST_L1A.003:2021396759
46	FMG	17 Oct 2003	12:40:26	0	2.00	2.14	04.00R10	51.5640	20.0272	SC:AST_L1A.003:2018036297
47		17 Oct 2003	12:40:35	0	2.00	2.14	04.00R10	52.4803	19.5337	SC:AST_L1A.003:2018036294
48		06 Jan 2001	13:27:24	54	2.00	2.04		52.3487	40.1727	SC:AST_L1A.003:2004085789
49		06 Jan 2001	13:27:33	28	2.00	2.04		52.4772	39.6391	SC:AST_L1A.003:2004085791
50		22 Nov 2001	13:19:15	12	2.00	2.05		47.8165	39.0549	SC:AST_L1A.003:2005067298
51	FBP	22 Nov 2001	13:19:24	4	2.00	2.05		48.0090	38.5670	SC:AST_L1A.003:2005067300
52		07 Nov 2002	13:28:26	47	2.00	2.09		44.0958	35.8569	SC:AST_L1A.003:2009058253
53		02 Feb 2003	13:34:34	25	2.00	2.12	04.00R09	49.9625	34.7835	SC:AST_L1A.003:2013964909
54		13 Jan 2004	13:28:22	41	2.00	2.16	04.00R10	53.4859	38.5368	SC:AST_L1A.003:2019780186
55		26 Jan 2003	13:30:17	1	2.00	2.11		54.7272	30.7804	SC:AST_L1A.003:2011173022
56	FBF	26 Jan 2003	13:30:26	0	2.00	2.11		55.1506	30.2846	SC:AST_L1A.003:2011173025
57		22 Jan 2005	13:34:40	0	3.00	2.19	05.00R01	54.4774	31.5063	SC:AST_L1A.003:2027574136
58	HAG	02 Jan 2002	13:13:06	0	2.00	2.06		53.9076	36.3237	SC:AST_L1A.003:2005692604
59		02 Jan 2002	13:13:15	0	2.00	2.06		54.4958	35.9648	SC:AST_L1A.003:2005692609
60		08 Jan 2001	13:14:49	2	2.00	2.04		52.2405	40.4690	SC:AST_L1A.003:2004102903
61		28 Sep 2001	13:14:36	3	2.00	2.05		39.3058	22.3761	SC:AST_L1A.003:2004349260
62		18 Jan 2002	13:10:59	20	2.00	2.06		54.3310	38.1645	SC:AST_L1A.003:2005839332
63		18 Jan 2002	13:11:08	0	2.00	2.06		54.3938	37.5878	SC:AST_L1A.003:2005839335
64	JRI	29 Dec 2002	13:03:40	24	2.00	2.11		54.4371	40.4810	SC:AST_L1A.003:2010352317
65		05 Dec 2003	13:21:58	10	2.00	2.14	04.00R10	45.5777	42.0811	SC:AST_L1A.003:2019246233
66		02 Feb 2004	13:03:13	2	2.00	2.16	04.00R11	54.9908	33.7012	SC:AST_L1A.003:2020410756
67		25 Feb 2004	13:09:10	0	2.00	2.16	04.00R11	48.9700	27.3907	SC:AST_L1A.003:2021396864
68		25 Feb 2004	13:09:19	1	2.00	2.16	04.00R11	49.3314	26.9941	SC:AST_L1A.003:2021396835
69		15 Nov 2001	13:12:16	66	2.00	2.05		45.6643	39.8599	SC:AST_L1A.003:2005556218
70	KGI	22 Oct 2004	13:07:04	0	3.00	2.18	05.00R00	44.2618	32.5628	SC:AST_L1A.003:2026307427
71		17 Jan 2005	13:13:28	2	3.00	2.19	05.00R01	54.8865	39.9491	SC:AST_L1A.003:2027524647
72		24 Nov 2000	13:47:34	29	2.00	2.04		44.6539	37.4374	SC:AST_L1A.003:2004036061
73		04 Jan 2001	13:40:43	11	2.00	2.04		52.5747	37.8407	SC:AST_L1A.003:2004076906
74		04 Jan 2001	13:40:52	3	2.00	2.04	04.00R02	52.8367	37.2485	SC:AST_L1A.003:2004076911
75		27 Dec 2001	13:49:44	1	2.00	2.06		49.2433	39.0762	SC:AST_L1A.003:2006637985
76		25 Dec 2002	13:29:43	4	2.00	2.11		53.9859	37.8277	SC:AST_L1A.003:2010196883
77	MGB	02 Jan 2004	13:47:46	19	2.00	2.15	04.00R10	51.1539	38.5559	SC:AST_L1A.003:2019544986
78		20 Jan 2004	13:35:19	29	2.00	2.16	04.00R10	54.3136	34.5272	SC:AST_L1A.003:2020012711
79		20 Jan 2004	13:35:28	0	2.00	2.16	04.00R10	54.5369	34.0663	SC:AST_L1A.003:2020012723
80		27 Jan 2004	13:41:21	12	2.00	2.16	04.00R10	51.8139	33.0423	SC:AST_L1A.003:2020246943
81		29 Jan 2005	13:39:56	14	3.00	2.19	05.00R01	52.1890	32.4516	SC:AST_L1A.003:2027650383
82		19 Sep 2005	13:33:26	4	3.00	2.21	06.10R01	43.5561	14.8590	SC:AST_L1A.003:2030971130
83	REI	11 Jan 2004	13:40:54	0	2.00	2.16	04.00R10	53.3975	38.6948	SC:AST_L1A.003:2019764177
84		11 Jan 2004	13:41:03	0	2.00	2.16	04.00R10	53.4936	38.1120	SC:AST_L1A.003:2019764172

To be able to finally evaluate the resulting ASTER derived DEMs an independent DEM data set for the test site must be available. This was a further constraint on possible test sites.

For only two out of the nineteen pre-defined sites large scale DEMs have been available: Fossil Bluff and Marguerite Bay. For both sites exist large scale DEMs generated by conventional aerophotogrammetric techniques. However, considering the number and altitude of glaciers and the characteristics of the terrain, Fossil Bluff area is regarded less representative for the Antarctic Peninsula than the area of Marguerite Bay.

Consequently, we decided to use Marguerite Bay as the main test site both for the generation of ASTER derived DEMs and also for the subsequent development and evaluation of the basin extraction processing. For this reason in the following chapters we will use mainly products generated from scenes of this region (i.e. scenes number 72 to 82 in Table 3.5).

3.3.2 ASTER-DEM Processing

3.3.2.1 *Image matching as crucial point*

The technique to produce digital elevation models based on line scanner images is comparable but different from the well known photogrammetric methods (KÄÄB, 2005). The images taken with a traditional airborne or spaceborne photogrammetric camera are based on a geometry of central projection. For DEM extraction using these images techniques of the classical optical stereoscope are used that follow the beam geometry in the stereomodel, nowadays also simulated by computer algorithms. On the other hand, spaceborne line scanner images are based on a cylindrical projection with two different kinds of geometry, in along track and across track direction. In contrast to airborne methods earth rotation and earth curvature have considerable effects (TOUTIN, 2004). However, the flight track of a satellite is disturbed much less by high-frequency variations than are airborne platforms (KÄÄB, 2005).

To obtain stereoscopy with images from satellite scanners, two sources are possible:

- the along-track stereoscopy from the same orbit using nadir and fore or/and aft images; and
- the across-track stereoscopy from two different orbits.

From these the simultaneous along-track stereo-data acquisition gives a strong advantage in terms of radiometric variations versus the multi-date stereo-data acquisition with across-track stereo. It is recommended for applications in glaciology (TOUTIN, 2001; KÄÄB, 2005).

ASTER, like few other satellites (e.g. JERS, SPOT5), provides images from an along-track stereoscopy acquisition system that meets the requirements of topographic mapping. The ASTER configuration, as is shown in Figure 3.3a, accounts for a B/H ratio of 0.6. According to Light *et al.* (1980), typical Base-to-High ratios (B/H) values must be between 0.6 to 1.2.

In Figure 3.9 we see the imaging geometry of ASTER's nadir and backward viewing scan. The stereo capability in this case is based on the different meaning of the along track component and the across track component of the parallax.

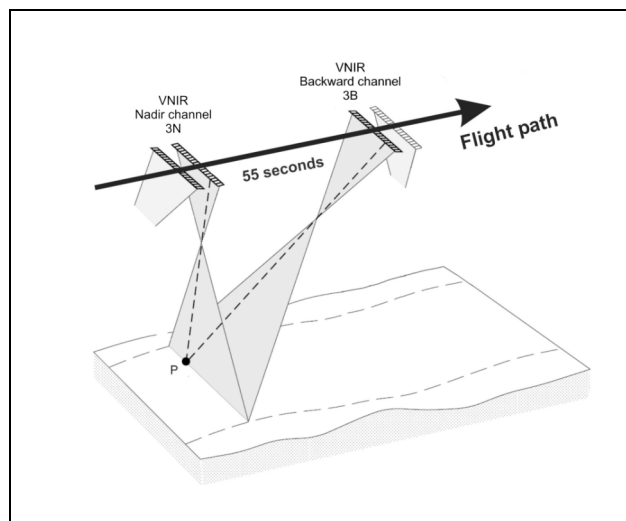


Figure 3.9: Principle of ASTER stereo capability with its nadir and backward viewing pushbroom scanners. The same across-track line recorded by the nadir telescope at time t_0 (3N) is scanned 55 seconds later for the backward telescope (3B) forming the stereo image.

P is the point under consideration (conjugate point)

Source: Adapted from KÄÄB (2005)

Looking towards the flight direction, as is shown in figure 3.10a, and perpendicularly to the flight direction, as in figure 3.10b, we see that the across track shift given by the particular elevation and location of the point under consideration, is the same in both scanned lines. This displacement, an error by elevation and by pointing, can be recalculated from the altitude, when constructing the orthorectified image.

The altitude itself is given by the along track shift of the point taken from the backward beam (see Figure 3.10b). Therefore we have two steps in the algorithms:

- to measure the along track shift of conjugate points (corresponding points in the two images) and to calculate the resulting altitude based on the observation geometry and the sensor parameters. This will result in the digital elevation model.
- to calculate the across track parallax of each point and to apply it on the nadir image. This will result in the orthorectified image.

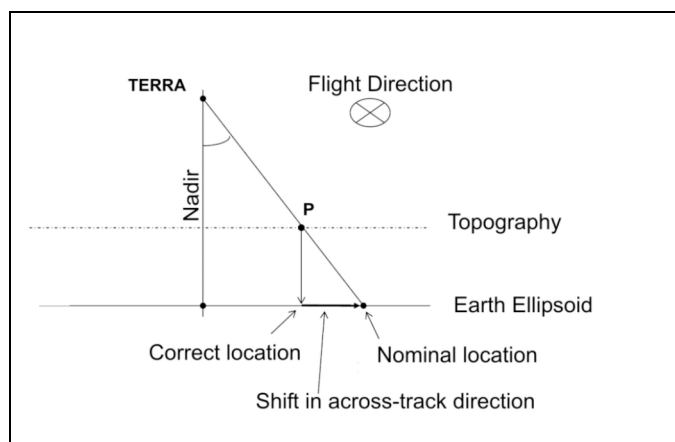


Figure 3.10 a: Error for elevation and across-track components of parallax geometry within the Nadir channel and the Backward channel of an ASTER scene. Caused by CCD scanner's cylindrical projection this figure is the same for both the Nadir and the Backward channel. Consequently the across-track shift does not contribute to the parallax between Nadir and Backward Line-of-Sight of point *P*.

Source: Adapted from WATANABE (2005)

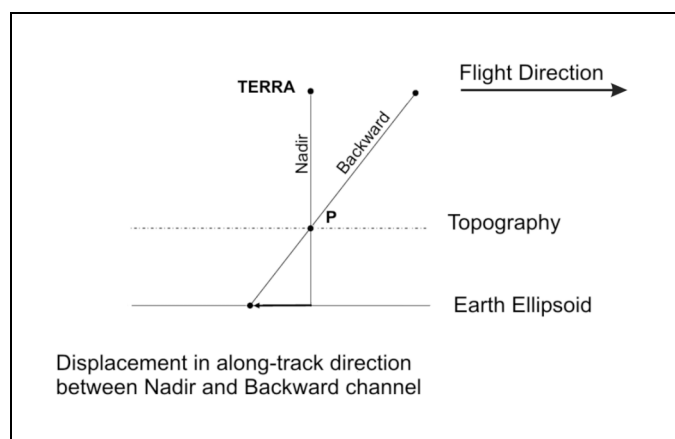


Figure 3.10 b: Along-track components of the parallax geometry between the Nadir channel beam and Backward channel beam for any point within the ASTER scene. This parallax component is proportional to the altitude being independent from the location of the point in the scene. This means independent from the shift in across-track direction, error caused by elevation and pointing.

Source: Adapted from WATANABE (2005)

But how to measure the along track parallax? This means, how to estimate the displacement between conjugate points?

To solve this problem different methods of *image matching*, or in other words finding conjugate points automatically, have been widely studied and applied to remote sensing data. The technique comes from stereo photogrammetry as an automatic alternative to the analogue and analytical photogrammetry, and requires as a basic condition that dense grids of points be matched. However, it is obvious that the information content in the intensity value of a single pixel is too low for unambiguous matching. In practice, coherent collection of pixels are matched (BARNARD & FISCHLER, 1982).

The required process of *image matching* is the most complex and difficult part of the whole procedure of generating elevation models. This is especially true over surfaces of ice and snow with low contrast and a lack of structure. The generation of artifacts in the DEM is a function of the miscorrelation produced when conjugate pixels in the nadir and backward bands of an ASTER scene (band 3N and 3B respectively) are unmatched. Substantial efforts are required to overcome this problem and this step is the crucial point of the whole work.

Nevertheless, in principle the concept of image matching is simple. First we have to understand the different structure of bands 3N and 3B in the ASTER scene. These are presented in Figure 3.11. With the same nominal pixel size of 15 m, band 3B has 900 columns and 800 rows more than band 3N. This happens for two different reasons:

- The 900 sensor cells more in the backward viewing array - black bar on the right side of Figure 3.11 – are needed to overcome the Earth rotation during the 55 seconds between the take of correspondent scans. The band 3B data is not only rotated backward direction by 27.6 degrees around the pitch axis but also 1.33 degrees by roll axis to compensate the Earth Rotation.

Thus, in the band 3B sensor there are 5,000 CCDs., When the data is downloaded from the Terra satellite, a subset of 4,100 pixel per row are selected in function of the latitude to compensate the Earth Rotation. To keep the pixel size of the Band 3B the same as that of the band 3N, the Instantaneous Field of View (IFOV) is designed slightly smaller than that of band 3N (respectively, 21.3 and 18.6 micro radian).

- The elongation in flight direction is needed to allow the search window shift, explained with Figure 3.12, far enough to cover all possible along track parallaxes.

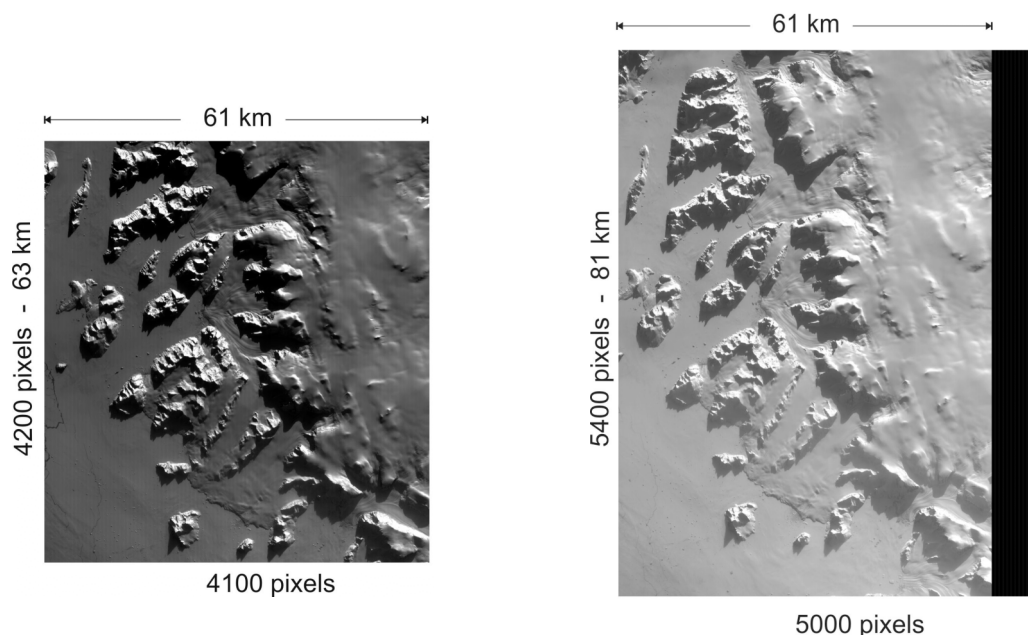


Figure 3.11: Band 3N (left) and 3B (right) of ASTER scene SC:AST_L1A.003:2030971130, Sept. 19, 2005, 13:33:26, Fallières Coast, Marguerite Bay area.

The larger extension of the 3B sensor array is necessary to overcome the Earth rotation during the 55 seconds time difference between corresponding scans. Sensor cells corresponding to pixels outside of the 3N-scan are set inactive and produce a black stripe in the 3B image.

The problem of image matching can be stated as follow (SCHENK, 1999):

- Select a matching entity in one image;
- Find its conjugate entity in the other image;
- compute the 3-D location of the matched entity in object space;
- Assess the quality of the match.

Most of the matching systems operate on reference to search windows. To perform the image matching for each pixel is chosen a rectangular neighbourhood as a template or search window, within the nadir image. Then, the same window is taken from the same nominal position in the backward band and the correlation within both windows is calculated.

The matching is evaluated by different methods to measure how well matching entities correspond to each other. Generally, the degree of similarity is measured by a cost function. In its simplest form, this may be the cross-correlation coefficient or the standard deviation in least-squares matching.

There are at least three methods that perform the similarity measure of matching entities: area-based, feature-based or symbolic matching. Our approach implements the first one, the area-based matching as shown in Figure 3.12. The template is moved row by row along the parallel to the flight line (quasi-epipolar line), looking for the best correlation or best matching. The quasi-epipolar line is analogue to the polar line of the stereoscopic model.

The successful matching will be reported as a maximum of correlation as can be seen in Figure 3.13a, as the evaluation of the cost function along the quasi-epipolar line. If the maximum correlation value should be verified in the template position depicted in the Figure 3.12, the resulting shift between the position of the conjugate points (red arrow) will be the parallax that is proportional to the elevation that we look for.

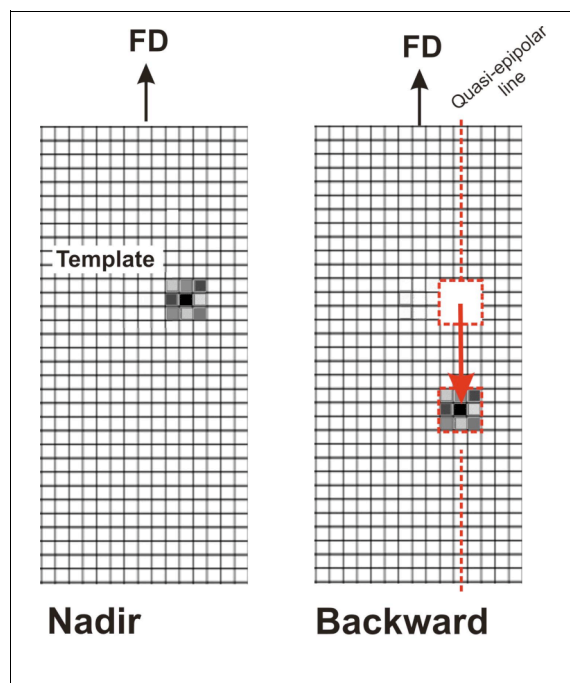


Figure 3.12: Area-based matching between Nadir and Backward images of an ASTER scene (SCHENK, 1999).

For each pixel a matrix of $N \times N$ elements ($N=3,5,7,9 \dots 13$) is used as template.

The templates taken from the Nadir image are brought to the corresponding position in the Backward image and from here shifted pixel by pixel along the quasi-epipolar line (flight direction).

After each step a cross-correlation between the template pixel values and the underlying Backward image pixels is carried out. The best correlation coefficient indicates the pixel displacement [parallax] that is searched for.

These parallaxes will be used later to calculate the DEM altitudes. The correlation coefficients will be the values in the so-called correlation score map of the DEMs.

Frequent problems we have to face (see figure 3.13) are:

- a very flat correlation curve due to a weak signal to noise ratio,
- several peaks of the correlation curve due to repetitive pattern in the image,
- an existing peak but on a very low correlation level.

Our approaches to overcome these problems are:

Modelling with different template sizes. In the following we will try the search window sizes 3, 5, 7, 9, 11, and 13, which means search windows of 3x3, 5x5, 7x7, 9x9, 11x11 and 13x13 pixels.

- Modelling with additional parameters. For that we can use a “water detection”, which means to exclude water surfaces by a predefined mask of coast lines surfaces, or “extended correlation”, which means a second run with an extended search window size.

Now, we need to choose the appropriate software platform with which the processing to derive DEMs from ASTER L1A scenes can be implemented. We have already reported problems detected on the PCI platform used to generate the standard AST14 DEM (WATANABE, 2005; KÄÄB, 2005). Available software alternatives include Leica Orthobase and the AsterDTM module for ENVI. Considering the results of a benchmark evaluation done by WATANABE (2005), we decided to base our processing on the AsterDTM v2.24 software. This package provides all functionality required to take into account the considerations previously mentioned.

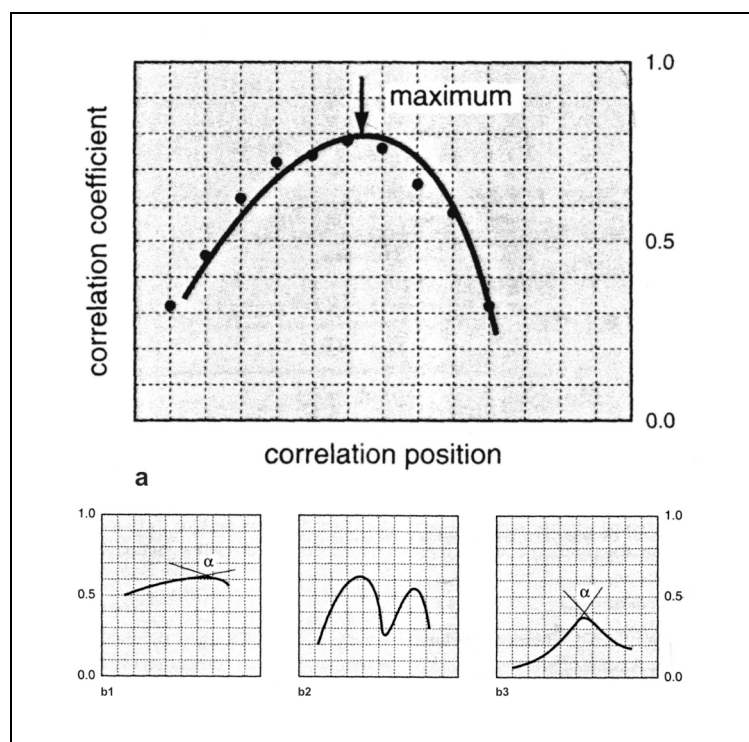


Figure 3.13: Cross-Correlation Coefficients between pixel values of templates and the matching window during the shift of the template along the quasi-epipolar line (SCHENK, 1999).

a) theoretical situation

b) occurring problems under different circumstances:

b1) no clear peak because of low SNR [signal to noise ratio]

b2) more than one peak because of repetitive patterns in the image

b3) there exists a peak but on a very low correlation level

Using this software we created 24 different models for our standard example in the Marguerite Bay area (SC:AST_L1A.003:2030971130, 19 September 2005): 6 different search window sizes, each with four variations (no additional parameter, water detection, extended correlation, water detection and extended correlation). Table 3.6 gives the abbreviations we use to name these different models in the following sections.

Table 3.6: Names for the 24 digital elevation models generated using the AsterDTM v2.24 software selecting different combinations of the processing parameters 'water detection', 'extended correlation' and 'correlation matrix size'.

DEM Name	Water Detection	Extended Correlation	Correlation Matrix Size
3_DEM	no	no	3x3
3a_DEM	yes	no	
3b_DEM	no	yes	
3c_DEM	yes	yes	
5_DEM	no	no	5x5
5a_DEM	yes	no	
5b_DEM	no	yes	
5c_DEM	yes	yes	
7_DEM	no	no	7x7
7a_DEM	yes	no	
7b_DEM	no	yes	
7c_DEM	yes	yes	

DEM Name	Water Detection	Extended Correlation	Correlation Matrix Size
9_DEM	no	no	9x9
9a_DEM	yes	no	
9b_DEM	no	yes	
9c_DEM	yes	yes	
11_DEM	no	no	11x11
11a_DEM	yes	no	
11b_DEM	no	yes	
11c_DEM	yes	yes	
13_DEM	no	no	13x13
13a_DEM	yes	no	
13b_DEM	no	yes	
13c_DEM	yes	yes	

3.3.2.2 Processing chain

The processing chain from an ASTER Level 1A stereo pair to a digital elevation model (DEM) consists of many steps with the correlation matrix and the corresponding orthorectified satellite image as additional outputs. The processing chain was implemented using AsterDTM v2.24 for ENVI 4.2 software. We describe the chain according to Figure 3.14 in four stages:

- The first stage is the **Geometric and Radiometric Correction**, which transforms the data from Level1A to an equivalent Level 1B (“L1B”). That is the prerequisite to be able to extract elevation values through parallax evaluation. Based on header information of the scene we carry out several steps including the replacement of bad lines, application of radiometric calibration coefficients in order to remove banding and striping effects, removing any remaining high frequency noise from the 3N band, geometrically correcting bands 1,2 and 3N, and co-registering these bands with respect to each other. Finally the same processing is applied to band 3B. The resulting dataset is the “L1B” image, equivalent to the standard Level 1B product for the VNIR bands group.
- The second stage is the **Image Matching** according to the specifications explained in Section 3.3.2.1. We have to chose the correlation matrix size (search window size); and the additional parameters “water detection (yes/no)” and “extended correlation (yes/no)”. Other additional parameters can be used such as altitude values from external DEMs or GPS points, and areas of exclusion to avoid cloudy areas. We get two important output files of this step. One is an array of the along track parallaxes for all pairs of conjugate points, this means for all pixels of the nadir image. The other is the correlation matrix, which contains for each pixel the correlation coefficient of the 3N search window and the selected conjugate window in band 3B. These correlations provide an evaluation of the measured parallax.
- The third stage is the **Parallax to Altitude Conversion**. Based on flight geometry, orbit parameters, and the viewing angle now the measured parallaxes can be transformed into altitudes.
- The fourth stage is the **Pointing Correction and Orthorectification**. Each point on a scan line in the 3N band (nadir image) is, according to its altitude, shifted along this scan line nearer to or further away from the nadir point (see again figure 3.10a). Based on the altitudes we can now calculate this shift. Applying this shift on the matrix of altitudes we generate the digital elevation model. Applying this shift on the co-registered bands 1, 2 and 3N we create the orthorectified “L1B” –image.

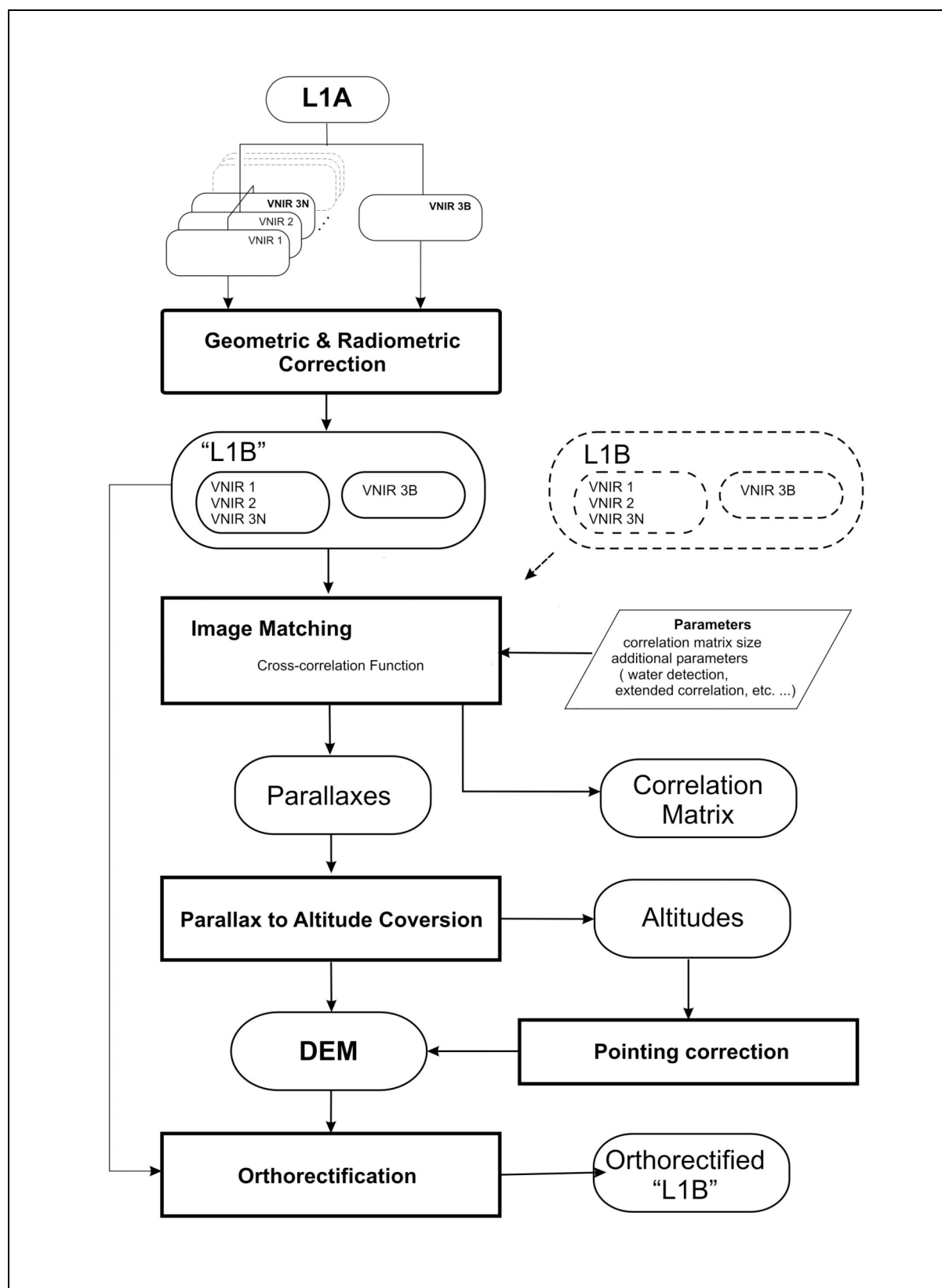


Figure 3.14: Flow diagram for DEM generation using AsterDTM v2.24 software. Chain of different processes starting with an ASTER Level 1A stereo pair [bands 3N and 3B] to produce a digital elevation model (DEM), the corresponding correlation matrix and the orthorectified image.

The so-called “L1B” intermediary product is equivalent to the L1B standard product distributed by the NASA/USGS EOS DGS.

3.3.3 ASTER-DEMs First Examples – Encouragement and Questions

We can now show first examples of digital elevation models and orthorectified images of Antarctic Peninsula landscapes based on ASTER L1A imagery. Figures 3.15, 3.16 and 3.17 cover the same regions as are used for example in Figures 2.11 and 3.7. We must remember that AST14DEM products (Figure 3.7) did show great data gaps over flat surfaces on ice and snow.

Image matching for the three following examples was carried out with a search window size of 3x3 pixels without additional parameters.

The double pages with Figures 3.15 to 3.17 have the same structure. On the left side four images: **a**, **b**, **c** and **d**, all with the same layout as follows:

- Upper left, **a** is a representation of the digital elevation model (full DEM) using a grey scale for the elevation values, where dark means low altitude and bright means high altitude
- Upper right, **b** is the corresponding correlation score matrix showing points with strong correlation in bright, points with weak correlation in dark grey. It indicates areas with low and high uncertainty in measuring the altitude.
- Lower left, **c** is the RGB-composite (red: band 3N, green: band 2; blue: band 1) of orthorectified “L1B” image “L1B” image.
- Lower right, **d** presents the DEM as image under artificial hill-shading. The used light beam has an azimuth of 50° (northeast) and an elevation of 30°.

On the right side we see in the top part **e** that is a 3D view of the whole area, and below this 3D views of selected parts **f**, **g**, etc. The view directions used for the sections are indicated in **e**. All these views are created by draping the DEM with the RGB-composite (red: band 3N, green: band 2; blue: band 1) orthorectified “L1B” image. Therefore the illumination is the natural with the sun standing more or less in the north. Digital files of plates used in this figures at full resolution are included in the Annex 1.

The three selected regions are

- James Ross Island, based on an ASTER summer scene of January 2001 (Figure 3.15). We see the more or less circular island widely covered by ice; in the centre the flat ice dome, surrounded by several glacier shaped valleys filled with down flowing ice; the glacier tongues partly join to small ice piedmonts. Along the coast float rests of sea ice.
- Detroit Plateau of the Trinity Peninsula, based on an ASTER winter scene of September 2001 (Figure 3.16). We see the ice covered plateau in the north of the Antarctic Peninsula with outlet glaciers on both sides flowing down through deep cut valleys. On the eastern side glacier tongues join to a small ice piedmont surrounded by a closed sea ice cover; on the western side they calve more or less individually into the open sea.
- Fallières Coast in the Marguerite Bay, based on an ASTER winter scene of September 2005 (Figure 3.17). We see the plateau and the net of ice fluxes down to the sea on the western side of the Antarctic Peninsula, ending in ice cliffs along the coast. The whole area is covered with snow, including the

ridges, nunataks and rock outcrops. The compact sea ice cover in the western fringe shows huge crack lines.

Summarizing we can state:

The orthorectified images **c** and all 3D views **e**, **f**, etc., demonstrate that ASTER DEMs under natural illumination give a very good impression of Antarctic scenery. The level of detail permits to realize the “real” nature of the landscape. Although we can correctly identify features at large scale on the 2D maps presented the interactive display of this 3-D representation is more impressive. Our evaluation of this material indicate that it is adequate to support many types of geo-based research in this remote regions. This can be amplified and intensified by the interactive handling of this material through the supporting data set included in Annex 1; and by the visualization of virtual flights also included in Annex 1.

Up to now the results demonstrate an impressive virtual reality but how “real” are this models? How accurate they are?

Serious questions arise if we study in detail the three cases of the respective Figures **b** and **d**:

- The correlation matrix shows that we have at least two levels of confidence in the models. Over open sea, ice plateaus and extended glacier surfaces with its dark grey we have to accept relatively low correlation coefficients. These indicate a high risk of miss-matching and associated artefacts, which result in significant errors in the altitudes we calculate.
- Artefacts are the reason for the granular structure of the images with artificial illumination, which partly show a real salt and pepper pattern. Many peaks and pits should exist in the DEM, hidden in 3D views by the natural illumination, but emphasized by the artificial hill-shading.

Therefore we have to concentrate now on how we can better detect, describe, quantify and suppress these artefacts. This will be our task in Chapter 4.

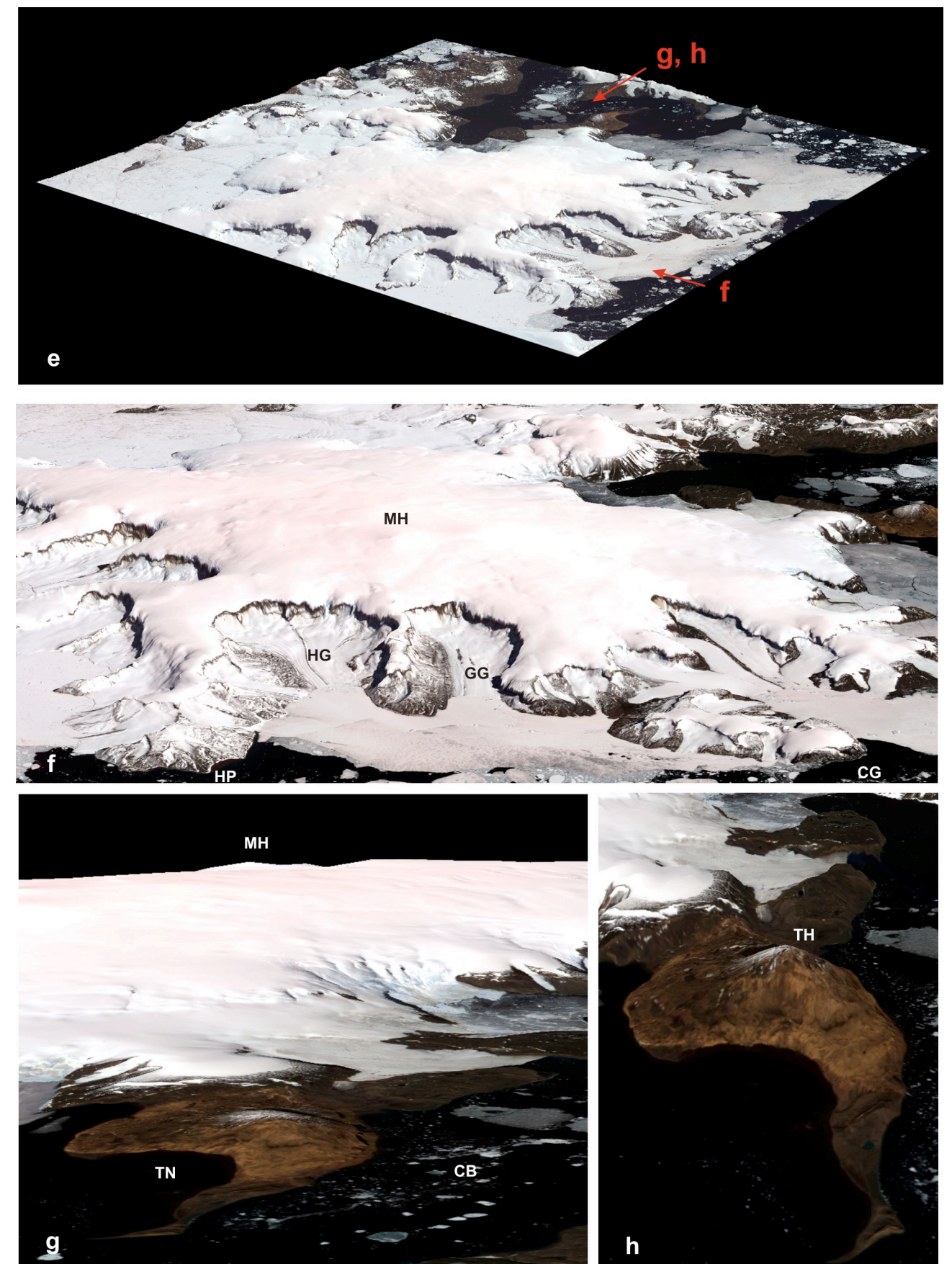
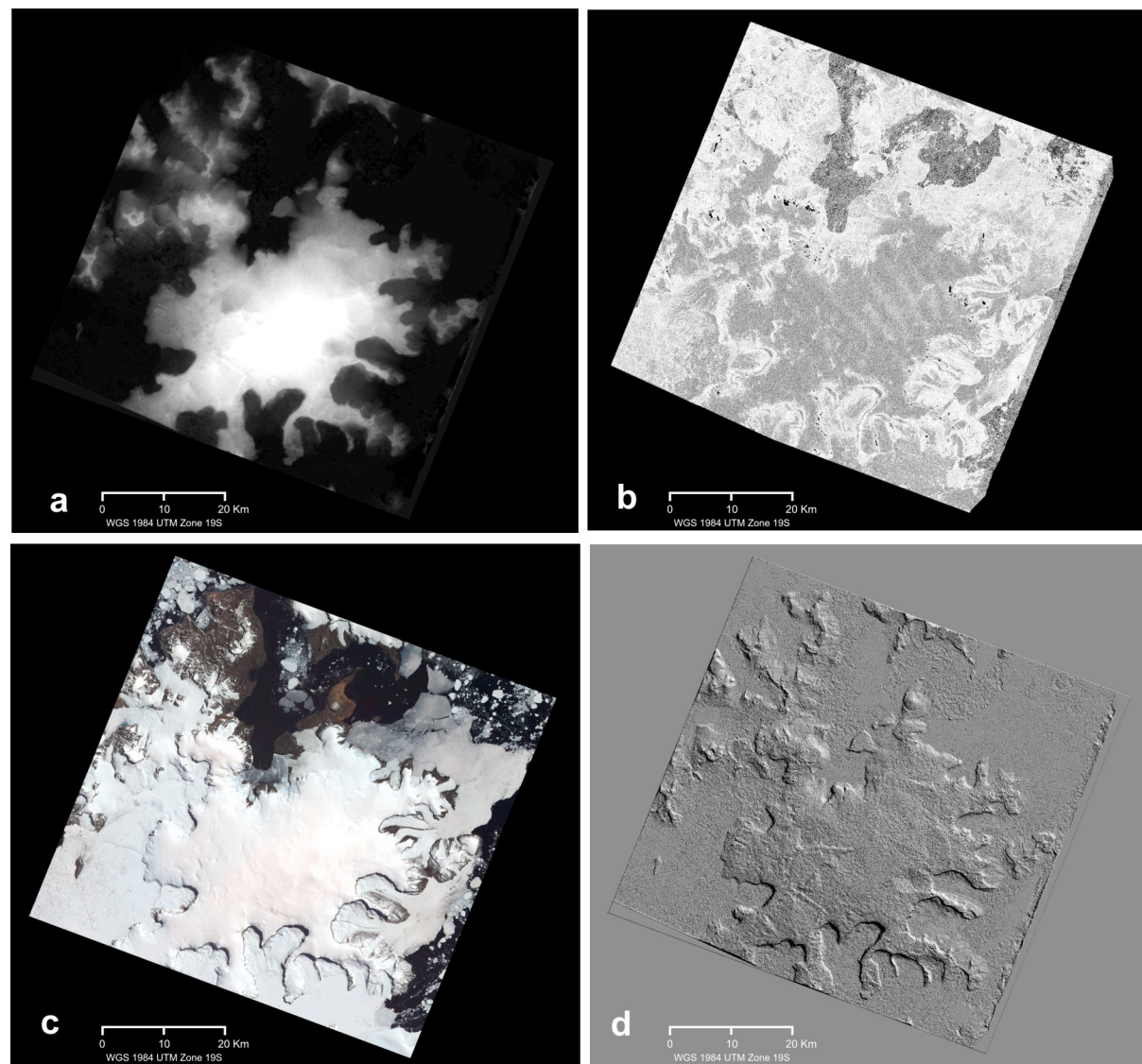


Figure 3.15: ASTER digital elevation model of James Ross Island, with different related data sets and aspects. Scene SC:AST_L1A.003:2004102903, Jan. 08, 2001, 13:14.

- a** Full DEM (bright = high, dark = low).
- b** Correlation score matrix (bright = high correlation, dark = low correlation).
- c** RGB-composite (red: band 3N, green: band 2; blue: band 1) of orthorectified "L1B" image.
- d** DEM with shadowing by artificial illumination (light: azimuth = 50°, elevation = 30°).
- e** Three dimensional view of the whole scene. Vertical exaggeration by factor 3.
- f** Detail 1: View from East-Southeast, Markham Bay between Hamilton Point (HP) and Gage Cape (GG); with Hobbs Glacier (HG), Gourdon Glacier (GG) and Mount Haddington (MH, 1628 m).
- g** Detail 2: View from North, Croft Bay (CB) and Peninsula The Naze (TN), in the background Mount Haddington (MH).
- h** Detail 3: Peninsula The Naze with Terrapin Hill (TH, 546 m).

In spite of artifacts evident in the DEM, correlation matrix and hill-shaded DEM (figures **a**, **b** and **d**), figures **e**, **f** and **g** show a quit good representation of the relief.

Digital files of plates used in this figures at full resolution are included in the Annex 1.

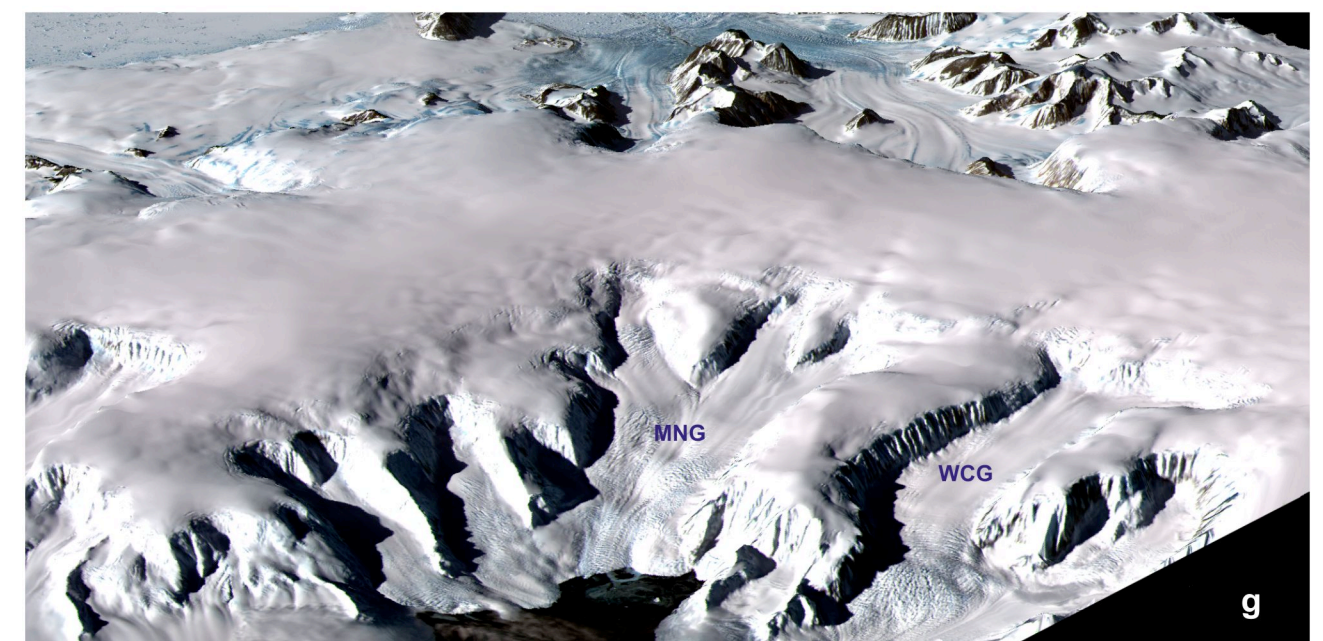
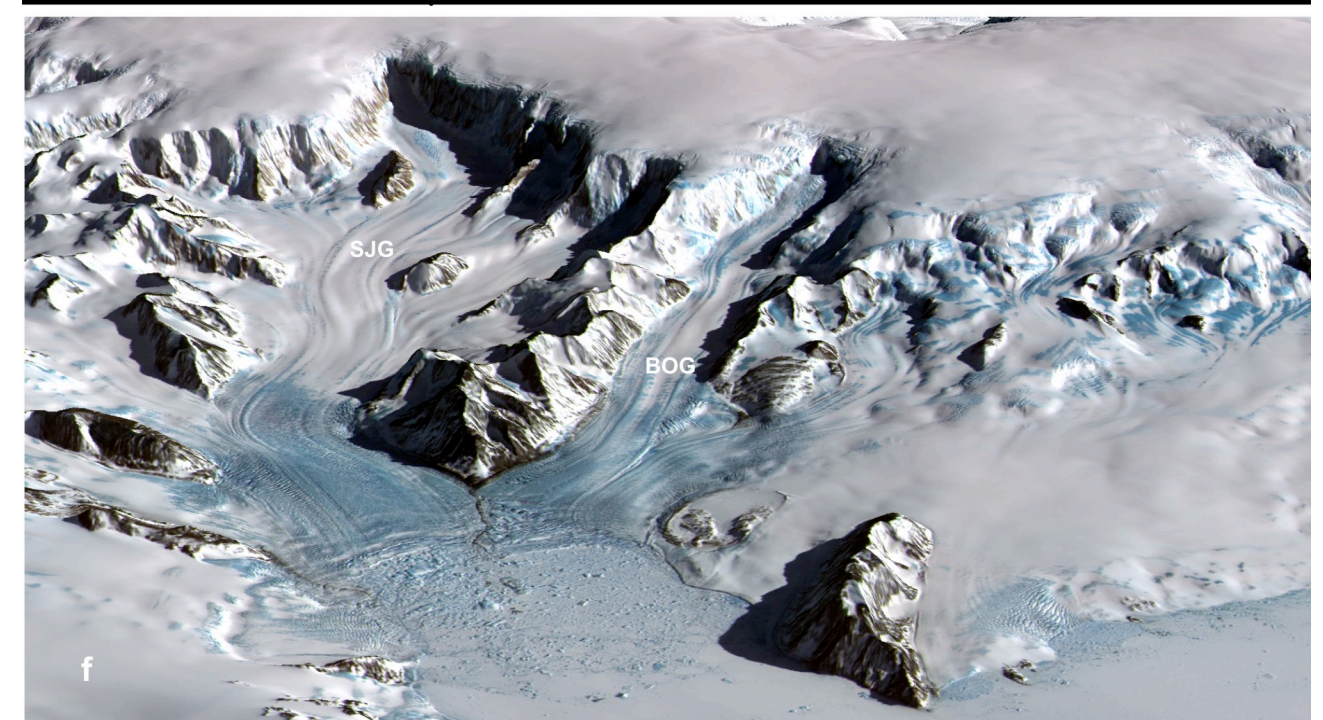
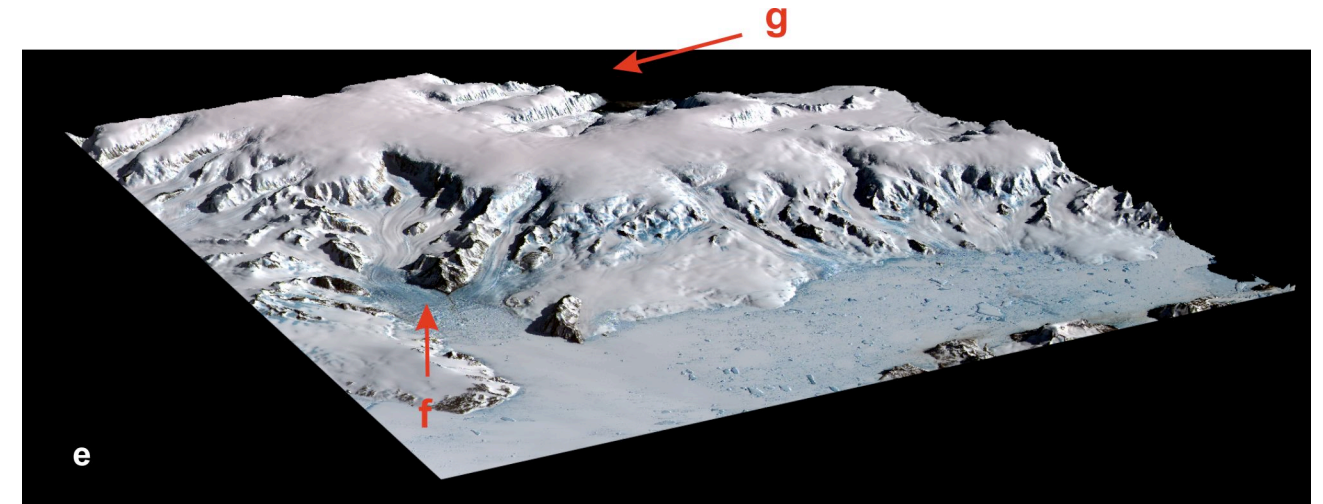
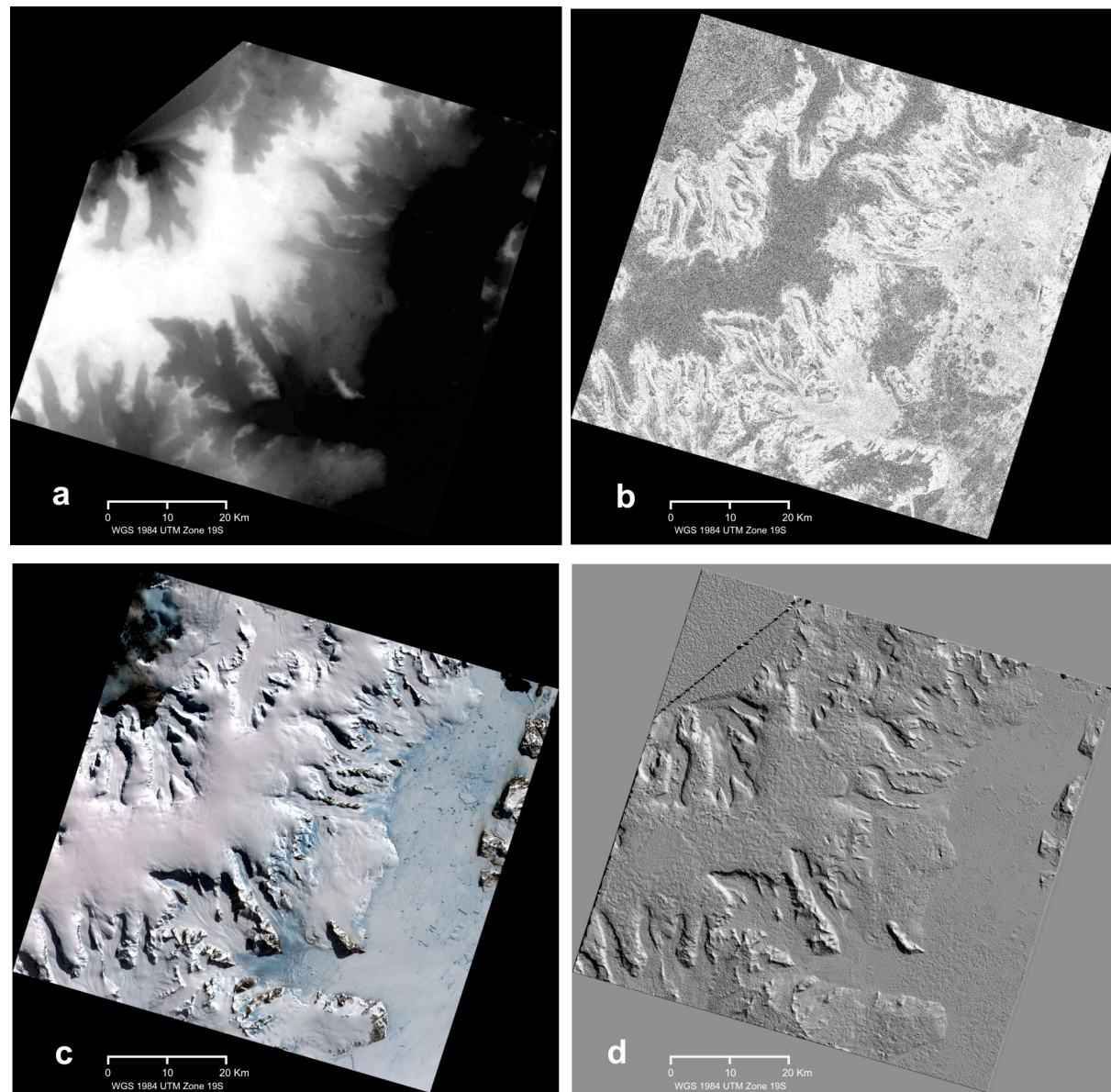


Figure 3.16: ASTER digital elevation model of the northern part of Detroit Plateau, Trinity Peninsula, with different related data sets and aspects. Scene SC:AST_L1A.003:2004337053, Sept. 26, 2001, 13:26:54.

- a** Full DEM (bright = high, dark = low).
- b** Correlation score matrix (bright = high correlation, dark = low correlation).
- c** RGB-composite (red: band 3N, green: band 2; blue: band 1) of orthorectified "L1B" image.
- d** DEM with shadowing by artificial illumination (light: azimuth = 50°, elevation = 30°).
- e** Three dimensional view of the whole scene. Vertical exaggeration by factor 3.
- f** Detail 1: View from Southeast, Sjögren Glacier (SJG) and Boydell Glacier (BOG).
- g** Detail 2: View from Northwest, McNeile Glacier (MNG) and Whitecloud Glacier (WCG).

Comparing figures **b** and **c** one can find: Low correlation are evident in the flat surface of Detroit Plateau. Strong correlation are produced on ridges and heads of valleys.

Comparing figures **c** and **d** one can find: Under artificial illumination of the DEM erroneous differences between neighbouring pixels are amplified. By this method artefacts of the model show up very clearly and give a first evaluation of the extracted surface.

In spite of evident limitations of the model in areas with low correlation, figures **e**, **f** and **g** show a very impressive representation of the relief. The rendered surface obtained from overlaying of the orthorectified "L1B" image on the extracted DEM is not disturbed by the high frequency variations of altitudes of the model at this scale.

Digital files of plates used in this figures at full resolution are included in the Annex 1.

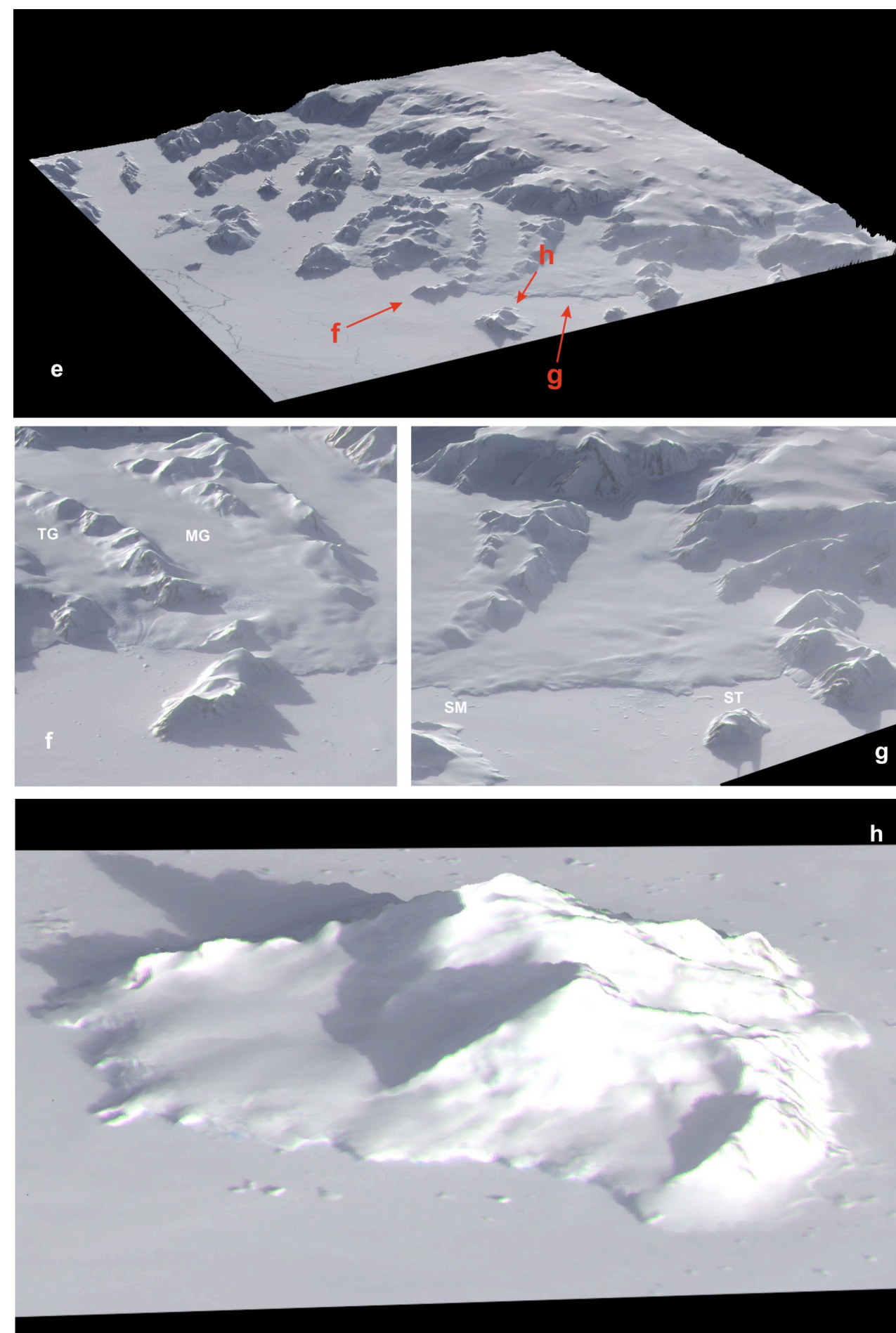
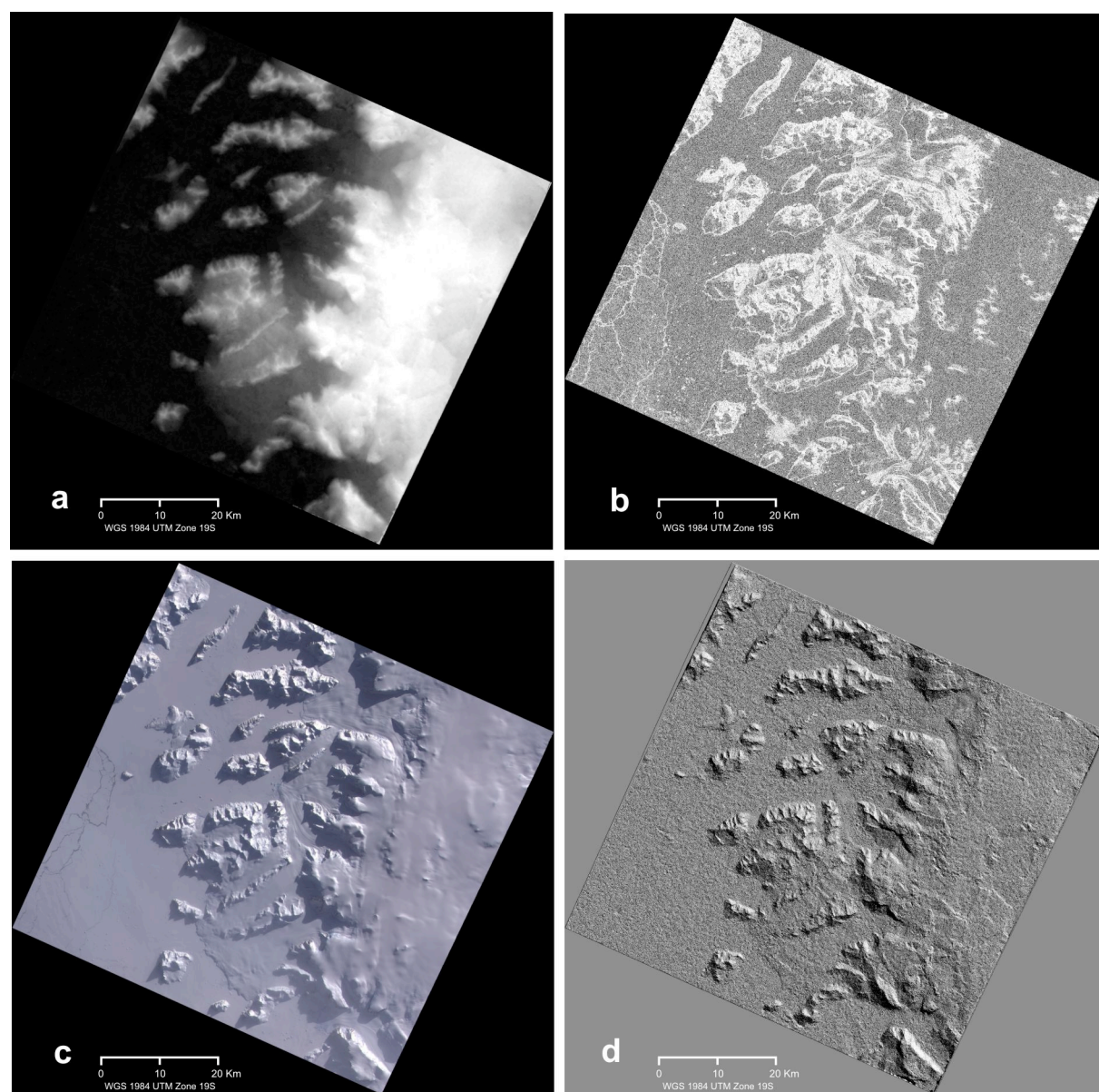


Figure 3.17: ASTER digital elevation model of Fallières Coast, Marguerite Bay area with different related data sets and aspects. Scene SC:AST_L1A.003:2030971130, Sept. 19, 2005, 13:33:26.

a Full DEM (bright = high, dark = low).

b Correlation score matrix (bright = high correlation, dark = low correlation).

c RGB-composite (red: band 3N, green: band 2; blue: band 1) of orthorectified "L1B" image.

d DEM with shadowing by artificial illumination (light: azimuth = 50°, elevation = 30°).

e Three dimensional view of the whole scene. Vertical exaggeration by factor 3.

f Detail 1: Cape Calmette with McClary Glacier (MG) and Todd Glacier (TG) seen from West.

g Detail 2: Northeast Glacier with Stonington Island (ST) and San Martin Base (SM) from Southwest.

h Detail 3: Millerand Island from East-Northeast

Comparing figures **b** and **c** one can find: Low correlation occurs in areas under shadows and on flat surfaces on snow and ice due to the lack of texture. Strong correlation produced on ridges and along cracks in the frozen sea.

Comparing figures **c** and **d** one can find: Artificial illumination of the DEM amplifies altitude changes between adjacent pixels. By this method artefacts show up very clearly. This gives a first evaluation of the extracted surface.

In spite of evident limitations of the model in areas with low correlation, figures **e**, **f**, **g** and **h** show a very impressive representation of the relief. The rendered surfaced obtained from the overlaying of the orthorectified "L1B" on the extracted DEM is not disturbed by high frequency variations of altitudes of the model at this scale.

Digital files of plates used in this figures at full resolution are included in the Annex 1.

4 ASTER derived DEMs and Reality

Monitoring of glaciers demands the control of its geometric characteristics in order to detect and measure changes. This pre-requisite is hard to meet on the Antarctic Peninsula where environmental conditions and logistic constraints prevent the availability of adequate geographical information from ground surveys. This suggests that efforts based on the processing of remote sensing data to generate such information are valuable, because they can provide the often lacking spatially referenced geometric information. The stereoscopic capability of the ASTER sensor offers the opportunity to produce medium scale spatial resolution digital elevation models. For quality assurance these DEMs must be compared with and tested against suitable reference data. Consequently, a validated test site is needed.

For many reasons a portion of Fallières Coast in front of the Marguerite Bay area has been chosen as a test site. Not only a well documented independent physiographic data set exists but there is also a multi-national long tradition of exploration, occupation and scientific researching in this part of the West Antarctic Peninsula.

Application of space borne optical imagery from the Antarctic Peninsula is often hindered by the frequent cloud cover. The currently available multi-temporal coverage of ASTER scenes with a low percentage of cloud cover for the Antarctic Peninsula also supports the selection of this area. The comparably large amount of (almost) cloud free ASTER scenes for this specific region can presumably be attributed to an atmospheric circulation pattern, where depression centers pass the Northern part of the Antarctic Peninsula from west to east and produce a lee condition westward of the central plateau in this area. All these aspects support the area as the best available test site. It provides a suitable location against which the DEMs produced from ASTER data can be compared.

4.1 Marguerite Bay Test Site and its Reference Terrain Model

4.1.1 Test site area description

The Marguerite Bay Test Site is centered approximately at 68°05'S and 67°W. It covers an area of roughly 600 square kilometers on the central section of the

Fallières Coast, a territory situated between the head of Bourgeois Fjord and Cape Jeremy on Palmer Land, located on the western side about 600 km south of the northern tip of the Antarctic Peninsula.

The area was first explored and charted by Jean-Baptiste Charcot on board of the ship *Pourquoi-Pas?* during the Fourth French Antarctic Expedition (1908-1910) (FOGG, 1992). This fact explains the French names of the most relevant geographical features, e.g.: Fallières Coast, in honor of Charcot's contemporary President of France and expedition sponsor, Mr. Clement Armand Fallières (SCAR, 2006). Marguerite Bay is named in honor of Charcot's wife; Millerand Island (MI) and Cape Calmette (CC) also feature French names (Figure 4.1).

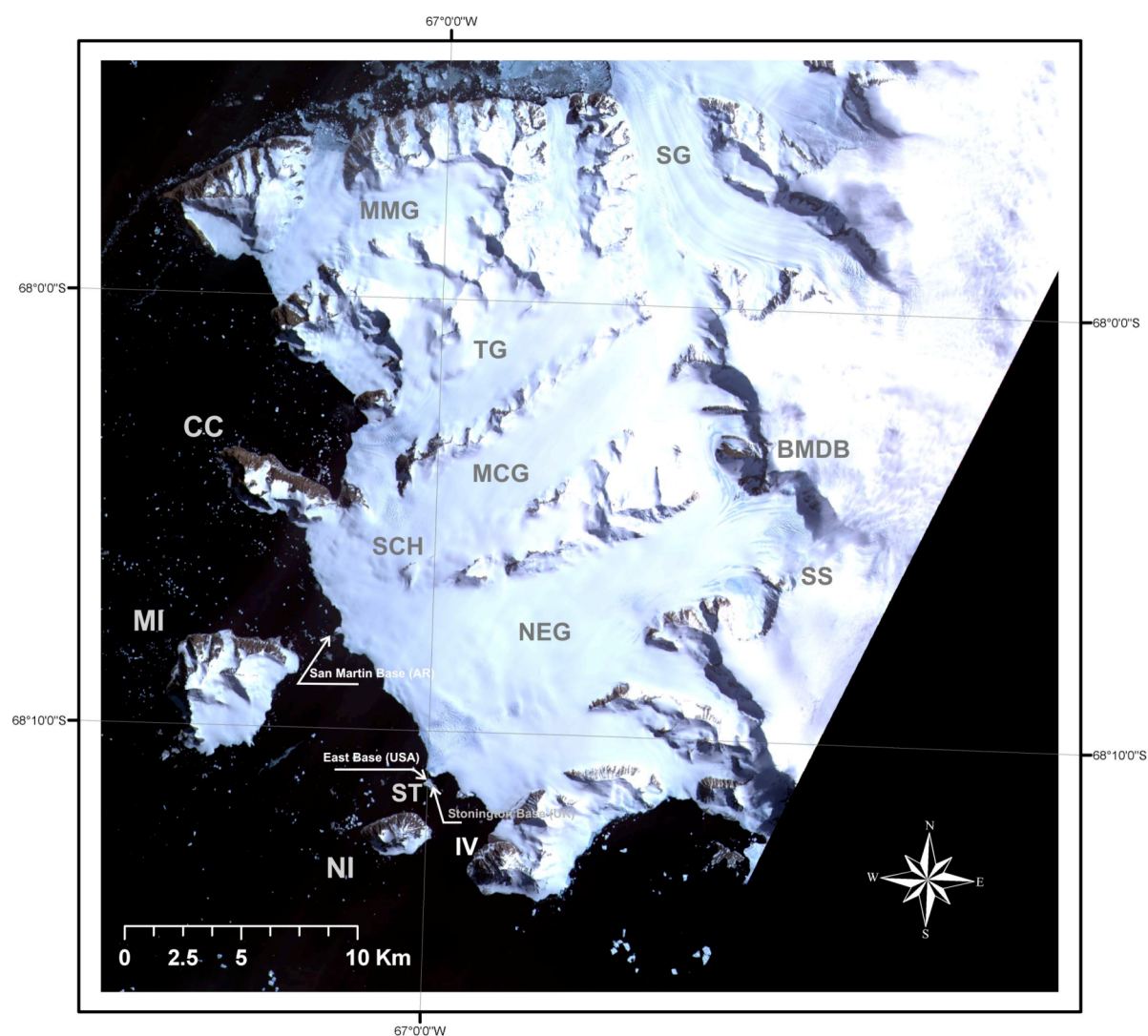


Figure 4.1: Image map of Fallières Coast, Marguerite Bay. Main geographical features and historical and recent research bases.

Glaciers: Northeast Glacier (NEG), McClary Glacier (MCG), Todd Glacier (TG), Swathbank Glacier (SG) and McMorris Glacier (MMG). Landmarks: Cape Calmette (CC), Roman Four Promontory (IV), Schauinsland (SCH), Blow Me Down Bluff (BMDB) and Sodabread Slope (SS). Islands: Millerand (MI), Neny (NI), Stonington (ST).

Source: ASTER mosaic (SC:AST_L1A.003:2004076906 & SC:AST_L1A.003:2004076911) acquired on 04.01.2001.

The test site area is almost completely covered by ice and snow, having a geographical setting composed by a variety of forms in which ice occurs in Antarctica. The ASTER mosaic (Figure 4.1) shows Swithinbank (SG) and Northeast (NEG) outlet glaciers, with 15-20 km length and 2-10 km width and their frontal ends calving in the coast. They have compound basins and a heavily crevassed main upper section that connects with the ice-field that covers the higher central plateau. McMorris Glacier (MMG) is composed of several basins that coalesce and descend from the upper glacier section to lower altitudes and then separate into two branches flowing to the north and to the west, calving at sea from a crevassed frontal area. Todd (TG) and McClary Glaciers (MCG) run parallel separated by a mountain ridge in a southwest direction, receiving their main ice inputs from the higher surrounding elevations. TG has in its upper section compound basins but not MCG. Both are calving to Marguerite Bay coast where their boundaries meet. In addition to these most important glaciers other small glaciers are located in the area, e.g. those with none- coalescing catchments situated on the northern coast calving directly at sea.

Topography rises rapidly from the head of the glaciers to the central plateau. Few alternatives to the steep cliffs exist. Sodabread Slope (SS), located in the south side of the amphitheatre feature, is an exception that proved to be the only practicable pass to climb the plateau from the west to the east at this latitude, accounting a slope gradient of one in two-and-a-half (FUCHS, 1982). Altitude is above 1800 m in the neighbourhood of Blow-Me-Down Bluff (BMDB), a feature that is approximately the medium altitude of the central plateau. A well defined cirque glacial system is observed in the head of the glacier catchments evidencing that avalanches from the upper hanging glaciers contribute to the glacier nourishment where the ice flow is interrupted by very steep cliffs.

Rock outcrops of predominantly acidic igneous materials emerge scattered on flanks and peaks of several mountains and promontories along the area. Some of them are shown in Figure 4.1, e.g. the mounts between McClary (MCG) and Northeast Glaciers (NEG); Roman Four Promontory (IV); Cape Calmette (CC); Neny Island (NI); Millerand Island (MI); and Schauinsland promontory. Furthermore a considerable number of outcrops with a metamorphic component is found near to the coast (Knowles, 1945).

Topography and other geographical features of the area can be identified in additional charts and maps currently available at different scales (e.g. BAS, 1963; HO, 1995; IfPK TUD, 1999).

4.1.2 Area Occupation and Scientific Activities

Marguerite Bay has also a long tradition of human occupation with supporting facilities for scientific activities. After the exploratory trip of Charcot in 1909, the British Graham Land Expedition 1934-37 lead by John Rymill visited the region and over-wintered at Debenham Islands in 1936-37 (BLACK, 1945; FOGG, 1992). Using a small plane for exploration Rymill introduced the aerial survey in Antarctica (BLACK, 1945; WROBEL ET AL. 2000). At the same time started the ground based survey of parts of the region (FOGG, 1992; BLACK, 1945).

Few years later at Stonington Island (ST), the East party of the United States Antarctic Service Expedition (USASE) 1939-1941, established East Base (68°12'S, 67°03'W). This expedition, the best equipped and most extensive in organization and

objectives so far, accomplished much in exploration and research. The scientific purpose of USASE was inspired by the example of previous expeditions that collected important amounts of scientific data (WADE, 1945). Consequently, a comprehensive scientific program including biology, geology, glaciology, marine biology, ornithology, meteorology and human biology disciplines, was planned and executed. For instance, the meteorological program was featured by the establishment of a completely equipped mountain weather outpost, the Plateau Weather Station ($68^{\circ}07'S$, $66^{\circ}30'W$), situated over 1.800 m on the plateau (Figure 4.2). The station was operative from November to December 1940 and was planned among other reasons to support the aviation operations (DORSEY, 1945). Similar to the previous British expedition they also used a plane for exploration and aerial reconnaissance. But the problem of identification of ground control points for mapping surveyed by land based parties was better solved. References to many of those science reports can be found in the same volume of the PROCEEDINGS OF THE AMERICAN PHILOSOPHICAL SOCIETY (1945).

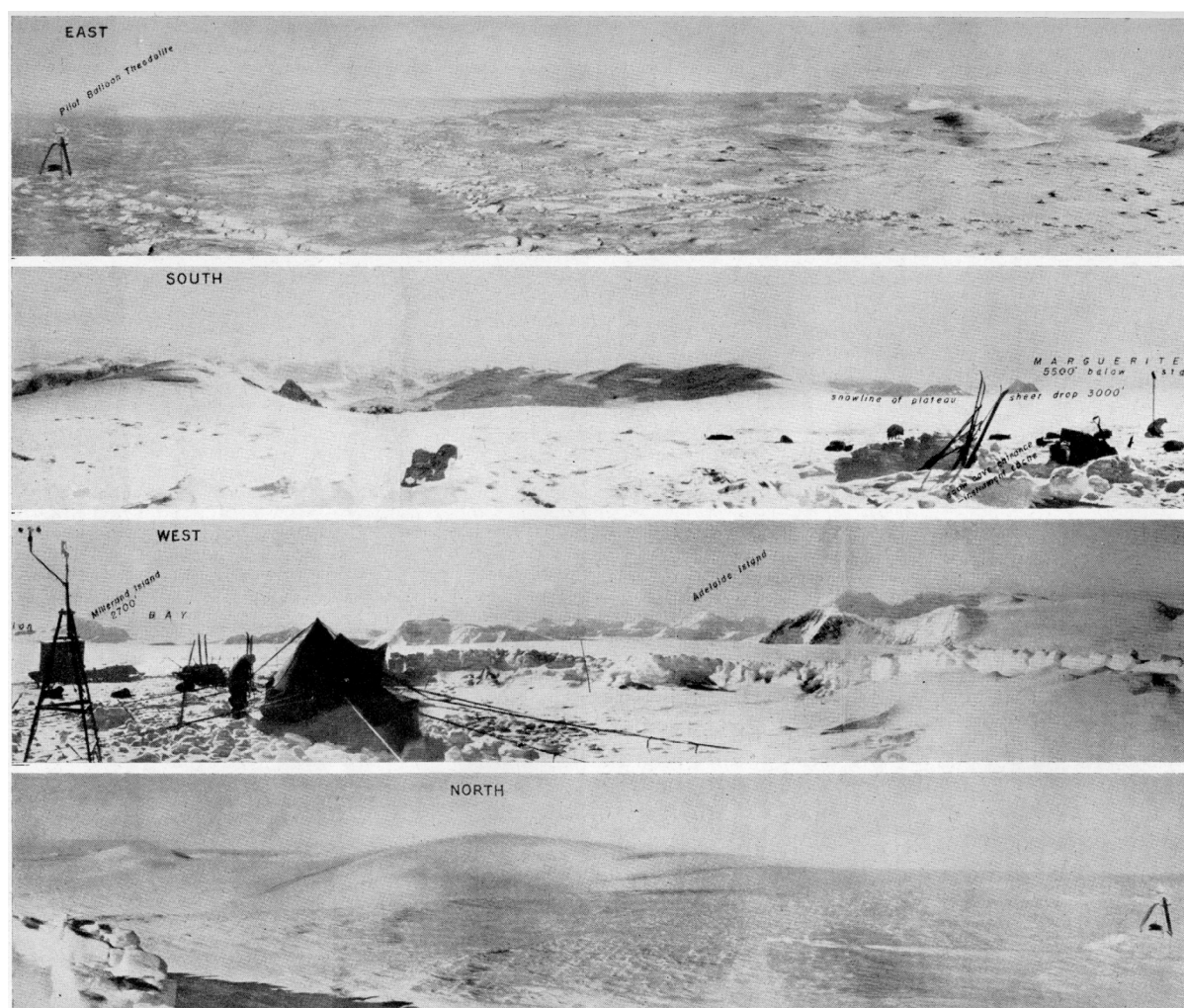


Figure 4.2: Panoramic photos taken during the United States Antarctic Service Expedition (USASE), East Base party, showing the weather station installed on the plateau (ca. 1800 m) and surrounding landscape during summer 1940-41.

Source: DORSEY (1945)

Later, the United Kingdom under the Operation Tabarin deployed to this area a party from the Falkland Island Dependencies Survey (FIDS), the former organization that gave origin in 1962 to the current British Antarctic Survey (BAS). Stonington Base was erected at the homonym islands in 1946. For many years parties were traveling from there to places as far as Ronne Ice Shelf on the other side of the Antarctic Peninsula and to the southwestern entrance of George VI Sound, proving that Alexander island was not a peninsula of the Antarctic continent. Some years later in 1954, Argentina founded the Base General San Martin (BGSM), which is the most southern permanent facility located on the western side of the Antarctic Peninsula. At Base San Martin programs of geophysics, upper atmosphere physics and meteorology have been started and are still carried out.

In the 90's BGSM facilities and the glaciers of the region became important to the support of remote sensing activities. When the European Space Agency (ESA) launched Earth Resources Satellites (ERS) 1 / 2 this area was included as a test site for ground truth and for scientific investigation based on the new active microwave sensors of the ERS 1/2 satellites. In addition to the scientific value of the glaciological system of this area one important reason to chose this area was the feasibility of near real time radio links with the German-Chilean Antarctic Receiving Station (GARS) located at the Chilean O'Higgins Base. This allowed at that time the close control synchronization of activities. Corner reflectors were prepared and deployed on the glaciers to serve as reference markers in the acquired image frames of ERS 1/2 radar image acquisitions (shown in Figure 4.3). Simultaneous with satellite image acquisitions snow sampling was carried out as ground truthing to facilitate the derivation of ice-snow parameters from the remotely sensed data.

In the frame of the "Ozean-Eis_Atmosphäre (OEA)" and the „Dynamische Prozesse in Antarktischen Geosystemen (DYPAG)" projects several studies were carried out in this region. The Institut für Physische Geographie from the Albert-Ludwigs-Universität Freiburg (IPG), Germany, performed several summer campaigns (1993-1997) to study the cryospheric processes by means of remote sensing methods. The joint work with other German and Argentinian institutions who supported the year-round measurements and observations, produced several PhD. thesis (e.g. WUNDERLE, 1996; SCHNEIDER, 1998; RAU, 2004) and a number of reports (e.g. IPG, 1998).



Figure 4.3: IPG's field camp and corner reflector settled on the McClary Glacier during the 1994 ground truth campaign within DYPAG project activities. In the background Mount Schauinsland (ca. 450 m) taken from the camp site.

Source: Photos by H. Gossmann.

The collaborative work within the DYPAG activities between the Institut für Photogrammetrie und Kartographie Technische Universität Darmstadt (IfPK TUD), the Bundesamt für Kartographie und Geodäsie (BKG, formerly IfAG) and IPG, produced two important geographical datasets for the Marguerite Bay area. These products are of relevance for our work because they are used as the reference topographic data base to compare ASTER derived digital elevation models with independent control data.

4.1.3 Technical University of Darmstadt Digital Terrain Model (TUD DTM) and Base General San Martín Photo Map (TUD Karte) datasets.

Table 4.1: *Parameters of Technical University Darmstadt Digital Terrain Model (TUD-DTM) data set.*

Source: WROBEL ET AL. (2000).

<p>Projection:</p> <p>Lambert Conformal Conic Datum WGS 72 68° 40' S 1st standard parallel 71° 20' S 2nd standard parallel Latitude of origin 71° 20' S Longitude of central meridian 0° False easting at central meridian 10.000.000 m False northing at origin 10.000.000 m Heights reference mean sea level</p>
<p>Vertical Accuracy:</p> <p>+/- 3-10 m : mountain ranges, rock areas, snow-free zones</p> <p>+/- 10-20 m : crevasses, ice faults, structured, snow-covered terrain</p> <p>+/- 50 m or more: monotonous without structures, snow-covered areas</p>

The best available terrain representation for the area of interest is provided by two geographical datasets that resulted from the DYPAG activities mentioned previously. They were created by IfPK TUD from black and white aerial photography taken by BKG in February 1989. The images cover 580 square kilometers of terrain. The geodetic control data was collected by researchers from IPG during several summer campaigns between 1993/94 and 1996/97. The aerial photographs feature a good image quality and large overlaps. Further details about their parameters can be found in WROBEL ET AL. (2000). The images were processed largely automatically using the digital photogrammetry software PHODIS by ZEISS and modules of the MICROSTATION package of BENTLEY. The software was used to evaluate and select the best stereo pairs, for automatic extraction of digital elevation models and to combine DEM results of individual stereo models into an adjusted topographic data set.

Eighteen of the available twenty eight stereo pairs were selected because of the relatively large mutual overlap.

The DEMs were computed and integrated to generate the “Technical Universität Darmstadt Digital Terrain Model (TUD-DTM)” (WROBEL ET AL., 2000). It must be noted that the orientation of images was based only on ground control points without support from photo flight GPS data (WROBEL ET AL. 2000). The resulting data set has a spatial resolution of 30 m. The DEM accuracy depends completely on local textures. Additional details about the parameters of the cartographic projection and values of vertical accuracy are included in Table 4.1.

An orthophoto of the region was produced using the previously computed DEM. Due to the fact that the aerial photographs were taken with a super-wide angle camera

images overlap in steep slopes to a higher extent than with other aerial photographs, especially when situated near the image margins. Consequently, the central zone of the images were cropped and integrated into one final image. Topographic details provided by IPG members and additional cartographic information from other sources (e.g. British charts from the years 1960 and 1982) were compiled and included in a final multi-coloured digital map. This product at 1:50.000 scale was named “Base General San Martín Aerial Photo Map (TUD-Karte)” (IfPK TUD, 1999). The corresponding topographic frame, reduced by factor 4 and excluding text and legend boxes, is shown in Figure 4.4. The digital map version has a 4 m pixel resolution. A printed version of this map can be found in WROBEL ET AL. (2000).

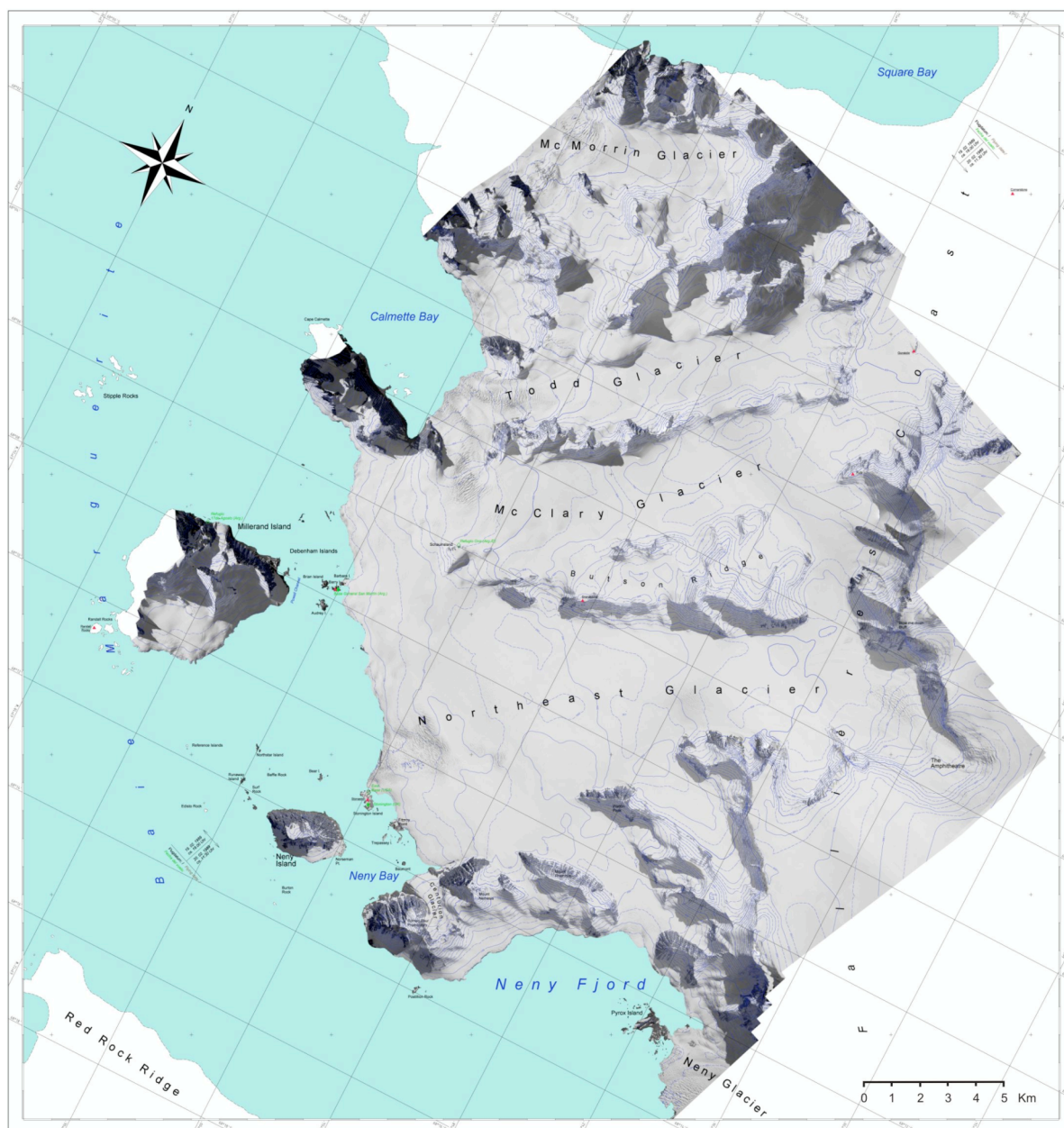


Figure 4.4: Base General San Martín aerial photo map prepared within the DYPAG project. Original scale 1:50.000, reduced by factor 4.

Sources : Aerial photography (1988/89) by Bundesamt für Kartographie und Geodäsie (BKG, former IfAG); stereo modelling and DEM production by Technical University of Darmstadt (TUD); topographic features by Institute of Physical Geography University of Freiburg (IPG); see WROBEL ET AL.(2000).

4.1.4 Post-Processing of the TUD DTM

When using the TUD DTM (TUD model) data set as reference surface and for comparison with ASTER derived elevation models some considerations must be accounted for. Under the native raster data structure of both DEMs it is possible to use a pixel to pixel comparison of elevation values. For this reason an identical grid size is convenient and facilitates corresponding matching of pixels. To achieve this an optimal co-registration of both data sets is essential.

The raw TUD-DTM data consists of two ASCII data files. The first one includes the elevation of 645.280 over land points, referenced to mean sea level and sampled using a regular 30 m posting. The second file holds 6.178 points with 0 m of altitude representing the coastline. The coastline points are distributed along the shoreline with a variable distance of 10 to 50 m between them. Because this set defines the open sea boundary, it was decided to not consider it for the preparation of a TUD-DTM raster grid of elevations. Therefore, the raster surface created from the over land altitudes has 1283 columns and 1089 rows, with no-data values assigned to cells that do not have an elevation value and to those sampled coastline points of the second file. The dynamic range of altitudes of raw TUD-DTM varies from 0,2 to 1.861,7 m above mean sea level. A subset of the grid is shown in Figure 4.5. The original Lambert Conformal Conic (WGS72) projection of the TUD-DTM is reprojected to UTM Zone 21S (WGS84), that is the projection used for the ASTER scenes and derived products.

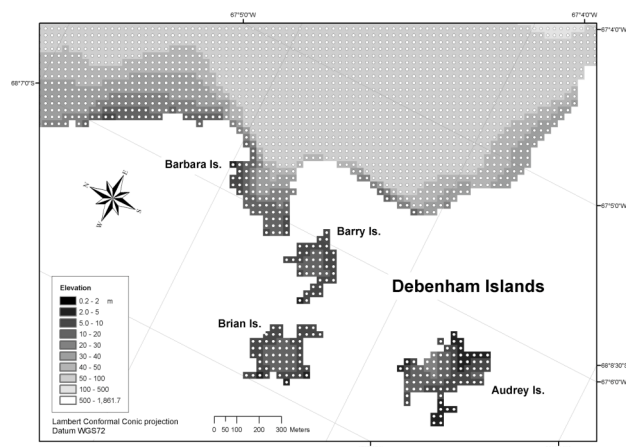


Figure 4.5: Map of Debenham Islands and front of McClary and Northeast glaciers based on raster representation of TUD-DTM, according to the original 30 m grid cell size and Lambert Conformal Conic projection.

The quality of the data has been assessed using software tools for 3D rendering of the raw TUD-DTM surface. Missing data can easily be detected in a 2D representation (e.g. see Figure 2.12).

Other artefacts remain hidden in that representation. These are more evident when the surface is displayed in three dimensions. For instance, the magnitude of steps crossing the longitudinal section of McClary and Northeast Glaciers are more notorious and marked in the 3-D block shown in Figure 4.6 than in the 2-D image.

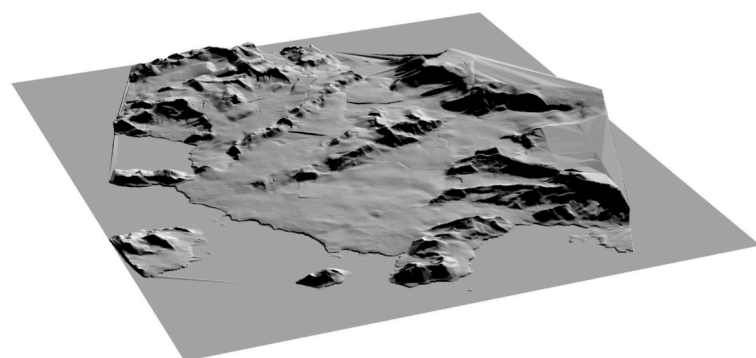


Figure 4.6: Three dimensional representation of the Technical University of Darmstadt digital terrain model (TUD-DTM) generated by photogrammetric techniques draped out with its corresponding hill shaded image.

Lambert Conformal Conic (WGS 72) projection. Vertical exaggeration 2x

The complete workflow used and the intermediary products generated to create a surface suitable for comparison and fusion with other raster data sets is presented in the flow diagram of Figure 4.7.

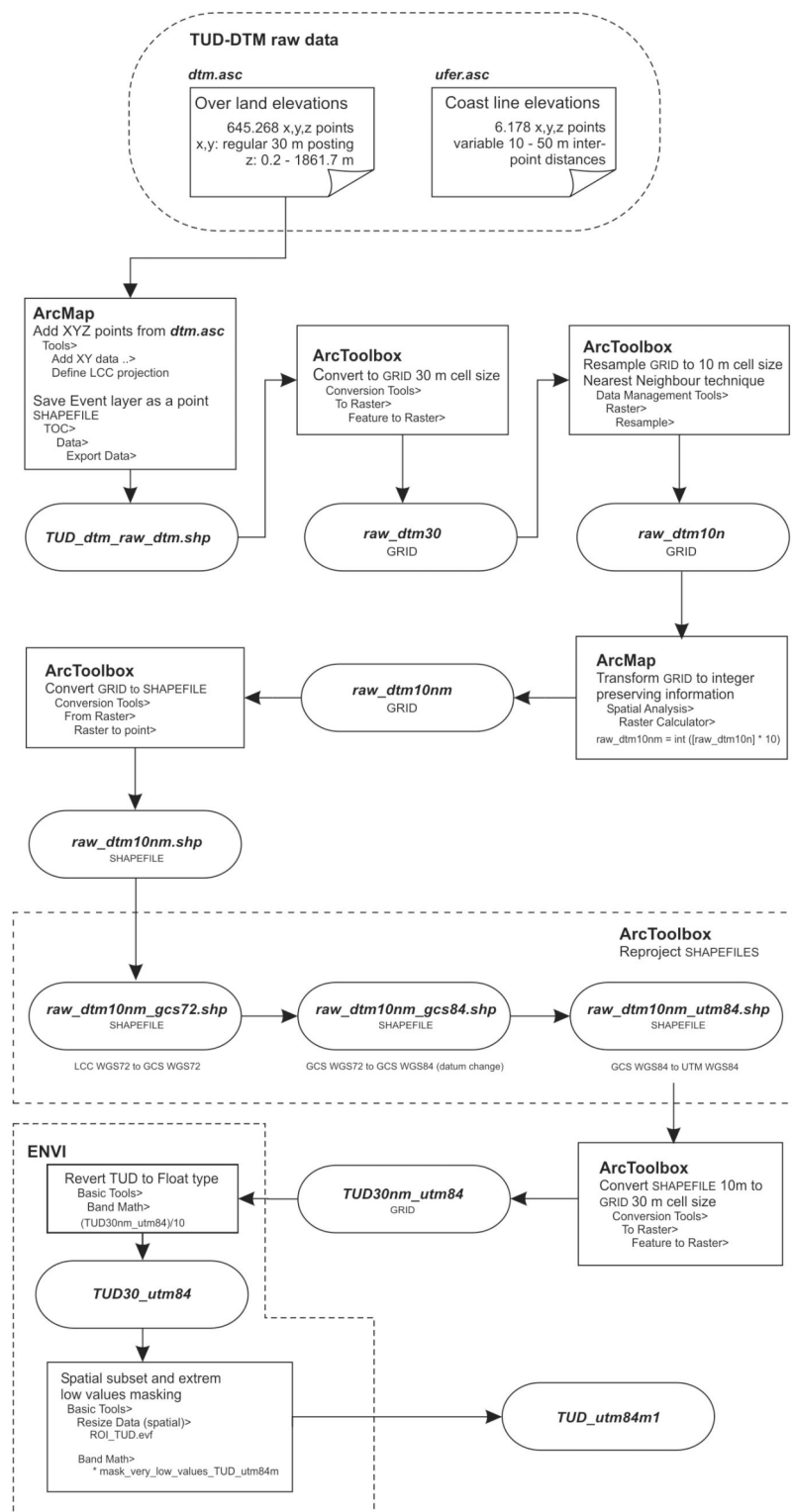


Figure 4.7: Flow diagram used to process the TUD-DTM raw data and to prepare it for registration and comparison with ASTER and RAMP DEMs.

The process chain used to convert the raw TUD-DTM data consists of four sections:

- Grid creation
- Up-scaling of raw grid size from 30m to 10m
- Reprojection from LCC WGS 72 to UTM WGS 84
- Down-scaling from 10m to 30m

The reading of the TUD model over land points coordinates and the creation of a regular grid of 30 m cell size (ESRI format) and no-data values in all the complimentary cells is the first step to prepare the DEM for processing.

The main consequence of a change of cartographic projection is the change of original data values due to the geometric distortions introduced by the transformations (rotation, translation, scaling, etc) and the resampling of data to assign a value to cells in the new projection. To minimize the impact of the required processing GOSSMANN (1984) developed a method that allows to largely preserve the original data in the processing. The Gossmann method considers the subdivision of each cell in 3x3 sub-cells assigning the original cell data value to all sub-cells.

After the transformations required for the change of projection the data is resampled again to the original 30 m grid size. Thus data loss and errors produced by the necessary transformations from one coordinate system to the other are minimized. The statistical comparison of the raw TUD-DTM with the reprojected TUD data set is shown in Table 4.2 giving clear evidence of the advantage of the method.

Table 4.2: Statistical comparison of original and reprojected TUD model (TUD-DTM).
Values in m.

	TUD-DTM (LCC WGS 72)	TUD_DTM (UTM WGS 84)
Min	0.20	0.20
Max	1861.70	1861.60
Mean	574.52	572.87
Std.dev	353.03	354.56

A pool of commercial off-the-shelf software (ENVI 4.2, ArcGIS 9.0, ERDAS Imagine 8.9) has been used to process the data set. The *ESRI GRID* and *SHAPEFILE* data formats were chosen seeking the best compatibility that allow a transparent interchange of data between software packages. These formats are native to ArcGIS and ArcInfo software, offering advantages in relation with the storage and a less demanding processing load compared with other data formats (ESRI, 1998).

Furthermore, translators are implemented in ENVI and ERDAS Imagine software. Nevertheless, in spite of the use of appropriate filters, some difficulties to read and recognize the projection parameters of ESRI software processed files occurred. In order to minimize software compatibility complications and to provide a procedure to prepare the TUD-DTM data set for comparison with the other DEMs, the steps graphically summarized in the flow diagram shown of Figure 4.7 had been tested and adopted.

4.2 Post-processing of ASTER DEMs

As described in section 3.3.2, we produced 24 elevation models based on one ASTER scene covering the test site (Scene SC:AST_L1A.003:2030971130, 19 September 2005) applying different combinations of parameters (see Table 3.6). On the one hand we found that the main topographic features can be reproduced to a great extent (see Figure 3.17). But on the other hand we must recognize that they are polluted to a substantial part with high frequency noise and artefacts.

This can be seen in the DEM presentation on Figure 3.17d. We now are looking for methods to reduce this errors by a convenient post processing of the created surfaces.

Altitude anomaly values (outliers or blunders) in our derived models can be attributed to miscorrelation in terrain under clouds, shadows, or with a lack of recognizable patterns for correlation. Different approaches are being used to detect and minimize these errors.

These techniques include the statistical approach for detection (FELICÍSIMO, 1994), editing of derived DEMs (ANIELLO, 2003); the application of filtering operations, and the averaging of terrain parameters derived from multiple realizations of DEMs (HENGL ET AL., 2004). Based on the technique recommended by HENGL ET AL.(2004) we decided to integrate a method with two steps:

- a first reduction of noise in the individual models by spatial averaging, and
- cell based averaging in a layer stack of our 24 models to obtain the central value for each cell in the grid.

The question then is, which kind of averaging is appropriate in the two steps?

In general we see that the irregularities in our models consists only partially of normal noise but also to some extent of local outliers of high magnitude. Consequently, for filtering a median approach fits better as the average or algebraic mean. Single errors of high magnitude have strong influence on the algebraic mean but not on the median of the data set. Therefore we use in the following the median filter technique in a twofold way: first as a spatial filter to smooth single surfaces and then as an operator to create a new surface from a layer stack.

The decision to use a zonal median filter for the reduction of noise is supported by the fact that terrain elevations at any point of the Earth surface would likely have a similar height to points located close to its vicinity. Exceptions to this assumption can be detected at positions where steep cliffs or artefacts occur and both situations can be evaluated after the noise removal. The median statistical parameter will filter extreme minimum and maximum values, selecting the value that is in the middle of the ranking of altitudes for a defined kernel size around each grid cell.

The used ENVI's Median Filter replaces each center pixel with the median value within the neighborhood specified by the filter kernel size (RSI, 2005). Also, median filtering smoothes an image, while preserving edges larger than the kernel dimensions. For this reason median filters are well suited to remove salt and pepper noise or speckle. As first step of the processing chain, all models of Table 3.6 were filtered using a 9x9 kernel size median filter. Then the individual DEM layers have been compiled to a layer stack of 30 m grid cell size.

Care was taken to chose the adequate kernel size to reduce the noise to an acceptable degree but to preserve the information at the required level.

To determine the suitable kernel size a vertical profile section approximately 38 km in length (AA') (Figure 4.8) was defined across the test site in order to investigate the altitude characteristics of our ASTER derived DEMs.

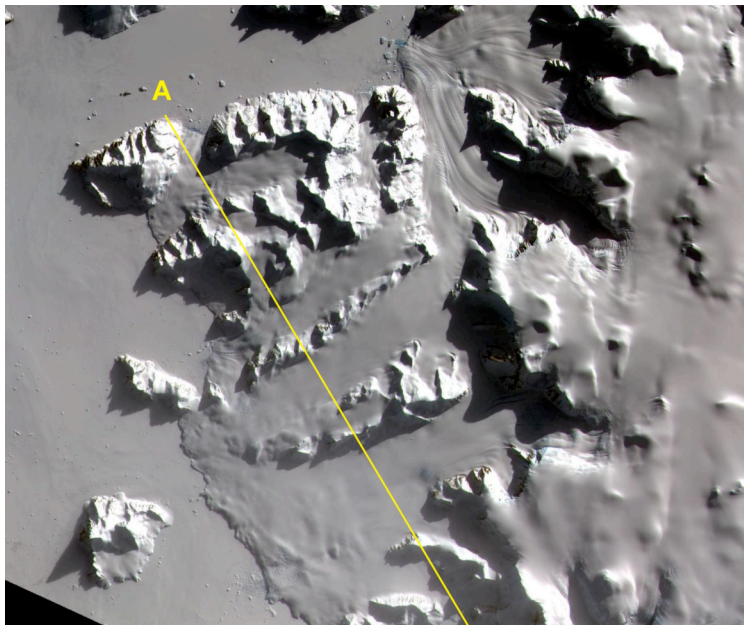


Figure 4.8: Profile section crossing glaciers and ridges along test site on Marguerite Bay region, which will be used for comparison of the effect of median filtering with different kernels in Figure 4.9.

ASTER Scene SC:AST_L1A.003:2030971130, 19 Sept. 2005.

Profile AA' crosses areas of different relief, range of altitudes, slopes orientation and exposition to solar illumination. The application of profile AA' to the ASTER DEMs provides for a representative set of samples of oversaturated areas as well as from locations under shadows where poor conditions of surface patterns render the image matching difficult. Different kernel sizes were used on one of the available models (ASTER DEM3) and a comparison of noise suppression was performed. Results are depicted in Figure 4.9. A 9x9 pixels kernel size has been considered to offer a suitable compromise.

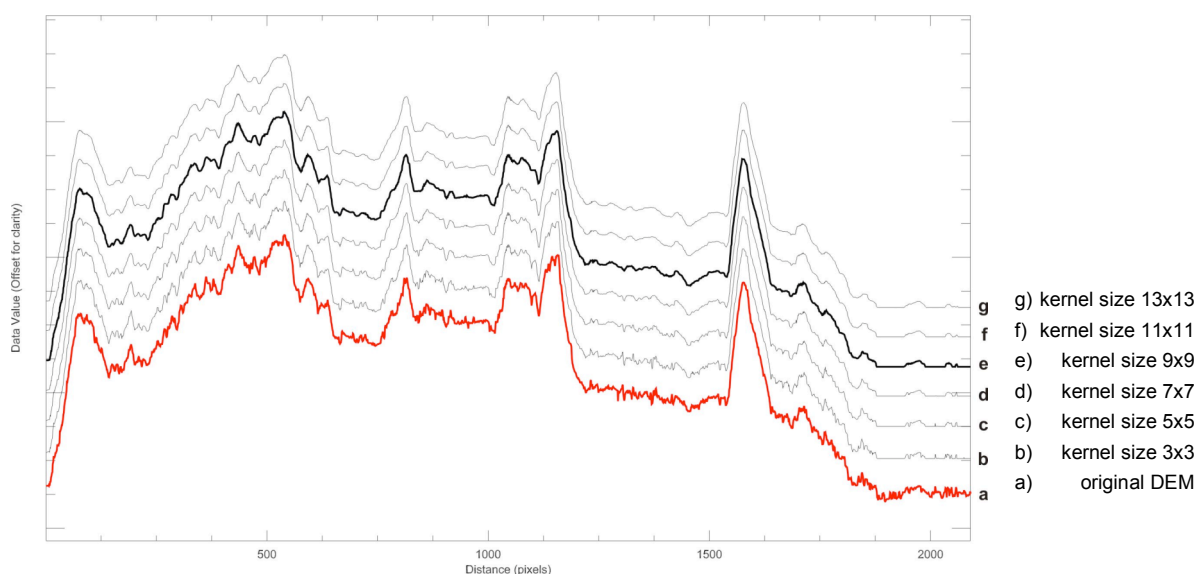


Figure 4.9: Profile AA' over a 15 m spatial resolution model (ASTER DEM3, see Table 3.6) after application of median filter of different kernel sizes.

The best compromise between the suppression of noise and the preservation of details is shown in profile e) based on the kernel size 9x9.

The models in the layer stack still contain artefacts where the zonal median filtering was not able to smooth the impact of strong errors introduced by large outliers (peaks or pits) originating from miscorrelation of conjugate points. Some models are providing a better surface than others. This is because altitude differences among models are not only depending on conditions of the terrain surface and illumination that produce a specific local surface pattern, but also on the combination of different search window sizes and the set of additional parameters used for the image matching process.

Thus, the supplementary stack-based median filter processing of the 24 filtered models provides an averaged surface not affected by the extreme values of outliers which occurs in less than 50% of the 24 models. This task was performed using the *stack median* statistics function of the ERDAS Imagine Modeler module. The resulting MED-MED model is shown in Figure 4.10. This representation of the surface will be further evaluated in order to assess its quality and measure the agreement with the “reality” under a visual inspection and profile comparison.

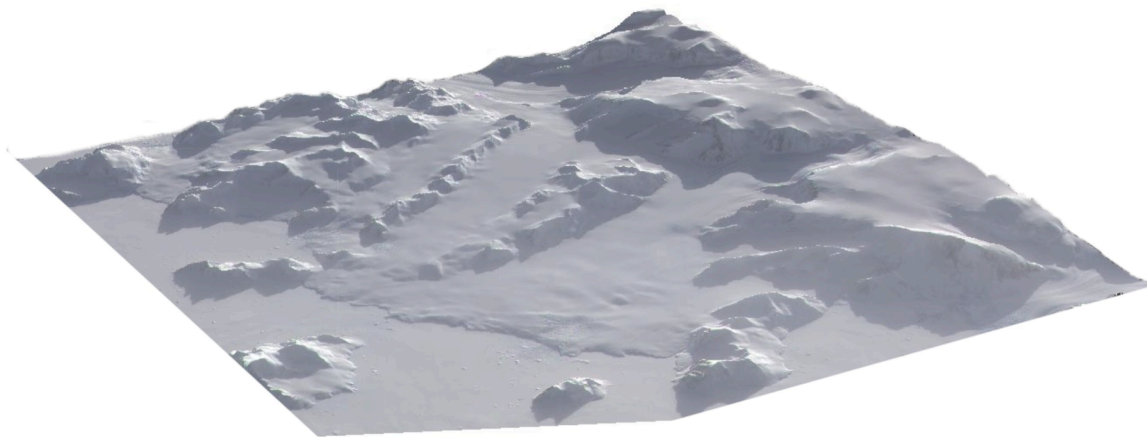


Figure 4.10: MED-MED model overlayed by the orthorectified ASTER scene, (SC:AST_L1A.003:2030971130, Sept. 19, 2005, 13:33:26) of Marguerite Bay test site. Vertical exaggeration by factor 1.5x.

The MED-MED model is the median surface of the 24 median filtered ASTER DEMs and will be used in sections 4.3.1 and 4.3.2 as “our best ASTER model” derived from a single scene.

4.3 Visual Comparison of derived ASTER-DEMs, TUD-DTM and Reality

Visual landscape assessments involve the inventory and evaluation of diverse visible attributes of the landscape. That kind of evaluation should consider the measurement of physical characteristics of the reality, independent of people; and in addition, the measurement of those characteristics depending of our individual perceptions (PALMER & HOFFMAN , 2001).

We do this assessment in two ways: by comparing visually virtual (i.e. computer generated) and real (i.e. photographic) images of the landscape, and by evaluating the profiles taken from our model with the corresponding profiles taken from RAMP and TUD models.

4.3.1 Real and virtual landscapes

Two parameters to perform an assessment of landscape are well known from the literature (PALMER & HOFFMAN, 2001):

- reliability, the degree of similarity between evaluators, and
- validity, the equivalence of judgments made from synthetic pictures extracted from the model and real photographs.

From the Marguerite Bay test site there exists an important number of terrestrial and aerial photographs. Based on our model we create corresponding virtual views. The virtual landscape we use consists of the MED-MED elevation model draped by the corresponding orthorectified ASTER scene (Scene SC:AST_L1A.003:2030971130, 19 Sept. 2005), from which the DEM was derived.

Three examples with corresponding virtual and real landscape are presented in Figure 4.11.

On the left side the real photographs are shown, and on the right side the virtual images are displayed.

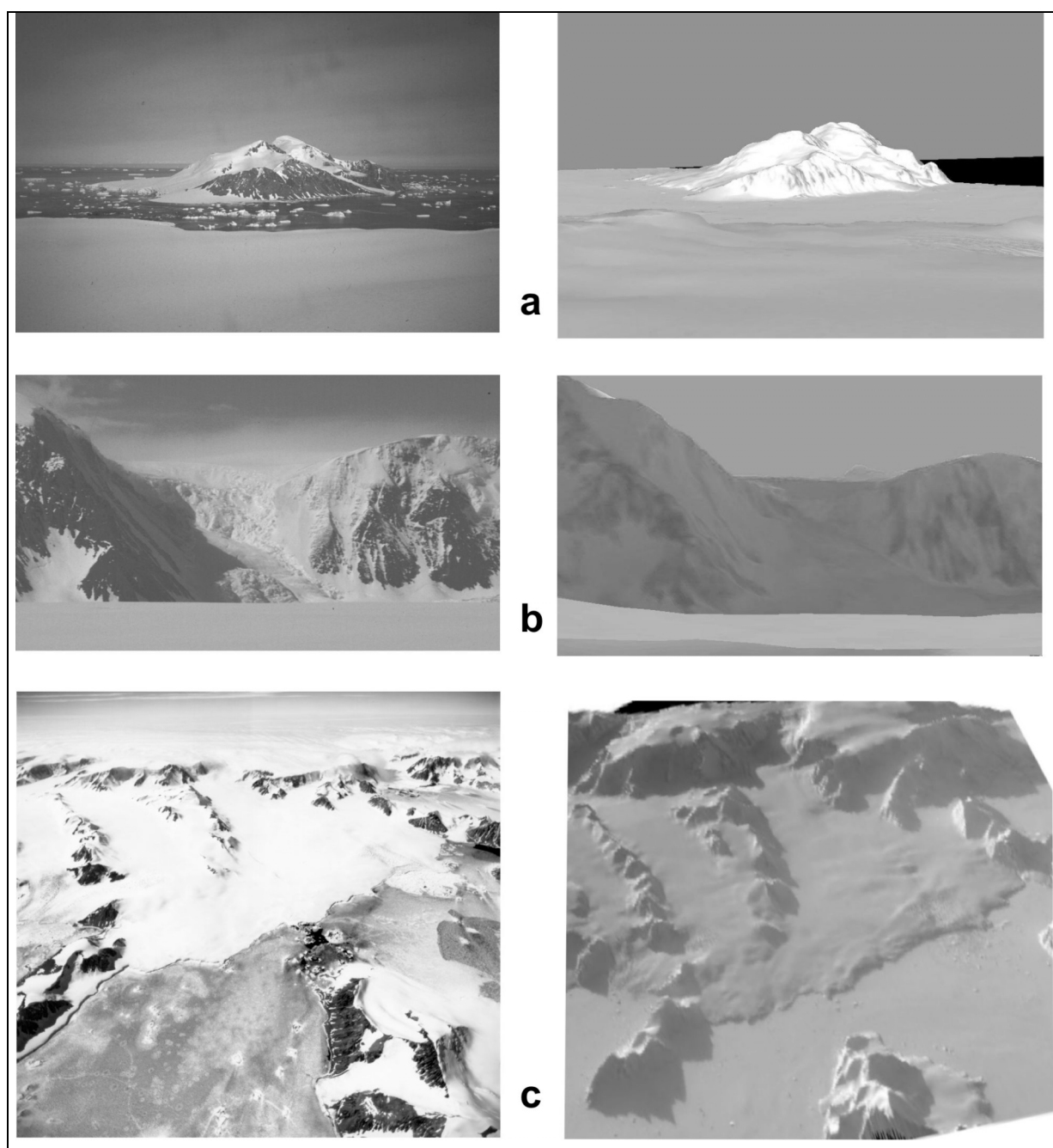


Figure 4.11: Photos of DYPAG field campaigns and an overflight and corresponding ASTER virtual landscape. Vertical exaggeration 1.5x.

a) Millerand Island seen from Schauinsland Mountain (Photo by H. Gossmann)

b) Plateau escarpment with Blow Me Down Bluff seen from Northeast Glacier (Photo by H. Gossmann).

c) General view of McClary and Northeast Glaciers seen from an aircraft overflight (Aerial photography Trimetrogon 1969: F31 USNGS T17511263 Peninsula TMA 2166-313)

Figure 4.11a gives a view from Mount Schauinsland westward towards Marguerite Bay. Millerand Island is located in the center of the image. The shape of the virtual terrain fits quite well the real one being conform with most of the topographic elements. Differences we recognize are the disparity of sea ice and snow coverage. These are due to the different times of acquisition: the terrestrial photo was taken in summer (February) 1994, and the ASTER scene was taken at the end of winter (September) 2005.

Figure 4.11b provides a view from the surface of Northeast Glacier eastward to the escarpment of the Antarctic Peninsula Plateau. We see from left to right: (a) Blow Me Down Bluff; (b) one of the great ice falls, which feed Northeast Glacier and (c) some avalanche channels with accumulation cones. The virtual image looks smoothed and shows less detail than the photograph. Note that both images do not have exactly the same point of view and scale. The different illumination affects the recognition of more details in the virtual image.

Figure 4.11c shows the view of an aerial photograph taken over the Marguerite Bay eastward covering most parts of our test site. Despite of the different inclination angle in both images we can appreciate a great correspondence between the real and the virtual landscape. Glacier surfaces, glacier fronts and the mountain ridges between the glaciers, as well as the details of the plateau escarpment, have a very good representation in the virtual image. It has to be noted that the virtual image has a better contrast and shows many features clearer than the real, however old, aerial photograph.

In the same way we can demonstrate the very good virtual representation of many features of our test site up to Sodabred Slope that was used by the old American and British expeditions climbing up to the plateau of Antarctic Peninsula.

An enhanced and extended visual perception of the ASTER derived DEMs can be achieved by a representation in three dimensions. An interactive manipulation of the derived models, draped with a corresponding ASTER scene, provides a way to inspect details of the terrain that improve our understanding. It is possible to focus on specific features (e.g. bare ice sectors, ice falls, moraines, artefacts, etc.) to observe these under different points of view and at different scale. It is even possible to compile a sequence of snapshots along a route to create a virtual flight through the observed landscape. Such a product is included as "Virtual Flight over Marguerite Bay Test Site Area" in the attached CD-ROM of this Thesis (Annex 1).

4.3.2 Profile comparison

A complimentary method to evaluate surfaces of elevation models is the use of profile analyses. This graphic method shows pixel by pixel the height values and vicinity relation along the profile, giving a detailed description of the surface properties. At the same time it provides a way to perform a semi-quantitative measurement, because it allows to compare altitude deviations with respect to other models.

Consequently, in this section we evaluate the MED-MED model against the two reference models introduced in the previous sections: the TUD and RAMP models. In the figures of this section we put the MED-MED model data together with the corresponding data sets of the TUD and RAMP models.

Four profiles were traced on the area of our test site as are shown in Figure 4.12.

They were chosen in order to cover all different types of relief and glacier sections in this area, including also segments in problematic locations. Thus, shadowed spots were crossed, as well as over-saturated places, in order to investigate the properties in critical segments of the ASTER derived DEM.

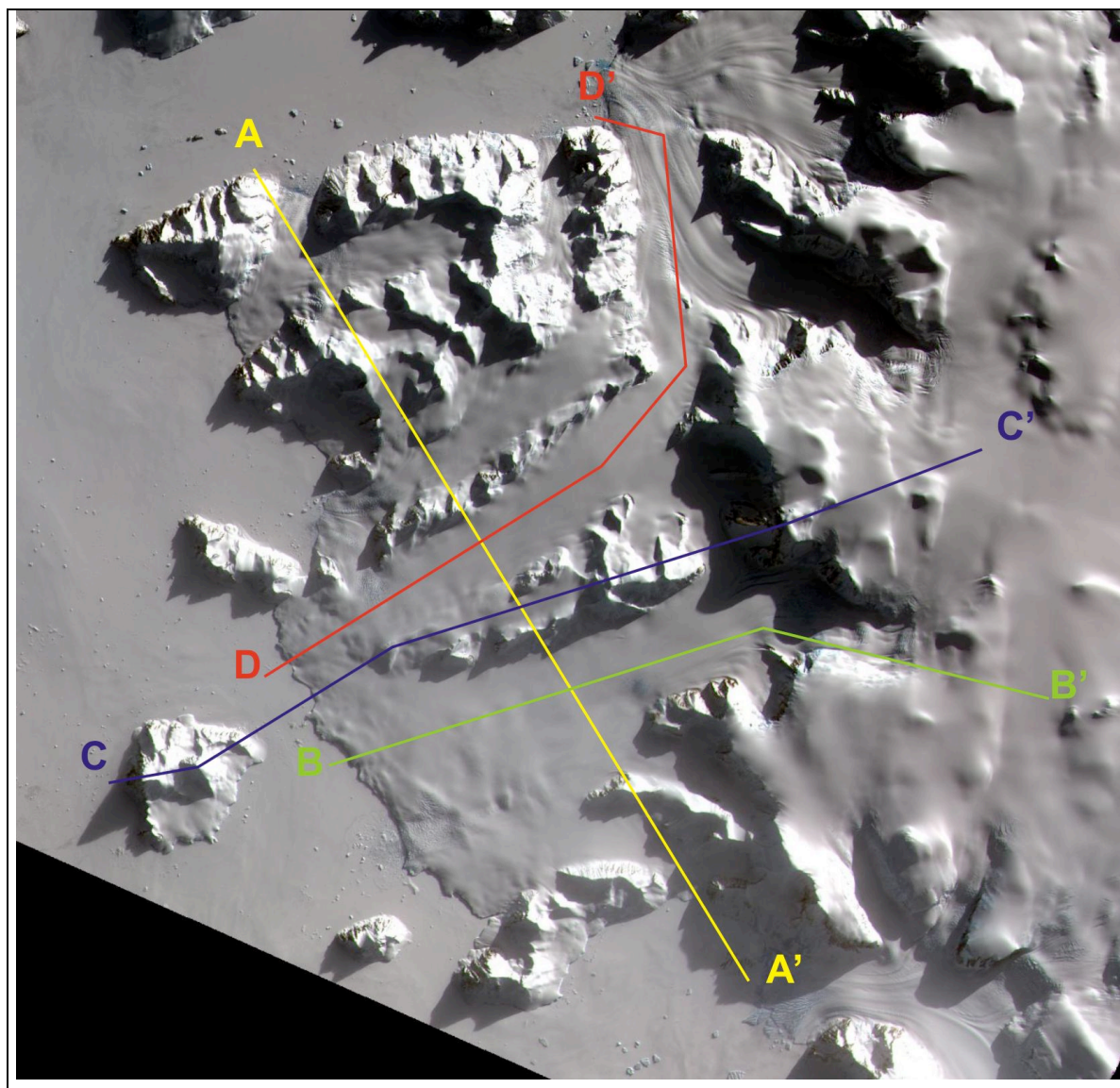


Figure 4.12: Location of vertical profiles in the test site area.

AA': Profile Northwest - Southeast crossing the glaciers

BB': Northeast Glacier - Sodabread Slope - Plateau

CC': Millerand Island - Butson Ridge – Blow Me Down Bluff - Plateau

DD': McClary Glacier - Swithinbank Glacier

Figure 4.12 shows the location of the four profile lines:

Profile AA' stretches out 38 km in NW-SE direction from Square Bay to Neny Fjord. It crosses transversally several main glaciers of our test site: McMorris Glacier, Todd Glacier, McClary Glacier and Northeast Glacier. Very bright areas are included on the north oriented slopes of several crossed ridges. Conversely, shadow areas are present in the south facing slopes.

Profile BB' spanning over 26 km, rises along the Northeast Glacier from the sea level, changing direction and passing the Sodabred Slope up to the plateau (ca.1800 m). The purpose of this section is to report how good our model can describe the surface following the main flow direction of the glacier.

Profile CC' with a length of approximately 37 km starts in the western margin of the test site crossing Millerand Island and finishing in the heights of the central plateau of the Antarctic Peninsula. It traverses the elevations of Butson Ridge and passes conflictive bright and shadowed areas at the steep ascent of Blow Me Down Bluff. It allows to check how the models reflect the situation in areas with strong relief.

Profile DD' is the second profile alongside the central part of a glacier. Having a length of approximately 30 km it runs up from the Marguerite Bay coast along the McClary Glacier to the ice divide, then it leads down the other side following a tributary of the Swithinbank Glacier to the sea. The motivation to chose this profile was to see how the models reproduce the location of this ice divide.

In Figure 4.13 we find in different colors the altitudes along these profile lines given by the RAMP model (magenta), the TUD-DTM (blue) and our ASTER derived MED-MED model (green). On the X-axis starting from the origin, distance is labeled by a pixel count corresponding to the 30 m grid cell size. The Y-axis represents elevations in meters. The vertical exaggeration factor is 5.

The comparison of altitudes and shapes within these profiles reveals interesting insights:

In most profiles the RAMP model exhibits a high disparity. This situation is not very surprising if we consider that the source RAMP model has a spatial resolution of 200 m, 6 times less than the other two models. Additionally, its vertical accuracy is also poor as has been reported in section 2. We observe vertical distortions of up to 500 m (profile CC' close to pixel 1000), and horizontal distortions of up to 3 km (profile AA' close to pixel 1100).

The best agreement is observed on the relatively flat surface along the Northeast Glacier (profile BB'). Nevertheless differences are larger in the other profiles evidencing that at this scale the RAMP model does not provide an acceptable representation of the surface. Consequently, RAMP will not be considered furthermore as a reference model for comparisons in the next sections. The model evaluation will be based solely on the use of the TUD-DTM) as the central reference that has the best accuracy reported for DEMs in the test site are.

Along the four profiles the TUD reference model and the MED-MED ASTER derived model have a high degree of equivalence in form and altitude. Shapes of both models follow the same general trend in all profiles. Remarkably the MED-MED model agrees with the TUD model quite well in specific locations. The two profiles seem to be almost identical in (a) the U-shaped cross section of Northeast Glacier between pixels 1200 and 1600 of profile AA', (b) on the lower parts of the Northeast Glacier, the first 9 km of profile BB', and on McClary Glacier, the first 12 km of profile

DD', and (c) on many east facing slopes between Millerand Island and Blow me Down Bluff on profile CC'.

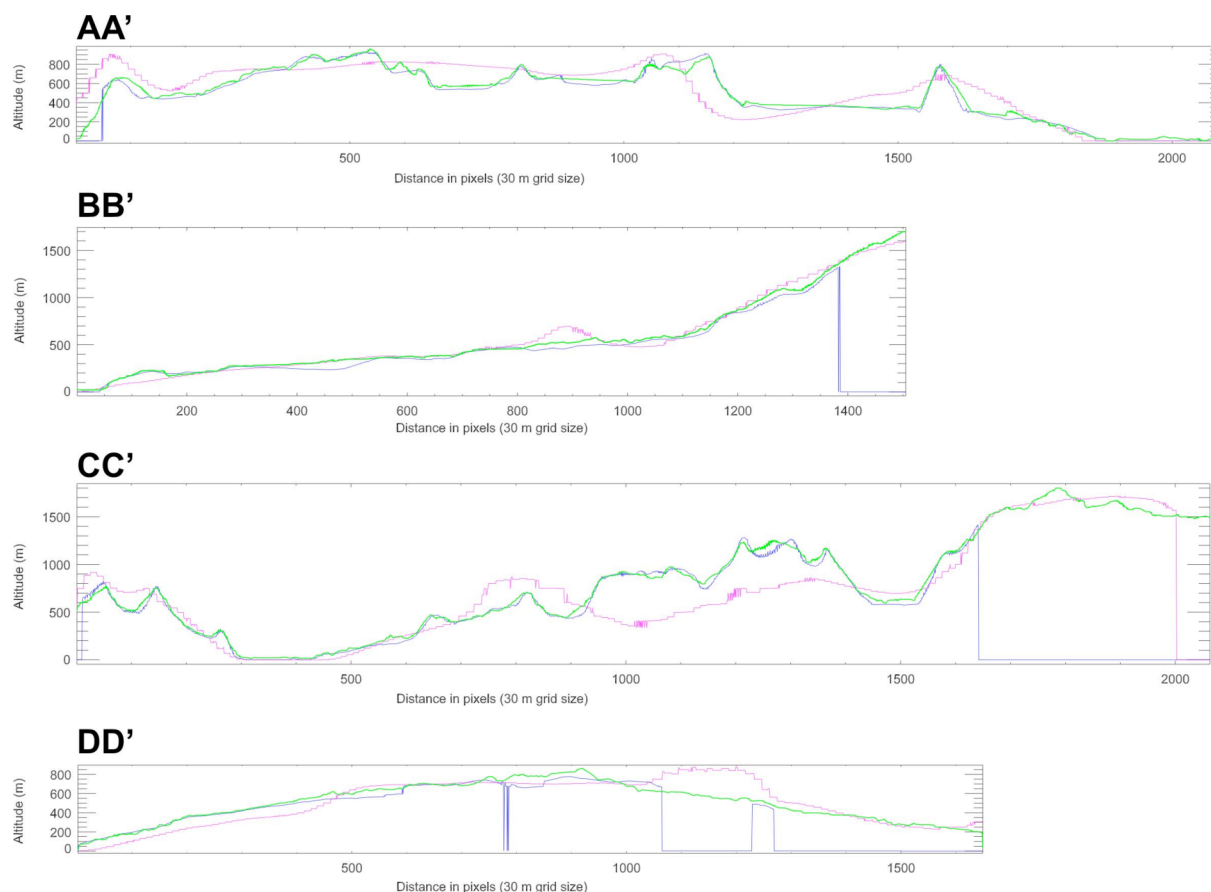


Figure 4.13: Comparison of hypsometric profiles taken from RAMP (magenta), TUD (blue) and the ASTER derived MED-MED (green) models. Vertical exaggeration of all profiles by factor 5.

AA': Profile Northwest - Southeast crossing the glaciers

BB': Northeast Glacier - Sodabread Slope - Plateau

CC': Millerand Island - Butson Ridge - Blow Me Down Bluff - Plateau

DD': McClary Glacier - Swithinbank Glacier

In general altitude deviations are in the range of meters and few decameters. Few extreme deviations, as in profile AA' (pixels 120, 600, 1150 and 1700), profile BB' (pixels 470 and 940), profile CC' (pixels 580, 920 and 1250) and profile DD' (pixels 500-600, 800-850, 920 and 1050) rise up to 200 m. They may have two different origins:

Our TUD reference model itself may have some deficiencies. This is suggested by the step-like change of altitude in the longitudinal portion of McClary Glacier (profile DD' pixel 600). There is also a lack of information in some parts of the profile (e.g. profile DD' pixels 780, 1080-...).

On the other hand, the shape of the profile in our ASTER derived DEM around points with extreme deviations suggest the presence of artefacts (e.g. profile AA' pixels 600 and 1700, profile CC' pixel 580 and around 1250). These are artefacts produced

during the image matching process by weak or wrong correlation not totally suppressed by our double median filter processing method. Potential factors can be the possible existence of thin clouds, shadows, and the lack of patterns over snow surfaces due to over-saturation. These influences vary from time to time and depend on the characteristics of scene acquisitions. This suggest that models based on different scenes will contain artefacts in different locations.

As a consequence, we can expect that a method based on the use of more than one scene, that is, a multi-temporal approach, might minimize or even suppress the artefact problem.

4.4 Multitemporal approach

In many studies based on remote sensing data results could be substantially improved by using multi-scale, multi-sensor or multi-temporal image data of the target under study.

For our surface modeling up to now we have followed a multi-DEM approach based on the use of only one scene which has been processed at constant 15 m spatial resolution under a set of 24 different parameter combinations. A similar approach has been used by KÄÄB (2005). He found that for optimal DTM generation from satellite stereo data multiple DTMs should be computed from one stereo data set with different resolutions and different sizes for the image block (window search kernel) used for DTM matching. Further enhancement can be achieved by the fusion with additional models from other sources (CUARTERO ET AL., 2005).

In previous sections we have demonstrated that results produced by the MED-MED method from one scene represent well the surface of our test site area, but still include remnants of artefacts. The visual evaluation of the model and the graphical estimation of the altitude deviations have shown that part of the errors is related to temporal phenomena over conflictive areas. In this section we explore the potential minimization of this kind of error by the use of a multi-temporal approach.

4.4.1 Method

To suppress the artefacts of ASTER derived DEMs by the use of a median filter in a multi-temporal layer stack we need a sufficient large number of scenes. If they are available, as is the case for our test site area, the question may arise which method can offer the most efficient processing to produce an acceptable DEM.

The processing chain used to generate 24 different models in section 3.3.2 (see Figure 3.14 and Table 3.6), required an important allocation of computational resources. The CPU time to process $n \times 24$ models (n =number scenes) and the needed disk space to store the resulting data dramatically will increment the requirements. Our idea is that a best combination of parameters exists that will produce acceptable results with a minimum effort. For this reason, it is necessary to avoid the considerable effort used to process a single scene and try to find which is the best set of parameters to use in combination.

Therefore, the question is which of these 24 possible single models already produced, are the nearest to the MED-MED model? We investigated the 24 produced models to find which of these match best the doubly filtered MED-MED model. The way to perform this search is through a two steps procedure:

- the comparison of 2D altitude scatterograms from each ASTER derived DEM versus the MED-MED model, and
- the inspection of the hill shaded surfaces of the ASTER derived DEMs

Figures 4.14a and 4.14b show the complete set of 24 altitude scatterograms.

Each plot has the altitude of the MED-MED model as abscissa and the altitude of the ASTER derived DEM as ordinate. Six cases for the '*correlation matrix size*' parameter (3x3, 5x5, 7x7, 9x9, 11x11 and 13x13) are grouped in columns, and four possible combinations for the '*water detection*' and the '*extended correlation*' parameters are presented in rows (see Table 3.6).

It can be noted that the differences between scatterograms within columns are very small compared to the differences presented within rows. Obviously the impact of the '*correlation matrix size*' parameter is more important than the variation of the two additional parameters.

Considering the shape of the cloud of points and their deviation from the central diagonal line, notoriously the highest agreement is presented by the plots corresponding to cases with 3x3 and 9x9 pixels as the '*correlation matrix size*'. Also, it has to be noted that if we compare the different rows we see that the models generated with additional parameters do not give additional benefit in spite of their higher demand of CPU processing time.

If we compare only the scatterograms for the 3x3 and 9x9 pixels correlation matrix sizes without additional parameters (i.e. the uppermost boxes in both columns), the best agreement with the MED-MED model is presented for the model extracted with a 3x3 pixels window size. Consequently, the 3_DEM within the group of 24 ASTER derived DEMs generated with different combination of parameters is the closest to the MED-MED model. This suggests that the best set of parameters is provided by the use of a 3x3 pixels '*correlation matrix size*' without additional parameters.

This is supported also by the visual inspection of the corresponding images of artificially illuminated (hill shaded) DEMs. As it is shown in Figure 4.15a the shaded relief for model 3_DEM shows a relative low impact due to artefacts compared with all other models, while the shaded image of model 9_DEM presented in Figure 4.15b, shows clearly a great number of large facets due to the impact of artefacts in the interpolation process.

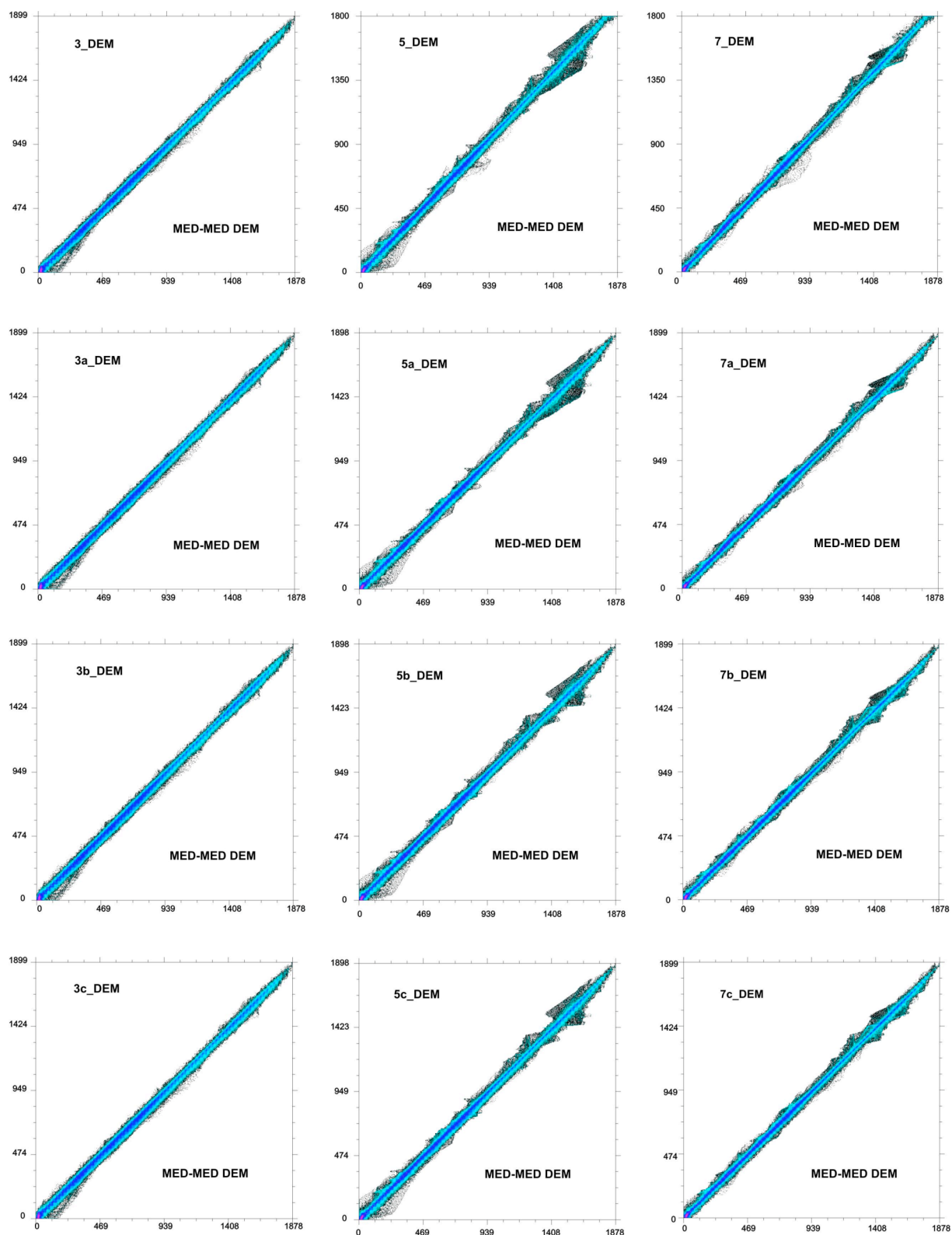


Figure 4.14 a: Accuracy evaluation of 24 ASTER derived elevation models for Marguerite Bay test site by analysis of altitude scatterograms. Each box shows altitudes of MED-MED model as abscissa and the altitudes of one ASTER derived DEM as ordinate.

Columns: 'correlation matrix size' values of 3, 5 and 7 pixels.

Rows : combinations of additional parameters ('water detection', 'extended correlation').

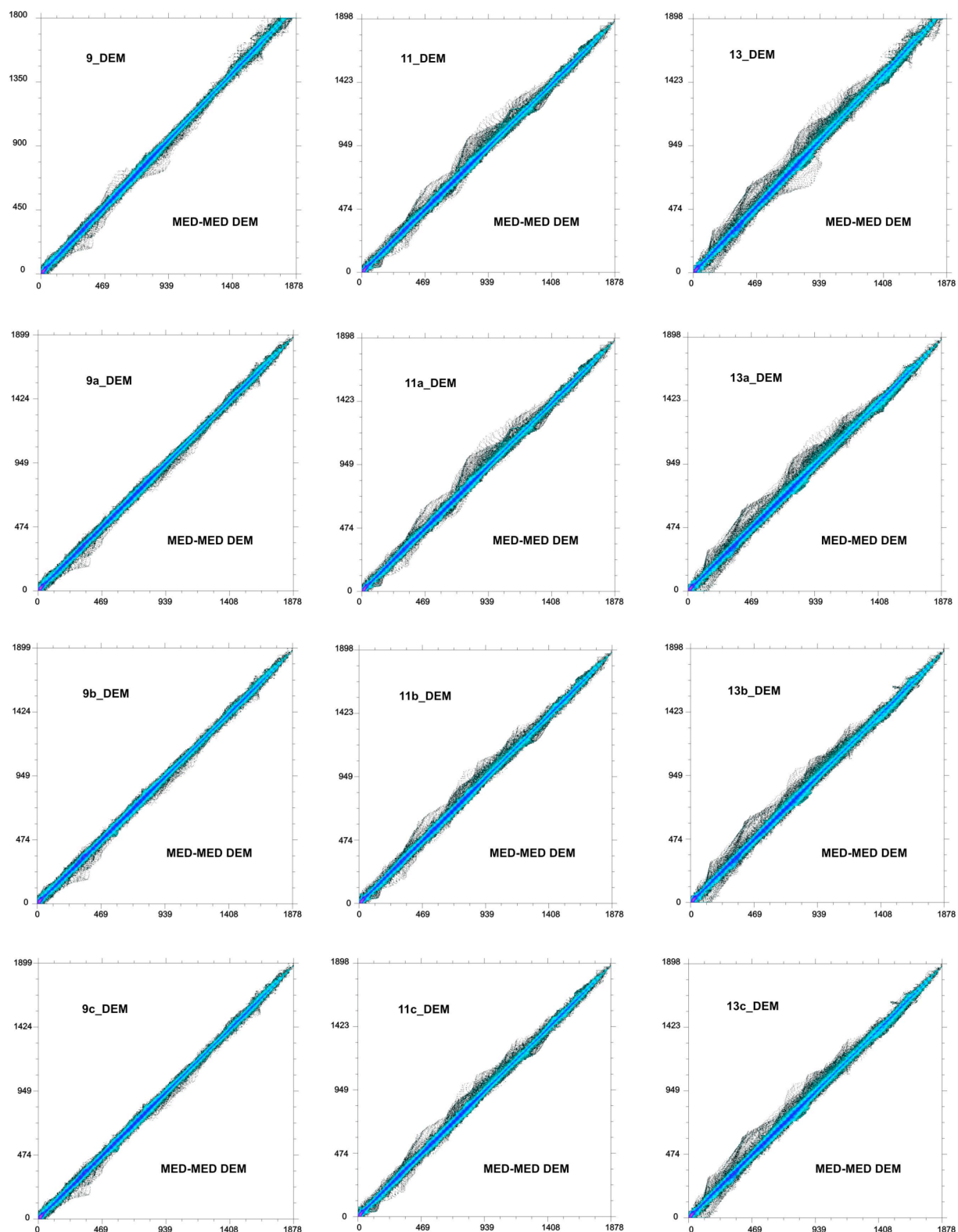


Figure 4.14 b: Accuracy evaluation of 24 ASTER derived elevation models for Marguerite Bay test site by analysis of altitude scatterograms. Each box shows altitudes of MED-MED model as abscissa and the altitudes of one ASTER derived DEM as ordinate.

Columns: 'correlation matrix size' values of 9, 11 and 13 pixels.

Rows: combinations of additional parameters ('water detection', 'extended correlation').

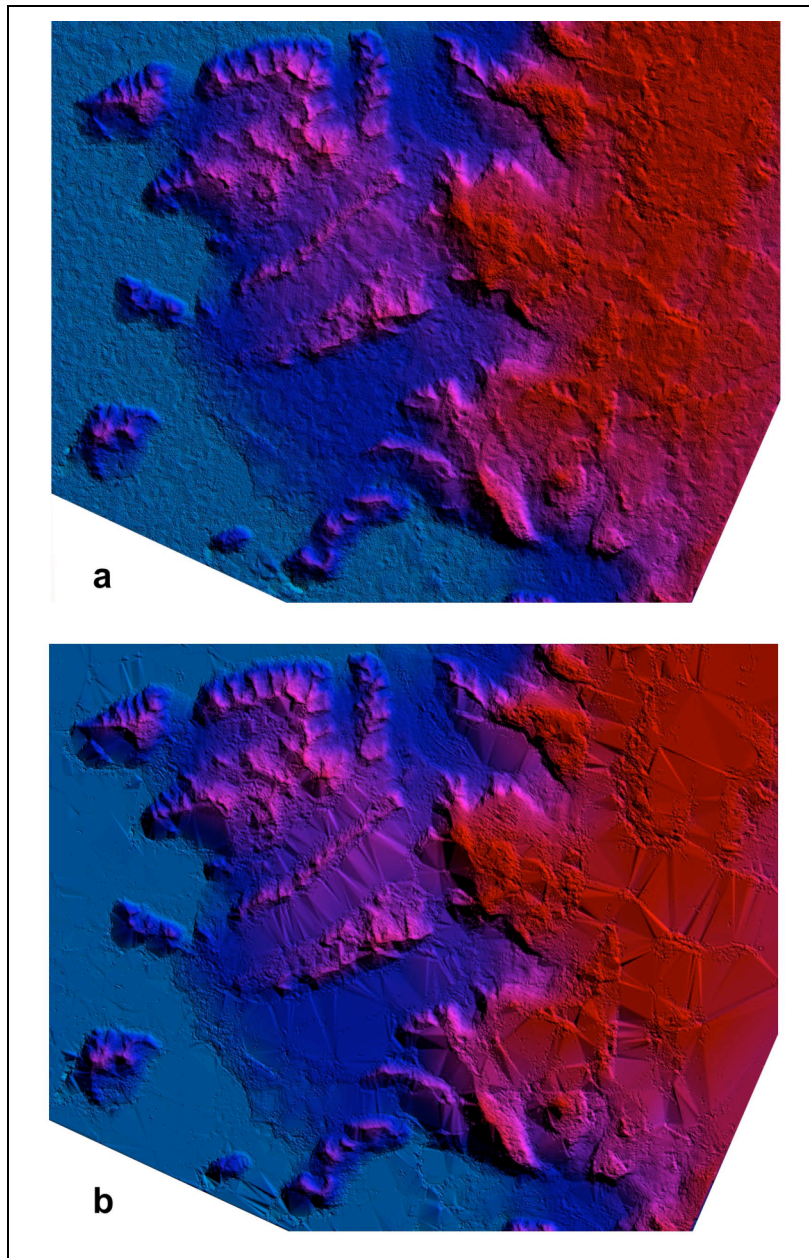


Figure 4.15: Demonstration of differences and impact of artefacts between two ASTER derived DEMs using images of shaded relief (hill shading). (SC:AST_L1A.003:20309711 30, Sept. 19, 2005, 13:33:26),

a) Section of the model 3_DEM on Marguerite Bay test site extracted with 3x3 pixels correlation matrix size and without additional parameters.

b) Section of the model 9_DEM on Marguerite Bay test site extracted with 9x9 pixels correlation matrix size and without additional parameters.

The complete series of shaded relief images for the 24 different models generated for the test site area (see Table 3.6), is included in Annex 1.

Thus, visual inspection of hill shading images of DEMs generated with different combinations of parameters shows that the 3x3 pixels '*matrix correlation size*' parameter provides a surface where artefacts are locally concentrated. Here the artefacts have a spot-like influence while in all the others models artefacts have a wide and far reaching impact producing large facets in the surface.

Based on the previous results the use of a 3x3 pixels '*correlation matrix size*' value without other additional parameters offers the best combination out of the set of 24 combination cases available. Consequently, this combination has been chosen to process the multi-temporal derivation of DEMs.

Based on this knowledge and considering further requirements stemming from the multi-temporal approach, we adapted and complemented the processing chain used in Section 3.3.2.2 to derive DEMs. The flow diagram of the multi-temporal processing is shown in Figure 4.16. It combines processes executed with AsterDTM, ENVI and Imagine Modeler modules.

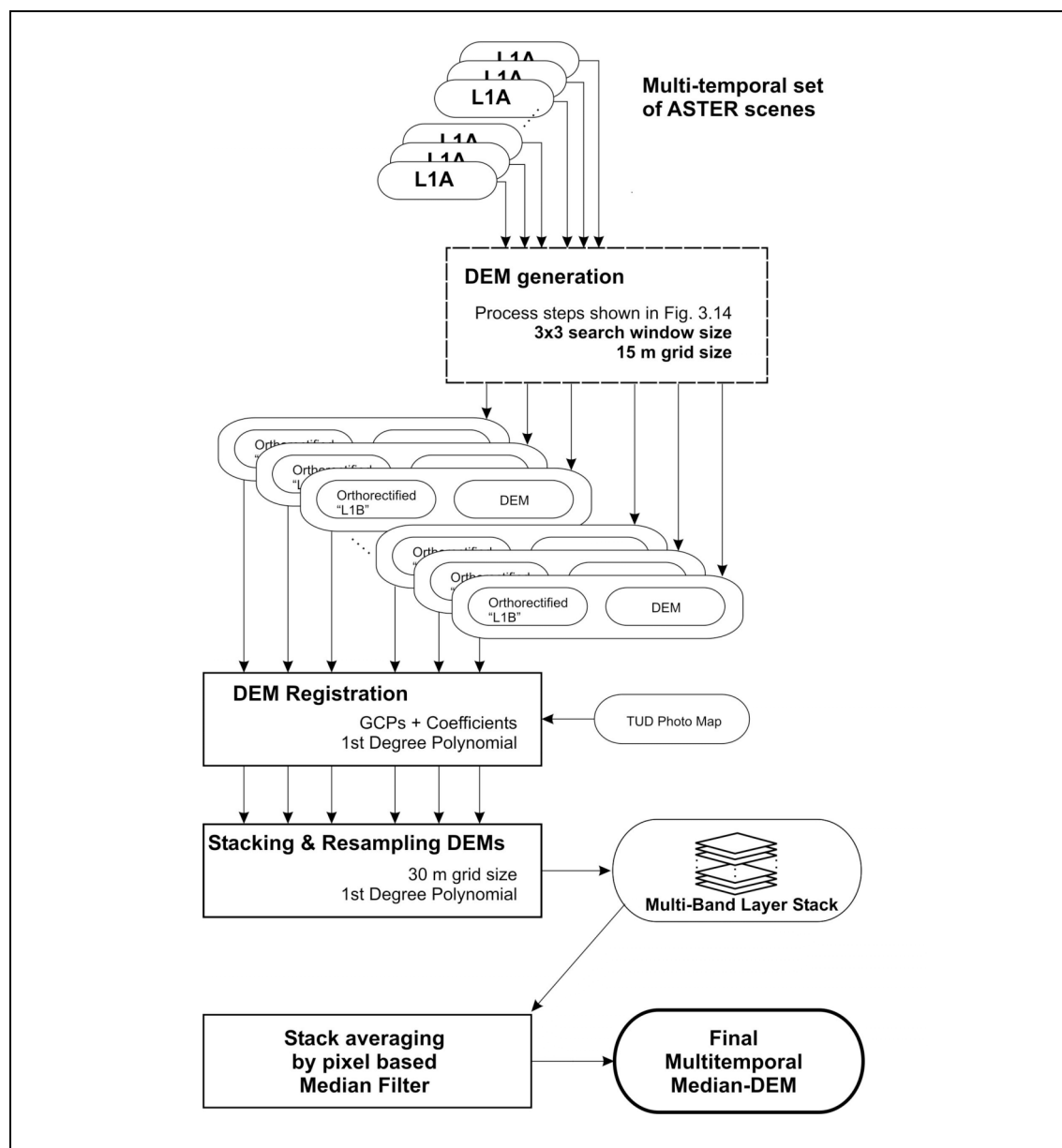


Figure 4.16: Flow diagram for the multi-temporal ASTER scenes processing approach. Production of an averaged DEM by pixel based median filtering within a layer stack.

The process chain to derive the multi-temporal median DEM has the following main sections:

- **DEM generation**
 DEMs are derived for all available scenes using a fix combination of parameters with 15 m output pixel size, a 3x3 pixels ‘correlation matrix size’, no ‘water detection’ and no ‘extended correlation’. A terrain geometric correction for each ASTER “L1B” scene is performed using the derived DEM to produce the corresponding orthorectified image. The constitutive steps of the DEM generation process using the AsterDTM software have been explained with more detail in Section 3.3.2.2 and are depicted in Figure 3.14. The termin “L1B” is defined at this place too.

- DEM registration
A registration process is carried out in two steps to register each ASTER derived DEM with the reference TUD model. Because of the difficulties and inaccuracies of image to image registrations based just on two DEMs, firstly the registration of the orthorectified “L1B” image with the TUD Karte image is performed. This step provides the GCPs and the coefficients for the 1st degree polynomial correction applied in each registration. Finally, an image (in this case the DEM) to map registration using the GCPs and coefficients calculated in the previous step is carried out for each DEM.
- Stacking and Filtering
The coregistered DEMs are added to a layer stack. Within this step we masked sea water areas and resampled the data from 15 m to 30 m by the nearest neighbor method. Finally, the stack median function available in ERDAS Imagine Modeler is used to filter extreme values of pixels in the derivation of the multi-temporal median DEM, the MT-MED model which is our final product.

To derive the MT-MED model of our test site eight ASTER L1A scenes with an acceptable cloud coverage were used from a total of 32 scenes acquired between November 2000 and September 2005. Their specifications are summarized in Table 4.3.

Table 4.3: L1A scenes used for the derivation of the Multi-temporal Median DEM (MT-MED model) on the Marguerite Bay Test Site.

The ASTER HDF metadata keywords are used as column headlines.

CALENDAR DATE	TIME OF DAY	GRANULE	SCENE CLOUD COVERAGE	SOLAR AZIMUTH ANGLE	SOLAR ELEVATION ANGLE
24 Nov 2000	13:47:34	SC:AST_L1A.003:2004036061	29	44.65	37.43
04 Jan 2001	13:40:43	SC:AST_L1A.003:2004076906	11	52.57	37.84
04 Jan 2001	13:40:52	SC:AST_L1A.003:2004076911	3	52.83	37.24
27 Dec 2001	13:49:44	SC:AST_L1A.003:2006637985	1	49.24	39.07
25 Dec 2002	13:29:43	SC:AST_L1A.003:2010196883	4	53.98	37.82
02 Jan 2004	13:47:46	SC:AST_L1A.003:2019544986	19	51.15	38.55
20 Jan 2004	13:35:19	SC:AST_L1A.003:2020012711	29	54.31	34.52
19 Sep 2005	13:33:26	SC:AST_L1A.003:2030971130	4	43.55	14.85

Table 4.4: Basic statistics of MT-MED model and its derived RMS grid. Values in m.

	Min	Max	Mean	Stdev
MT-MED	-50	1811	530.26	488.80
MT-MED_RMS	0	566.50	16.32	14.25

General statistics of the MT-MED model and of its derived RMS grid are shown in Table 4.4.

As we did with the MED-MED model we now carry out an evaluation of the MT-MED model in order to assess its quality and to measure the agreement with the “reality” under a profile comparison.

4.4.2 Profiles comparison

In this section we use the same argumentation as given in Section 4.3.2, to justify a DEM comparison based on profile analysis. We investigate visually and semi-quantitatively the accuracy of the multi-temporal ASTER derived MT-MED model. The profile sections specified in Figure 4.12 and described in section 4.3.2, are used to compare the ASTER derived DEMs and the TUD reference model.

In Figure 4.17 we find in different colors the altitudes over these profile lines given by plots of the MED-MED model (green), TUD-DTM (blue) and our ASTER derived MT-MED model (red). On the X-axis starting from the origin, distance is labeled by a pixel count corresponding to the 30 m grid cell size. The Y-axis represents elevations in meters.

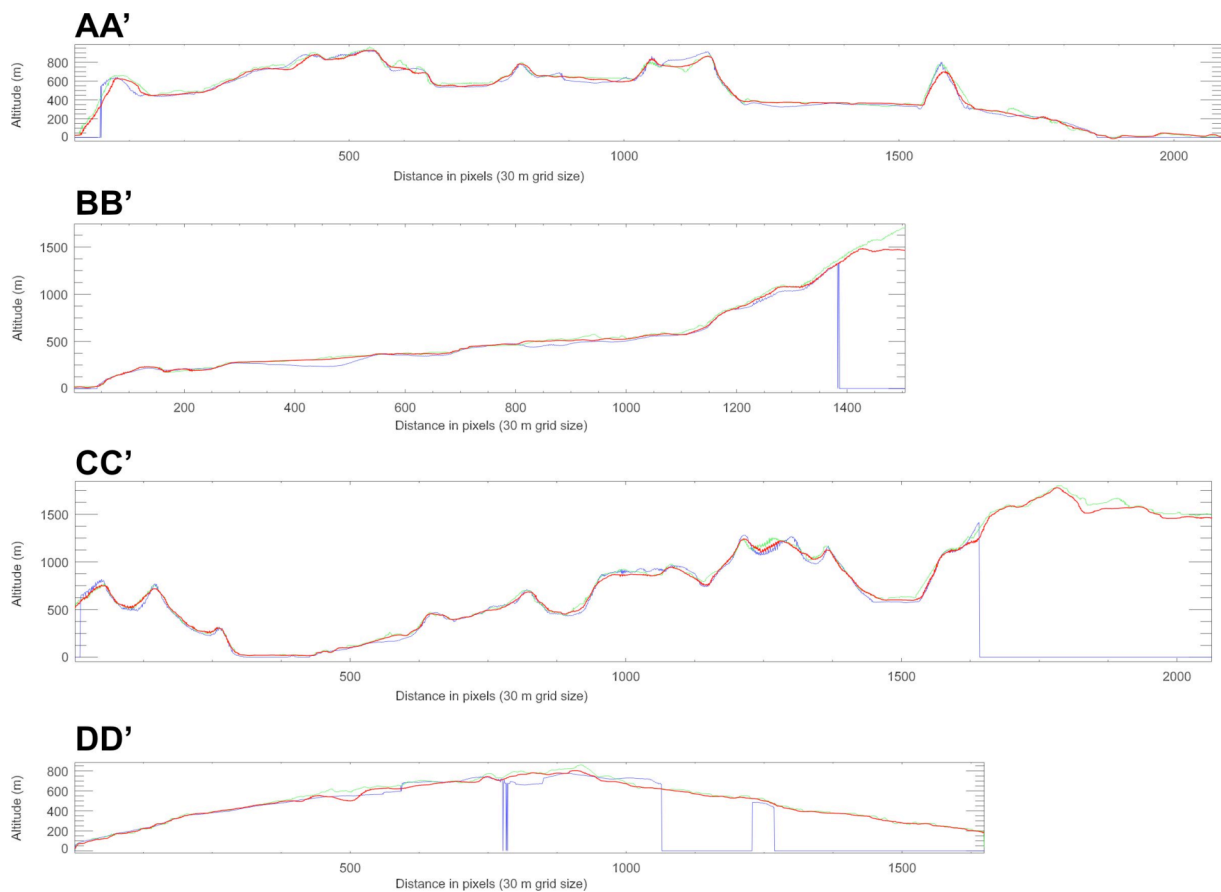


Figure 4.17: Comparison of the Multi-temporal Median model (MT-MED) against other hypsometric profiles. Curves are taken from the ASTER derived MED-MED model (green), TUD-DTM (blue) and the ASTER derived MT-MED model (red). Vertical exaggeration of all profiles by factor 5.

AA': Profile Northwest - Southeast crossing the glaciers

BB': Northeast Glacier - Sodabread Slope - Plateau

CC': Millerand Island - Butson Ridge - Blow Me Down Bluff - Plateau

DD': McClary Glacier - Swithinbank Glacier

The comparison of shapes and altitudes within these profiles gives us the following information:

In general along the four profiles the best agreement with the reference TUD model is provided by the MT-MED model. Once again this confirms the high degree of correspondence between the ASTER derived DEMs with the reference model. Shapes are preserved and altitudes are equivalent. But the MT-MED model shows clear improvements compared with altitudes represented in the MED-MED model. This better performance is evident in segments where the MED-MED model exhibits departures from the TUD model caused by artefacts which are eliminated in the MT-MED process.

Particularly, the altitude differences between TUD and the MT-MED model are few and smaller compared to those between TUD the MED-MED model. Maximum values for this variation are up to ca. ± 100 meters. Nevertheless, sectors where agreement continues being poor can be identified and in some specific segments deviations from TUD has even worsened.

To inspect these issues with more detail we present now a number of examples to discuss advantages and disadvantages introduced by the MT-MED model:

- First, in Figures 4.18a-d we show examples for advantages of the MT-MED model in more detail.
- Afterwards, in Figures 4.19a-c we show and discuss the different types of error-prone situations.

Figure 4.18a shows a more detailed close-up with the location of the ice divide of McClary Glacier on the profile DD'. In red the MT-MED shows a more reliable surface. This assumption is supported by: (a) it smoothes the artefacts of the MED-MED model (green), and (b) averages the ca. 60 m step-like discontinuities (close to pixels 590 and 850) and no-data voids in the TUD reference model (blue) (around pixel 780, pixels 1060-1225, 1270-). It must be noted that the TUD step-like discontinuities are neither detected on the TUD Photo Map (TUD Karte) nor on several ASTER scenes inspected. This suggests that these discontinuities are artefacts.

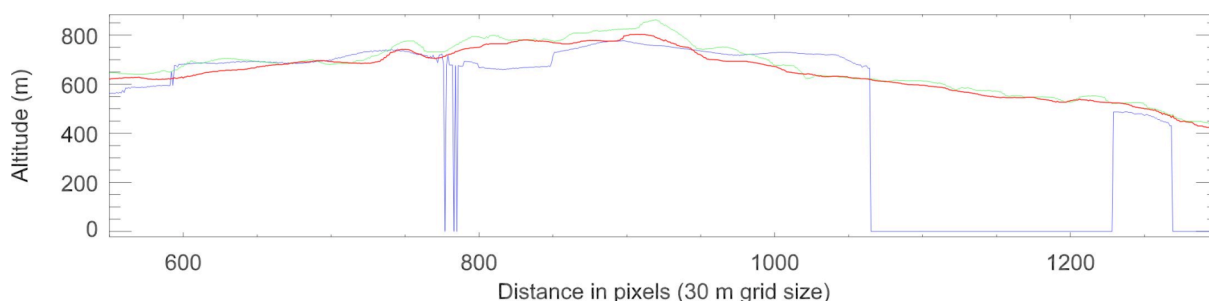


Figure 4.18a: Ice divide of McClary Glacier (see Profile DD'). Best representation is provided in the MT-MED model (red), better than in MED-MED model (green) and better than TUD-DTM (blue). Vertical exaggeration by factor 5.

The improved capability of MT-MED to suppress artefacts present in the MED-MED model is confirmed at several locations shown in Figure 4.18b (close to pixel 600, around pixels 1050, 1110 and 1220). A positive effect of the median filtering is observed on the north flank and cross section of the Todd Glacier surface (pixels 640-770). There the difference between the MT-MED and the TUD reference model is less than 20 m. Surprisingly, the MT-MED model seems to better represent the cross section of the Northeast Glacier by a slight constant inclination.

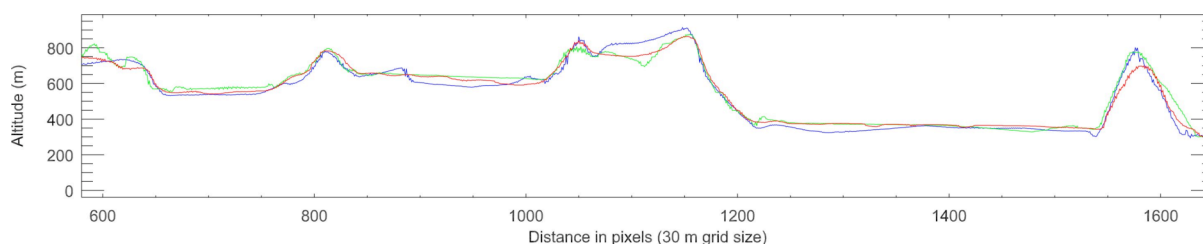


Figure 4.18b: Cross sections NW-SE over three glaciers (Todd Glacier, McClary Glacier and Northeast Glacier; section of Profile AA'): The profile of the MT-MED model (red) shows very well the main transversal inclination of the surfaces, while suppresses some specific features visible in the MED-MED (green) and TUD (blue) models, which probably may be artefacts. Vertical exaggeration by factor 5.

A good agreement between the three models can be seen along almost the entire profile BB' presented in the Figure 4.18c. The notable differences in two portions of the longitudinal section of the Northeast glacier might be caused by temporal changes in the glacier surface. TUD model is based on aerial photographs taken in February 1989, and ASTER scenes used to derive MT-MED were acquired between 11-16 years later, most of them during spring season.

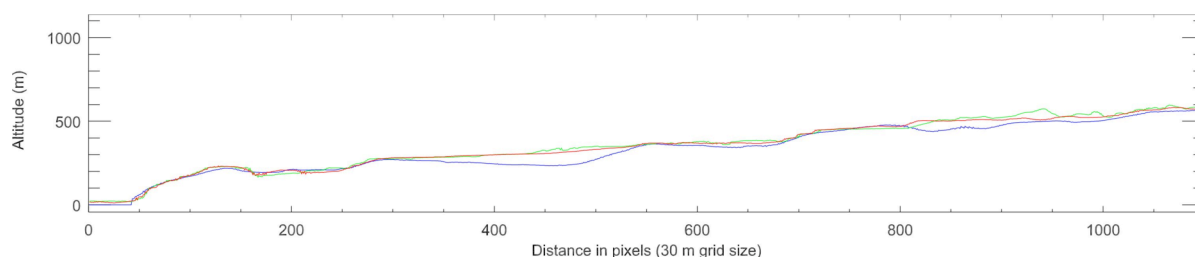


Figure 4.18c: Down-slope profile of the Northeast Glacier (section of Profile BB'). The surface given by the MT-MED model (red) matches quite well the inclination represented by the TUD model (blue) in different parts of the glacier, while avoiding some artefacts represented by the MED-MED model (green). The relative low altitudes of the TUD model within pixels 325-540 and 800-900, might be explained as effects of temporal changes of the surface altitude or as artefacts in the TUD model. Vertical exaggeration by factor 5.

The capability of ASTER scenes to model with acceptable accuracy small topographic features is demonstrated by the example shown in Figure 4.18d. In general both ASTER derived models (MED-MED and MT-MED) are able to provide a conformal representation of the rising ramp and the flat step as it is found in the sector of Sodabread Slope (see also Figure 4.12). Altitudinal differences with respect to the TUD model are located only in one section of the profile (pixels 1210 – 1325).

They are in the range of one or two decameters and likely can be explained as result of changes in the ice thickness.

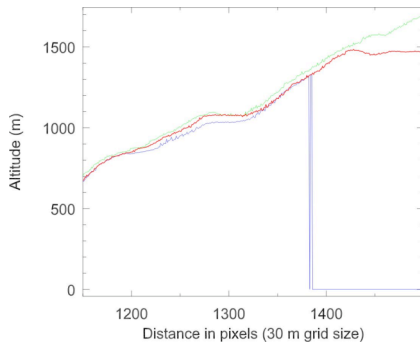


Figure 4.18d: Moraine ramp between head of Northeast Glacier and Plateau of the Antarctic Peninsula (the so-called Sodabread Slope; section of Profile BB'; see figure 4.12). The profile given by the MT-MED model (red) matches well the surface in different parts of this ramp. The ongoing rise of the MED-MED model (green), on the right end of the profile, might be an artefact of the source scene, which is eliminated by the multi-temporal approach used to create the MT-MED model.

The plot also shows in the section where TUD features missing data that the MT-MED model is able to correct artefacts present in the MED-MED model. Artefact generation at the right end of the MED-MED model (pixels 1420 -) can be attributed to the source scene used with the MED-MED generation. The scene shows on this section a combination of shadows and bright spots due to irregular ice features. However, the median filtering process used to derive the MT-MED model provides a more reliable topography given by the median altitude of the available DEMs. The MT-MED model represents this segment more in agreement with the known shape of this part of the central plateau of Antarctic Peninsula.

The previous remarks were centered on the advantageous aspects of the MT-MED model surface. Nevertheless, there exist problems not yet solved for the evaluation of the resulting MT-MED model surface. The following examples shown in Figures 4.19a-c correspond to three types of potential sources of errors. They have an impact on the accuracy assessment of the ASTER derived DEMs.

Figure 4.19a reports the effect of a weak or imprecise registration of some of the data sets used to derive the multi-temporal median DEM. When the median altitude in the layer stack is extracted from a group of DEMs that had a poor or miss-registration the resulting multitemporal median DEM will be impacted in these areas for corresponding errors. This situation can be observed on the two segments of MT-MED extracted from profile AA' compared with the TUD model: left box exhibits a southeast displacement of the MT-MED model (around pixels 100 and 400), whereas right box exhibits a good agreement on both slopes of Butson Ridge but a clear deviation on top of the ridge.

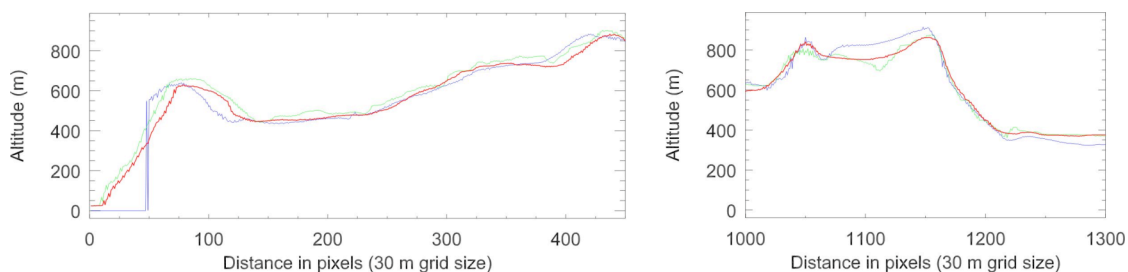


Figure 4.19a: Problems detected in the different models: Weak co-registration between the TUD model and both MED-MED and MT-MED ASTER derived models. Displacement of surfaces is visible in sections of profile AA' which cross ridges in the North-South direction. Vertical exaggeration by factor 5.

The case where the number of available scenes suffer from biasing is exemplified by Figure 4.19b. When more than 50% of the DEMs have a bias in the same direction the resulting filtered altitude will be chosen from this group, and consequently the estimated elevation will be biased. This situation can be ambiguous and wrongly evaluated in cases where the compared glacier surfaces are affected by seasonal or temporal ice thickness changes. The left plot might represent this situation whereas the undulating surface of the right plot likely is a biased determination of MT-MED altitudes.



Figure 4.19b: Problems detected in the different models: Impact of artefacts within the available number of ASTER scenes. Undulations are noted if more than 50% of the surfaces used to create the MT-MED model have an artefact in the same direction. Left figure section of profile CC', right figure section of profile DD'. Vertical exaggeration by factor 5.

Finally, the lack of data and suspicious or clearly wrong altitudes of the reference TUD model must be considered as a source of uncertainty when evaluating the quality of the ASTER derived DEMs. This situation can be observed in Figure 4.19c. The left plot shows suspicious altitude values (ca. pixels 590 and 850) and lack of data (around pixel 780) that made TUD surface in this section unreliable. Noise on the TUD model section surface shown in the right plot are associated to a difficult image matching in this section. It is interesting to note that the zone crossed by the profile segment between pixels 1200 and 1350, presents problems for all the three models. Inspection of the orthorectified ASTER scene indicates though that the MT-MED represents this segment best.

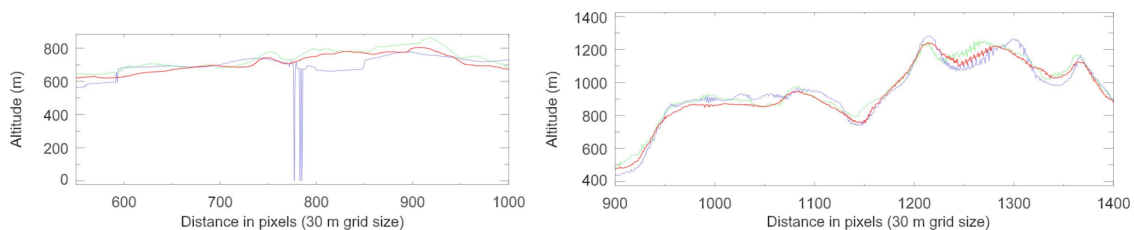


Figure 4.19c: Problems detected in the different models: Uncertainties in the TUD reference model due to artefacts (holes and some noise). Left figure section of profile DD', right figure section of profile CC'. Vertical exaggeration by factor 5.

Again the visual analysis has proven to be a valid technique to inspect in detail the ASTER derived DEMs and to achieve a semi-quantitative evaluation. The performance of the MT-MED model was examined closely and pros and contras studied. It could be shown clearly that MT-MED is superior to the MED-MED derived model. Also, the comparison of the MT-MED model with the TUD reference model has been satisfactory reporting an excellent agreement with differences of ca. ± 10 m to ± 20 m. Few extreme deviations which are in the range of ± 100 m, a very conservative value considering the relative nature of our ASTER derived DEMs, were detected and the potential reasons commented.

We can conclude that our ASTER derived multi-temporal median model (MT-MED) approach provides an acceptable representation of the Marguerite Bay test site topography. This confirms also that the MT-MED processing schema offers the best result compared to the single scene derivation alternative.

Still the quality assessment was carried out along profiles representative of the relief and the error for the whole model is still unknown. Additionally, a numerical comparison of the differences between the MT-MED model and TUD is required to estimate the MT-MED model error. This will be completed in the next section.

4.5 Statistical Comparison of ASTER Derived DEMs, RAMP and the TUD Reference Model

Until now we have evaluated the similarity of two kind of ASTER derived DEMs with respect to the TUD reference model. This has been done based mainly on the visual comparison of the corresponding surfaces. The methodology used included the inspection of 2D images (i.e. DEMs, artificially illuminated DEMs and ASTER scenes), as well as the interactive manipulation of 3-dimensional models draped with images (e.g. shaded relief and orthorectified images). Additionally, this visual assessment was complemented with the analysis of four profiles crossing the Marguerite Bay test site with a total length of approximately 130 km. The profiles traverse representative surface terrain including problematic areas and relief features. They were analysed to obtain a semi-quantitative evaluation on the accuracy of both the MED-MED and the MT-MED models.

The results from the profile assessment suggest that the derived DEMs provide an acceptable representation of the surface despite the difficult topography and glaciated surface of the Antarctic Peninsula. Moreover, both models present a better agreement with TUD reference model than the RAMP model does. The improved quality together with the enhanced spatial resolution (30 m vs. 200m) support the claim about their superior quality compared to the currently available RAMP data set. The analysis showed that the MT-MED model, derived under a multi-temporal approach, is the closest to the TUD reference surface. However, both derived models show that along the profiles altitude errors remain. This raises the question on the overall estimation of the error magnitude and how these are distributed over the test site.

Errors are inherent to any measurement. TAYLOR (1997) wrote that "the best you can hope to do is ensure that errors are as small as reasonably possible and to have a reliable estimate of how large they are". For this reason we focus in this section on the description of the errors of the ASTER derived models in the form of an accuracy assessment. We will compare altitudes of each model with the TUD reference model, pixel by pixel. This allows to obtain corresponding altitude deviation maps and the numerical characterization of their errors.

The standard RAMP model is also considered in this evaluation to have an alternative element of comparison and to know the magnitude and spatial distribution of its error in this area.

RAMP and the ASTER derived models were each subtracted from the TUD reference model. Using ENVI v4.2 software map algebra operations (i.e. subtraction and masking) were applied to generate three altitude deviation maps. The resulting

maps and a figure depicting the location of the four profile sections are shown in Figure 4.20. A blue-red bi-polar colour schema is used to represent the magnitude and the sign of the altitude deviation values. Blue colours represent an elevation of ASTER or RAMP models higher than corresponding TUD elevation; red colours represent an elevation of ASTER or RAMP models lower than corresponding TUD elevation. White colour represents an altitude deviation less than 10 m (Figure 4.20).

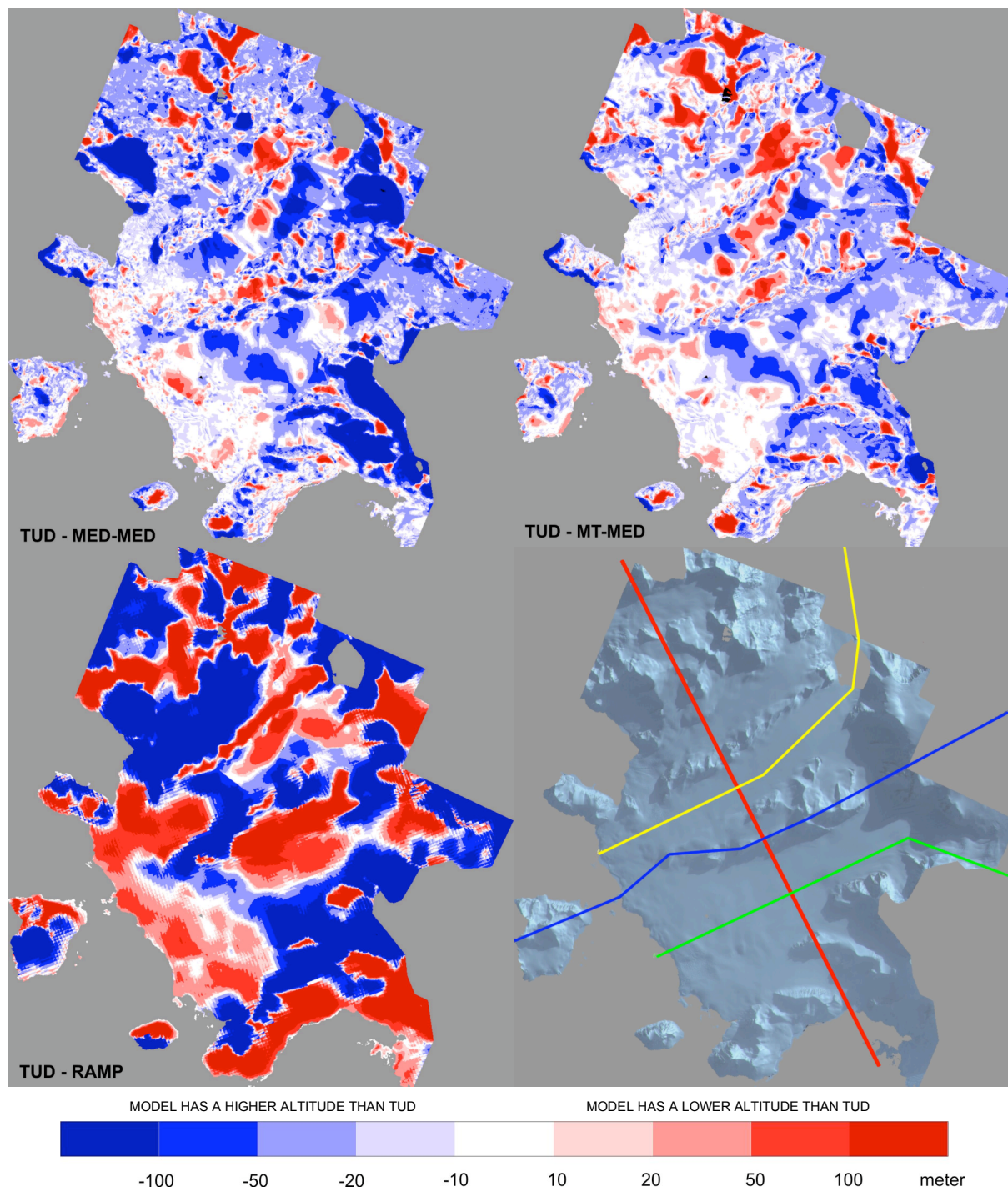


Figure 4.20: Altitude deviations between TUD reference model vs. ASTER derived models and RAMP DEM.

Upper left panel : MED-MED model

Upper right panel : MT-MED model

Lower left panel : RAMP

Lower right panel: Orthorectified ASTER scene with profile lines used in sections 4.3 and 4.4.

We observe in each map the following magnitudes and distribution characteristics associated with the altitude deviations from the TUD reference model:

TUD – RAMP

A gross homogeneous pattern is present in this map. It is composed by large patches of predominant deviations larger than 100 m (dark-blue and dark-red colours), filled in between by reduced zones of deviations between 100 m and 10 m (light-blue or light-red colours). Only a few small fringes show deviations lower than 10 m (white sectors). This represents a panorama with widespread areas of strong positive and negative altitude deviations. This situation is in agreement with the analysis of the profile sections in chapter 4.3.2 as is shown in Figure 4.13.

Examining the TUD-RAMP map it is clear the higher frequency of gross errors and how the error distributed over the test site. The gross errors can be attributed to the scale and accuracy of the RAMP model already mentioned in section 2.3 and section 4.3.2.

TUD – MED-MED

This map shows a more granulated pattern. It consists of considerably more extended patches with altitude deviations less than 10 m (white colour) and altitude deviations between -50 m and -10 m (light-blue colour). These are located specifically in the lower parts of the glaciers, showing in these areas a good agreement between TUD and the MED-MED model. Negative altitude deviation (blue colours) is the dominant trend, showing the areas where MED-MED elevations are higher.

This suggests that the mean elevation in the MED-MED model is higher than in the TUD reference model. Moderate large patches with negative altitude deviations more than 100 m (dark-blue colour) are located in areas under shadows and in sectors associated with artefacts in the MED-MED model. These artefacts, as we can see in the profiles of Figure 4.13, are mostly pixel blunders with overestimated altitudes. Some relatively small zones of positive deviations more than 100 m (dark-red colour) can be found, too. These are mainly distributed over nearly flat terrain on the northern part of the test site. Some are also localized on the summits of Neny Island and Roman Four Promontory.

TUD – MT-MED

Here a fine granulated pattern is distributed widespread, showing a majority of patches with altitude deviations less than 10 m (white colour) and negative altitude deviations between -50 m and -10 m (light-blue colour). Altitude differences smaller than ± 10 m are distributed extensively but concentrated mainly in low altitude elevation areas. Apart from sectors with small errors the general distribution shows that negative (blue colour) and positive (red colour) altitude deviations are more or less balanced. This suggests that both models have approximately the same mean altitude. Patches with positive altitude deviations between 10 m and 50 m (light-red colour) are more frequent here than in the MED-MED model. This can be a consequence of the reduction of patches with strong negative deviations present in shadowed areas of the MED-MED altitude deviation map by the removal of artefacts through the multi-temporal (MT-MED) processing. Altitude deviations greater than 50

m (dark-red colour) are located in some areas of high altitude, strong relief and bright north facing slopes. These cases might be associated with horizontal displacements due to small errors of model co-registration. Areas where negative strong deviations (dark blue colour) swap immediately to strong positive deviations (dark-red colour) indicate that these areas are to be considered critical parts of the TUD model. Such areas are mainly located on glaciers. This shows clearly that the TUD model is not free from artefacts, too (see profile CC' in Figure 4.19c).

Comparing the three altitude deviations maps we can observe on the MT-MED the preponderance of altitude differences less than 20 m. In this range the distribution of errors is more concentrated and they are smaller than as is the case with the MED-MED map. Accordingly, the MT-MED model shows the best matching with the reference TUD model. This indicates that the best accuracy with ASTER DEMs can be achieved by the multi-temporal approach versus the alternative single scene schema.

To confirm this hypothesis by means of accuracy statistical parameters we compare quantitatively the altitudes of the model under consideration with the altitudes of our TUD reference model. We do this pixel by pixel without referring to the geographical position of the pixel; that means without considering the spatial distribution of the values. Generally we build the differences surface between the model under consideration and the TUD model as is presented in the maps of figure 4.20.

Then we describe the distribution of this population of differences with instruments of one-dimensional statistics, that is, by frequency curves as well as by the basic parameters which are minimum, maximum, mean, standard deviation, percentiles and class frequencies.

A specific and frequently used descriptor to quantify the adjustment of a DEM to a reference surface is RMSE, the root mean square error (WOOD, 1996; WECHSLER, 2000; KÄÄB, 2005). It is a dispersion measure, being approximately equivalent to the average (absolute) deviation between two data sets. A large value for the RMSE involves a bigger difference of the same elevation between two data sets. Its widespread use can be attributed to the relative ease of calculation and reporting (usually a single figure) and the ease with which the concept can be understood by most users of elevation data (WOOD, 1996).

The root mean square error is expressed as:

$$RMSE = \sqrt{\frac{1}{n} \sum_i^n (x_i - a_i)^2}$$

where a_i is the accepted elevation value at that location in the reference model, x_i is the model's elevation for the same pixel and n is the number of pixels used to compare the sample. Since $(x_i - a_i)$, as the local vertical distances between the model and the reference surface, are equal to the deviations d_i of our differences surface, the RMSE value is the nearer to the standard deviation of this dataset the closer its mean is to zero.

A set of corresponding accuracy measurement values given by the non-spatial statistical parameters associated to the distribution of deviations TUD against RAMP, TUD against MED-MED, and TUD against MT-MED, is presented in Tables 4.5, 4.6 and 4.7.

If we analyse this material we can state:

Frequency curves of Figure 4.21 confirm the general findings extracted from the map of deviations presented in Figure 4.20.

Looking at the figures in Tables 4.5 and 4.6, we have to understand the values for the mean parameter represented in Table 4.5. Why are they not equal to zero? In comparison with the TUD model the average altitude is overestimated in RAMP by 25.4 m, in MED-MED by 32.1 m and in MT-MED by 8.5 m.

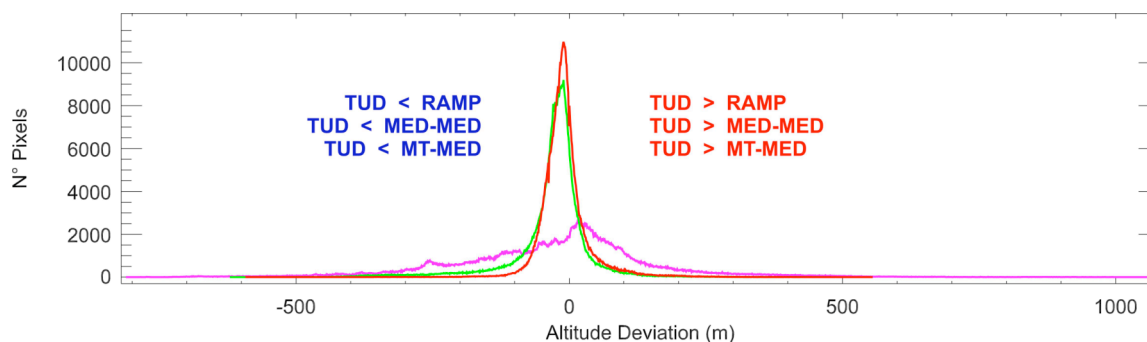


Figure 4.21: Frequency curves of altitude deviations between different elevation models.

MAGENTA: TUD - RAMP GREEN: TUD - MED-MED RED: TUD - MT-MED

Table 4.5: Basic statistics parameters of altitude deviations between different elevation models (TUD - RAMP, TUD - MED-MED and TUD - MT-MED): Sample size, Minimum (Min), Maximum (Max), Arithmetic Mean (Mean), Standard Deviation(Stdev) and Root Mean Square (RMS) error.

	Pixels	Min (m)	Max (m)	Mean (m)	Stdev (m)	RMS (m)
TUD - RAMP	622345	-812	1069	-25.4	179.3	181.1
TUD - MED-MED	622345	-621	479	-32.1	72.8	79.6
TUD - MT-MED	622345	-593	555	-8.5	46.8	47.5

The properties and vertical accuracy of the RAMP data set are already known from previous sections (see section 2.3). Investigation of the RAMP altitude deviation from the TUD model shows that the RAMP accuracy in the test site area is less than the general values reported for the whole RAMP data set.

This is not only confirmed by the magnitude and distribution of the errors along the different types of relief as is observed in Figure 4.20. Together with a relative low value obtained for the mean altitude difference (-25.4 m), the RAMP model also has relatively high values for its standard deviation and RMS error.

The analysis of both ASTER derived models yields contrasting results. The MED-MED model shows a 6.7 m larger deviation than the RAMP mean altitude error. Nevertheless, in despite of this situation, MED-MED exhibits a better accuracy than RAMP. This is supported by a more than two times lower standard deviation value (72.8), and also a smaller RMS error (79.6 m). Considering these values the resulting accuracy of MED-MED model is clearly better. This is confirmed by the corresponding map in Figure 4.20. However, the most likely reason that explains the

still relatively high values is associated to the presence of artefacts not reduced by the median filtering process used to derive MED-MED.

The analysis of the error associated to the MT-MED model shows the best results. It has the smallest statistical parameter values of the three models compared. The relatively small mean altitude deviation value (-8.5 m) and its corresponding moderate low standard deviation (46.8 m) and RMS error (47.5) verify the best matching with the TUD model. This is also confirmed in the associated map of altitude deviations (Figure 4.20). Given the widespread errors of low magnitude the deviations of larger magnitude only have a strong impact on specific sectors. The better performance can be associated to the capacity of the multi-temporal approach to better suppress artefacts .

The accuracy obtained by each model is also described by the number of pixels included in the middle part of the curves of frequency depicted in Figure 4.21. This information is aggregated in classes in Table 4.6 representing the altitude deviations between TUD and the different models. The greyed out central rows show the relative percentages with lower error.

Table 4.6: Distribution of altitude deviations between different elevation models (TUD – RAMP, TUD - MED-MED and TUD - MT-MED): Absolute and relative frequencies in classes used in Figure 4.20. Greyed rows represent high accuracy classes.

Altitude Ranges m	TUD - RAMP		TUD - MED-MED		TUD - MT-MED	
	Pixels	%	Pixels	%	Pixels	%
-800 -- -100	178896	28.7	58645	9.4	7016	1.1
-100 -- -50	61474	9.9	78595	12.6	51427	8.3
-50 -- -20	48063	7.7	179356	28.8	173244	27.8
-20 -- -10	16116	2.6	87901	14.1	100601	16.2
-10 -- 10	40177	6.5	123960	19.9	161628	26.0
10 -- 20	25242	4.1	28907	4.6	36700	5.9
20 -- 50	68084	10.9	35365	5.7	48472	7.8
50 -- 100	77576	12.5	18513	3.0	26163	4.2
> 100	106715	17.1	10862	1.7	16934	2.7

In accordance with previous findings the analysis of these statistical parameters shows that the accuracy of each model varies.

The quantification of the more extended distribution of higher altitude deviations present in the RAMP model, reveals its poor accuracy with respect to the TUD model. 68.2% of pixels have an error greater than 50 m and only the 13.2% of pixels have an error less than 20 m.

The MED-MED model exhibits an improvement to RAMP. It has 38.6% of the pixels concentrated in the class of altitude deviations less than 20 m. That is almost three times better than the RAMP accuracy. The number of pixels with an error greater than 50 m is consistently small, representing only 26.7% of the pixels.

The evaluation of the MT-MED model display the best results. 48.1% of pixels have differences of altitude with respect to the TUD reference model less than 20 m. From this set 26% of the pixels correspond to the class of deviations better than 10 m. Consequently the MT-MED model can be considered the best independent model

available. The better accuracy is the result of the enhanced processing used to derive MT-MED.

The percentiles presented in Table 4.7 also show the increasing accuracy between RAMP, MED-MED and MT-MED models.

Table 4.7: Distribution of altitude deviations between three different elevation models (TUD – RAMP, TUD - MED-MED and TUD - MT-MED): Median (P50), Quartiles (P25, P50, P75) and selected Deciles (P10, P40, P60, P90).

Percentil	P10	P25	P40	P50	P60	P75	P90
TUD - RAMP	-257.0	-127.6	-52.2	-13.6	+14.1	+58.8	+153.8
TUD - MED-MED	-100.1	-49.3	-32.9	-25.0	-17.9	-6.6	+17.0
TUD - MT-MED	-53.5	-34.5	-22.8	-16.6	-10.7	+0.6	+29.5

The percentiles also provide an quantitative answer to the question how the improvements of MT-MED against MED-MED can be measured. The results show that the smaller range of errors on different levels (20%: 15.0 m to 12.1 m; 50%: 42.7 m to 35.1 m; 80%: 117 m to 83.0 m) is a remarkable improvement.

The span of the inner 20% of differences against TUD changes from 66.3 m (-52.2/+14.1) over 15.0 m (-32.9/-17.9) to 12.1 m (-22.8/-10.7); the span of the inner 50% changes from 186.4 m (-127.6/+58.8) over 42.7 m (-49.3/-6.6) to 35.1 m (-34.5/+0.6); and the span of the inner 80% changes from 410.8 m (-257.0/+153.8) over 117.1 m (-100.1/+17.0) to 83.0 m (-53.5/+29.5).

Additionally the percentiles show the general shift to higher altitudes from the MT-MED to the MED-MED model and the specific role of remaining artefacts in the MED-MED model indicated by the different deviations against TUD.

We see the following shift amounts:

P90 = 12,5 m (+17,0/+29,5)	P75 = 7,2 m (-6,6/ +0,6)	P60 = 7,2 m (-17,9/ -10,7)
P50 = 8,4 m (-25,0/ -16,6)	P40 = 10,1 m (-32,9/ -22,8)	P25 = 14,8 m (-49,3/ -34,5)
P10 = 46,6 m (-100,1/-53,5)		

These values express that MED-MED compared with MT-MED generally features a stronger overestimation of altitudes of about 10 m. Since the models are relative, produced without reference to prefixed altitudes this is not a surprise. But on the tail of the 10 percent of pixels with highest overestimation against TUD this overestimation in the MED-MED model is much higher than in the MT-MED model: an additional quantitative measure for the influence of the gross artefacts forming peaks in the DEM.

Concluding section 4.4 we can state the following findings:

DEM and Photo Map of the Technical University of Darmstadt (TUD-DTM and TUD-Karte) are not totally free from errors but provide the best available photogrammetric documentation of a characteristic glacier dominated region on the Antarctic Peninsula. The TUD products can serve as reference for all satellite derived DEMs of the same region and as the base for studying the accuracy of RAMP and ASTER derived DEMs.

The digital elevation model derived within the Radar Antarctic Mapping Project (RAMP) does not provide the accuracy which is necessary for quality tests of ASTER derived DEMs. This is due to the data sources compilation and the scale of the RAMP DEM. The accuracy parameters of the RAMP model which we found in our test site are less acceptable than those reported in the literature (LIU ET AL. 1999, BAMBER ET AL., 2005).

The accuracy parameters of our ASTER derived digital elevation models based on the double median filtering scheme (MED-MED) and on the multi-temporal median scheme (MT-MED) are higher than reported in the literature. The double Median filter, incorporating spatial median and multi-process median, widely achieves the suppression of artefacts of a single scene. The multi-temporal median (MT-MED) uses for each point the altitude values which are not affected by artefacts.

All the material presented, such as profiles, error maps, statistical parameters including the root mean square error (RMSE) shows that models derived by the MT-MED approach have the highest accuracy. Notably, this result is achieved without the use of pre-fixed altitudes given by ground control points.

5 Drainage Basins Delineation

5.1 From DEM to catchment extraction

Many sub-disciplines of geosciences deal with fluxes on the Earth surface. Gravity driven fluxes of water, air and ice play an important role in climatology, hydrology and glaciology as well as in physical geography and landscape ecology. All these fluxes can be understood only if we organize our model of the landscape in well defined units which sample the flowing agent and have a common outflow, the so called catchment areas, or if we look on the moving medium, the flow units. HARDY ET AL. (2000) write: "In order to allow a better understanding of nature and spatial pattern of any observed imbalance, it is needed to examine each flow unit independently". Clearly, this is also true in large scale mass balance studies where an estimate of the catchment area or drainage basin for a particular glacier is required (BAMBER ET AL., 2005; WUNDERLE & SCHMIDT, 1997).

The broadest development and use of catchment analysis we find in the hydrology literature where catchment is a central term in many hydrological studies. Climatology has also demonstrated the need to study processes in single catchment areas, especially in its meso- and microscale aspects. Studies of local diurnal wind systems are an example where catchment analysis plays a pre-eminent role (e.g. SCHWAB, 2000). Surveying such work we find many methods of upscaling and downscaling, as well as up stepping (e.g. from a river mouth) or down stepping (e.g. from crests and upper slopes) procedures. All such studies are based in hydrological thinking.

Similar approaches can be found in the delineation of ice drainage basins on Antarctica's and Greenland's ice-sheets as shown in section 2.3 (Figures 2.4a-b, 2.6, 2.7, 2.8, 2.9 and Table 2.1). In most of these works delineation of ice divides is based on visual interpretation and done manually (GIOVINETTO, 1964; RABASSA ET AL., 1983; GIOVINETTO AND BENTLEY, 1985; WILLIAMS ET AL., 1989; SIMOES ET AL., 1999; BRAUN ET AL., 2001; BREMER ET AL., 2004; AHLERT, 2005).

We learn from this work that a manual method for the ice catchment delineation has to incorporate a modification from the conventional scheme used in hydrology to delineate watersheds. In most cases the ice flow is following the slope inclination by gravity action. But the glacial catchments do not always consist of a defined network

of channels as happens in hydrological catchments. Glacier basins assembled together connect with each other on ice divides where ice masses coalesce or contribute, having limits defined by marked changes of gradient and divergent ice flow movement. However, the most important consideration is that ice catchments do not pour for a well defined point or at least a reduced cross section such as a river mouth. In the Antarctic Peninsula most of the ice catchments end at sea along an almost continuous ice cliff.

Consequently, the manual delineation requires at least a topographic map to trace the ice divides following the ridgelines position. Additional terrain information such as stereoscopically viewed aerial photographs, remotely sensed optical data or a DEM, will facilitate the tedious task of synthesizing the boundaries in this analogue way. Examples of such applications at smaller scale are the delineation of the most probable catchment boundary in the ice-streams feeding Ross Ice Shelf, using velocity vectors and a set of derived flow lines based on interpolation of field data (PRICE & WHILLANS, 1998). Another example of such a delineation of ice divides and drainage basins based on the interpretation of remotely sensed data (Landsat, KFA-1000 and ERS-1 SAR) is given in DOWDESWELL ET AL. (1995) for the high Arctic.

Only few approaches of digital delineations of catchments and ice divides in Antarctica are reported in the literature. Some results of these studies are shown in section 2.3 (Figure 2.4c-d, Figure 2.5a-b, Table 2.1), related to the authors LIU (1999), VAUGHAN ET AL. (1999) and LANG (2002). All these works were done at continental scale and are not easily usable for regional studies of glacier behaviour.

Therefore, we agree with WEIDICK & MORRIS (1998) when they stress that in the Antarctic Peninsula further work must be done to establish mass-balance curves for the region and for “that the primary need is for mapping on a sufficiently detailed scale to resolve the form of local glaciers and enable a more precise estimate of their area to be made”.

Now the DEMs based on ASTER stereo data offer a new possibility to achieve this goal. The work of KÄÄB (2005) AND PAUL ET AL. (2004) for test sites in the Alps shows first steps in this direction.

Using our MT-MED digital elevation model of the Marguerite Bay test site we will now study how a semi-automatic catchment extraction method can be applied to the glacier systems of Antarctic Peninsula. This semi-automatic approach allows to generate reliable results whilst minimizing the processing time.

5.2 Algorithm and workflow

Our approach to derive ice catchments is based in the use of a modified cell-based hydrologic catchment model proposed by O'CALLAGHAN & MARK (1984). This approach is still a common choice for the determination of drainage networks from digital elevation models and for their subsequent use to derive corresponding basins. Other alternative schemes as the TIN approach proposed by JONES ET AL. (1990) and NELSON ET AL. (1994), or contour-line based approach as favoured by MOORE & GRAYSON (1991) have been discarded. Generally, these algorithms have not become widespread because in spite of their complexity they often do not provide appropriate results.

The *Deterministic 8* method (D8, O'CALLAGHAN ET AL., 1984) is based on a raster DEM. It defines in each step altitude differences or gradients between the pixel under consideration and its 8 immediate neighbours. This approach is the common characteristic of flow accumulation models, which by this way determine the catchment area considering each cell of the DEM.

According to FAIRFIELD & LEYMARIE (1991), the D8 approach has disadvantages because the flow is separated into only one of eight possible directions resolving it to coarsely.

Nevertheless, TARBOTON (1997) stated that this discretization of the flow in 45° minimizes the flow dispersion in D8; adding that is a robust method with the ability to cope with difficult data (i.e. saddles, pits and flat areas). It can also be implemented numerically with simple and efficient algorithms. When comparing D8 with to other methods, he found no differences for large specific catchment areas and for small ones differences with the best evaluated method where not substantial (specific catchment area is small in hill-slopes and large in valleys). Consequently, the application of D8 is considered to be adequate for our purpose of delineating ice basins composed of mainly glacier valleys with dimension of several km of extension.

Hydrological models require a so-called hydrological correct DEM. This means that starting out from any cell and following the largest slope gradient we can reach the edge of the DEM. Consequently it is not allowed that the DEM includes sinks. From the two methods known for creating hydrological correct DEMs, i.e. filling sinks or deepening drainage routes (HUTCHINSON, 1989), we choose the first. Especially if there are pits as remnants of artefacts, the filling of sinks procedure is the only possible handling of the problem.

When applying hydrological models we always work under the assumption that surface inclination and flow direction would correspond strongly. Since ice is not a real fluid, exceptions from this rule exist. These will not be covered by the model. Another specific problem of the hydrological model applied to ice is that we do not have a single outflow point as with rivers. Starting at the coast with an ice cliff the model has to create a series of “mini-basins”, which reach so far upward the glacier until one of them will be dominant. Often this requires a specific post-processing of the catchments. If this requirement is taken into account this approach provides for a reliable derivation of the basic information and results in raw basins that are not biased by operator intervention.

Keeping these aspects in mind a processing chain was built (Figure 5.1), which is able to produce in four steps a separation of the test site in different catchments based on our MT-MED model. It is based on ArcGIS software and incorporates processes executed with functions of its Spatial Analyst module. Two of these four steps are combined in an iterative routine in the beginning of the operation.

Consequently we see in Figure 5.1 three main sections:

- Filling pits and determination of flow directions

This is an iterative routine, organized as cycle of two major and some minor processes. These are: the determination of flow directions of the surface with the D8-calculus, the identification of closed depressions by searching pixels without outflow; calculating for each depression the depth between sink point and pouring point, and filling up all depressions to the level of the pouring point. As sinks are filled, others can be created at the boundaries of the filled areas,

which have to be removed in the next iteration. The function iterates until all sinks within the specified limit are filled and we have created a “depressionless DEM” together with its raster image of “flow directions”. The algorithm uses the ArcGIS routines FocalFlow, FlowDirection, Sink, Watershed and ZonalFill.

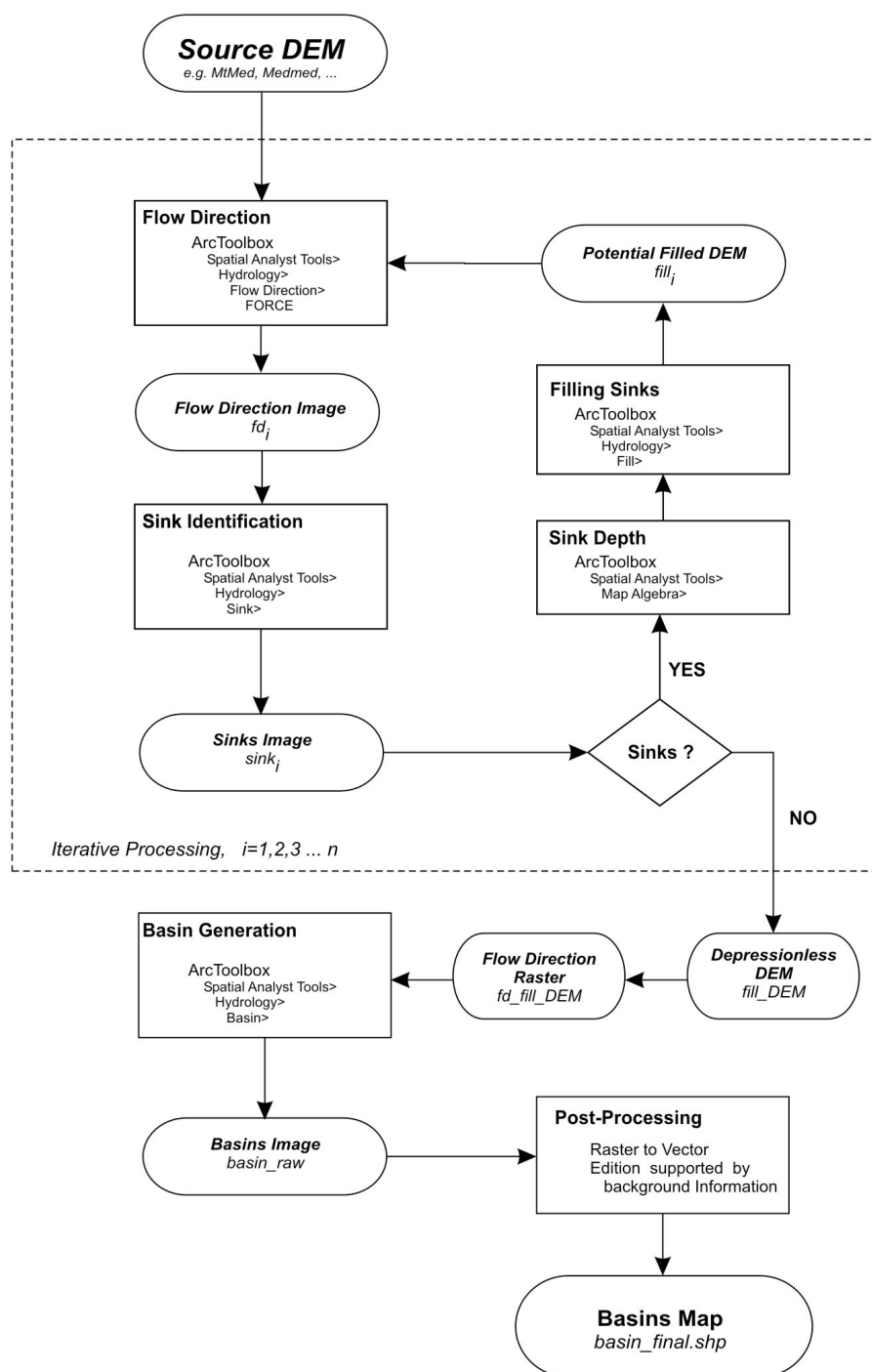


Figure 5.1: Flow diagram for the ArcGIS based method to derive glacier basins from large scale ASTER DEMs.

- **Basin Generation**

The Basin function delineates drainage basins within the analysis window by identifying ridge lines between basins. Basin analyzes the flow direction raster to find all sets of connected cells that belong to the same drainage basin. The drainage basins are created by locating the pour points at the edges of the analysis window (where water would pour out of the raster), as well as sinks, then identifying the contributing area above each pour point. A watershed is the upslope area contributing flow to a given location. Such an area may also be referred to as a basin, catchment, iceshed, or contributing area. A sub-watershed is simply part of a hierarchy implying that a given watershed is part of a larger watershed. Watersheds can be delineated from a DEM by computing the flow direction and using it in the Watershed function. The Watershed function uses a raster of flow directions to determine the contributing area. This results in a raster of drainage basins.

- **Post-processing**

Post-processing groups all activities aiming both at analyzing the raw basins data set and performing the aggregation of its corresponding polygons into meaningful ice catchments. This task is supported with the integration of all the additional topographic and remotely sensed data available. The work is performed using ENVI and ArcGIS software.

A three dimensional representation of the terrain is build with the digital elevation model that we used to derive the basins, over this an ASTER ortho-rectified image is draped. All the additional derived information, i.e. contour lines and raw basin polygons, are integrated over this representation. The interactive observation of the landscape with its associated data sets is produced by spatial manipulation using different oblique perspectives and by scaling the model. Thus, the integrated simultaneous visualization at a large scale of the raw basin boundaries in the context of the modelled relief, optimizes the process of evaluation and supports the decision about which adjacent polygons must be merged to produce the final ice catchment.

The validation of this methodology is presented in the following section as a case study carried out on our Marguerite Bay test site.

5.3 Results of derivation of ice catchments on Marguerite Bay test site.

This section provides details and discusses the outcomes collected during the application of the proposed methodology to derive ice catchments in the Marguerite Bay test site. We refer here to both the process of automatic basin extraction and to the subsequent integration of raw basins to find the boundaries of the main catchment of this area.

The first two components of our approach, that is the generation of the depressionless DEM and the automatic extraction of ice basins, were based in the use of the MT-MED model. Commands and functions of the ArcToolbox modules ArcGIS 9.0 environment have been used. After the second iteration of the processing

steps shown inside of the dotted rectangular box of Figure 5.1, we obtained a depressionless DEM. The processing warranted reliable results and permitted us to continue with the following step.

The process of automatic basin derivation produced a raster file with the full set of automatically generated raw basins. After a raster to vector conversion was applied and a corresponding raw basins shapefile created we were able to examine in detail the resulting polygons. These are depicted in the Figure 5.2.

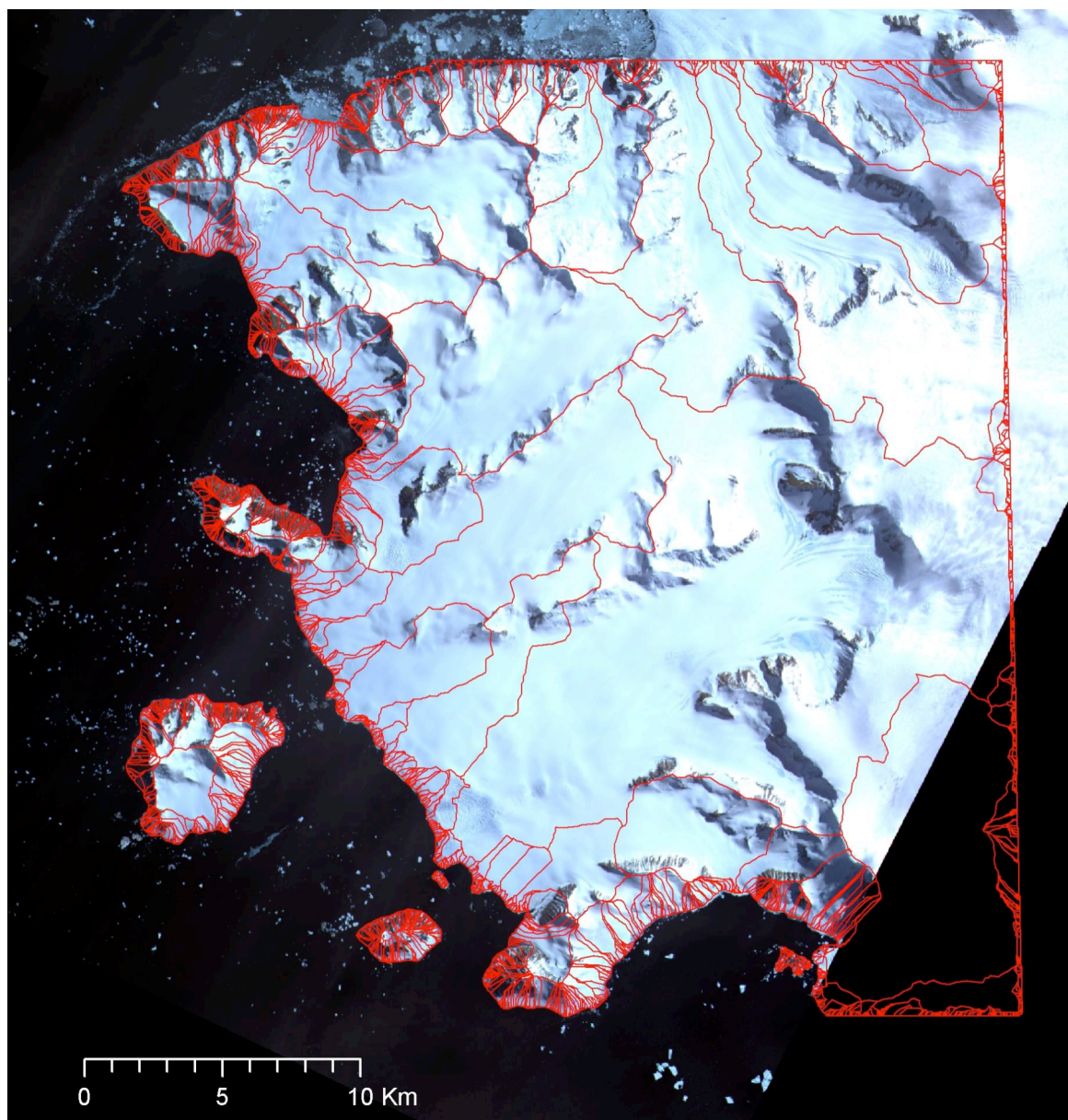


Figure 5.2: Raw results from the ArcGIS based catchment extraction method applied to MT-MED DEM. Crude basin polygons that need to be post-processed. The main limitation of the hydrological model used is reflected by spurious and irregular basins generated at the edges of the DEM and along the coastal ice front. Nevertheless, reasonable boundaries between the upper parts of the great glaciers are created, extracted automatically independent of any operator. To judge their reliability see figure 5.3.

Background: Ortho-rectified ASTER "L1B" mosaic (SC:AST_L1A.003:2004076906 & SC:AST_L1A.003:2004076911, acquired on 04.01.2001).

Red: Raw basin boundaries.

We see a considerable amount of “mini-basins” along the coast and along the DEM borders. These are the expected result of the application of the hydrologic model on glacier surfaces which do not feature a well defined pour point. In the upper parts of the glaciers we find clearly defined basins, partly separated by ridges but also by basin boundaries that cross snow and ice-fields. This answers one of the central questions of this work related to the ice divides: The method is suitable to define the culmination zones between the glacier basins.

The following manual post-processing consisted of two passes: the analysis of the raw basins and a subsequent synthesis of a selected number of them into larger units.

The first task is focused on answering the question about the correctness of the extracted basins performing an assessment of their boundaries. We based our analysis in two different methods.

A first evaluation was carried out through the overlay of the raw basins shapefile over the independent dataset TUD Karte photo map. In general the comparison proved to be successful. It shows a good matching of basin boundaries over ridgelines. Nevertheless, minor deviations between boundaries were detected in certain areas. Some of them must be recognized as uncertainty associated with the accuracy of our MT-MED DEM. However in other places, as can be seen in the enlarged section in Figure 5.3, the basin boundary does not follow the ridgeline defined by the highest peaks.

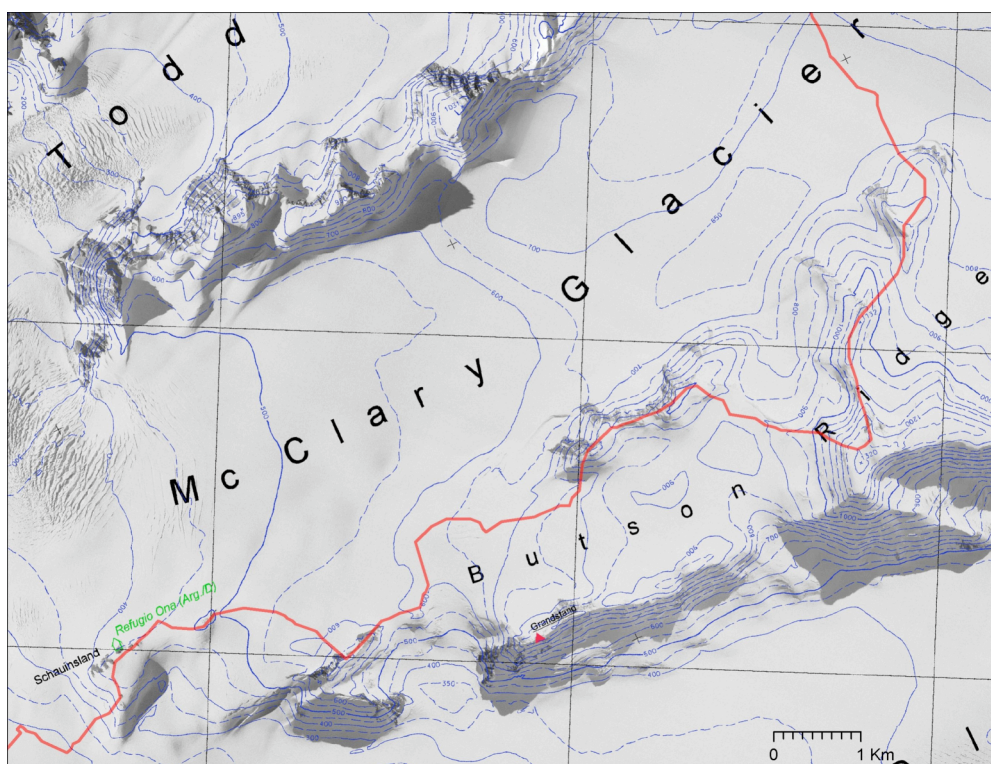


Figure 5.3: Example of derived boundaries: Overlay of automatically extracted basin boundary of McClary and Northeast glaciers in the area of Butson Ridge over the aerial photo map of the Technical University of Darmstadt, TUD Karte (IfPK TUD, 1999). At first sight it may be surprising that the border is not crossing the southern high peaks of the ridge. But comparing the border with the TUD Karte contour lines we must state: The result of MT-MED based catchment extraction shows a quite good agreement with the real situation.

This example is not an error due to wrong DEM elevations or inexactness in the basin extraction method but a correct determination of the boundary. The ice drainage is defined by a lower altitude ice divide.

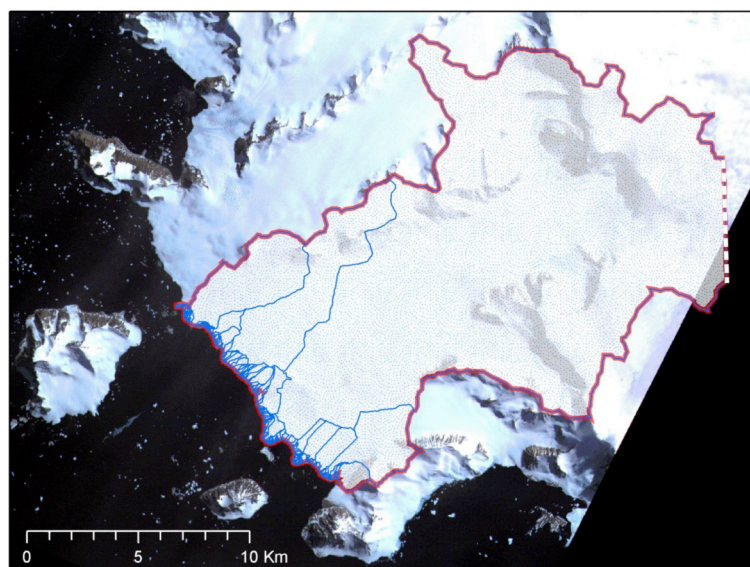
A second method to validate the boundaries of the basins consisted in the interactive inspection of a three dimensional representation of the derived data sets. The raw basin polygons were overlayed together with the contour lines given by the DEM, over the MT-MED DEM draped with the ortho-rectified ASTER image. This technique provided valuable results because it was possible to check the correctness at a conveniently large scale, rotating the model as required to follow the boundaries and visualizing at the same time the topographic information. The result confirms the quality and consistence of the derived raw basin boundaries. The robustness of the derivation method and the common source provided by MT-MED to the other derived data sets are the causes.

The following task consists in the aggregation of the basins. For this we have to build a criterion with the definition of what an ice drainage catchment is. Based on JONES (2002) definition "...catchment area is that area of a watershed that lies upstream from a point", we must precise that "*point*" in this context is in reality a cross section of the river bed. In the case of glacier catchment the corresponding cross section is larger and must be defined conveniently. Thus, ice drainage catchment is the area contributing to the ice flux through a defined cross section. This area is formed by basins that contribute or coalesce into a clear and well defined main ice flux until a certain outlet cross section.

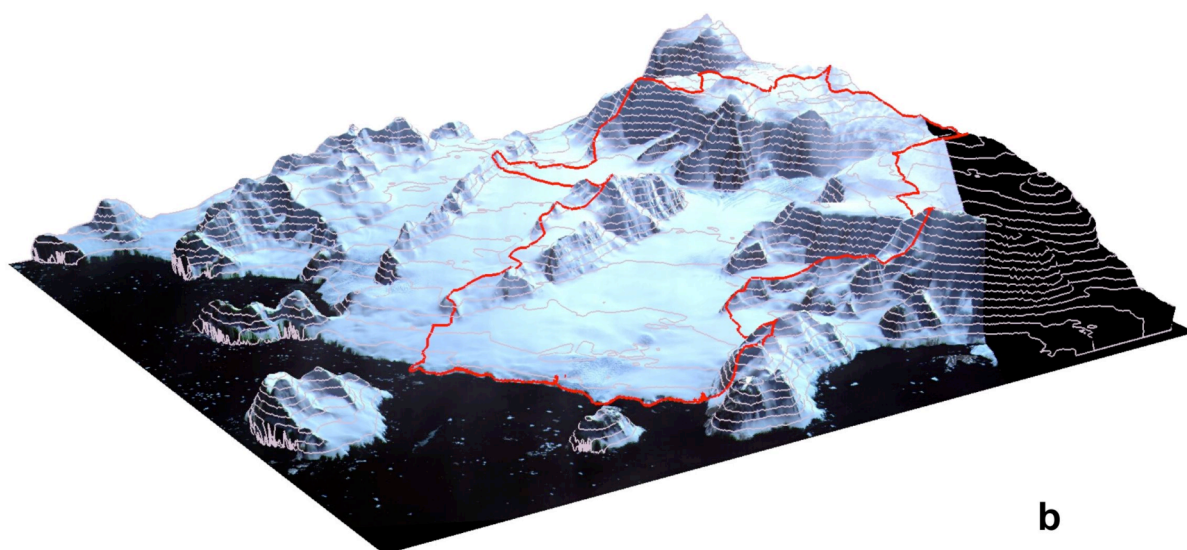
Consequently, the process starts by choosing a cross section that can be used to aggregate all basins that converge to the ice flux that drains this referential main segment. For the case study of the Northeast Glacier the ice drainage catchment that we have defined drains through a cross section situated along the frontal end of the glacier; between a point located at the footstep of Mount Nemesis in the south and a point located in Barbara Island in the north.

The results shown in the Figures 5.4a and 5.4b depict two representations of the Northeast Glacier ice drainage catchment. In Figure 5.4a we see the plan view of the assemblage of 210 raw basins (blue), including noisy mini-basins located in the front, and the catchment boundaries (red) covering an area of 260.95 km². Note that the segment marked as dashed line indicates the limit of the MT-MED DEM used for processing and does not correspond to the ice divide. The extraction method consistently generated large basins in the in the upper parts of Marguerite Bay test site and decreasing smaller ones closer to the coast. The Northeast Glacier catchment has 190 of 210 raw basins smaller than 0.1 km² that totalize only 3.28 km², the 1.26% of the total catchment area. This is observable in Figure 5.2 and Figure 5.4a where a complex of many small basins is located in the lower elevations.

The interactive manipulation of the 3D representation together with the visualization of the topographic data enhanced the capacity to detect conflictive areas and to examine closely boundary sections of interest. Figure 5.4b shows the limits of Northeast Glacier catchment overlaying a 3D view of the terrain as well as the contour lines of the MT-MED DEM. This representation confirms the matching of the ice catchment boundaries with the ridgelines of the surrounding topography. It also depicts the location of the ice divides between McClary Glacier and Northeast Glacier, Northeast Glacier and Swithinbank Glacier, and Northeast Glacier and Uspallata Glacier.



a



b

Figure 5.4: Northeast Glacier catchment area resulting from manual post-processing of the automatically derived raw basin data. For merging all the sub- and mini-basins into one ice drainage catchment, two additional data products have been used: a set of contour lines given by the MT-MED DEM and a set of 3D-views based on the MT-MED DEM draped with one of the ortho-rectified ASTER “L1B” images.

a) Map presentation, showing an ortho-rectified ASTER “L1B” mosaic (SC:AST_L1A.003:2004076906 & SC:AST_L1A.003:2004076911, acquired on 04.01.2001), together with the catchment boundary (red) of the Northeast Glacier and the sub- and mini-basins ice divides (blue) given by the raw product. The dashed red and white line shows the border of the used MT-MED DEM.

b) Three dimensional view of the MT-MED DEM draped with the ortho-rectified ASTER image, together with the contour lines given by the DEM and with the derived ice catchment boundary.

Vertical exaggeration by factor 5.

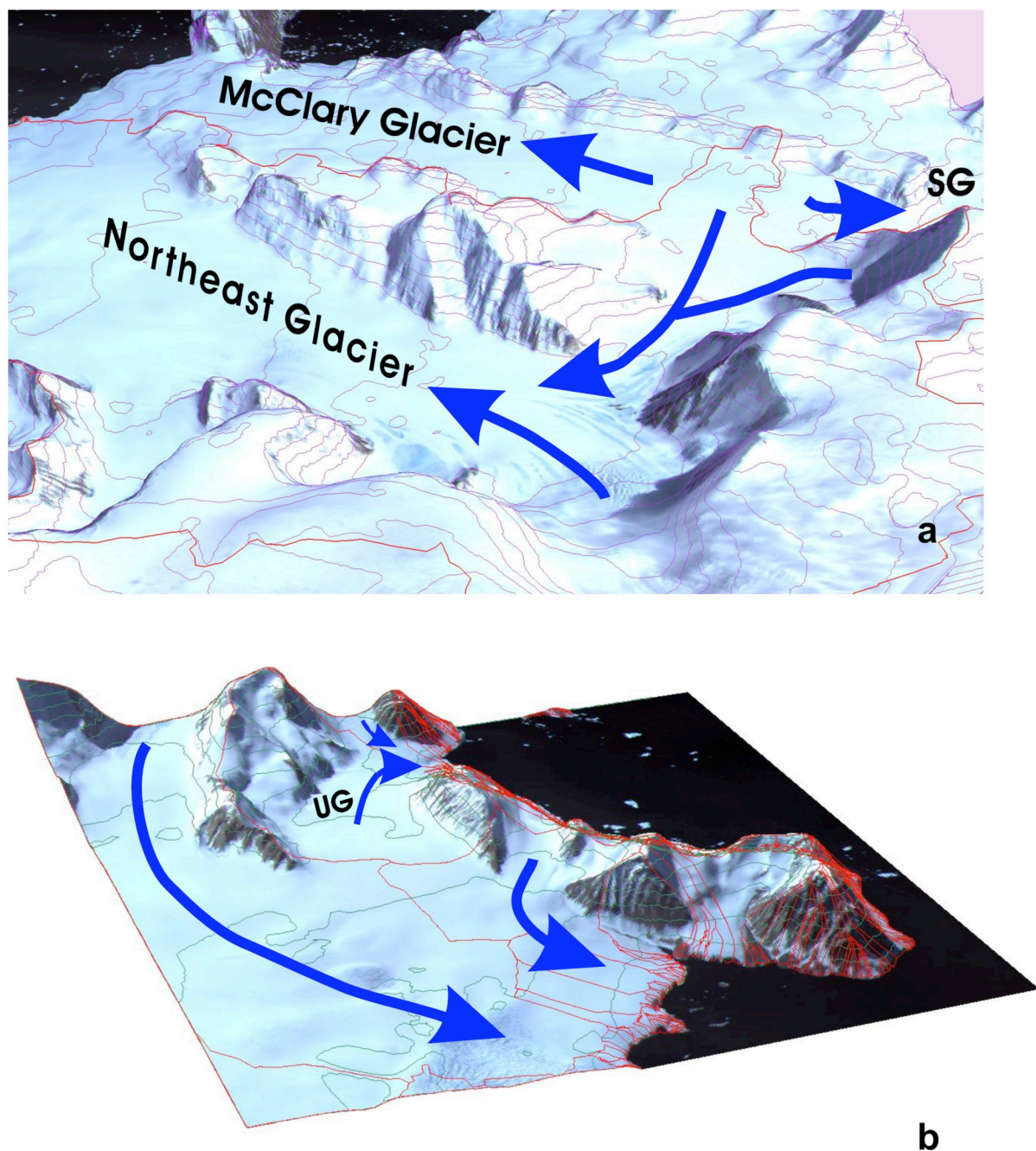


Figure 5.5: Different views on Northeast and McClary glaciers. Flow directions of ice indicated by blue arrows. The 3D-views produced on the basis of an ortho-rectified ASTER “L1B” mosaic (SC:AST_L1A.003:2004076906 & SC:AST_L1A.003:2004076911, acquired on 04.01.2001) draped over the MT-MED digital elevation model with its contour lines.

Vertical exaggeration by factor 5.

a) View from south-east (upper Sodabred Slope) on Northeast Glacier, McClary Glacier and part of Swithinbank Glacier (SG) with Northeast Glacier catchment border traced in red. Note the area where McClary Glacier, one branch of Northeast Glacier and one branch of Swithinbank Glacier have their origin.

b) View from northwest on lowest parts of Northeast Glacier with the ice divide between Northeast Glacier and Neny Fjord. In red all basin borders produced by the automatic extraction. Note the flat ice divide in the center of the image between Northeast Glacier and the southward flowing Uspallata Glacier (UG).

These three boundaries can be better understood when observed using a 3D oblique perspective as is shown in Figure 5.5a. This is a 3D view of the upper section of Northeast Glacier ice catchment seen from the heights of Sodabread Slope. It shows an interesting result from our work. The catchment delineation yields that a feeding branch of Northeast Glacier comes from an ice section located between McClary and Swithinbank Glaciers. This evidence changes the previous estimation for the location of the corresponding ice divides given by WUNDERLE & SCHMIDT (1997).

Finally, Figure 5.5b illustrates the case where the basin boundaries are located in areas of reduced gradients. In such areas it is not evident to which direction the ice flows and consequently to which catchment the basin should be assigned. The verification of the preponderant general flow direction of the basin located southward of Walton Peak was readily performed through inspection with the 3D viewing technique. A divergence of the ice flux was confirmed and consequently the basin was not included in the Northeast Glacier ice catchment.

As a concluding remark the utility of the approach used to obtain the area drained by the Northeast Glacier can be confirmed. The methods proved to be successful in the generation of raw basins data sets. This was verified by evaluation based on associated source material. The subsequent integration of basins to define the Northeast Glacier catchment according to the operational criterion adopted produced highly satisfying results. This also demonstrates the quality which is achieved by the methodology.

6 Results and Outlook

6.1 Review of results

Considering our initial motivation we now review the previous chapters to collect and to comment the results against what has been specified as our original goals.

6.1.1 Data needs

- Measuring glacier morphology and defining ice drainage catchments by means of remote sensing techniques is a basic need of glaciological and climatologic research in Antarctica, especially on the Antarctic Peninsula. In this area rapid changes in the glacial systems have been observed in the last decades. The lack of adequate topographic reference data to monitor these changes has been verified.

We found only six catchment delineation data sets already completed for sectors in the area of the Antarctic Peninsula. Three of this areas correspond to islands: King George Island (3), James Ross Island(1) and Brabant Island (1), and the last is located in a section of Danco Coast and Anvers Island (Figures 2.6-9 and Table 2.1b).

Additionally, we found that appropriate cartographic data covering most parts of the Antarctic Peninsula at medium and large scales does not exist. Consequently, glaciological mapping with the level of detail required is hindered. The RAMP digital elevation model currently is the only standard data set that covers all the Antarctic Peninsula being based in a compilation of most of the geodetic and cartographic information currently available (Figure 2.1). Nevertheless, its spatial resolution and, following our assessment in our test site in Marguerite Bay, its vertical accuracy proved to be largely unsatisfactory.

- The USGS standard digital elevation models (AST14DEM) automatically derived from ASTER scenes and offered in the EOS data catalogs, over polar glaciers do not fulfill the demands we need to define ice divides on the Antarctic Peninsula. Their automated production cannot overcome the problems of weak correlation of nadir and backward bands on flat snow and ice surfaces.

The few available AST14DEMs by now generated for the Antarctic Peninsula region (only 16) contain large voids of no-data, hampering their use for automatic ice drainage catchment delineations (Figures 3.7a-c and Table 3.4).

These findings underpin the need for suitable digital elevation models in order to perform the delineation of ice catchments and the corresponding characterization of ice masses in the Antarctic Peninsula.

6.1.2 New data source

- The ASTER sensor on the Terra satellite provides an important new source of data for modeling the surfaces of Antarctic glaciers and for mapping their catchment basins and drainage areas.

The present availability of suitable ASTER along-track stereo satellite image data to derive digital elevation models over the Antarctic Peninsula has been evaluated. The analysis of 3,280 ASTER day-acquired scenes that cover the land ice over the Antarctic Peninsula were reduced to a subset that contains 84 scenes concentrated on 19 sites (Figure 3.8 and Table 3.5). These scenes were selected from the created ASTER L1A scenes database (see Annex1), under the criteria of an absent or reduced cloud coverage and the concentration on sites that permit multi-temporal processing. Then an on-line visual inspection of their quick-looks was carried out and the final selection performed.

- The use of ASTER stereo data and related procedures for DEM generation and basin extraction on ice and snow covered areas has been established and evaluated.

The design and calibration of the working procedures for the automatic DEM generation as well as for the subsequent basin extraction on ice and snow covered areas were investigated. Two different approaches for DEM derivation have been used: a double median processing and a multi-temporal approach. Then using an automatic GIS-based procedure the basin extraction was performed.

6.1.3 ASTER DEM generation

- For the generation of elevation models using satellite stereo pairs taken by a line-scanner the photogrammetric theory has to be adjusted to the specific geometry of the scanned images with its different along-track and across-track projection.
- For the generation of elevation models based on ASTER level 1A data pre-processing with geometric and radiometric correction of the VNIR bands is necessary. With the ENVI software package an intermediary product “L1B” can be produced which is equivalent to the NASA L1B standard product.
- Using the AsterDTM software for image correlation and co-registration of 3N and 3B bands different parameter sets, varying in “search window size” and

additional parameters like “water detection and “extended correlation”, result in partly different artefacts in form and location.

- Our tests showed that to eliminate or at least to minimize these large errors a median filtering process is much more efficient than averaging by algebraic mean.
- Using the data of only one scene, a double median process (MED-MED model) with first a spatial median (windows size e.g. 9x9 pixels) and then a median over the models resulting from the different parameter combinations (in our case 24 different combinations) are a reasonable approach to derive a DEM.
- In three sectors of the Antarctic Peninsula DEMs derived from single ASTER scenes and draped with the corresponding ortho-rectified ASTER “L1B” scene as three-dimensional view give a very good impression of the area and show a lot of interesting details. This type of visualization proved to be highly satisfactory and promising for digital terrain representation (Virtual Flight Annex 1 and Figures 3.15-17).
- Nevertheless, if presented as DEM only with an artificial shadowing, they reveal artefacts including peaks, pits and wrong triangular facets. Consequently, procedures to overcome these errors had to be developed.
- Using the data of several scenes of the same area, a multi-temporal approach has been implemented. The multi-temporal median (MT-MED) suppresses all artefacts, which are present only within a minority of the models. In this case a relatively simple model of each scene (e.g. derived with a 3x3 search window size and without any additional parameters) can be used.
- With the MT-MED approach the ASTER along-track stereo near infrared nadir- and backward looking bands provide the possibility to create digital elevation models of acceptable accuracy for glaciological studies at catchment scale in the Antarctic Peninsula.

We were able to use the ASTER stereo pairs to derive reliable digital elevation models in three sectors of the Antarctic Peninsula and different levels of evaluation had been performed.

The quantitative evaluation of our ASTER derived DEMs generated by two different approaches reported RMSE of 79.6 m and 47.5 m. This values are far better than the 181.1 m reported for the standard RAMP data set. Our best model accounted 83.9% of the pixels with altitude differences less than 50 m and 48.1% of differences less than 20 m compared with the TUD reference model.

6.1.4 ASTER derived DEMs and Reality

- The Marguerite Bay test-site with its research tradition is a well suited locality for testing new remote sensing methods in glaciological research. Comparison of virtual reality given by ASTER DEMs and corresponding ortho-rectified scenes with terrestrial and aerial photography shows the conformity of virtual

reality with the landscape that can be achieved. This comparison showed a good agreement with the reality (Figure 4.11a-c).

- The independent elevation model of this region, derived from aerial photography by the Technical University of Darmstadt (TUD-DEM), together with its associated Aerial Photo Map (TUD-Karte), though not perfect, are excellent reference data sets to test ASTER derived DEMs against reality.
- Profile analysis performed along four lines (130 km) in the Radar Antarctic Mapping Project (RAMP) model, the ASTER MED-MED DEM and the TUD-DEM shows that
 - by reasons of scale and data source properties RAMP can not be used as a reference or control for ASTER DEMs quality
 - ASTER MED-MED DEM and TUD model correspond in most parts of the profiles quite well. Greater differences in altitude have their origin mainly in localities of very strong decorrelation between 3N- and 3B-bands of the scenes. Here artefacts in nearly all single models exist and remain effective also in the median product.
- The multi-temporal approach (MT-MED model), based on time-series of scenes covering the same area, is suited to overcome the problem of artefacts. Comparisons between single models and the MED-MED model by means of scatterograms as well as visual inspection of DEMs with artificial hill shading suggest that the model with minimum resource consumption (3x3 search window size, no additional parameters) is the best to be used for this approach.
- Profile analysis comparing the same profile lines in the ASTER MT-MED DEM, the ASTER MED-MED DEM and the TUD-DEM show, that
 - the suppression of artefacts is significant
 - we do not find further artefacts in MT-MED model
 - some deviations of MT-MED and MED-MED against the TUD model can be attributed to errors in the TUD DEM or as changes over time in nature between the late 80ies (TUDs aerial photography) and November 2001 (first ASTER scene of Marguerite Bay)
- Aerial and statistical comparisons between ASTER derived DEMs, RAMP and TUD reference models confirm and quantify the insights gained from the profile comparisons.

Less than 10 m difference in altitude against the TUD model show 6.5 % of the pixels in the RAMP model, 19,9 % in the MED-MED model and 26,0 % within the MT-MED model. Less than 20 m difference in altitude against the TUD show 13,2 % of RAMP-pixels, 38,6 % of MED-MED pixels, and 48,1 of all pixels in MT-MED model. More than 100 m difference in altitude against the TUD model show 45,8 % of the RAMP pixels, 11,1 % of MED-MED pixels, and 3,8 % of all pixels in the MT-MED mode. The outstanding “large errors” of more than 50 m in the MT-MED model are not resulting from wrong altitudes but from errors in co-registration and horizontal mismatching over steep slopes.

6.1.5 Drainage Basin Delineation

- For basin extraction its possible to use an hydrological model with an algorithm implemented in ArcGIS, in spite of the differences between water and ice catchments types.
- The raw basin product generated by this algorithm shows two aspects:
 - Along the model boundary and along the coastline (ice cliff) a great amount of irregular mini-basins are generated, which have to be eliminated by post-processing.
 - Ice divides calculated for the higher parts of the glacier can be considered as reliable.
- The post-processing of the raw basins in order to aggregate basins of minor hierarchy can be assisted conveniently by additional products generated from the derived DEM:
 - The prerequisite for catchment delineation is the definition of the correspondent outflow cross-section of the glacier under consideration.
 - Interactive processing by means of additional information given from the same model (contour lines, three dimensional perspective views) allow to merge the raw basins to final glacier catchments. When ice flow direction vectors are not available it is useful to consider the orientation of slopes and the contour lines given by the model in cases where it is not evident to which catchment an individual basin is associated.
 - Examples on the location of ice divides found between the Northeast Glacier, McClary Glacier and Swithinbank Glacier, on one side; and the ice divide found between Northeast Glacier and Uspallata Glacier on the other side, confirm the relevance of the new ASTER based methodology.

6.2 Outlook

During the development of this work several ideas related to the further use of the digital elevation models generated for the Antarctic Peninsula region become more and more possible. These new applications are now possible thanks to the improved quality obtained from the two approaches that we have finally used.

The following use of ASTER derived DEMs is suggested for future activities:

6.2.1 Use of DEMs and corresponding orthorectified images

- There are new possibilities of visual inspection of the Antarctic Peninsula's scenery by means of interactive handling of virtual ASTER based landscapes. Three-dimensional representations can be made based on ASTER derived DEMs draped with the orthorectified images. The adequate spatial resolution of the models admit a representation of the surface for interactive manipulation (scaling, rotation, etc.) and for the generation of animations and virtual flights.
- ASTER derived DEMs provide a new basis for the generation of vector fields of ice-movement by different techniques. Using ortho-rectified multi-temporal VNIR ASTER data determination of vectors by the feature tracking technique can be implemented. At the same time, both the improved spatial resolution and improved accuracy of ASTER derived DEMs will also be suitable for the elimination of the topographic effect required in the generation of vector fields of ice-movement by INSAR-technology.

6.2.2 Enhancement of GLIMS database over the Antarctic Peninsula

- In the Antarctic Peninsula GLIMS database the locations of more than 950 glaciers flowing to Weddell Sea and Bellingshausen Sea are defined by corresponding points located along the central flowline of the glaciers. After defining the respective outflow cross-sections the method shall allow to generate automatically the corresponding ice drainage catchment boundaries.
- Required additional parameters needed for the classification of glaciological features can be derived when catchment polygons are created. Measurement of distances and areas along and across the ice drainage features can be easily implemented by a GIS-based approach. Additional other geographical statistics can also be performed (e.g. median altitude of basins, etc.).

6.2.3 Glacier basin delineations

- The analysis of the automatically generated raw basins can be complemented by the use of glacier velocity vectors to reach the most detailed level of mapping. This information would be conclusive in cases where glacier basins coalesce and the location of the boundary is not clear.

References

- ABRAMS, M., HOOK, S., RAMACHANDRAN, B. (2002): ASTER User Handbook, ver.2. Jet Propulsion Laboratory, EROS Data Center.
- ABRAMS, M. (2005): ASTER. MS-PowerPoint presentation given at JPL (02.08.2005), (http://asterweb.jpl.nasa.gov/aster_talk.zip, visited 05.02.2006).
- ADD CONSORTIUM (2004): Antarctic Digital Database (www.add.scar.org). Online topographic database of Antarctica. Cambridge, Scientific Committee on Antarctic Research. (<http://www.add.scar.org/>, Antarctic Digital Database v4.1. Visited 18.07.2005)
- AHLERT, S., ARIGONY, J. & SIMÕES, J. C. (2005): Classificação morfológica das geleiras da ilha Brabant, Antártica através de sensoriamento remoto. Anais XII Simpósio Brasileiro de Sensoriamento Remoto, Goiânia, Brasil, 16-21 abril 2005, INPE, p. 2431-2438.
- ANIELLO, P. (2003): Using ASTER DEMs to Produce IKONOS Orthophotos. Earth Observation Magazine, Vol.12 (5), p. 22-26.
- BAMBER, J.L. (1994): A digital elevation model of the Antarctic ice sheet derived from ERS-1 altimeter data and comparison with terrestrial measurements. Annals of Glaciology, Vol.20, p.48-54.
- BAMBER, J.L. & R.A. BINDSCHADLER (1997): An improved elevation dataset for climate and ice-sheet modelling: validation with satellite imagery. Annals of Glaciology Vol.25, p.438-444.
- BAMBER, J. L., VAUGHAN, D. G. & JOUGHIN, I. (2000): Widespread Complex Flow in the Interior of the Antarctic Ice Sheet. Science, Vol.287, p.1248-1250.
- BAMBER, J. & GOMEZ-DANS, J. L. (2005): The Accuracy of Digital Elevation Models of the Antarctic Continent, Earth and Planetary Science Letters, Vol.237, p.516-523.
- BARKER, P. F., DALZIEL, I. W. D. & STORY, B. C. (1991): Tectonic development of the Scotia Arc Region. In: The Geology of Antarctica, Tingey, R. J. (Ed.). Oxford Science

Publication, Monograph on Geology and Geophysics, 27, Claredon Press, Oxford. p.215-248

BARNARD, S. T. & FISCHLER, M. A. (1982): Computational Stereo. Computing Surveys, Vol.14(4), p. 553-572.

BAS – BRITISH ANTARCTIC SURVEY (1963): Falkland Islands Dependencies, Graham Land W6866 Topographic Map. DCS 601, DOS 610 (D501) SERIES: 1:200,000. Stanfords catalogue number 8745.

BLACK, R. B. (1945): Geographical Operations from East Base, United States Antarctic Service Expedition, 1939-1941. Proceedings of the American Philosophical Society, Vol.89(1), p. 4-12.

BRAUN, M., SIMÕES, J. C., VOGT, S., BREMER, U. F., BLINDOW, N., PFENDER, M., SAURER, H., AQUINO, F. E. & FERRON, F. (2001): An Improved Topographic Database For King George Island: Compilation, Application And Outlook. Antarctic Science, Vol.13(1), p. 41-52.

BREMER U. F., ARIGONY-NETO, J. & SIMOES, J. C. (2004): Teledetecção de mudanças nas bacias de drenagem do gelo da ilha Rei George, Shetlands do Sul, Antártica, entre 1956 e 2000. Pesquisa Antártica Brasileira, Vol.4, p. 37-48.

CLARK, A. N. (1992): Longman Dictionary of Geography, 4th impression. Longman Group, UK.

CUARTERO, A., FELICÍSIMO, A.M. AND ARIZA, F.J. (2005): Accuracy, reliability, and depuration of SPOT HRV and Terra ASTER digital elevation models. IEEE Transactions on Geoscience and Remote Sensing, Vol.43(2), p.404-407.

CUTTER, S. L., GOLLEDGE, R. & GRAF, W. (2002): The Big Questions in Geography. The Professional Geographer, Vol.54(3), p. 305–317.

DOMACK, E., BURNETT, A. & LEVENTER, A. (2003): Environmental setting of the Antarctic Peninsula. In: Antarctic Peninsula Climate Variability: Historical and Paleoenvironmental perspectives, Domack, E., Leventer, A., Burnett, A., Bindshadler, R., Convey, P. & Kirby, M. (Eds.). Antarctic Research Series Vol. 79, p.1-13.

DORSEY, H. G. (1945): An Antarctic Mountain Weather Station. Proceedings of the American Philosophical Society, Vol. 89(1), p. 344-363.

DOWDESWELL, J. A., GLAZOVSKY, A. F. & MACHERET, Y. Y. (1995): Ice divides and drainage basins on the ice caps of Josef Land, Russian High Arctic, defined from Landsat, KFA-1000, and ERS-1 SAR satellite imagery. Arctic and Alpine Research, Vol.27(3), p. 264-270.

DREWRY, D. J. (1983): The surface of the Antarctic Ice Sheet. Sheet 2 of Antarctica: Glaciological and Geophysical Folio, D. J. Drewry, Ed., Scott Polar Research Institute, 1 p.

ERSDAC - EARTH REMOTE SENSING DATA ANALYSIS CENTER (2005): ASTER User's Guide Part III - DEM Product (L4A01), Ver.1.1., July 2005.

ESRI - ENVIRONMENTAL SYSTEMS RESEARCH INSTITUTE, INC. (1998): ESRI Shapefile Technical Description -An ESRI White Paper. July 1998, 34 p.

- EVANS, D.J.A. (2003): Introduction to glacial landsystems. In: Evans, D.J.A. (Ed.), *Glacial Landsystems*. Arnold, London, p.1-11.
- FAIRFIELD, J. & LEYMARIE, P. (1991): Drainage Networks from Grid Digital Elevation Models. *Water Resources Research*, Vol.27(5), p. 709-717.
- FELICISIMO, A. (1994): Parametric statistical method for error detection in digital elevation models. *ISPRS Journal of Photogrammetry and Remote Sensing*, Vol.49(4), p. 29–33.
- FOGG, G. E. (1992): *A Study of Antarctic Science*. Studies in Polar Research. Cambridge University Press, Cambridge. 483 p.
- FUCHS, V. (1982): *Of Ice and Men – the history of British Antarctic Survey*. BAS Printers Limited, Over Wallop, England.
- FUJISADA, H., BAILEY, G. B., KELLY, G. G., HARA, S. & ABRAMS, M. J. (2005): Aster DEM Performance. *IEEE Transactions on Geoscience and Remote Sensing*, Vol.43(12), p. 2707-2714.
- GIOVINETTO, M. (1964): The drainage systems of Antarctica: Accumulation. In: Mellor, M. (Ed.) *Antarctic Snow and Ice Studies*. Antarctic Research Series, Vol.2, p. 127-155.
- GIOVINETTO, M. & BENTLEY, C.R. (1985): Surface balance in ice drainage systems of Antarctica. *Antarctic Journal of the United States*, Vol.20, p. 6–13.
- GLOBE TASK TEAM ET AL. (HASTINGS, DAVID A., PAULA K. DUNBAR, GERALD M. ELPHINSTONE, MARK BOOTZ, HIROSHI MURAKAMI, HIROSHI MARUYAMA, HIROSHI MASAHARU, PETER HOLLAND, JOHN PAYNE, NEVIN A. BRYANT, THOMAS L. LOGAN, J.-P. MULLER, GUNTER SCHREIER, AND JOHN S. MACDONALD, EDS.) (1999): *The Global Land One-kilometer Base Elevation (GLOBE) Digital Elevation Model, Version 1.0*. National Oceanic and Atmospheric Administration, National Geophysical Data Center, 325 Broadway, Boulder, Colorado 80303, U.S.A. Digital data base on the World Wide Web (URL: <http://www.ngdc.noaa.gov/mgg/topo/globe.html>) and CD-ROMs.
- GOSSMANN, H. (1984): *Satelliten Thermabilder Ein Neues Hilfsmittel für die Umweltforschung?*. Bundesforschungsanstalt für Landeskunde und Raumordnung. Fernenkundung in Raumordnung und Städtebau, Heft 16.
- HANSEN, J., RUEDY, R., GLASCOE, J., SATO, M., (1999): GISS analysis of surface temperature change. *Journal Geophysical Research*, Vol. 104, 30997.
- HANSOM, J. D. & GORDON, J. E. (1998): *Antarctic Environments and Resources – A Geographical Perspective*. Addison Wesley Longman Limited, New York, U.S.A.
- HARDY, R. J., BAMBER, J. L. & ORFORD, S. (2000): The delineation of drainage basins on the Greenland ice sheet for mass-balance analyses using a combined modeling and geographical information system approach. *Hydrological Processes*, Vol.14, p. 1931-1941.
- HENGL, T., GRUBER, S. & SHRESTHA, D. P. (2004): Reduction of errors in digital terrain parameters used in soil-landscape modelling. *International Journal of Applied Earth Observation and Geoinformation*, Vol.5, p. 97–112.

- HERZFELD, U. C. & MATASSA, M. S. (1999): *GEOSAT Radar Altimeter DEM Atlas of Antarctica North of 72.1 Degrees South*. Boulder, CO, USA: National Snow and Ice Data Center. Digital media
- HIRANO, A., WELCH, R. & LANG, H. (2003): Mapping from ASTER stereo image data: DEM validation and accuracy assessment. *ISPRS Journal of Photogrammetry & Remote Sensing* Vol.57, p. 356– 370
- HUTCHINSON, M. F. (1989): A new procedure for gridding elevation and stream line data with automatic removal of spurious pits. *Journal of Hydrology*, Vol.106, p. 211-232.
- HO - HYDROGRAPHIC OFFICE, MINISTRY OF DEFENCE, UK (1995): Rothera Point to Neny Island Hydrographic Chart, Edition 2. Scale 1 : 100 000, Ref. Number 3580.
- IfPK TUD – INSTITUT FÜR PHOTOGRAMMETRIE UND KARTOGRAPHIE TECHNISCHE UNIVERSITÄT DARMSTADT, (1999): Aerial Photo Map – 1:50.000. Base General San Martin, Baie Marguerite, Antarctic Peninsula. Produced by the „Dynamische Prozesse in antarktischen Geosystemen (DYPAG)“, research project done in collaboration with the Bundesamt für Kartographie und Geodäsie (BKG) and the Institut für Physische Geographie (IPG) – Albert-Ludwigs-Universität Freiburg and supported by the Bundesministerium für Bildung, Wissenschaft Forschung und Technologie (bmb+f).
- IHDE, J., ECK, J. & SCHIRMER, U. (2002): A Digital Terrain Ice Model of Antarctica derived by ERS Radar Altimeter Data, CD-ROM, BKG.
- INGÓLFSSON, Ó., HJORT, C. & HUMLUM, O. (2003): Glacial and Climate History of the Antarctic Peninsula since the Last Glacial Maximum. *Arctic, Antarctic, and Alpine Research*, Vol.35(2), p.175–186.
- IPG – INSTITUT FÜR PHYSISCHE GEOGRAPHIE UNIVERSITÄT FREIBURG (1998): DYPAG-Abschlussbericht, Band 1.
- IWASAKI, A. & FUJISADA, H. (2005): ASTER Geometric performance. *IEEE Transactions on Geoscience and Remote Sensing*, Vol.43(12), p. 2700-2706
- JONES, R. (2002): Algorithms for using a DEM for mapping catchment areas of stream sediment samples. *Computers & Geosciences* Vol.28, p. 1051–1060.
- JONES, N. L., WRIGHT, S. G. & MAIDMENT, D. R. (1990): Watershed delineation with triangle-based terrain models. *Journal of Hydraulic Engineering*, Vol.116, p. 1232-1251.
- KÄÄB, A. (2002): Monitoring high-mountain terrain deformation from repeated air- and spaceborne optical data: examples using digital aerial imagery and ASTER data. *ISPRS Journal of Photogrammetry & Remote Sensing* Vol.57, p.39–52
- KÄÄB, A. (2005): Remote Sensing of Mountains and Permafrost Creep. *Schriftenreihe Physische Geographie Glaziologie und Geomorphodynamik*, Vol.48, Geographisches Institut der Universität Zürich. 266 p.
- KING, J. (1994): Recent climate variability in the vicinity of the Antarctic Peninsula. *International Journal of Climatology*, Vol.14 (4), p.357-369.
- KING, J.C., HARANGOZO, S.A. (1998): Climate change in the western Antarctic Peninsula since 1945: observations and possible causes. *Annals of Glaciology*, Vol.27, p.571-575.

- KING, J. C., TURNER, J., MARSHALL, G. J., CONNOLLEY, W. M. & LACHLAN-COPE, T. A. (2003): Antarctic Peninsula climate variability and its causes as revealed by analysis of instrumental records. In: Antarctic Peninsula Climate Variability: Historical and Paleoenvironmental perspectives, Domack, E., Leventer, A., Burnett, A., Bindschadler, R., Convey, P. & Kirby, M. (Eds.). Antarctic Research Series Vol.79, p. 17-30.
- KNOWLES, P. H. (1945): Geology of the Southern Palmer Peninsula, Antarctica. Proceedings of the American Philosophical Society, Vol.89(1), p. 132-145.
- LANG, O. (2002): Radar Remote Sensing in Western Antarctica with Special Emphasis in Differential Interferometry. Dissertation, Bayerische Julius-Maximilians Universität Würzburg. 143 p.
- LAUDON, T. S., BEHRENDT, J. C. & CHRISTENSEN, N. J. (1964): Petrology of rocks collected on the Antarctic peninsula traverse. Journal of Sedimentary Research, June 1964; Vol. 34(2), p. 360-364.
- LIGHT, D.L., BROWN, D., COLVOCORESSES, A., DOYLE, F., DAVIES, M., ELLASAL, A. , JUNKINS, J., MANENT, J., MCKENNEY, A., UNDREJKA, R. & WOOD G. (1980): Satellite photogrammetry, in: Manual of Photogrammetry (Chapter XVII), p. 883-977.
- LIU, H., JEZEK, K. & LI, B. (1999): Development of Antarctic digital elevation model by integrating cartographic and remotely sensed data: A geographic information system based approach. Journal of Geophysical Research Vol.104, NO.B10, p.23,199-23,213.
- LIU, H. (1999): Development of an Antarctic Digital Elevation Model. BPRC Report No.19, Byrd Polar Research Center, The Ohio State University, Columbus, Ohio, 157 p.
- LIU, H., JEZEK, K., LI, B. & ZHAO, Z. (2001): Radarsat Antarctic Mapping Project Digital Elevation Model Version 2. Boulder, CO: National Snow and Ice Data Center. Digital media.
- MARK, D. M. & SMITH, B. (2004): A science of Topography: From qualitative ontology to digital representations. In: Bishop, M.P. and Shroder Jr., J.F., eds., Geographic Information Science and Mountain Geomorphology, Springer, Praxis, Chichester, UK, 75-100
- MOORE, I. D. & GRAYSON, R. B. (1991): Terrain-based catchment partitioning and runoff prediction using vector elevation data. Water Resources Research, Vol.27, p. 1177-1191.
- NASA EOS (2006): Algorithm Theoretical Basis Documents (ATBD). (http://eospsso.gsfc.nasa.gov/eos_homepage/for_scientists/atbd/viewInstrument.php?instrument=4, visited June 2006)
- NELSON, E. J., JONES, N. L. & MILLER, A. W. (1994): Algorithm for precise drainage-basin delineation. Journal of Hydraulic Engineering, Vol.120, p. 298-312.
- O'CALLAGHAN, J. F. & MARK, D. M. (1984): The Extraction of Drainage Networks From Digital Elevation Data. Computer Vision, Graphics and Image Processing, Vol.28, p. 328-344.
- PALMER, J.F. & HOFFMAN, R.E. (2001): Rating reliability and representation validity in scenic landscape assessments. Landscape and Urban Planning, Vol.54, p. 149-161.

- PATERSON, W. S. B. (1994): The physics of glaciers. 3. Auflage. Elsevier Science Ltd., Oxford, 480 S.
- PAUL, F. (2001): Evaluation of different methods for glacier mapping using Landsat TM. EARSel eProceedings, Vol.1, p.239-245.
- PAUL, F., KÄÄB, A., MAISCH, M., KELLENBERGER, T. & HAEBERLI, W. (2002): The new remote-sensing-derived Swiss glacier inventory: I. Methods. Annals of Glaciology, Vol.34, p.355-361.
- PAUL, F., HUGGEL, C. & KÄÄB, A. (2004): Mapping of debris-covered glaciers using multispectral and DEM classification techniques. Remote Sensing of Environment, Vol.89(4), p. 510-518.
- PRICE, S. F. & WHILLANS, I. M. (1998): Delineation of catchment boundary using velocity and elevation measures. Annals of Glaciology, Vol.27, p. 140-44.
- RABASSA, J., SKVARCA, P., BERTANI, L. & MAZZONI, E. (1983): Glacier inventory of James Ross and Vega Islands, Antarctic Peninsula. Annals of Glaciology, Vol.3, p. 260-264.
- RAU, F. (2004): Schneeeigenschaften und Gletscherzonen der Antarktischen Halbinsel im Radarbild - Thermische Phänomene der Schnee- und Firndecken im Hinterland der großen Schelfeisabbrüche. PhD Thesis, Fakultät für Forst und Umweltwissenschaften Universität Freiburg, 193 p.
- RAUP, B. H., KIEFFER, H. H., HARE, T. M & KARGEL, J. S. (2000): Generation of Data Acquisition Requests for the ASTER Satellite Instrument for Monitoring a Globally Distributed Target: Glaciers. IEEE Transactions on Geoscience and Remote Sensing, Vol. 38(2), March 2000, p. 1105-1112.
- REYNOLDS, J. M. (1981): The distribution of mean annual temperature in the Antarctic Peninsula. British Antarctic Survey Bulletin Vol.59, p.123-131.
- RIGNOT, E. & THOMAS, R. H. (2002): Mass balance of Polar Ice Sheets. Science Vol.297, p.1502-1506
- RSI, RESEARCH SYSTEMS INC. (2005): ENVI v4.2 On Line Help. (<http://www.ittvis.com/tutorials/index.asp>, last visited June 2006)
- SCAMBOS, T., HULBE, C. & FAHNESTOCK, M. (2003): Climate-induced ice shelf disintegration in the Antarctic Peninsula. In: Antarctic Peninsula Climate Variability: Historical and Paleoenvironmental perspectives, Domack, E., Leventer, A., Burnett, A., Bindshadler, R., Convey, P. & Kirby, M. (Eds.). Antarctic Research Series Vol. 79, p. 79-92
- SCAR - SCIENTIFIC COMMITTEE ON ANTARCTIC RESEARCH (2006): SCAR Composite Gazetteer of Antarctica. (http://www3.pnra.it/SCAR_GAZE, last visited 4 May 2006).
- SCHENK, T. (1999): Image matching fundamentals. In: Digital Photogrammetry, Vol.I, p. 231-266
- SCHWAB, A. (2000): Reliefanalytische Verfahren zur Abschätzung nächtlicher Kaltluftbewegungen. – Dissertation, Geowissenschaftlichen Fakultät der Universität Freiburg. Freiburger Geographische Hefte 61. (<http://www.geographie.uni-freiburg.de/ipg/publikationen/fgh61.html>, last visited 2 June 2006).

SCHNEIDER, C. (1998): Zur raumzeitlichen Differenzierung der Energiebilanz und des Zustandes der Schneedecke auf zwei Gletschern der Marguerite Bay, Antarktische Halbinsel. PhD Thesis, Freiburger Geographische Helfte 56, 251 p.

SIMÕES, J.C.; BREMER, U.F.; AQUINO, F.E.; & FERRON, F.A. (1999): Morphology and variations of glacial drainage basins in the King George Island ice field, Antarctica. *Annals of Glaciology*, 29, p. 220-224.

SKVARCA, P. & DE ANGELIS, H. (2003): Impact assessment of regional climatic warming on glaciers and ice shelves of the northeastern Antarctic Peninsula. In: *Antarctic Peninsula Climate Variability: Historical and Paleoenvironmental perspectives*, Domack, E., Leventer, A., Burnett, A., Bindshadler, R., Convey, P. & Kirby, M. (Eds.). *Antarctic Research Series Vol.79*, p. 69-78

TARBOTON, D. G. (1997): A new method for the determination of flow direction and upslope areas in grid digital elevation models. *Water Resources Research*, Vol.33, p. 309-319.

TAYLOR, J., (1997): *An Introduction to Error Analysis: The Study of Uncertainties In Physical Measurements*. University Science Books, Sausalito, CA, 327 pp.

TOUTIN, T. (2001): Elevation Modelling from Satellite visible and infrared (VIR) data. A review. *International Journal of Remote Sensing*, Vol.22(6), p. 1097-1125.

TOUTIN, T. & CHENG, P (2002): Comparison of automated digital elevation model extraction results using along-track ASTER and across-track SPOT stereo images. *SPIE Journal, Optical Engineering*, Vol.41(9), p. 2102-2106, September 2002.

TOUTIN, T. (2004): Geometric processing of remote sensing images: models, algorithms and methods. *International Journal of Remote Sensing*, Vol.25(10), p. 1893-1924.

TURNER, J., LACHLAN-COPE, T. A., THOMAS, J. P. & COLWELL, S. R. (1995): The synoptic origins of precipitation over the Antarctic Peninsula. *Antarctic Science*, Vol.7, p. 327-337.

USGS – U.S. GEOLOGICAL SURVEY (1994): *Spatial Data Transfer Standard*. Gaithersberg, Maryland: National Institute of Standards, FIPS Publication 173.

USGS - U.S. GEOLOGICAL SURVEY (1996): *GTOPO30 Digital Elevation Model data set*. (<http://edc.usgs.gov/products/elevation/gtopo30/gtopo30.html> , last visited March 2006)

VAUGHAN, D. (1999): A review of the causes and mechanisms that may lead to globally significant change in the Antarctic ice sheet. A preparatory review prepared by D. G. Vaughan, NERC British Antarctic Survey in conjunction with Det Norske Veritas under contract of the UK Dept. of Environment, Transport and the Regions.

VAUGHAN, D. G., BAMBER, J. L., GIOVINETTO, M., RUSSELL, J. & COOPER, A. P. R. (1999): Reassessment of Net Surface Mass Balance in Antarctica. *Journal of Climate*, Vol.12, p. 933-946.

VAUGHAN, D. G., MARSHALL, G. J., CONNOLLEY, W. M., KING, J. C. & MULVANEY, R. (2001): Devil in the Detail. *Science*, Vol. 293, Issue 5536, p1777-1779.

VAUGHAN, D. G. (2005): How Does the Antarctic Ice Sheet Affect Sea Level Rise?. *Science*, Vol. 308.p. 1877-1878

- WADE, A. (1945): An introduction to the Symposium on Scientific Results of the United States Antarctic Service Expedition, 1939-1941. Proceedings of the American Philosophical Society, Vol.89(1), p. 1-3.
- WATANABE, H. (2005): Global Coverage of ASTER And Its Accuracy and Availability. 11th International Symposium on Remote Sensing, Chiba University, Japan, December 13, 2005.
- WECHSLER, S. P. (2000): Effect of DEM Uncertainty on Topographic Parameters, DEM Scale and Terrain Evaluation. PhD Thesis, 380 p.
- WEIDICK, A. & MORRIS, E. M. (1998): Local glaciers surrounding the continental ice sheets. In: Haeberle, W., Hoelzle, M. & Suter, S. (eds.): Into the second century of world-wide glacier monitoring – prospects and strategies. UNESCO, Paris, Studies and Reports in Hydrology 56, p. 197-207.
- WELCH, R., JORDAN, T., LANG, H. & MURAKAMI, H. (1998): ASTER as a Source for Topographic Data in the Late 1990's. IEEE Transactions on Geoscience and Remote Sensing, Vol.36(4), p. 1282-1289.
- WILLIAMS, C. BOIES, C & DOMACK, E. (1989): Glacial drainage systems along the Antarctic Peninsula and Palmer Archipelago, United States Antarctic Journal, Vol.24(5), p. 116-117.
- WOOD, J., (1996): The Geomorphological Characterization of Digital Elevation Models. Ph.D. Dissertation, Department of Geography, University of Leicester, Leicester, UK, 1996.
- WROBEL, B. P.;WALTER, H.; FRIEHL, M.;HOPPE, U.; SCHLÜTER, M. & STEINECK, D. (2000): A Topographical Data Set of the Glacier Region at San Martin, Marguerite Bay, Antarctic Peninsula, generated by Digital Photogrammetry. Polarforschung, Vol.67(1/2), p. 53-63.
- WUNDERLE, S. (1996): Die Schneedeckendynamik der Antarktischen Halbinsel und ihre Erfassung mit aktiven und passiven Fernerkundungsverfahren. PhD Thesis, Freiburger Geographische Hefte 48, 172 p.
- WUNDERLE, S. & SCHMIDT, J. (1997): Fluctuations and Ice-Flow Velocity of the Northeast and McClary Glacier on the Antarctic Peninsula derived from Remote Sensing Data and SAR interferometry. Polarforschung, Vol. 67(1/2), p. 41-51.
- ZWALLY, J. & BRENNER, A. (1998): *Seasat and GEOSAT altimetry for the Antarctic and Greenland Ice Sheets*. Boulder, CO, USA: National Snow and Ice Data Center. CD-ROM.